UNIVERSITY OF CALGARY

"Integration of the seismic data with rock physics and reservoir modeling in the FRS project"

by

"Davood Nowroozi Charandabi"

A THESIS

SUBMITTED TO THE FACULTY OF GRADUATE STUDIES

IN PARTIAL FULFILMENT OF THE REQUIREMENTS FOR THE

DEGREE OF "DOCTOR OF PHYLOSOPHY"

GRADUATE PROGRAM IN GEOLOGY AND GEOPHYSICS

CALGARY, ALBERTA

JUNE, 2017

Abstract

This thesis is related to a CO_2 injection project from the well logging to seismic modeling and imaging, so many disciplines are involved. The reservoir is at a shallow depth of 300 m so it is in a low temperature and low pressure state. A black-oil reservoir simulation was not appropriate for the study, so a compositional method was used for the fluid simulation. The change of phase possible around the anticipated pressure and temperature for CO_2 injection is another limitation for a compositional simulation, so the gas phase injection was selected for the simulation modelling. Results show that the CO_2 injection will decrease the density of formation around 3%, and the P-wave velocity between 7 and 15%. It can also affect the S-wave velocity, and in the seismic studies, there is enough of a change in the S-wave velocity to consider PS and SS-wave data for the reservoir characterization. The rock physics equations solved for the pressure changes by the Equation of State for CO_2 and for the brine and a set of curves related to the fluid mixed type were introduced. After 5 years of injection at bottom-hole pressure of 4.9 MPa, the injected CO_2 plume has a diameter of 185 m

The seismic studies based on the rock physics models show that the fluids mix type is a determinative factor for interpretability of a reservoir. Seismic forward modelling was undertaken using both acoustic and elastic finite difference approaches, and imaging was done using reverse time migration. For patchy or semi-patchy saturation, mixed with a linear (or near linear) converter, the saturation is calculated with an acceptable error by the acoustic, seismic response. In a parabolic converter as Reuss average in a fine mixed type, the time-lapse acoustic response is insufficient to identify saturation explicitly.

Acknowledgements

Foremost, I would like to express my sincere gratitude to my supervisor Dr. Don Lawton for his unsparing guidance and support that helped me a lot to accomplish writing this thesis. I thank the sponsors of CREWES for continued support and CMC Research Institutes Inc for access to the data. This research was funded by CREWES industrial sponsors and NSERC (Natural Science and Engineering Research Council of Canada) through the grant CRDPJ 461179-13. I would like to thank Schlumberger for the use of OMNI, VISTA, Petrel and ECLIPSE and Computer Modeling Group LTD. for CMG simulation software.

Also, I would like to thank Amir Ghaderi for help and supervise the reservoir simulation section, Hassan Khaniani for significant aid in the seismic imaging, Mohammad Soroush for assist in the geomodeling, Helen Isaac for the seismic data processing and Andreas Cordsen for some excellent points in the seismic design.The VSP Seismic data acquisition has done by CREWES team (Malcolm Bertram, Kevin Hall, and Kevin Bertram).The CREWES project was managed successfully during my research by Laura Baird, that I would like thank her.

Dedication

To Ava and Alma

Table of Contents

Abstract ii
Acknowledgements iii
Dedication iv
Table of Contents v
List of Tables viii
List of Figures and Illustrations ix
List of Symbols, Abbreviations and Nomenclature xxiii

CHAPTER 1. INTRODUCTION 1
1.1 Research procedure and resources 1
1.2 Accomplishments and goals 2
1.2.1 Software 5
1.2.2 Data Resources 6
1.2.3 Background 6
1.3 CO_2 sequestration 10
1.3.1 Introduction 10
1.3.2 CO_2 in the atmosphere 10
1.4 CO_2 sequestration, a method for decreasing CO_2 concentration in the atmosphere 14
1.4.1 CO_2 trapping mechanism 15
1.4.2 CO_2 gas injection in the brine 18

CHAPTER 2. THE FIELD RESEARCH STATION (FRS) PROJECT 19
2.1 Introduction 19
2.2 Geological setting 21
2.3 Petrophysical study and Interpretation 25
2.4 Core study 30
2.5 Lithology and Mineral study of the Belly River sandstone 32
2.6 Core analysis 34

CHAPTER 3. SEISMIC DESIGN FOR 3C-4D PROPOSE IN THE FRS 36
3.1 Introduction 36
3.2 Background information 36
3.3 Considerations for a 4D seismic design and acquisition 37
3.4 Targets 38
3.5 Frequency content 39
3.6 Velocity-depth function 40
3.7 Bin size 40
3.8 Box size and geometry 42
3.9 Design option 42
3.9.1 The acquisition parameters 43
3.10 PS survey design 48
3.11 A criterion for fold distribution 51
3.12 Improving PS fold coverage: randomize pattern 52

CHAPTER 4. THE BASELINE SEISMIC DATA, INTERPRETATION AND GEOMODEL DEVELOPMENT....55
4.1 Introduction....55
4.2 Field acquisition....55
4.3 LMO effect and fold taper....58
4.4 Seismic data resolution and coherency....59
4.5 Seismic PP and PS-wave data after processing....61
4.6 Seismic interpretation: The phantom horizons methods....64
4.7 Well ties....65
4.8 Attributes study....72
4.8.1 Generic Inversion....72
4.9 Fault detection attributes....74
4.9.1 Structural smoothing....75
4.9.2 Dip Deviation....75
4.9.3 Chaos....75
4.9.4 Variance....75
4.9.5 Ant tracking....76
4.10 The velocity model....81
4.11 Geomodel of the project area....82
4.12 Introduction to Geostatistics:....85
4.12.1 Variogram:....85
4.12.2 Variogram models:....86
4.12.3 Anisotropies....88
4.12.4 Kriging:....89
4.13 Primary models....89
4.14 The isotropic geomodel for fluid simulation....91
4.15 The geomodel for the seismic modeling and imaging....94

CHAPTER 5. RESERVOIR FLUID SIMULATION FOR FRS PROJECT....96
5.1 Introduction....96
5.2 Initial state of the FRS reservoir....97
5.3 The reservoir concepts and simulation methods....99
5.3.1 Relative permeability....99
5.3.2 Anisotropy of the permeability....101
5.3.3 Formation compressibility....102
5.3.4 Darcy's law....104
5.3.5 Simulation methods....105
5.3.6 Black-oil simulator....108
5.3.7 Specifications and Advantages of Compositional Simulator....109
5.4 The result of the reservoir simulation....110
5.5 Simulation results....112
5.6 The CO_2 gas injection effect on fluid phase in the reservoir....116
5.7 Injection with different BHP....117
5.8 Long-term prediction....118
5.9 Conservation of CO_2 mass after stopping the injection....122
5.10 An injection/production pattern for improved gas phase injection....126
5.11 Injection at higher BHP....129

CHAPTER 6. ROCK PHYSICS STUDY FOR THE FRS PROJECT 140
6.1 Introduction 140
6.2 The complexity of a solid or fluid 141
6.3 The physical properties of the mix phases 144
6.4 Voigt and Reuss average 144
6.5 Brie's average for fluid mix 146
6.6 Hashin-Shtrikman (HS) Bounds 147
6.7 Fluid properties 151
6.7.1 Brine 151
6.7.2 Carbon dioxide 155
6.8 Mixed fluid properties 157
6.9 Effect of pore pressure on seismic velocity 160
6.10 The physical properties in the matrix 162
6.11 Fluid substitution 164
6.12 Model Assumption 165
6.13 Practical usage of the Gassmann's equation 167
6.14 The CO_2 gas injection effect on the formation velocity in the field and lab test .169
6.15 Time delay caused by the injected fluid 173
6.16 The formation velocity and density after CO_2 injection in the FRS reservoir 174
6.17 The velocity and density model based on the rock physics study 176

CHAPTER 7. SEISMIC IMAGING 183
7.1 Introduction 183
7.2 The research method 184
7.3 Acoustic forward modeling strategy 185
7.4 RTM migration strategy 186
7.5 Boundary Conditions 187
7.5.1 The Perfectly Matched Layer (PML) 188
7.6 Low-frequency noise due to RTM procedure 192
7.7 Condition for successful 4D study 193
7.8 Interpretability of an event 194
7.9 Plume size and velocity variation 195
7.10 A diffusive and solid velocity model 196
7.11 Seismic response of a solid and diffusive velocity model 198
7.12 Acquisition geometry for 4D seismic surveys 205
7.13 Seismic interpretability of a diffusive velocity model 209
7.14 Seismic imaging for FRS project 211
7.15 FRS reservoir seismic time-lapse results 226
7.16 The elastic medium and the seismic response of the reservoir 232
7.17 Seismic response of CO_2 injection in a complex geological setting 236

CHAPTER 8. CONCLUSIONS AND THE RECOMMENDATIONS FOR FUTURE WORK 240
8.1 The research trend in the future 242

APPENDICES 245

REFERENCES 250

List of Tables

Table 1-1: The large-scale CCS were operated in Canada (Source: Global CCS Institute)......... 15

Table 2-1: The mineral types in the reservoir zone by the well log data analysis (from Figure 2-12).. 32

Table 2-2.Effective porosity and water and gas saturation in the core 34

Table 2-3.The measured total porosity and water and gas saturation in the core 34

Table 3-1.The Targets were considered for the seismic design purpose. 38

Table 3-2. The acquisition parameters. 43

Table 3-3.The variance test result for 12 different acquisition pattern. 54

Table 5-1.The initial properties of the injection target 99

Table 5-2. The different BHP and related figures. 129

Table 6-1. The fraction of the minerals in the reservoir based on the well log data analysis. 163

Table 6-2.The mixed minerals bulk and shear modulus calculated by three average methods. . 163

Table 7-1: Acquisition parameters and patterns 207

Table 8-1: The specification of FWI study. 244

List of Figures and Illustrations

Figure 1-1.The disciplines used for the reservoir integration in this thesis 2

Figure 1-2.Schematic view of the research procedure. 3

Figure 1-3: The concentration of CO_2 and the temperature of the atmosphere from late Precambrian to recent. The blue line demonstrates the temperature fluctuations, (Scotese et al. 2002) (Pagani et al. 2005). 11

Figure 1-4. Temperature, CO_2, and dust concentration in the atmosphere from 400,000 years ago. Temperature has a strong correlation with the CO_2 concentration in the atmosphere and reverses relation with the dust. The loess sediments are a real proof of dust concentration in the atmosphere during the cold stages (Petit et al., 1999). 12

Figure 1-5. CO_2 in atmosphere and temperature from 50,000 years ago, by Vostok ice cores study (Petit et al., 1999, and joannenova.com.au). 13

Figure 1-6: The concentration of CO_2 in the atmosphere since 1958 to 2015 (Measured at the Mauna Loa Observatory, https://www.co2.earth). 13

Figure 1-7: World energy consumption by source (based on data from BP Statistical review, 2014) 14

Figure 1-8. CO_2 trapping mechanisms and increasing CO_2 storage security over time (Pooladi-Darvish, 2009). 17

Figure 2-1.The map of project area, it is located in 017-16-W4. 20

Figure 2-2. The satellite image of the FRS, the green rectangle shows the project area and the yellow points are the well sites with log data (Source: Google Earth). 20

Figure 2-3.The outcrop of two upper formations in the Belly River group in the Bow River valley near the Bow City, west of project area and 7.5 km far from the well site (AGS, 2010). 22

Figure 2-4.The stratigraphic correlation and table of formations in the southern plain (Alberta Geology Survey (AGS), 2010). 23

Figure 2-5. The Stratigraphic chart for the well 10-22 (from well 10-22 drilling data combined with the adjacent wells data, Schlumberger, 2015). 24

Figure 2-6. P-wave versus s-wave slowness in the well 10-22. The color-bar shows the gamma ray log, and the size of circles are for density porosity. The Vp/Vs ratio is between 1.8 in the deep layers to 2.6 in the shallow formations. 26

Figure 2-7. The well log data for seismic porosity (SPHI), density porosity (DPHZ), TCMR porosity, the average of mentioned three porosity (PHI), the permeability (KTIM: Timure-Coates, KSDR: Schlumberger-Doll-Research model), upscaled data for PHI and KTIM, and Vp/Vs ratio near the injection zone. 27

Figure 2-8: The Timur-Coated model permeability (mD) vs. density porosity (v/v). The different statistical populations are recognizable because of the different lithological and sedimentation condition. 28

Figure 2-9: Petrophysical interpretation result for the injection zone and around. The minerals type was characterized by the well logs. 29

Figure 2-10. There is no relation between KTIM and other log data. Just a meaningful relation is between CMFF (free fluid porosity (index) from CMR) and KTIM. The coordinate is full logarithmic scale. For more information see Appendix A. 30

Figure 2-11. Core photo from the injection zone (sandstone) (taken by Schlumberger). 31

Figure 2-12: The result of the mineral types discriminated by the well log data (Kirk Osadetz, personal conversation) 33

Figure 2-13: Before and after log-to-core calibration of K_INT data for the injector 35

Figure 3-1. Frequency analysis: for the shallowest target (A) and the deepest targets (B) 39

Figure 3-2. A linear function for velocity is used for calculation of bin size and migration aperture. Velocity function for FRS project regards to well log data (wells 11-22-17-16 (a) and 7-22-17-16 (b) and 10-22-17-16 (c)) is V=V0+kz=2650+z. 41

Figure 3-3. Bin size for the shallow target with 80Hz max frequency (left) and the deep target with 65Hz (right). 42

Figure 3-4.The survey geometry. The red points demonstrates shot points, and the blue ones are receivers. There are a dense shot and receiver points in the mid of survey with dimension equal to 500*500 m. 44

Figure 3-5. A. The fold map. The highest numerical range for the fold is 220 for both shown by the red color in the scalebar. The yellow circle shows the fold range between 30-40. B. The fold map for offset 0-700 m. 44

Figure 3-6. A. The azimuth distribution in the full fold zone. It shows a proper azimuthal coverage; the azimuth depends on the shorter offsets. B. The offset distribution in the full fold box. The acquisition covers full offset ranges. 45

Figure 3-7. A. Azimuth distribution in the target range (0-700 m offsets). B. Offset distribution in the full fold box for 0-700 m. 45

Figure 3-8. A. Offset redundancy, the target zone demonstrated by the black lines. B. Azimuth redundancy, the number of traces that fall in each section; gaps indicate missing azimuth 46

Figure 3-9. A. Histogram of Fold, the numbers of bins that fall in each range of fold values. B. Histogram of Offset, the number of traces that fall in each range of Offset values 46

Figure 3-10. A. Histogram of azimuth, the number of traces that fall in each range of azimuth values. B. Offset versus azimuth diagram. 47

Figure 3-11. The PS fold map (non-asymptotic method) for a target in 400 m depth, Vp to Vs ratio is considered equal 2. 48

Figure 3-12. A. The PS azimuth distribution in the full fold boxes. B. Offset distribution for the PS wave. 49

Figure 3-13. Offset redundancy for PS wave, the number of traces that fall in each section; gaps indicate missing offsets.The curve of boomerang shape distribution is a function of p to s wave velocities ratio. 49

Figure 3-14. Azimuth redundancy for PS wave, the number of traces that fall in each section; gaps indicate missing azimuth.It shows a proper azimuth distribution. 50

Figure 3-15.A sample of the suggested regular survey (rectangular box) and randomized receivers pattern. 53

Figure 3-16. The fold map for regular rectangular box pattern (left) and randomized receivers pattern (right) 53

Figure 4-1. The seismic survey map of FRS project. The blue points are the receivers and red shows the sources. Two pipelines caused some change in the shot point coordinates. (Satellite image source: Google Earth) 56

Figure 4-2.The PP-wave fold map for (a). total nominal fold and (b). 0-300 m source-receiver offsets. 57

Figure 4-3. (a). Azimuth distribution and (b). Offset distribution 57

Figure 4-4. The PS-wave fold map for the target in the 300 m depth. 58

Figure 4-5.The low fold zone and acquisition on the acquired seismic data. 59

Figure 4-6.The configuration of acquisition were used for the processing. Left survey shows and right is the same survey after eliminating the dense center region. 60

Figure 4-7. The result of processing for the acquired PP seismic data in (left) and after eliminating the dense source-receiver CMPs (right).The arrows show the main differences between two seismic sections. 61

Figure 4-8. The seismic data, A. processed PP-wave data, B. processed PS wave data 62

Figure 4-9. PP-wave migrated seismic section on inline 41 63

Figure 4-10. PS-wave migrated seismic section on inline 41 63

Figure 4-11.The TWT conversion diagram between PP and PS seismic sections. The injection target at 233 ms for PP time and 364 ms for PS time. It was calculated from the P and S-wave slowness logs. The velocity for no well log data zone calculated by the seismic analysis. 64

Figure 4-12. Flowchart that shows the simplified stages of work for a general structural interpretation. 67

Figure 4-13: schematic of procedure used for well to seismic calibration 67

Figure 4-14. Ricker wavelet and the synthetic seismogram from well log data against processed seismic data. 68

Figure 4-15.The wavelet calculated by extended white method for the Sensor processed data set. The reflectors correlation is acceptable in the 200-300 ms range. 68

Figure 4-16. PP seismic interpretation in time domain including the main formations and phantom layers (time domain). The line is passing of the main well. 69

Figure 4-17. The top Basal Belly River sandstone as the top of the reservoir in the seismic cube in time domain. 69

Figure 4-18. Time structure of the top of the Basal Belly River sandstone.................................. 70

Figure 4-19. Depth structure of the top of Basal Belly River Formation. 71

Figure 4-20.Genetic Inversion (time slice is 235 ms near the top of reservoir) 73

Figure 4-21.Genetic Inversion on the top reservoir surface 73

Figure 4-22. Fault detection using the multi-attribute method. 74

Figure 4-23.Smoothing attribute is the first step of the multi-attribute method for faults recognition. 77

Figure 4-24.The single attribute study (dip deviation) for fault recognition. 77

Figure 4-25.The chaos attribute applied to the smoothed data cube.. 78

Figure 4-26. The variance attribute applied to the smoothed data cube. 78

Figure 4-27. AntTrack attribute applied to the Smoothed Chaos data cube. 79

Figure 4-28. AntTrack attribute on the Smoothed Variance attribute result 79

Figure 4-29.A multi-attribute map (Structural- Chaos – Ant track) for the fault discrimination. 80

Figure 4-30. A multi-attribute map (Structural - Variance – Ant track) for the fault discrimination. 80

Figure 4-31.The P-wave velocity in the well 10-22 with simplified gradients for time to depth conversion 81

Figure 4-32.The time to depth conversion for the PP, PS and SS wave in the well 10-22........... 82

Figure 4-33: The procedure for producing a geomodel in the FRS project................................. 83

Figure 4-34. The upscaled well log data for building geomodel in well 10-22 before permeability calibration. 84

Figure 4-35: A typical Variogram diagram and main parameters. 86

Figure 4-36: Three variogram models. 87

Figure 4-37: The histogram (to check the distribution type of the data) and semi-variance with a spherical model fitted for the density porosity variable (The nugget effect = 0.0002080, the sill= 0.0023660, the range= 2.0700 m for h=15 cm in the well direction). . 88

Figure 4-38. A geomodel made from 11 wells and a small cell size around the injection well. The dimension of geomodel is 3900*3000 m... 90

Figure 4-39.The geometry of layers in the geomodel from the seismic interpretation. Colors shows the main geological events and formations, dimension is 1000*1000 m 90

Figure 4-40.The revised geomodel derived from log data from three wells. The dimension of geomodel is 1000*1000 m. 91

Figure 4-41.The porosity geomodel made up with the well log data. The geomodel size is 1000*1000*240 m. 92

Figure 4-42. A section of the xy permeability geomodel shows the grid size in the injection layer and others. The red rectangle shows the injection layer (i.e. Basal Belly River) 92

Figure 4-43. A section of geomodel for the permeability in z direction...................................... 93

Figure 4-44. A section of geomodel for the porosity.. 93

Figure 4-45.The P-wave velocity model. This model was used for the seismic imaging. 94

Figure 4-46. The density model used for seismic modelling.. 95

Figure 4-47: The P-wave velocity oriented by seismic layers (a 2D view of Figure 4-45 in a section passing of the 10-22 well). The section is W-E and view is to the North. 95

Figure 5-1. Disciplinary contributions to reservoir flow modeling (after Fanchi, 2006) 96

Figure 5-2.Hydrostatic and lithostatic pressure in the reservoir; the latter is calculated from the density log data. 98

Figure 5-3. Trapping efficiency in sandstone based on previous work in Alberta (Bachu, 2013) 101

Figure 5-4. The relative permeability curve calculated for the reservoir. 101

Figure 5-5.Geomechanical properties of the reservoir in the well 10-22-17-16. The compressibility was demonstrated by c_f (the unit is 1/GPa). 103

Figure 5-6. Volume elements or grid block in reservoir simulation. 105

Figure 5-7.Reservoir gridblock, coordinate and directions 107

Figure 5-8. Appropriate situation for Compositional and black-oil and compositional simulators for oil and gas phases (ECLIPSE course material, 2016). 109

Figure 5-9: The phase diagram of carbon dioxide and pressure and temperature condition in the FRS project (Phase diagram from ChemicaLogic Corporation). 111

Figure 5-10. The phase diagram of CO_2 for the reservoir condition. This figure is a magnified image of Figure 5-9 near the reservoir condition. 111

Figure 5-11.The simulation result for the reservoir pressure by the CO_2 injection for five years with BHP=4.9 MPa. The scale is same as Figure 5-12.The unit for the pressure is MPa. 113

Figure 5-12. The CO_2 gas saturation for the five-year injection by BHP=49 bar (4.9 MPa) 114

Figure 5-13: Diagrams showing the result of injection for BHP=49 bar for five years (the x-axes show the year of injection) a. Cumulative gas mass (kg), b. Cumulative gas volume (m^3), c. Daily volume (SC) injected gas rate (m^3/day), d. Daily mass injected gas rate (kg/day), e.Well bottom hole pressure (kPa), f. Well block pressure (kPa), (SC stand for Standard Condition - 15^{o}C and 1 bar). 115

Figure 5-14.Results of visual inspection of the brine+CO_2-reacted sample; deposits of NaCl crystals (salt precipitation) and calcite dissolution textures at the outer surface of the sample in a lab test (Rathnaweera et al., 2016). 116

Figure 5-15. Gas saturation after five-year injection with BHP=48 bar. 118

Figure 5-16.The saturation after five-year injection by constant BHP. 119

Figure 5-17. Predicted CO2 saturation five years after discontinuing the injection 119

Figure 5-18. Predicted CO2 saturation ten years after stopping the injection 119

Figure 5-19. Predicted CO2 saturation 20 years after stopping the injection 120

Figure 5-20. Predicted CO2 saturation 40 years after stopping the injection 120

Figure 5-21. Predicted CO2 saturation 60 years after stopping the injection 120

Figure 5-22. Predicted CO2 saturation 80 years after stopping the injection 121

Figure 5-23. Predicted CO2 saturation 100 years after stopping the injection 121

Figure 5-24. The Bottom-hole pressure changes over a century. The pressure will be equal to initial reservoir pressure after the year 2044 (28 years after beginning the injection process). 122

Figure 5-25.The thickness of the plume in the injection point after stopping the injection. After 100 years, all cells in the plume show a saturation rate around the trapping efficiency, and so continued gas migration will change to a mainly horizontal direction.. 123

Figure 5-26. The result of long-term monitoring for the gas saturation after 233 years from the start of injection. The maximum plume thickness is 2 m. 126

Figure 5-27.The pressure condition in 25,50 and 200 m distance of injection well after one-year injection. 127

Figure 5-28.The plume size after 1 and 5-year injection and 100-year post-injection. 128

Figure 5-29. The production well(s) in X m distance to decrease the reservoir pressure, it can help to inject more mass in the gas phase. T is the angle between the wells. X, T and the number of wells are variable. 128

Figure 5-30. CO_2 saturation at pressure of 51.41 bar @ 20^{o}C. (a). after one-year injection(2017), (b). after five-year injection(2021), (c). after ten years of stopping the injection(2031). 130

Figure 5-31.The pressure change in the reservoir for BHP=51.41 bar and temperature =20^{o}C, (a). one year after injection, (b). Five-Year injection, (c). Two years after stopping the injection. 131

Figure 5-32.The cumulative gas mass (kg) injected at the constant BHP=51.41 bar. 132

Figure 5-33.The cumulative gas volume (m^3) in the standard condition (red graph) and the reservoir condition (blue graph) injected at the constant BHP=51.41 bar. 132

Figure 5-34. CO_2 saturation at pressure of 53.41 bar @ 20^{o}C. (a). after one-year injection(2017), (b). after five-year injection(2021), (c). after ten years of stopping the injection(2031). ... 133

Figure 5-35. The cumulative gas mass (kg) injected at the constant BHP=53.41 bar ... 134

Figure 5-36. The cumulative gas volume (m^3) in the standard condition (red graph) and the reservoir condition (blue graph) injected at the constant BHP=53.41 bar ... 134

Figure 5-37. CO_2 saturation at pressure of 55.41 bar @ 20^{o}C. (a). after one-year injection(2017), (b). after five-year injection(2021), (c). after ten years of stopping the injection(2031). ... 135

Figure 5-38. The cumulative gas mass (kg) injected at the constant BHP=55.41 bar ... 136

Figure 5-39. The cumulative gas volume (m^3) in the standard condition (red graph) and the reservoir condition (blue graph) injected at the constant BHP=55.41 bar ... 136

Figure 5-40. CO_2 saturation at pressure of 57.41 bar @ 20^{o}C. (a). after one-year injection(2017), (b). after five-year injection(2021), (c). after ten years of stopping the injection(2031). ... 137

Figure 5-41. The cumulative gas mass (kg) injected at the constant BHP=57.3 bar ... 138

Figure 5-42. The cumulative gas volume (m^3) in the standard condition (red graph) and the reservoir condition (blue graph) injected at the constant BHP=57.3 bar ... 138

Figure 5-43. The pressure over 5 years of injection at BHP=57.3 bar (5.73 MPa), and 10 years after injection. ... 139

Figure 5-44. Cumulative CO_2 mass for different BHP for a five-year injection plan. An exponential function describes the relation between BHP and injected gas mass. ... 139

Figure 6-1. The fluid substitution procedure used in this chapter. ... 142

Figure 6-2. A microscopic thin section of sandstone in the polarization microscope. It demonstrates a variety of minerals in a rock (source: micro.magnet.fsu.edu). ... 143

Figure 6-3: The bulk modulus for the mix of a porous sand with 100% plagioclase (as immature sand) and water. ... 146

Figure 6-4.Two phase material in the Hashin-Shtrikman bounds. ... 148

Figure 6-5.The average bulk modulus for a mixed case of quartz and calcite. The blue curves show Voigt, Reuss and VRH averages. The red curve is HS+ and green is HS-. The VRH is very near to Hashin-Shtrikman averages. ... 150

Figure 6-6. Matrix Properties calculated by Voigt (blue), Reuss (red) and VRH (green) methods for a mix of pure quartz and wet clay. ... 150

Figure 6-7. The density, bulk modulus and P-wave velocity of brine and water temperature from 13 to 28 ^{o}C (with 5 ^{o}C steps) and salinity equal to 8000 ppm from 2 to 8 MPa. 153

Figure 6-8.The density, bulk modulus and P-wave velocity of water and brine (salinity=8000 ppm) as a function of temperature. Each curve belongs to the pressure from 1 to 10 MPa in steps of 2 MPa... 154

Figure 6-9. The viscosity of brine (based on Batzle-Wang (1992)), the pressure does not have a significant influence on the brine viscosity.. 155

Figure 6-10.The bulk modulus and density of CO_2 at different pressures and temperatures. EoS described by Span and Wagner (1996) were used to generate the diagram (drawn by Yam,2011). 156

Figure 6-11. Density of CO_2 for 13 and 20^{o}C and 23<p<57 bar. 156

Figure 6-12. P-wave velocity of CO_2 versus pressure at T= 13 and 20 ^{o}C (the velocity calculated upper than 4 MPa at T=13 ^{o}C was unstable) 157

Figure 6-13. The density of the mixed fluid in T=13.8^{o}C and pressure from 30 to 60 bar (3 to 6 MPa).. 158

Figure 6-14. The bulk modulus for the mix of brine with 8000 ppm salinity and CO_2 in 13 ^{o}C and 4.5 MPa (45 bar). In the mixed fluid condition (as CO_2 and brine), the Hashin-Shtrikman averages (upper and lower bounds) are using the Reuss Average. 159

Figure 6-15. The P-wave velocity in the mixed fluid of the brine (8000 ppm salinity) and CO2 in T=13 oC and P=4.5 MPa (the reservoir condition during the injection procedure). 159

Figure 6-16. The bulk modulus of the mixed fluid with a different fraction of CO_2 and different mixed condition in P=30 bar (3 MPa) and 45 bar (4.5 MPa)............................. 160

Figure 6-17. The velocity change in the fluid phase of the reservoir (brine+CO_2) for a semi-patchy mixed fluid by pressure. The pressure increased from 3 to 4.5 MPa. 161

Figure 6-18: Bulk modulus estimation for different fraction of fluid mix by Reuss average (fine mixed fluids) in T=60 C and different pressures (16 to 40 MPa) (P and T for Nisku aquifer condition, WASP project; Nowroozi, 2014).. 162

Figure 6-19. The error in density calculated by the mineral discrimination method and well log data in the injection horizon.. 164

Figure 6-20. The influence of mixing method on the P-wave velocity. Reuss average is suitable for a fine mixed fluid, and the velocity change, in this case, is very dramatic in the low saturation of CO2.Over 15% of CO_2 saturation there is a slight increase in the velocity of the formation (a test with the low-frequency laboratory data). The Voigt average is for a patchy mixing, and the velocity change is almost a linear decrease with saturation (a test with the high-frequency laboratory data) (Smith, 2003). 170

Figure 6-21. P-wave velocity versus CO_2 saturation from a field study. The blue dots show the field data measurements from time-lapse well logs at the Nagaoka site in Japan (Lumley, 2010). 171

Figure 6-22. Results of lab test for the CO_2 injection into a sandstone (Alemo et al., 2011)..... 172

Figure 6-23. Laboratory and theoretical experiences for CO_2 and a water flood effect on the P-wave velocities (Wang, 2001). 172

Figure 6-24: Bulk modulus for CO_2 and brine mixed phase. 175

Figure 6-25. P-wave velocity after CO_2 injection in the reservoir calculated by Gassmann's equation, the shape of Vp diagram is a function of an average method for the fluid mix (CO_2+brine) properties calculation. The maximum possible CO_2 gas saturation in the FRS reservoir can reach to 50%. 175

Figure 6-26: The physical properties (S-wave velocity and density) change as a linear function of the CO_2 saturation in the reservoir condition in FRS project. 176

Figure 6-27: The density, and shear wave velocity change during the gas injection by the constant bottom hole pressure (49.4 bar for five-year). The shear modulus remains constant after injection, but decreasing in the density can make a small increase in the Vs value. 178

Figure 6-28. The P-wave velocity model based on the Reuss average method that shows a fine mixed fluid type after 1, 3 and five years' injection. This model shows a uniform velocity change in the reservoir volume. 179

Figure 6-29. The P-wave velocity model based on the Brie's average method that shows a semi-patchy mixed fluid type after 1, 3 and five years' injection...................................... 180

Figure 6-30. The P-wave velocity model based on the VRH average method that shows a semi-patchy mixed fluid type after 1, 3 and five years' injection...................................... 181

Figure 6-31. The P-wave velocity model based on the Voigt average method that shows a fully-patchy mixed fluid type after 1, 3 and five years' injection...................................... 182

Figure 7-1. Description of the abbreviations. 187

Figure 7-2.The Boundary condition in the seismic model. The orange rectangles show the internal boundaries. 188

Figure 7-3. The model boundary is shown by ABCD. AB, CD, and AD have a SPML boundary condition, and BC is a free surface boundary. 191

Figure 7-4. The different components of the wave at the PML absorption boundaries for a P-wave source in an elastic homogenous medium. 192

Figure 7-5. The internal structure of diffusive (an injective or productive point in the middle of the ellipsoid) and solid velocity models. The reduction is linear from the center to the outer bound in the diffusive model. The unit of velocity is m/s. The dimension of the ellipsoid will define with the big and small diameter (a,b). 197

Figure 7-6.The velocity model with two diffusive and solid velocity changes. The velocity change in the center of diffusive model or whole solid shape is -7% equal -175 m/s (2325 m/s). The size is ellipsoids are (200,40m). 198

Figure 7-7.The Uz component of the seismic response of diffusive and solid models in a homogeneous medium. The left is the SM(m), and the right is SM(m)-SM(baseline). 199

Figure 7-8. RTM(SM(m)) for Uz component and RTM(SM(m))-RTM(SM(baseline)) 199

Figure 7-9. RTM(SM(m)) for pressure component and RTM(SM(m))-RTM(SM(baseline)) .. 199

Figure 7-10.The velocity model for a. Three-layer model as baseline b. Model a with diffusive and solid velocity models as monitored model c. Subtracted result (Monitored-Baseline model) 201

Figure 7-11.The pressure component of the seismic acoustic model for: a. 3-layer baseline b. Baseline plus diffusive and solid velocity ellipsoids c. The difference 202

Figure 7-12. The Uz component (a.SM(base,Uz), b.SM(monitor,UZ), c.SM(base,Uz)-SM(monitor,Uz)). It is similar to the pressure component but with the lower amplitudes. 202

Figure 7-13.The Ux component for (a.) 3-layer baseline (b.) Baseline plus diffusive and solid velocity ellipsoids; (c.) The difference 203

Figure 7-14. a. diff (RTM (SM (baseline, Pressure))), b. diff (RTM (SM (m, Pressure))), ... 203

Figure 7-15. a. diff (RTM (SM (baseline, Ux))), b. diff (RTM (SM (m, Ux))),......................... 204

Figure 7-16. a. (RTM (SM (baseline, P))), b. (RTM (SM (m, P))), ... 204

Figure 7-17. (RTM (SM (baseline, Ux))), (RTM (SM (m, Ux))), ... 205

Figure 7-18. The diffusive velocity and density models for a 7% and 3% change in the ellipsoid shape. The ellipsoid dimensions are180m wide and 10m in thickness 207

Figure 7-19. The seismic model (a) and migrated section (b) for the surface survey. 207

Figure 7-20. A seismic record and migrated section for the VSP acquisition 208

Figure 7-21. a. The seismic response of cross well acquisition pattern of the model in Figure 7-18. b. After eliminating the surface and shot effects. c. The migrated data (from a). d. The noise reduced migrated section. 208

Figure 7-22: The seismic response (column b) and RTM result (column c) for a model (100 * 20 m) with a different velocity anomalies (column a). Higher velocity difference causes greater amplitudes for the surface acquisition survey. 210

Figure 7-23: The seismic response (column b) and RTM result (column c) for two models with a different plume size and 5% velocity change in the center of ellipsoids in column a. a1: 50*20 m and a2:200*20 m. 211

Figure 7-24. The baseline P (a) and S-wave (b) velocity (m/s) and density (c) (gr/cc) models. The reservoir saturation effect on the velocity and density after injection is included in these models. 213

Figure 7-25. The migrated acoustic Uz component for the baseline velocity and density model (surface seismic, five shots and 996 receivers). 214

Figure 7-26: The velocity and density models before and after five years' injection with a BHP=49.4 bar in the gas phase for the VRH average. The original physical properties oriented by the seismic interpretation result. a. The base model before injection. b. The perturbation model base on the saturation results. c. The physical properties after injection. d. The magnified figures on the reservoir zone. 215

Figure 7-27: The seismic model generated by the velocity and density patterns introduced in Figure 7-26 (VRH average) for a surface seismic experience with one shot in x=500 m and receivers with 1 m interval and from 0 to 1000 m. a. Baseline seismic model. b. Baseline RTM result. c. Monitor seismic model. d. Monitor RTM result. e. The difference between monitored and baseline seismic models (amplitude ten times magnified). f. The difference between RTM results (amplitude ten times multipled). 216

Figure 7-28.The amplitude of the seismic acoustic seismic modeling (Figure 7-27.A, section AA' on the red line) for the baseline, after one, three and five-year injection (VRH average method). 217

Figure 7-29: The seismic model generated by the velocity and density patterns introduced in Figure 7-26 (VRH model) for a VSP survey with one shot at x=400 m and receivers with 1 m interval at x= 600 and extending from 0 to 600 m depth. a. Baseline seismic model. b. Baseline RTM result. c. Monitor seismic model. d. Monitor RTM result. e. The difference between monitored and baseline seismic models. f. The difference between RTM results. 218

Figure 7-30. A VSP seismic model and image for a wide source to receivers aperture (400 m distance). a and b show the seismic model and image for the baseline and c and d are for the five-year injection calculated by Reuss average, d and e are the difference of the 5-year injected model and baseline (wavelet: 55 Hz Ricker). 219

Figure 7-31. The seismic model generated by the velocity and density patterns introduced in Figure 7-26 for a Cross-Well survey with one shot at x=400 m and 295 m depth and receivers with 1 m interval at x= 600 and extending from 0 to 600 m depth. a. Baseline seismic model. b. Baseline RTM result. c. Monitor seismic model. d. Monitor RTM result. e. The difference between monitored and baseline seismic models. f. The difference between RTM results. 220

Figure 7-32: The time lapse seismic models: a. The seismic model for one-year injection. b. The difference between the baseline and (a). c. The difference between seismic models after five and one year of injection. d. Migrated section of (a). e. The difference of migration sections between the baseline and one year of injection data. f. The difference of migrated data between five years and one-year of injection. 221

Figure 7-33. The migrated seismic data from the reservoir's response by different kinds of average related to the mixed fluid condition after a year injection. The left figures are the model made by the rock physics models after one year injection for the Reuss(a), Brie (b), VRH (c) and Voigt (d) averages. 222

Figure 7-34. The migrated seismic data from the reservoir's response by different kinds of average related to the mixed fluid condition after 5-year injection. The left figures are the model made by the rock physics models after five years injection for the Reuss(a), Brie (b), VRH (c) and Voigt (d) averages. 223

Figure 7-35.The variation of velocity due to injection after 5-year injection (calculated by Reuss average) and the time-lapse seismic migrated response of it (RTM(SM(5,R)-RTM(SM(base))) 224

Figure 7-36.The statistical distribution of the velocity change in the reservoir cells in the patchy mixed (Voigt average). 225

Figure 7-37. The statistical distribution of the velocity change in the reservoir's cells in the fine mixed (Reuss average). 226

Figure 7-38: The research routine to compare results of the seismic and reservoirs time lapse surveys. A. shows the direct seismic time-lapse, B. seismic time-lapse based on the reservoir time lapse 228

Figure 7-39. The difference model (time lapse) for the p wave velocity (by VRH average) in the reservoir between different years of injection. The result calculated according to the CO_2 saturation content and Gassmann's equation for a semi-patchy mixed condition. 229

Figure 7-40. Left: SM (R (5-year injection))-SM (R(1-year injection)) and right: SM (R ((5 year) - (1-year injection))). As mentioned previously, SM stand for seismic model (Acoustic), and R is calculated Vp based on reservoir simulation result 230

Figure 7-41. The difference between two model in Figure 7-40, the left figure shows same amplitude scale and the right one is 100 times magnified amplitude 230

Figure 7-42. The RTM results for the seismic models in Figure 7-40 230

Figure 7-43. The difference of RTM images in Figure 7-42. The left shows the difference in natural amplitude and the right figure shows 100 times magnified. 231

Figure 7-44. The saturation and P-wave velocity change distribution after a year stopping the injection.. 231

Figure 7-45. The acoustic (left) and elastic seismic response (right) for a three-layer model (top). 233

Figure 7-46. The P-wave seismic response for the acoustic wave propagation. a. shows the seismic response for the baseline model. b. the seismic model after five-year injection by Brie's model. c. the difference section shows a PP response of the reservoir. 234

Figure 7-47. The seismic response for an elastic model. a. baseline. b. after five-year injection by Brie's model. c. The difference section and PP, PS and SS seismic response of the reservoir. As demonstrated in Figure 7-45, the SS-wave amplitude is considerable at far offsets.. 235

Figure 7-48.The original Marmousi model (P-wave velocity) 237

Figure 7-49. A new physical property (Vp) defined as a CO_2 injected reservoir pointed by the red rectangle. 237

Figure 7-50.The seismic imaging result on the original Marmousi model. The acoustic wave forward modeling and RTM migration method was used. 238

Figure 7-51.The seismic imaging result for Marmousi model and the implemented reservoir.. 238

Figure 7-52.The subtract of monitor seismic model of the baseline model. The red rectangle shows the location of the reservoir. 239

Figure 8-1. The concept of FWI (Martinez, 2016). The FWI method is a suitable way for correcting the velocity model according to the initial model and seismic acquired data. It can be a revolutionary approach to explaining velocity change (that can be translated to the saturation) in a reservoir by seismic 4D data in the seismic resolution range. 243

List of Symbols, Abbreviations and Nomenclature

Symbol	Definition
B	Bin size
BHP	Bottom Hole Pressure
CCP	Common converted point
CCS	Carbone Capture and Storage
c_f	Compressibility
CGDN	Core density
CKAR	Core air permeability
CMFF	Standard free-fluid porosity
CMP	Common mid point
CPOR	Core Porosity
EOR	Enhanced Oil Recovery
f_{dom}	Dominant frequency
F_{ij}	Fold in bin number i*j
f_{max}	Maximum frequency
FRS	Field research site
G and µ	Shear modulus
GR	Gamma ray log
K	Bulk modulus
KINT	Intrinsic Permeability (ELAN)
k_{rg}	Gas relative permeability
krg	Gas relative permeability
k_{rw}	Water relative permeability
KSDR	Permeability (Schlumberger-Doll-Research model)
KTIM	Permeability (Timur-Coates model)
LMO	Largest minimum offset
PHI	Average porosity
PHIT	Total porosity
PIGN	log-derived effective porosity
RC	Reflection coefficient
RTM	Reverse time migration
SPHI	Porosity calculated by P-wave velocity

TCMR	Total CMR porosity
VCL	Volume of Clay
V_{int}	Interval velocity
Volume_Clay	Volume of Clay
Vp	Compressional wave velocity
Vs	Shear wave velocity
VSP	Vertical Seismic Profiling
VXBW	Volume of Bound Water

Chapter 1. Introduction

1.1 Research procedure and resources

CMC Research Institutes (CMCRI) and the University of Calgary are conducting a research project to monitor the behavior of subsurface CO_2 injection. The project is known as Field Research Station (FRS) which plans to study the trapping and leakage of CO_2 gas injection into a shallow target. I had been involved in the project from the initial steps of research, and so the dissertation reflected my work and studies in different branches of the geoscience and engineering. The thesis covers the geological studies, petrophysical analysis and interpretation, seismic design, geomodelling, reservoirs fluid simulation, rock physics studies and seismic forward modeling and RTM imaging for time-lapse study. Figure 1-1 and Figure 1-2 demonstrate the disciplines were used in the study and their link together.

The various kinds of analysis were used for the project and the principal methodology for the research includes:

1- Seismic design: PP and PS parameter design
2- Seismic interpretation: structural analysis and attributes study
3- Geomodelling: Geostatistical method, geometry from seismic and data from well log
4- Fluid Simulation: Compositional simulation
5- Rock Physics: Property average of the constituents for the solid and fluid phases, fluid substitution, applicating Gassmann's equation

6- Seismic modeling and imaging: Seismic forward modeling (acoustic wave equation solved by the finite difference method), Reverse Time Migration (RTM)

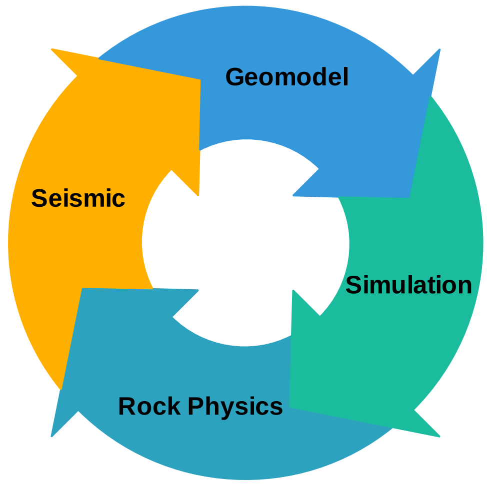

Figure 1-1.The disciplines used for the reservoir integration in this thesis

1.2 Accomplishments and goals

In the seismic design chapter, the goal is to improve PS fold in the acquisition design and define a criterion to compare the surveys based on the PS fold distribution. In the simulation chapter, the condition of the reservoir (shallow reservoir) was determined, and the CO_2 injection was simulated in gas phase. Gas phase of CO_2 was selected for two reasons: 1- In the gas injection, the density will drop to half of initial density, and it can cause a small increase in the shear wave velocity. This change will allow us to check elastic specifications of a reservoir; 2- The frack pressure due to the shallow depth of the reservoir and low lithostatic pressure is very low, and so pressure easily can exceed of the fracture gradient.

In the reservoir simulation study a scenario for the long-term monitoring (after a limited injection time) was formulated, and it describes the plume size after a long-term monitoring based on the simulation results of initial years after ceasing the injection.

As mentioned, the research covers a very broad technical range including fluid simulation, rock physics and seismic algorithms to make it possible to compare seismic migrated responses in different conditions that are possible in the FRS reservoir. In the rock physics chapter, the physical properties of the fluids in the reservoir, before and after injection were studied and the rock physics study is integrated with the reservoir simulation results. Different average methods related to the fluids mixed models (as patchy or uniform) were used to calculate the P-wave velocity after CO_2 injection, and they were the basis for the seismic modeling and imaging.

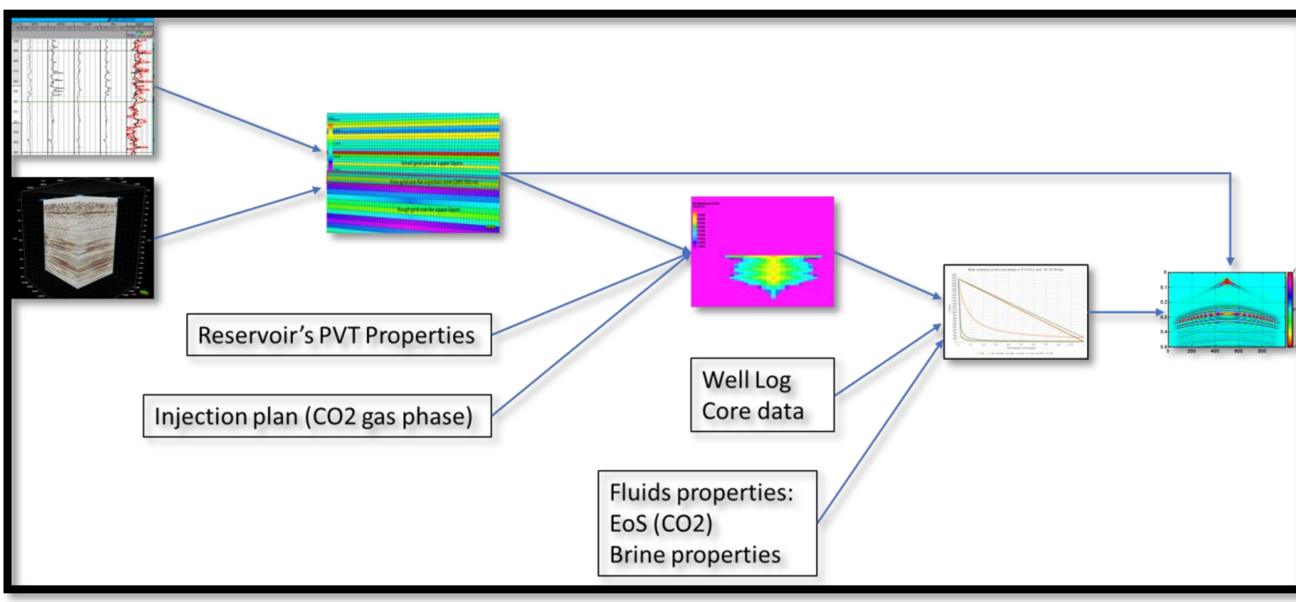

Figure 1-2.Schematic view of the research procedure.

The last chapter (seismic imaging) uses all processed data from geomodeling, the reservoir simulation, and rock physics. In this step, the main advance is in the seismic modeling of a reservoir under production/injection. For this purpose, the seismic forward modeling used the wave equation solved by the finite difference method. The imaging step took advantage of the Reverse Time Migration (RTM) method. The RTM is a two-way wave equation depth migration method that can handle complex velocity models (near the reservoir), and suitable for steep dips (to investigate the possible image of the plume in reservoir) and accurate amplitude estimation. In this chapter, the different models of geometries and velocity variation due to the fluid substitution and plume size in a reservoir were studied, and the seismic response of them was compared. The solid and diffusive velocity variations are two concepts in the reservoir study that are introduced. Also, the acquisition configuration influence was checked by surface seismic and well seismic (Vertical Seismic Profile (VSP) and Cross-Well survey type) that they could generate the different amplitudes and imaging conditions for the reservoir. Also, I engaged the different rock physics models (for the mixed type of the phases) to generate the seismic model and images to compare interpretability of models. Briefly, the main contributions of the thesis addressed the following subjects:

a- A criterion for PS fold evaluation in different surveys and test randomly located receivers point in the PS fold improvement.
b- Very long-term plume size estimation with the short-term simulation results.
c- The seismic response of solid and diffusive velocity variation due to reservoir activity.
d- The plume size and the velocity variation in the seismic response.
e- RTM noise reduction in a synthetic 4D seismic study.

f- The acquisition configuration influence on the reservoir study.

g- The rock physics and the influence of different mixing models on seismic results and interpretability.

h- The statistical condition of the velocity variation in the different fluid mixed models and relation between the velocity variation's statistical distribution and seismic inversion for saturation estimation.

i- The S-wave velocity changes by the density drop in a CO_2 injection project. The amplitude study of SS-waves can provide useful density information.

1.2.1 Software

The following software packages were used to this thesis:

1- Seismic design: OMNI (GEDCO, Schlumberger); this software is useful to study 2D and 3D seismic surveys with different acquisition parameters.

2- Seismic processing: VISTA (GEDCO, Schlumberger), Promax (Halliburton)

3- Seismic interpretation and data integration, geomodelling: Petrel (Schlumberger)

4- Reservoir simulation: ECLIPSE (Schlumberger), CMG (Computer Modeling Group)

5- Petrophysics: Techlog (Schlumberger)

6- Mapping: Google Earth and Map, AutoCAD Map

7- Log data: Accumap (IHS)

8- Programming: Matlab: This software was used for the following purposes:

    a- Seismic Forward Modeling

    b- Reverse Time Migration

c- Rock Physics calculation (average methods and fluid substitution)

d- Managing big data transferring between two software (file over 2 GB that is not manageable by the conventional software) and make suitable format for the next software

9- Numerical calculation: Excel (Microsoft)

For the rock physics study, a series of Matlab codes were prepared. In the seismic modeling chapter, the main code for the seismic forward modeling and RTM were in Matlab. Some codes also prepared for importing data from Petrel, CGM, and ECLIPSE to the seismic forward modeling and RTM imaging code.

1.2.2 Data Resources

The data and information that used in this research belong to CMCRI, Field Research Station project (FRS) and the dataset was generously available for my research purposes.

1.2.3 Background

In this section, a brief explanation about the available studies and papers are introduced about Carbon Capture and Sequestration (CCS), CO_2 related rock physics, 4D seismic and case studies.

A CCS study always needs a different level of science and engineering for the CO_2 capture and injection compared to hydrocarbon reservoir production. In this project, the following disciplines have used for the reservoir study and 4D seismic research:

1- The physical properties of CO_2 and the reservoir fluid (at the FRS it is brine with low salinity level).

2- The fluid simulation (a compositional method was used)

3- Rock physics of CO_2 injection in the reservoir. It contains the mixed fluids and matrix condition (for parameters average calculation) and fluid substitution.

4- Seismic response of CO_2 injection in the reservoir. The seismic models in the acoustic and elastic medium condition were generated, and the RTM method was used to image the acoustic.

5- Seismic time-lapse studies are examed through the difference between the synthetic monitor seismic data and the baseline data.

There are many papers for calculation of the physical properties of CO_2. Span and Wagner (1996) introduced a new Equation of State for CO_2 from the triple-point temperature to 826.85 ^oC (1100 K) at pressure up to 800 MPa (8000 bar). Sun (2009) modeled the velocity of CO_2 for temperature down to -10 ^oC and up to 200 ^oC and pressure up to 100 MPa. The first reference has a complex formulation and the second paper used simple equations that are easy to calculate. For the current research, the Span and Wagner methods were used for the calculations.

In the geomodelling stage, data from the well log and seismic structural interpretation were available. The geomodelling uses the geostatistical method (included variography and Kriging) for the best estimation of the properties of each cell. Geostatistics is a part of statistics that the coordinates of the samples (the spatial distribution of data) were considered. The main root of this science was the mining industry, and the initial concept was introduced by a South African mining engineer in 1950s (D.J. Krige). G. Matheron (A French engineer) expanded and formulated this method and established a branch of statistics that is useful in the mine, earth and atmosphere science and oil and gas industry as a powerful estimator.

In my prior work reviewing for the fluid simulation and also the WASP project, a black-oil simulator were used for the reservoir simulation considering PVT parameter tuning (Hassanzadeh et al., 2008). For the simulation formulation and explanation of the terms related to reservoir in the research, I used Fanchi (2006). The current project is a very shallow depth reservoir (very low pressure and temperature), and after checking both simulation methods (Black-Oil and Compositional) and given the limitation of the simulators, we decided to use the Compositional Simulator for this research.

In the rock physics study, the main goal is to determine the average physical property of the reservoir; e.g. Voigt and Reuss (Reuss, 1929) as the upper and lower bound limit with an average case of them (Voigt-Reuss-Hill) (Hill, 1952). Also, Hashin-Shtrikman's narrow bounds is a proper method for a better estimate of property fluctuation in a mixed material. Fluid substitution has many formulations based on the reservoir condition. Gassmann's relation at low frequencies (Gassmann, 1951) is a well-known method for this purpose, and we used the isotropic form of it for the velocity estimation after CO_2 injection. Kuster and Toksöz formulation (1974) is the other method for the P and S wave velocity estimation for a mixed material (after the fluid substitution procedure). It uses a long-wavelength first-order scattering theory (Mavko et al., 2009).

There is rock physics research related to the CO_2 injection and sequestration. Li et al., (2006) characterized rock physics properties for a CO_2 sequestration study. Kim et al., (2016) did a lab test and studied the seismic velocity change in a heterogeneous sandstone by the CO_2 drainage and imbibition conjugate with the resistivity measurements. Also, a lab test with a sandstone sample was done by Alemo et al. (2011) and a field work by Lumley (2010) that showed good compatibility of the rock physics study for the velocity estimation by the VRH average. Also, the theoretical calculations were compared with our study (Smith et al., 2003).

For the seismic modeling, the acoustic and elastic wave equations are solved by the finite difference method in MATLAB. The main base of the seismic studies in the research is the acoustic modeling and migration. The algorithm and formulas in the modeling section and the related code are from Brekhovskikh (1960), Zakaria et al., (2000) and Zho (2003).

Wave Equation Migration was introduced in 1982 by Whitmore in the 52nd SEG meeting. Loewenthal (1983) published an algorithm that he called Reverse Time Migration (RTM) based on a two-way wave equation migration solution. Also, Baysal (1983) published a paper about the RTM advantage compared with other methods. Levin (1984) also described this approach. In this research, to describe the methodology of RTM, we used Withmore (2012) and for describing the noise generated by the RTM algorithm, the research by Khalil (2014) was studied.

Seismic studies for CCS has expanded recently due to sequestration and EOR activities. Raji et al., (2017) discussed the tomography method for the CO_2 monitoring. Previously a very introductory paper about time-lapse imaging by Full Waveform Inversion (FWI) method was published for the velocity estimation of a reservoir (Ansari, 2012). The case histories of time-lapse study for CO_2 injection and sequestration shows many successful experiences done by VSP data (Chadwick et.al. 2009, Geng et. al. 2011, John et. al. 2004, Thomas et. al.2008). A walkaway VSP data on the SACROC field for EOR purpose tried to estimate velocity changes in the reservoir due to CO_2 injection by RTM and FWI method (Yang et al., 2014).

1.3 CO_2 sequestration

1.3.1 Introduction

In this section, I present the carbon cycle in the atmosphere from Precambrian to the Recent age. Carbon is an element with atomic number 6 and three natural isotopes that ^{12}C and ^{13}C are stable and ^{14}C is radioactive. In the earth crust and atmosphere, carbon is 15th most abundant element. In chemistry, the main element to generate organic molecules is carbon. It is an essential atom for the biological structures and life. It also contributes in the non-organic molecules, minerals, and sediments as graphite, diamond, calcite (limestone), dolomite and coal.

1.3.2 CO_2 in the atmosphere

The CO_2 concentration in the atmosphere has fluctuated through earth's history. A full record of CO_2 concentration in the atmosphere from late Precambrian is shown in Figure 1-3. Figure 1-4 shows the CO_2 concentration in the atmosphere and temperature in the early Quaternary that was obtained by ice core data (Petit et al., 1999). This work has shown that the CO_2 in the atmosphere shows a strong correlation with temperature, as shown in Figure 1-4 and Figure 1-5 (Scotese et al. 2002). CO_2 is a gas that can change the radiation rate of the heat from the planet and trap the energy in the atmosphere (greenhouse effect). The records show an increase in global temperature by 0.6 to 0.9 ^{o}C since 1906 (Earth Observatory, NASA). Figure 1-6 shows a dramatic increase in the CO_2 concentration in the atmosphere due to human activities after the industrial revolution in the 19th century. After the industrial revolution, the consumption of the fossil fuels (coal in 19th and oil in 20th centuries) increased shown in Figure 1-7. It means more CO_2 has been emitted into the atmosphere by the chemical reaction of combustion. The estimation of the CO_2 annual emissions in the world was around 1.5 (Gt) in 2011 (International Energy Administration (IEA)).

Figure 1-3 shows the CO_2 concentration and temperature of the atmosphere from Precambrian to the Recent age. The CO_2 had a high concentration in the Paleozoic, and it decreased in the Silurian eras (as late Carboniferous). The CO_2 concentration had been decreased after Jurassic-Cretaceous border gradually, and it has made a proper environment for mammals to evolve with the higher rate in Cenozoic.

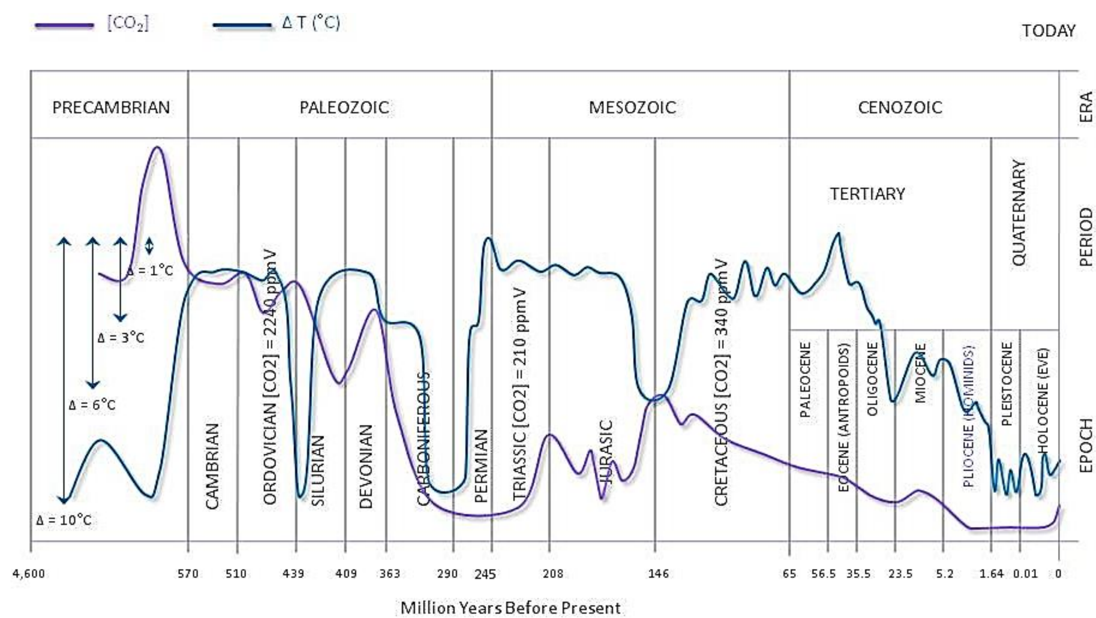

Figure 1-3: The concentration of CO_2 and the temperature of the atmosphere from late Precambrian to recent. The blue line demonstrates the temperature fluctuations, (Scotese et al. 2002) (Pagani et al. 2005).

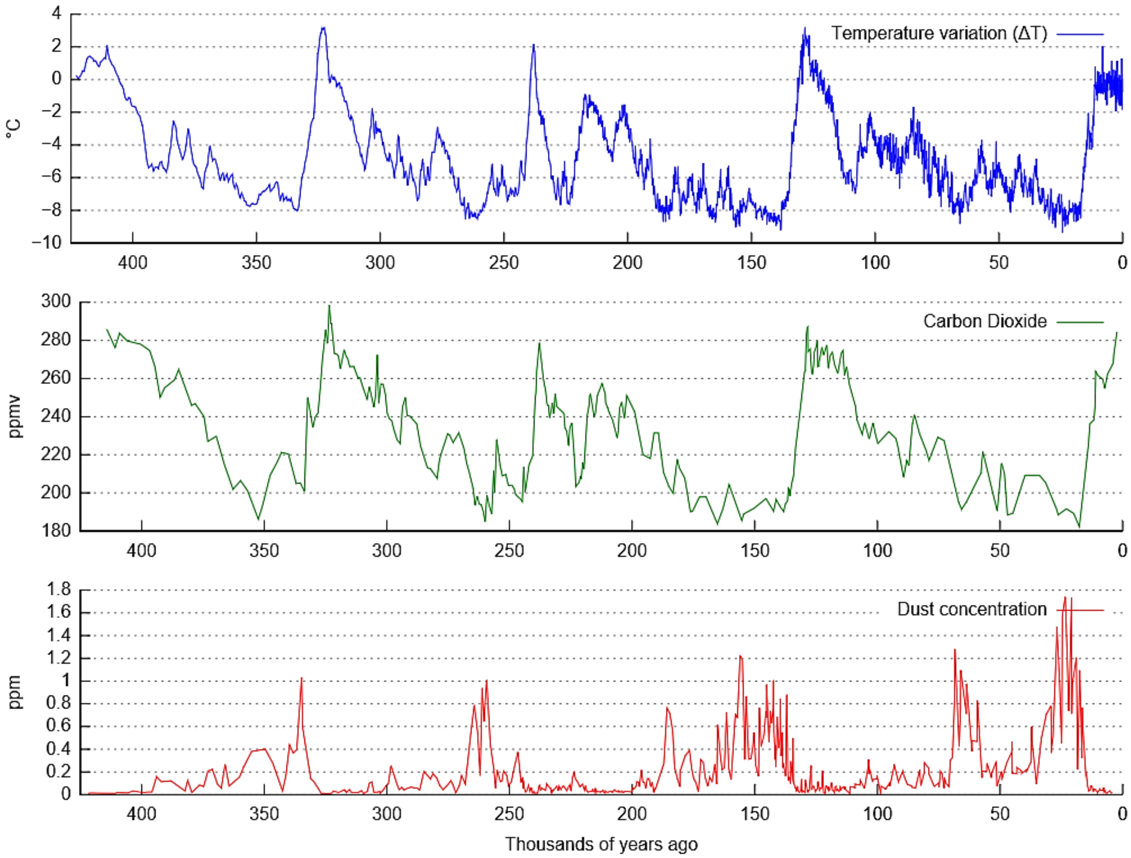

Figure 1-4. Temperature, CO_2, and dust concentration in the atmosphere from 400,000 years ago. Temperature has a strong correlation with the CO_2 concentration in the atmosphere and reverses relation with the dust. The loess sediments are a real proof of dust concentration in the atmosphere during the cold stages (Petit et al., 1999).

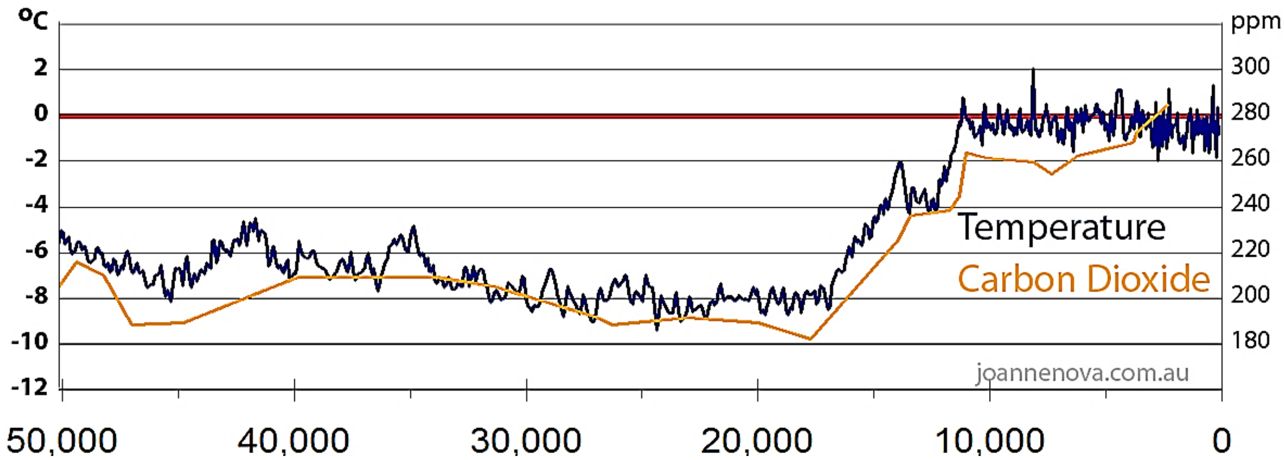

Figure 1-5. CO_2 in atmosphere and temperature from 50,000 years ago, by Vostok ice cores study (Petit et al., 1999, and joannenova.com.au).

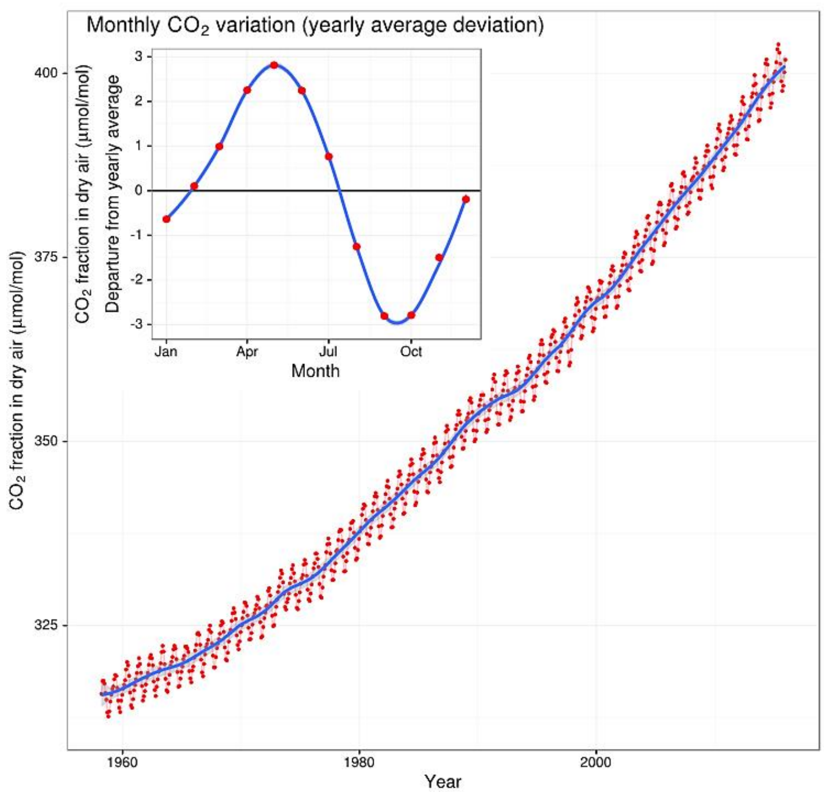

Figure 1-6: The concentration of CO_2 in the atmosphere since 1958 to 2015 (Measured at the Mauna Loa Observatory, https://www.co2.earth).

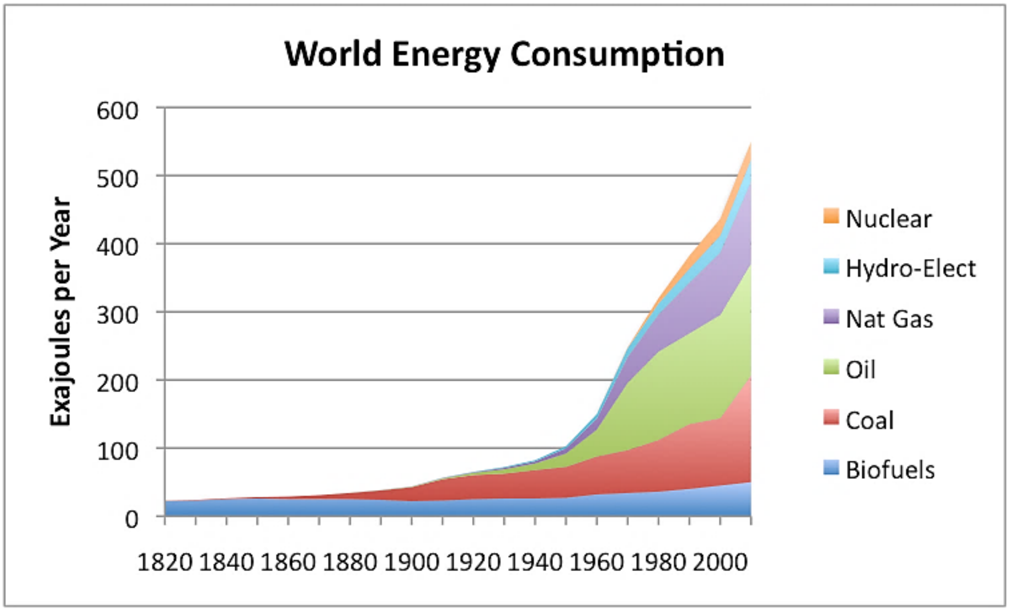

Figure 1-7: World energy consumption by source (based on data from BP Statistical review, 2014)

Figure 1-4, Figure 1-5 and Figure 1-6 demonstrate more detail about CO_2 in the atmosphere from the early Quaternary, 50,000 years ago, and after 1958.The relation between temperature and CO_2 concentration is very significant and also as related to the Milankovitch cycles (Hays et al., 1976).

1.4 CO_2 sequestration, a method for decreasing CO_2 concentration in the atmosphere

CO_2 reduction from the biosphere environment include methods and technologies that can help to reduce the emission of CO_2. Carbon Capture and Storage (CCS) (sequestration) in a geological trap is a well known globally and efficient method for reducing the concentration of this gas in the atmosphere.The CO_2 is injected into a formation for two reasons, a- storage for environmental reasons and b- for EOR (enhanced oil recovery). Sequestration programs usually inject CO_2 in a reservoir with reliable cap rock and fluids that are mainly brines.

There are 38 undertaked CCS projects (in operating, execute, define, evaluating stages) with 15 projects that have been undertaken in the world, with3 of them beeing in Canada, as listed in Table 1-1 (Global CCS Institute). The first attempt for enhanced oil recovery by CO_2 injection in an oil reservoir was in 1972, in Texas. However, the concept of CCS as an environmental method to prevent of CO_2 emission and to reduce the greenhouse gas concentration at the atmosphere was introduced in 1977 (IEA Greenhouse Gas R&D Programme).

Table 1-1: The large-scale CCS were operated in Canada (Source: Global CCS Institute)

Project name	Operation date	Industry	Capture type	Capture capacity (Mtpa)	Transport type	Primary storage type
Great Plains Synfuel Plant and Weyburn-Midale Project	2000	Synthetic Natural Gas	Pre-combustion capture (gasification)	3	Pipeline	Enhanced oil recovery
Boundary Dam Carbon Capture and Storage Project	2014	Power Generation	Post-combustion capture	1	Pipeline	Enhanced oil recovery
Quest	2015	Hydrogen Production	Industrial Separation	1	Pipeline	Dedicated Geological Storage

1.4.1 CO_2 trapping mechanism

Many papers have explained geological and reservoir concepts of CO_2 sequestration and trapping options. The gas-water relative permeability hysteresis and trapping efficiency have a significant role in the reservoir capacity; these parameters were studied in Alberta previously (Bachu et al., 2013). For example, in the FRS project, the permeability is low, and according to Bachu (2013) the trapping efficiency is around 50%.

The primary concern about the CO_2 sequestration in high volumes is the leakage risk into shallow aquifers or into the atmosphere that can cause significant damage and environment problem for living creatures and the biosphere. However, some researcher worked on the methods to decrease the CO_2 sequestration risks (Burton et al., 2009).

In a CO_2 sequestration process, four mechanisms are known to trap CO_2 (Figure 1-8):

1. Stratigraphic and structural trapping: In a reservoir, in the short term after injection, the CO_2 is free phase and can circulate in the reservoir space upward because of the density and gravitation effect and be trapped under the cap rock.
2. Residual Trapping: some injected CO_2 phase is trapped in the pores space and they do not move by gravitation.
3. Solubility Trapping: Water has a high capacity to dissolve CO_2 gas, and a considerable amount of CO_2 will dissolve in the brine right after injection (Eq. 1-1). A common sample of CO_2 dissolved in water is soda water.
4. Mineral Trapping: this stage is the most secure trapping method for CO_2. The minerals in the reservoir reacte with CO_2 with the water existence in the aquifer as a catalyzer, and it can precipitate the gas to a solid phase (as Eq. 1-2 and Eq. 1-3).

The first and second mechanisms are just a physical action; mechanism no. 3 is a physical action with a partial chemical change (Eq. 1-1) in brine, and the fourth trapping mechanism is an entirely chemical reaction between carbonic acid and hydrogen ion produced by mechanism no. 3 and minerals (Eq. 1-2 and Eq. 1-3).The chemical reaction of CO_2 with water can be explained as:

$$H_2O + CO_2 \leftrightarrow H_2CO_3 \leftrightarrow HCO_3^- + H^+ \qquad \text{Eq. 1-1}$$

With quartz and silicates:

$$SiO_2 + 4H^+ \leftrightarrow 2H_2O + Si^{4+}$$

Eq. 1-2

With kaolinite as a typical clay mineral

$$Al_2Si_2O_5(OH)_4 + 6H^+ \leftrightarrow 5H_2O + 2Al^{3+} + 2SiO_2$$

Eq. 1-3

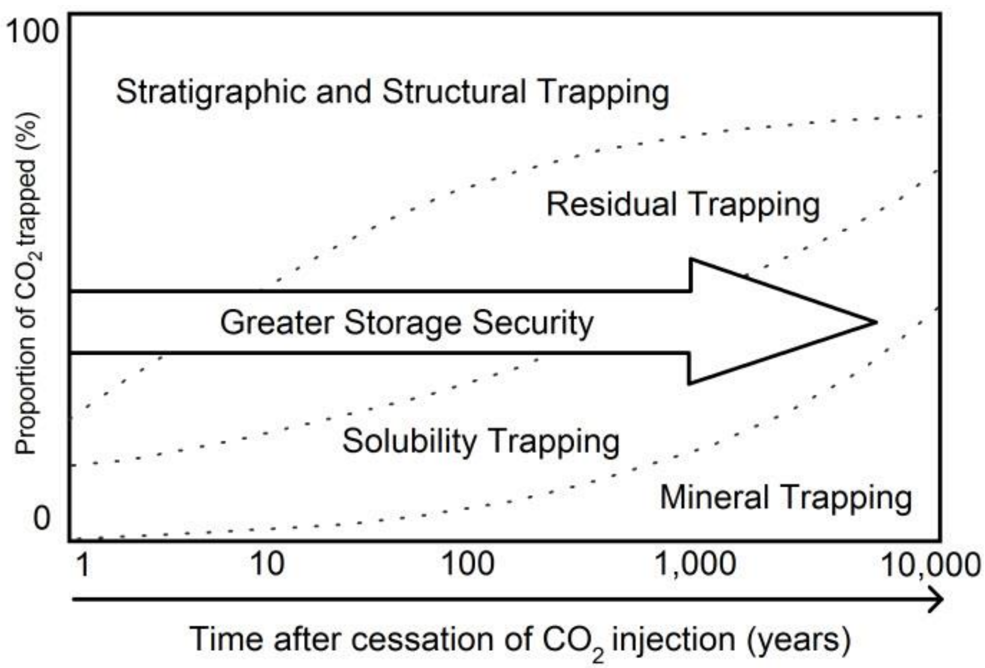

Figure 1-8. CO_2 trapping mechanisms and increasing CO_2 storage security over time (Pooladi-Darvish, 2009).

According to the trapping mechanism and storage stage (as shown in Figure 1-8) in the primary years of injection, structural and stratigraphic trapping play the main role, but after decades (or centuries), mineral trapping and solubility trapping are most important and thus CO_2 storage in aquifers will ultimately be secure.

1.4.2 CO_2 gas injection in the brine

During the injection of CO_2 gas in a reservoir with primary brine fluid in, some changes happen in the brine near the injection well (Hurter et al., 2007):

1- CO_2 dissolves in brine, because of some chemical action, this increases the density of the brine.

2- Dissolved CO_2 in the brine makes carbonic acid (Eq. 1-1).

3- The water can vaporize into the CO_2 gas; this procedure can decrease the immiscible water value and increase the salinity of the brine and make salt deposits near the well (dry and salting out).

The solubility of CO_2 in the water is significant, and for brine, the CO_2 solubility is a function of salinity. When salinity increases, the solubility of carbon dioxide decreases. Industrial simulators do not have an option for the salt or water vapor variation in the reservoir during the injection. For a detail simulation result, they should be considered in the reservoir's fluid simulation procedure.

More discussion about dry-out and salting-out effects are discussed in the reservoir simulation chapter.

Chapter 2. The Field Research Station (FRS) project

2.1 Introduction

This project is a CO_2 injection project, led by CMCRI and the University of Calgary. The project area is located southwest of Brooks City, west of the Newell Lake in southern Alberta. The geographic map of the project was shown in Figure 2-1. The satellite image of FRS project area (green square shows the 1*1 km area available for the project) and wells near the project area (yellow pins) are shown in Figure 2-2. The objective of this research is CO_2 injection in the shallow targets (300 m and 500 m depth) and study the behavior of the CO_2 migration, movement, and leakage and monitor the gas by the seismic method coupled with reservoir studies in the FRS project. Other geophysical methods (as microseismic, electrical methods and microgravity) will test for the gas monitoring. In this project, there is an emphasis on the leakage of CO_2 and detection methods.

The CO_2 injection procedure into the target needs some initial preparations. The field operations began in 2014. The preparation set-up included following:

1- A 3D seismic acquisition operation was done in May 2014 as the baseline seismic data.

2- An injection well drilled for the injection purpose (March, 2015).

3- A full log data set was gathered after drilling.

4- Electrical resistivity tomography data were collected from the project area (2015)

5- New seismic surveys (included surface and borehole seismic acquisition) was done after removing of drilling equipment (July, 2015).

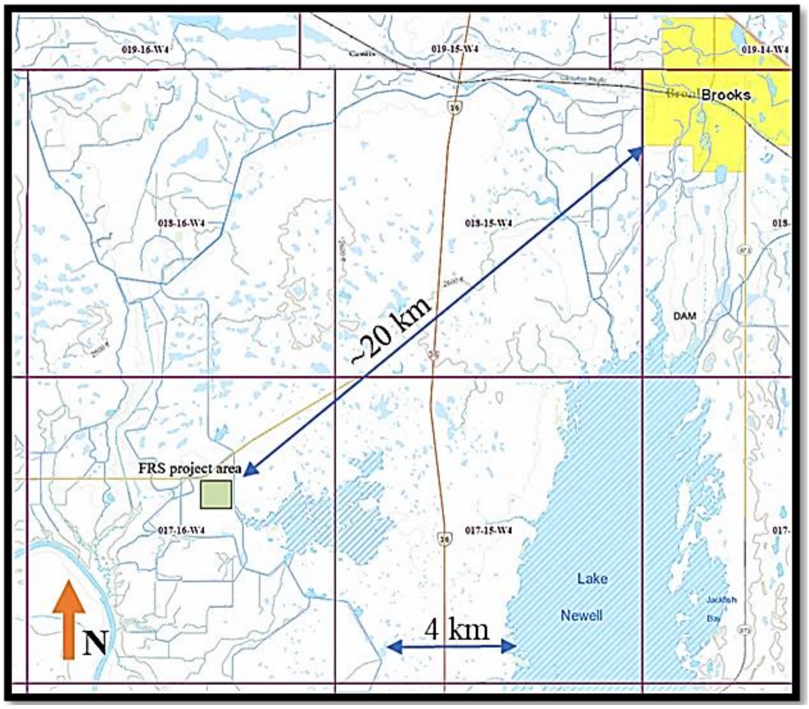

Figure 2-1.The map of project area, it is located in 017-16-W4

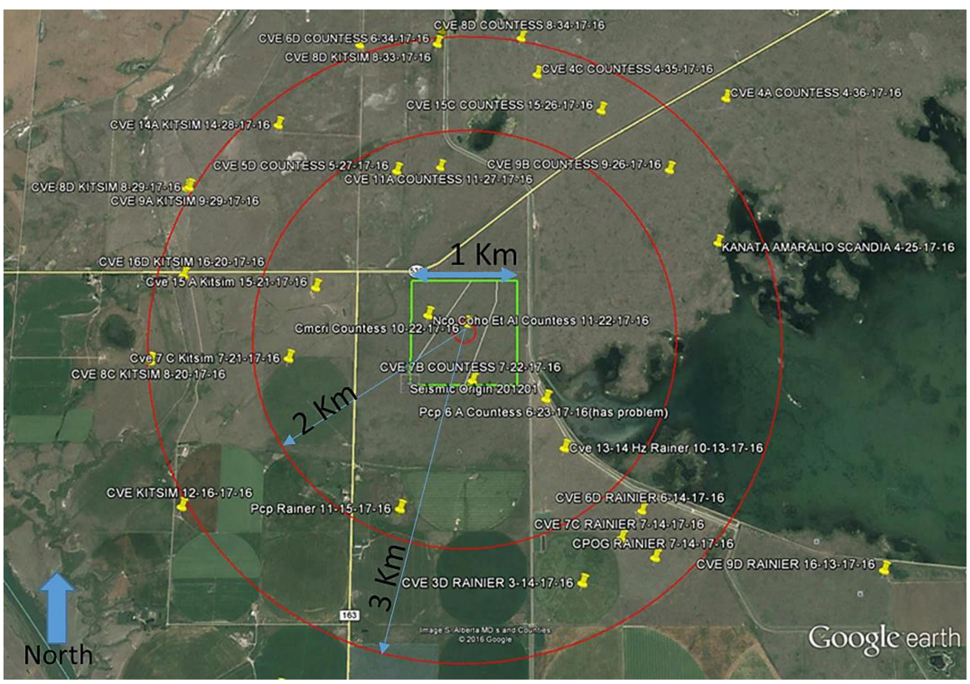

Figure 2-2. The satellite image of the FRS, the green rectangle shows the project area and the yellow points are the well sites with log data (Source: Google Earth).

2.2 Geological setting

The project area is in the southern plains of Alberta. The stratigraphic column for the southern plain is shown in Figure 2-4 (AGS, 2010). The information about the formations in well 10-22 were combined with the adjacent well data and the results are included in Figure 2-5 (Schlumberger, 2016). The formations in the project area include the following:

Glacial sediments: The Quaternary glacial sediments are on the surface. The thickness of glacial till reach 30 m in the well site.

Belly River Group: The glacial till (Quaternary deposits) overlies the Belly River (BR) Group. This group is a unit of upper Cretaceous and mid-Campanian stage. So, there are a significant hiatus between Cretaceous and Quaternary sediments in the well site. This group is subdivided to the three formations in the southern plain as: Dinosaur Park, Oldman, and Foremost formations. Figure 2-3 is a picture from the Bow River's valley near Bow City (near the project area) that shows the exposure of two upper formations in this group. Entirely the thickness of the BR Group is 272 m in the well 10-22, but it can reach a maximum thickness of 1300 m follow to the west. The upper formation in the group is Dinosaur Park Formation with 69 m thickness. The lithology of the formation is sandstone in the lower level and smaller grain size sediments as siltstone and mudstone in the upper sections. The reported lithology for this formation is sandy shale based on the well log data and the drilling report.

The Oldman and Foremost are two other formations in the group. They are detrital formation, mainly fine grain sandstone in the Oldman and shaly sandstone with coal layers in the Foremost Formation. The Basal Belly River Sandstone is the base member of Foremost, and it was selected as the first target for the CO_2 injection. It is a regressional shoreline sediment (Hamblin et al., 1996). The target layer is a sandstone with around 14-16% porosity and the permeability between 0.1 to 2 mD. In the research, the focus for geomodelling and the fluid simulation is on the Basal Belly River Sandstone.

In the petrophysical study of the 10-22 well, three coal layers were detected above the cap rock in the Foremost Formation from 285 to 295 m (Figure 2-9).

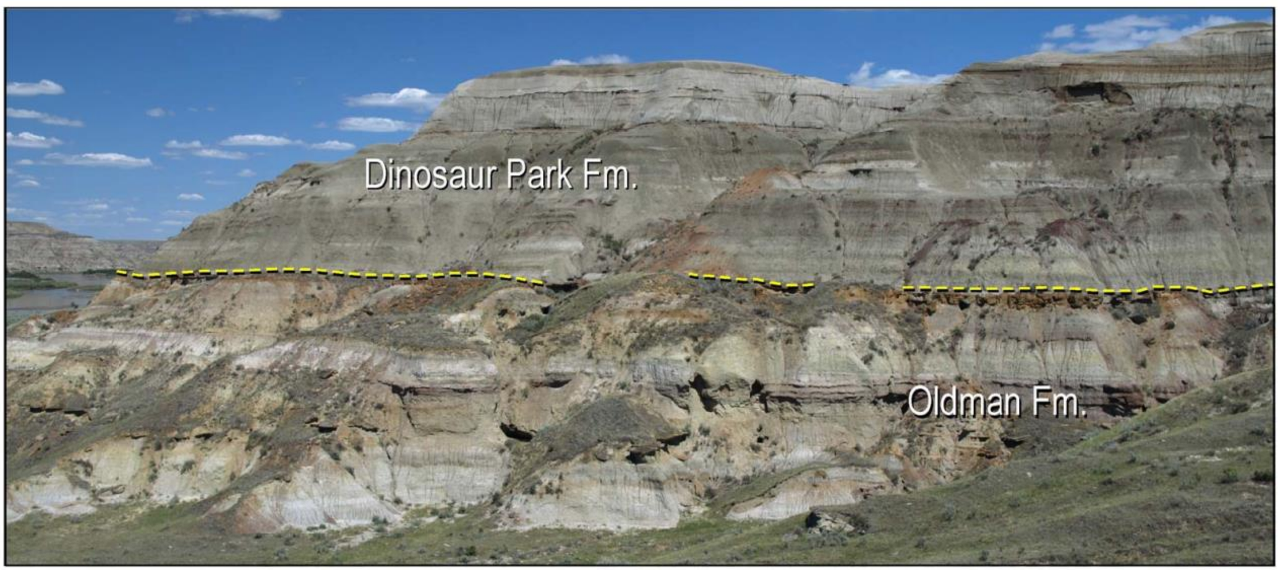

Figure 2-3.The outcrop of two upper formations in the Belly River group in the Bow River valley near the Bow City, west of project area and 7.5 km far from the well site (AGS, 2010).

Pakowki Formation: Pakowki is a detrital formation that gradationally underlays the Foremost Formation (here Basal Belly River member). The lithology is gray mudstone, olive siltstone, and very fine-grained sandstone. The base of the formation is marked by a thin pebble conglomerate.

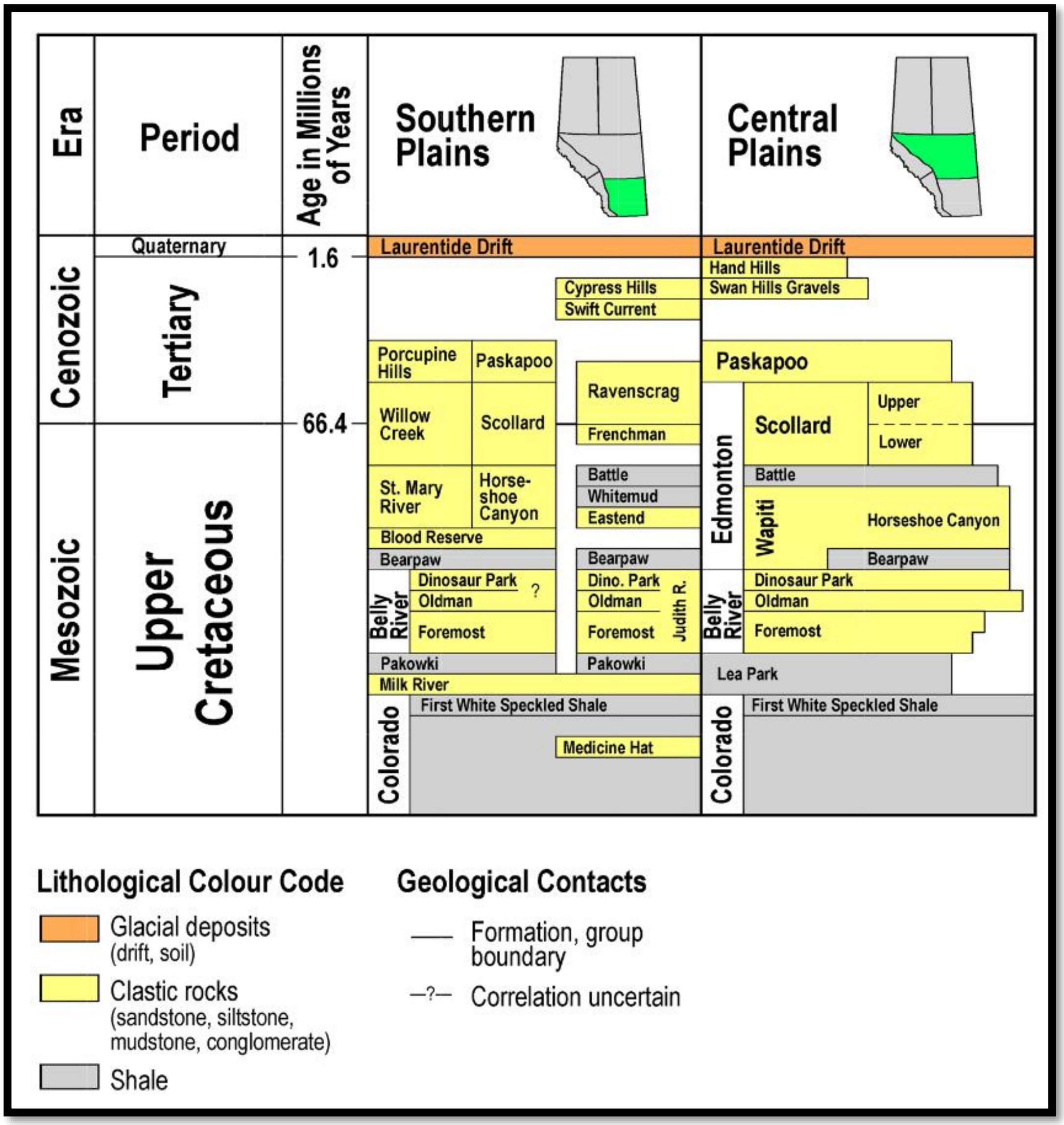

Figure 2-4.The stratigraphic correlation and table of formations in the southern plain (Alberta Geology Survey (AGS), 2010)

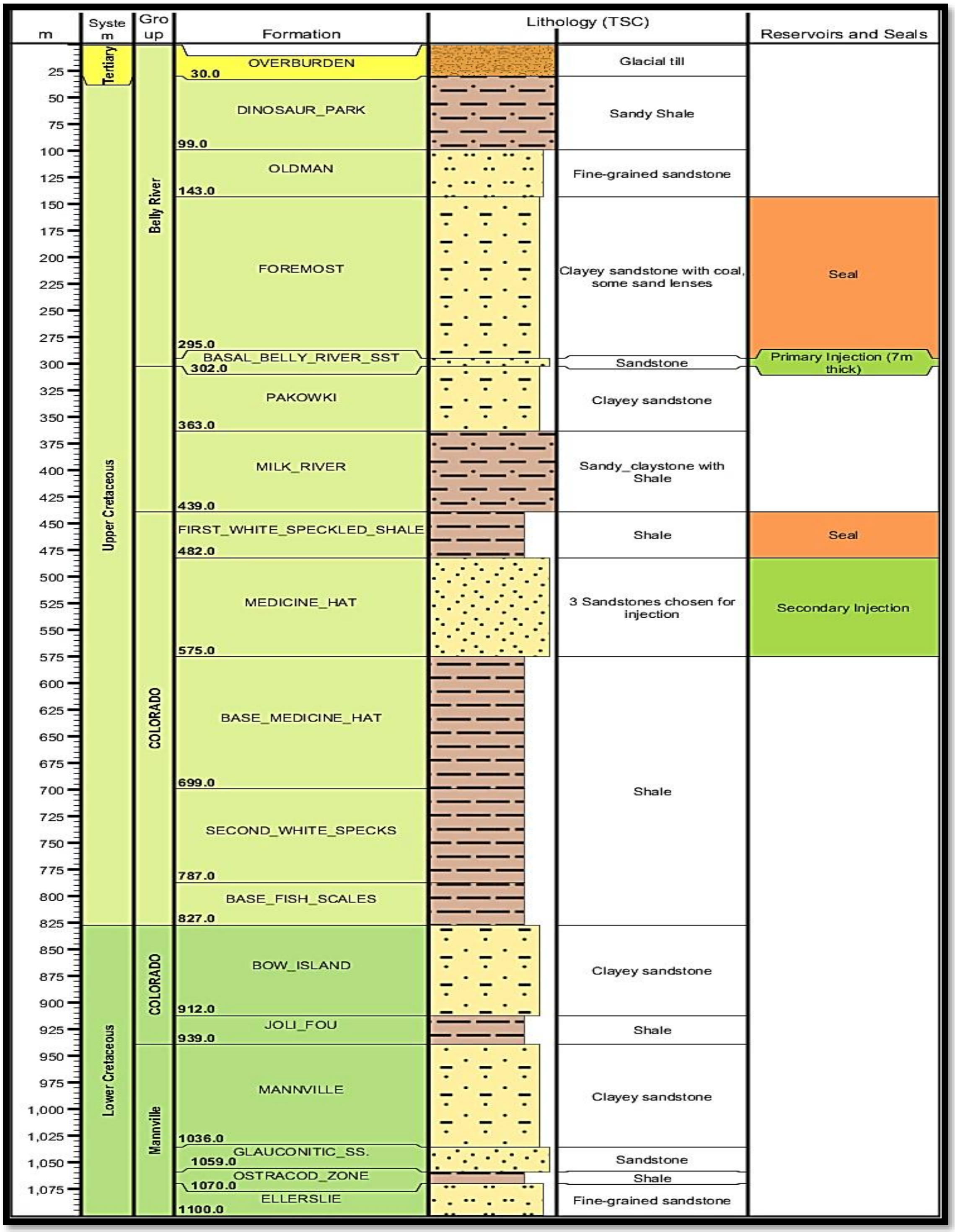

Figure 2-5. The Stratigraphic chart for the well 10-22 (from well 10-22 drilling data combined with the adjacent wells data, Schlumberger, 2015)

2.3 Petrophysical study and Interpretation

The well (CMCRI COUNTESS 10-22-17-16) is of primary importance for the research as it is planned to inject CO_2 through the well into the shallow target (i.e., Basal Belly River sandstone) and a wide range of the log data and core studies are available for the well and the injection zone.

As the core pictures demonstrate (Figure 2-11), the target zone is mainly sandstone between two layers in the up and bottom formed by the smaller grains size detrital sediments that can make a suitable trap for the CO_2 injection. The petrophysical study introduces the main parameters for the geomodel, including porosity and permeability and the physical properties of the formation. For the seismic study the P and S-wave velocity and density data were derived from the well log data, and will be used to generate synthetic seismic images. Some information and parameters as the mineralogy, the salinity of the brine and the free fluid amount in the injection layer are also predicted by the well log data.

In the initial log studies, the distribution of P and S-wave slowness are shown as scatter diagram in Figure 2-6 and Figure 2-7 shows Vp/Vs ratio for the well. In the diagram (Figure 2-6) the color bar shows the gamma ray content, and the circle size is for the density permeability.The shale in the rock sample shows a lower permeability, so the blue ellipsoid shows an area with the high velocity, low porosity, low permeability and shaly zone. As is shown in Figure 2-7, the Vp to Vs ratio is from 1.8 to 2.6. In the reservoir zone (295-302 m) this ratio is 2.0. Figure 2-7 also shows the well logs for porosity values estimated by the different methods (seismic porosity (SPHI), density porosity (DPHZ), TCMR porosity, the average of mentioned three porosity (PHI)) and the permeability calculated by Nuclear Magnetic Resonance (NMR) by two methods (Timur-Coates (KTIM) and the Schlumberger-Doll-Research model (KSDR)), neutron porosity and porosities determined by NMR logging. For the geomodeling, I used the average porosity estimated by all of these methods.The range of the porosities is 15 to 20% and they are available in the Figure 2-7.

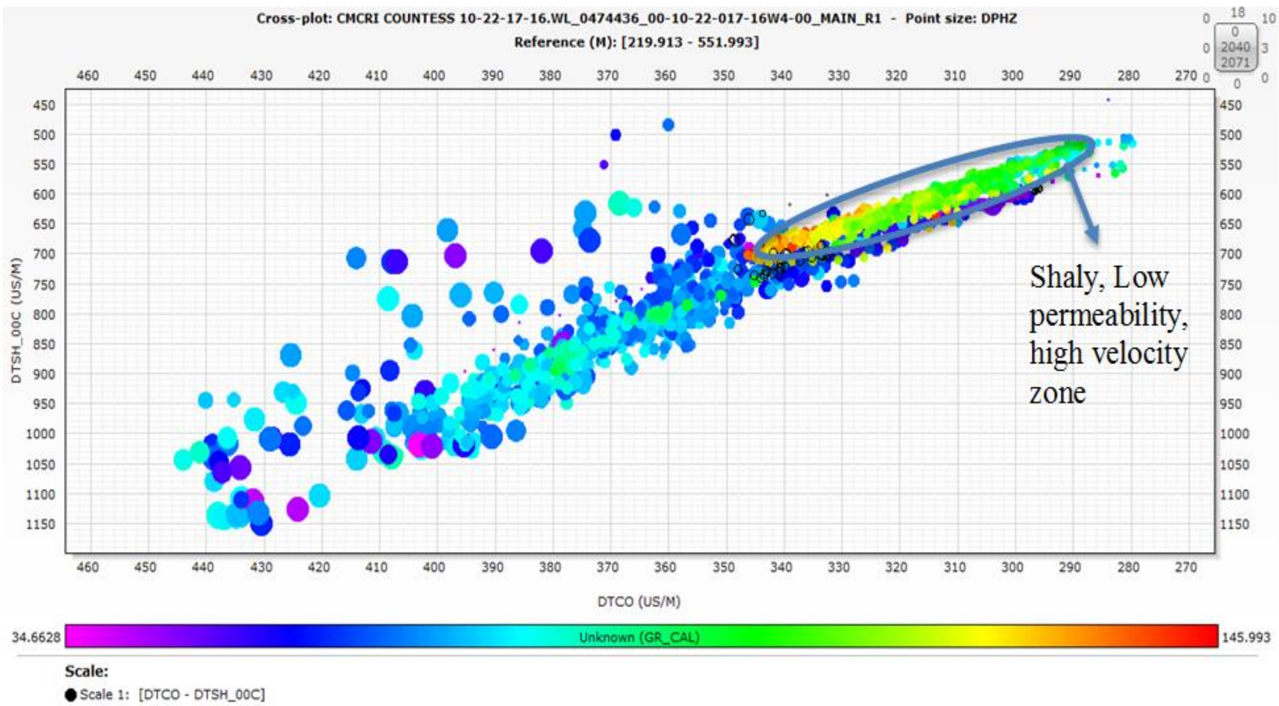

Figure 2-6. P-wave versus s-wave slowness in the well 10-22. The color-bar shows the gamma ray log, and the size of circles are for density porosity. The Vp/Vs ratio is between 1.8 in the deep layers to 2.6 in the shallow formations.

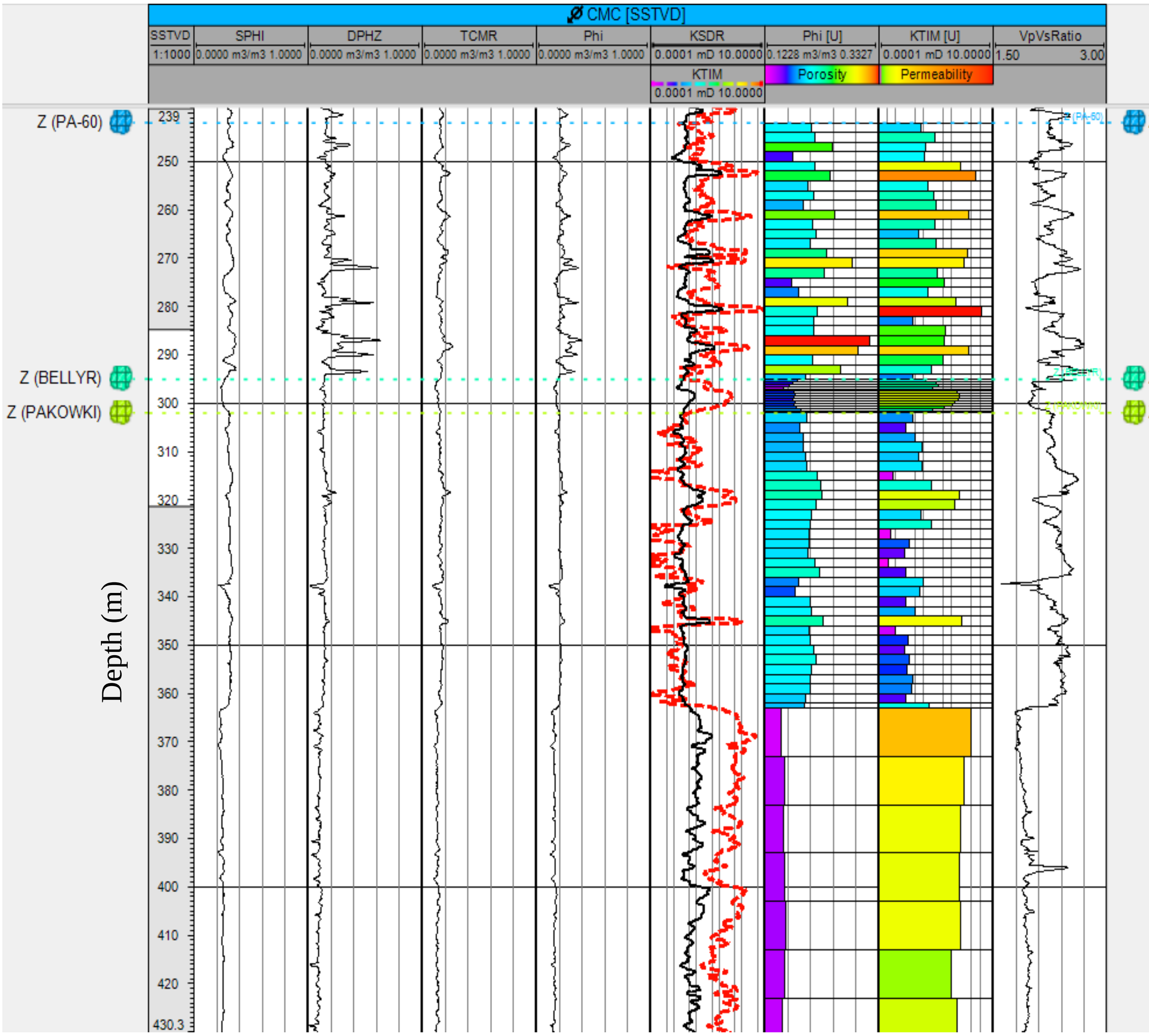

Figure 2-7. The well log data for seismic porosity (SPHI), density porosity (DPHZ), TCMR porosity, the average of mentioned three porosity (PHI), the permeability (KTIM: Timure-Coates, KSDR: Schlumberger-Doll-Research model), upscaled data for PHI and KTIM, and Vp/Vs ratio near the injection zone.

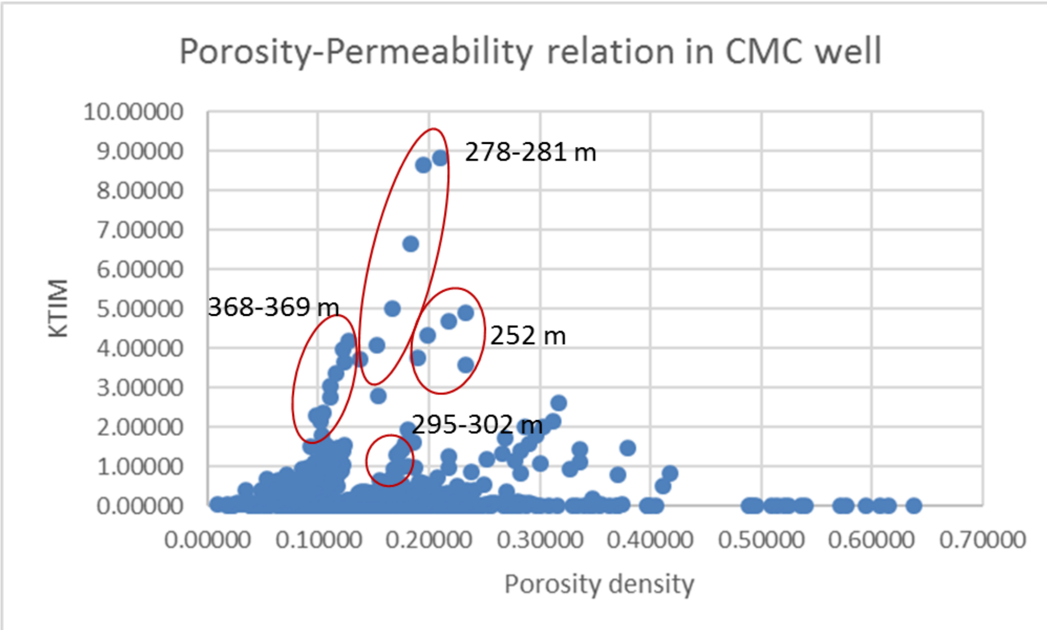

Figure 2-8: The Timur-Coated model permeability (mD) vs. density porosity (v/v). The different statistical populations are recognizable because of the different lithological and sedimentation condition.

In reservoir studies, the relation between permeability and porosity is a useful relation to estimate permeability from the porosity. Figure 2-8 shows the relation between porosity (density) and permeability (KTIM).There is no significant relation between two parameters in the whole well but it is possible to define a correlation between them in some formations and horizons.

Just there is a linear correlation in the fully logarithmic diagram between KTIM and CMFF (free fluid porosity (index) from CMR) (Figure 2-10).

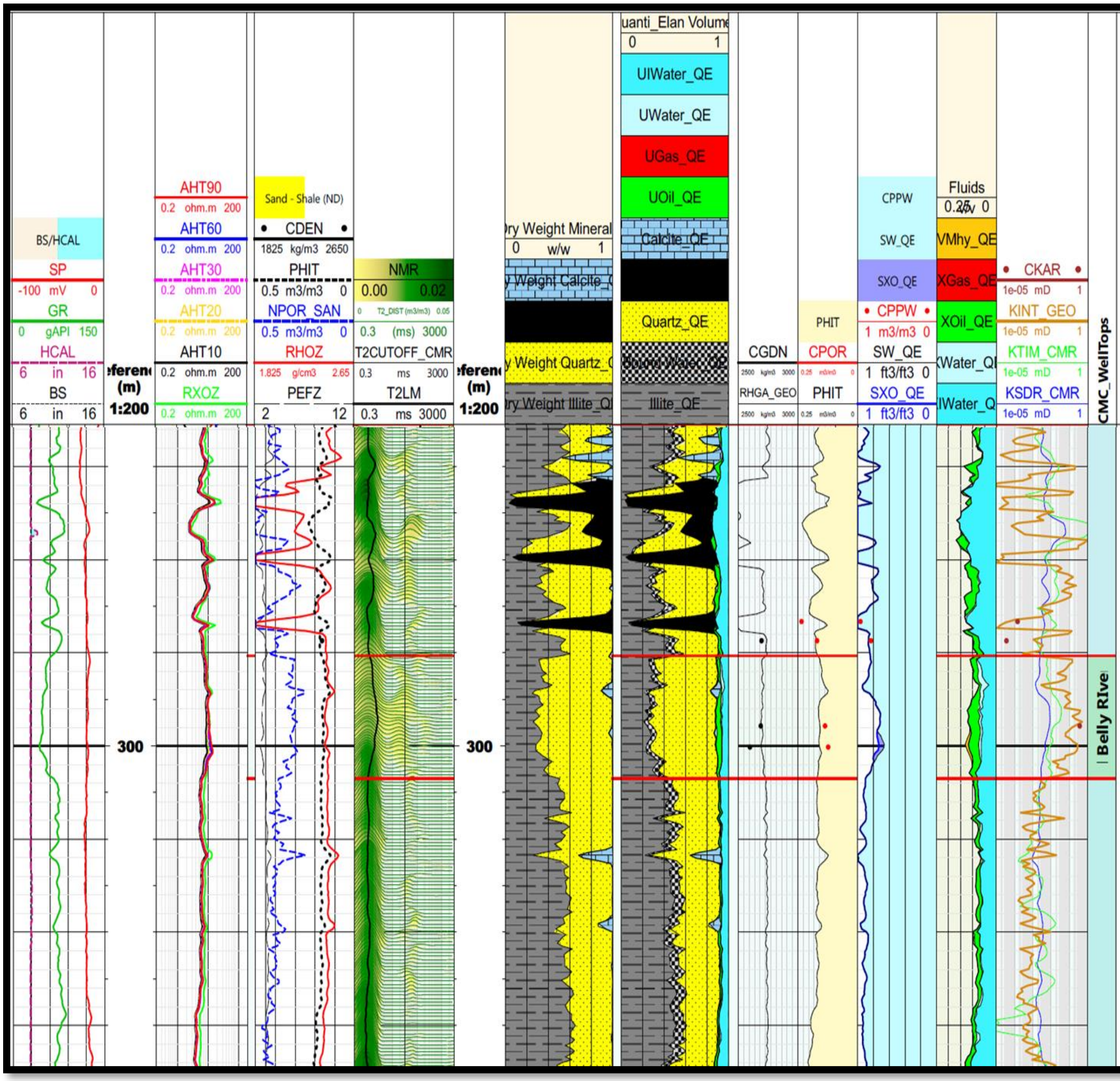

Figure 2-9: Petrophysical interpretation result for the injection zone and around. The minerals type was characterized by the well logs.

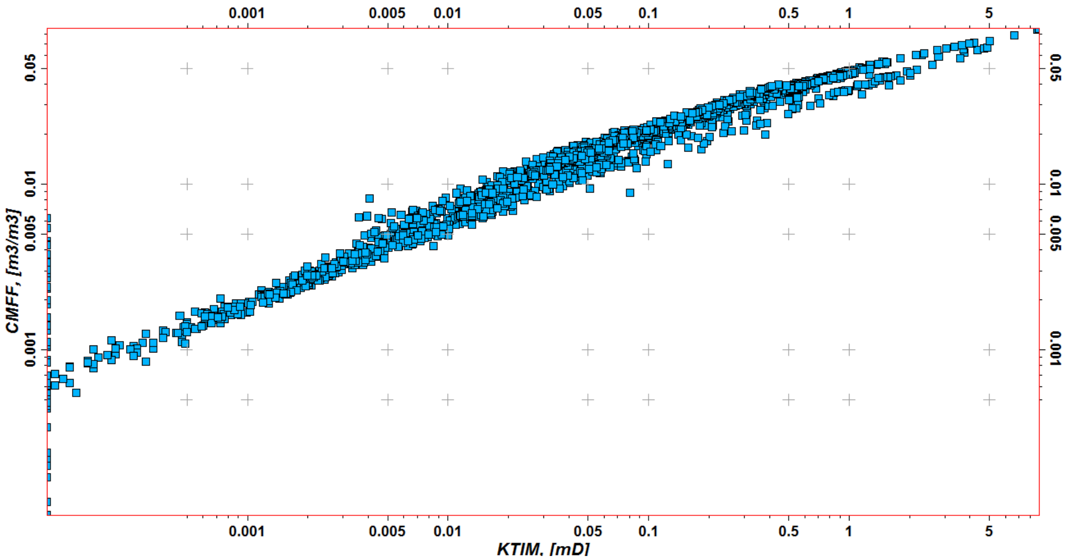

Figure 2-10. There is no relation between KTIM and other log data. Just a meaningful relation is between CMFF (free fluid porosity (index) from CMR) and KTIM. The coordinate is full logarithmic scale. For more information see Appendix A.

Figure **2-9** is a full interpretation of the well log data near the injection zone (BBR). The most useful part of the interpretation of the reservoir and seismic study is the lithological and mineralogical content of the target.

2.4 Core study

The core samples make it possible to do some measurements directly on the rock sample. In this section, the mineral discrimination study based on spectral gamma ray (combined with log data), and permeability and porosity of the rock sample were introduced.

Figure 2-11 shows core samples obtained from the core in the injection zone. The injection zone will be in depth of 295-302 m in the Basal Belly River Sandstone.

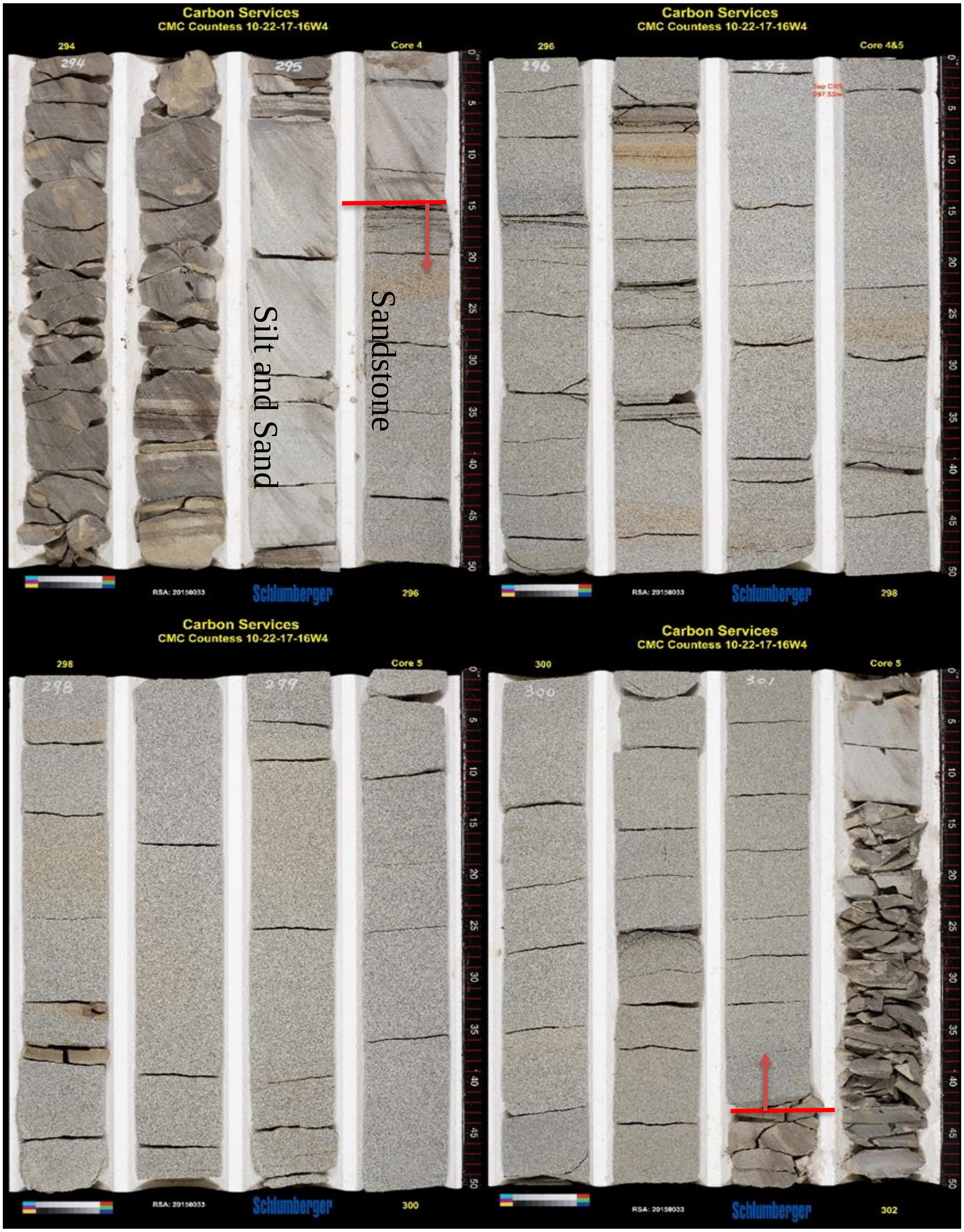

Figure 2-11. Core photo from the injection zone (sandstone) (taken by Schlumberger).

2.5 Lithology and Mineral study of the Belly River sandstone

The mineralogy and lithology information were extracted from the well log data. Some useful well logs for mineralogy and lithology analysis are:

Mineralogy: gamma ray, density, neutron porosity, neutral radioactivity, spectral gamma ray, nuclear magnetic resonance, acoustic log, caliper.

Lithology: Laterolog, induction, Microlaterolog, SP log, electromagnetic propagation, gamma ray, density, neutron porosity, neutral radioactivity, spectral gamma ray, nuclear magnetic resonance, acoustic log, caliper.

The main goal of mineral study and discrimination was for calculating the bulk modulus of minerals in the fluid substitution process. In this part, the available well logs were used to distinguish the mineral types in the reservoir zone.

Table 2-1: The mineral types in the reservoir zone by the well log data analysis (from Figure 2-12)

Mineral discriminated by well log analysis	Fraction
Quartz	40%
K Feldspar	4%
Albite	8%
Kaolinite	15%
Chlorite	7%
Illite-Smectite	11%
Siderite	15%

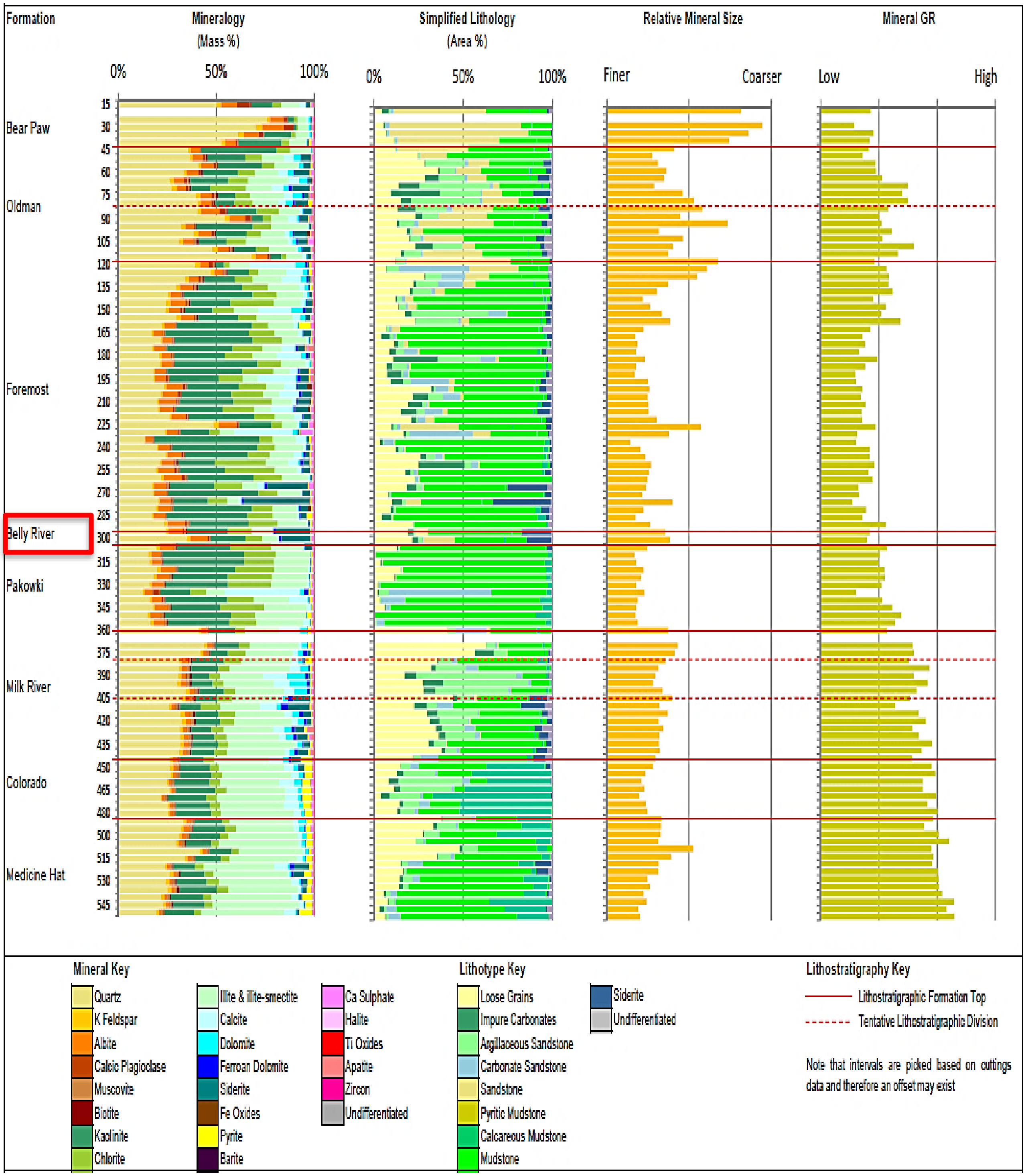

Figure 2-12: The result of the mineral types discriminated by the well log data (Kirk Osadetz, personal conversation)

2.6 Core analysis

The core study results make it possible to calibrate the well log data (permeability) with the directly measured data from the rock samples. The calibrated permeability uses core data and well log data, and it was used to make a geomodel (Chapter 4). The procedure for calibration for the well data was described by J. Dongass (2016). The final data for the reservoir zone in geomodel is demonstrated in Figure 2-13, and the used data are from the core study in Table 2-3.

Table 2-2.Effective porosity and water and gas saturation in the core

Core Depth	As Received Bulk Density (gr/cc)	As Received Grain Density (gr/cc)	Effective Dry Grain Density (gr/cc)	Gas Fielled Porosity (% of BV)	Hydrocarbon Fielled Porosity (% of BV)	Effective Porosity (% of BV)	Effective Water Saturation (% of	Effective Gas Saturation (% of PV)	Effective Oil Saturation (% of PV)
293.34	1.401	1.414	1.469	0.96	0.96	12.35	92.2	7.8	0
294.37	2.381	2.455	2.57	2.99	2.99	10.11	70.46	29.54	0

Table 2-3.The measured total porosity and water and gas saturation in the core

Sample ID	Core Depth (m)	As Received Bulk Density ($^{g}/_{cc}$)	As Received Grain Density ($^{g}/_{cc}$)	Total Dry Grain Density ($^{g}/_{cc}$)	Total Porosity (% of BV)	Total Water Saturation (% of PV)	Total Gas Saturation (% of PV)	Total Oil Saturation (% of PV)
W3-1	282.65	2.302	2.343	2.655	20.22	91.47	8.53	0.00
W4-1	293.34	1.401	1.414	1.537	23.43	95.89	4.11	0.00
W4-2	294.37	2.381	2.455	2.698	16.87	82.31	17.69	0.00
W7-1	479.12	2.419	2.468	2.699	15.28	86.99	13.01	0.00
W8-1	480.71	2.473	2.501	2.713	13.35	91.68	8.32	0.00
W9-1	494.22	2.466	2.487	2.716	14.05	93.95	6.05	0.00
W9-2	494.66	2.443	2.506	2.700	13.62	81.52	18.48	0.00
W10-1	502.64	2.472	2.538	2.710	12.37	79.08	20.92	0.00
W10-2	503.37	2.470	2.548	2.724	12.92	76.33	23.67	0.00

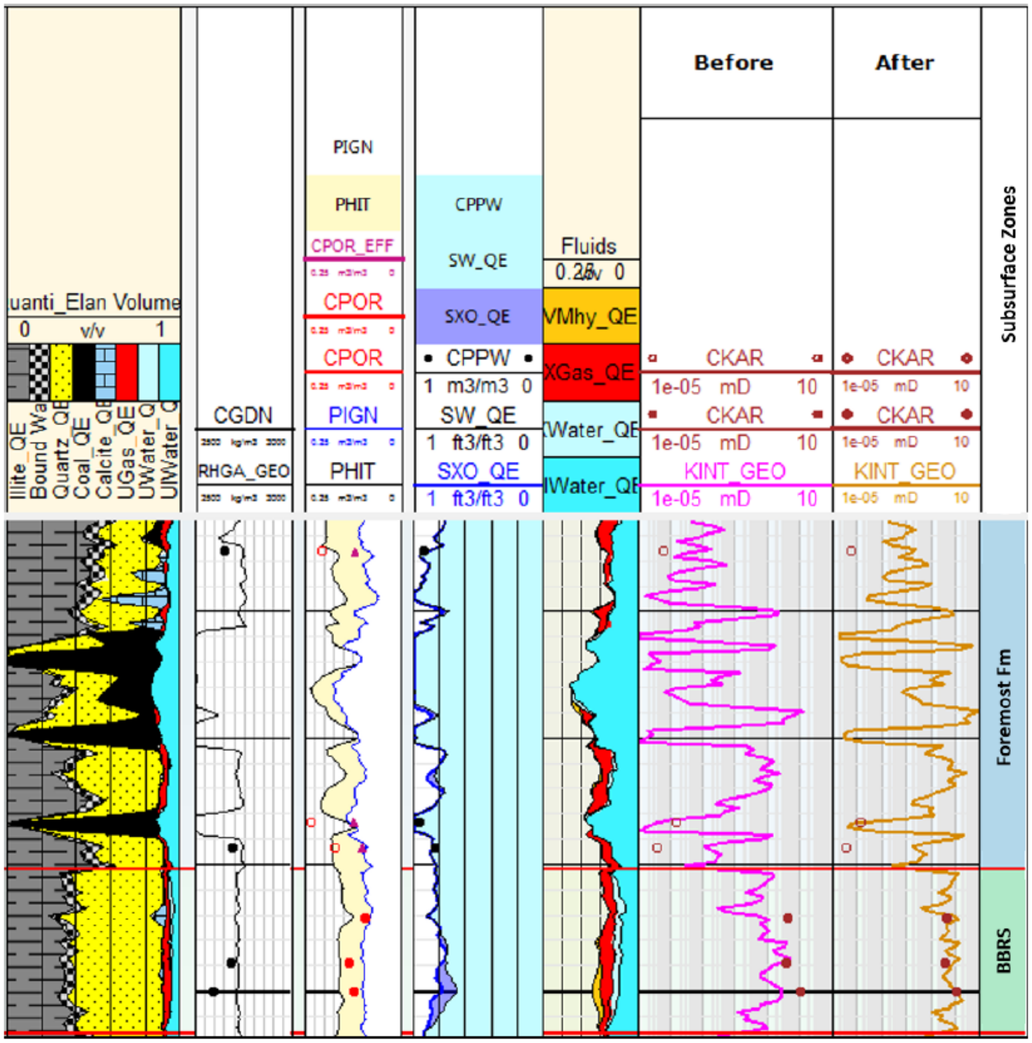

Figure 2-13: Before and after log-to-core calibration of K_INT data for the injector Well (10-22), from Swager (2015).

Chapter 3. Seismic design for 3C-4D propose in the FRS

3.1 Introduction

The primary objective of this section is to evaluate the 3D-3C seismic survey for time-lapse and reservoir studies to monitor CO_2 injection and map the underground layers and structures. The main targets for the seismic acquisition are two porous layers for the CO_2 injection in 300 m and 500 m. Technically two stages were done for seismic design: The first part is data gathering and analysis results for velocity functions and desired and dominant frequency content of targets (shallow and deep) and the second part is the parameter estimation for preventing spatial aliasing and to check the best acquisition parameters for proper horizontal and vertical seismic resolution. For the bin size and migration aperture estimation, constant and linear velocity methods were considered. Two seismic surveys were introduced, and their attributes (fold map for PP and PS data with different offset, offset and azimuth distribution) were compared. Finally, for improving PS fold, we tested a random receiver distribution. The concepts and formulas for this part are from Cordsen (2000), Vermeer (2002), Stone (1994) and Liner (1997,1999,2004).

3.2 Background information

For a regular onshore seismic design project, consideration related to the area's geological condition and the surface access that can make acquisition footprint are important. We introduce the required data and information for a successful design as the following items:

1- Geology of area (surface, subsurface, and structural condition as layers' dip angle)

2- Terrain conditions (topographic, permit)

3- Frequency contents (Max and dominant) in the targets and required resolution

4- Velocity and velocity as a function of depth

5- The objective of acquisition (image, reservoir study)

6- Full fold Image zone for structural or reservoir studies to estimate acquisition boundary and area by calculating migration aperture and fold taper

7- Seismic data (row shots for a better frequency analysis and sections for interpretation and evaluation and both for controlling quality of data and problems)

8- Technical part and existence technology (recording system)

9- Financial conditions and limitations

3.3 Considerations for a 4D seismic design and acquisition

For a seismic design in a conventional 3D project, geophysicist consider important points as:

1- Uniform PP fold in the image area

2- Full fold on the target horizons

3- Appropriate bin size to prevent aliased data acquisition

For a 4D seismic design, we need to repeat the baseline seismic acquisition geometry. To prevent for acquisition error and footprints, in the monitor surveys, the CMP points should be exactly at the baseline surveys CMP locations. This requires that the source and receiver points are exactly in the same place as the baseline seismic acquisition survey. So, for a 4D study in a big field, the seismic data should be acquired with the same survey and parameters as a baseline, and for the small fields and surveys, the geophones can be cemented in place.

3.4 Targets

As mentioned previously, the study area is in the southern Alberta plain. According to the well tops and existing old 2D and 3D seismic data, subsurface layers are almost flat in the target zone.The shallow target is the Basal Belly River sandstone and Pakowki Formation at 295-302 m depth (Table 3-1), mid-target is Medicine Hat Formation (~500 m) (the second injection option), and the deep target is the top of 2WSS (or Base_Medicine Hat Formation) at ~700 meters. A proper parameter design should guarantee full fold data and appropriate azimuth and offset distributions at the target horizons.

Table 3-1.The Targets were considered for the seismic design purpose.

Depth (m)	Formation Top	Period		
189.74	*Top of the available well log data*	Upper	Cretaceous	
295	*Basal Belly River Sandstone*			*Target*
302	*PAKOWKI*			
357	*MILK RIVER*			
441.5	*COLORADO SHALE*			
478.5	*MEDICINE HAT SANDSTONE*			
711	*SECOND WHITE SPECKLED SHALE*			
785	*FISH SCALES*			

3.5 Frequency content

For bin size estimation and design, the maximum and dominant frequency of seismic data from previous seismic acquisition surveys (VSP,2D or 3D) should be analyzed. The relation between frequency (f), dip angle (θ), interval velocity (V) and bin size (B) to prevent aliasing phenomena in spatial sampling is:

$$B = \frac{V_{\text{int}}}{4 f_{\max} \sin\theta}$$

Eq. 3-1

There are many old 2D and 3D seismic surveys in the area as used for the frequency analysis in Figure 3-1. According to frequency content analysis at the shallow and deep targets, as shown in Figure 3-1, the dominant frequencies for the target formations are between 30-60 Hz, and the maximum frequency is 80 Hz.

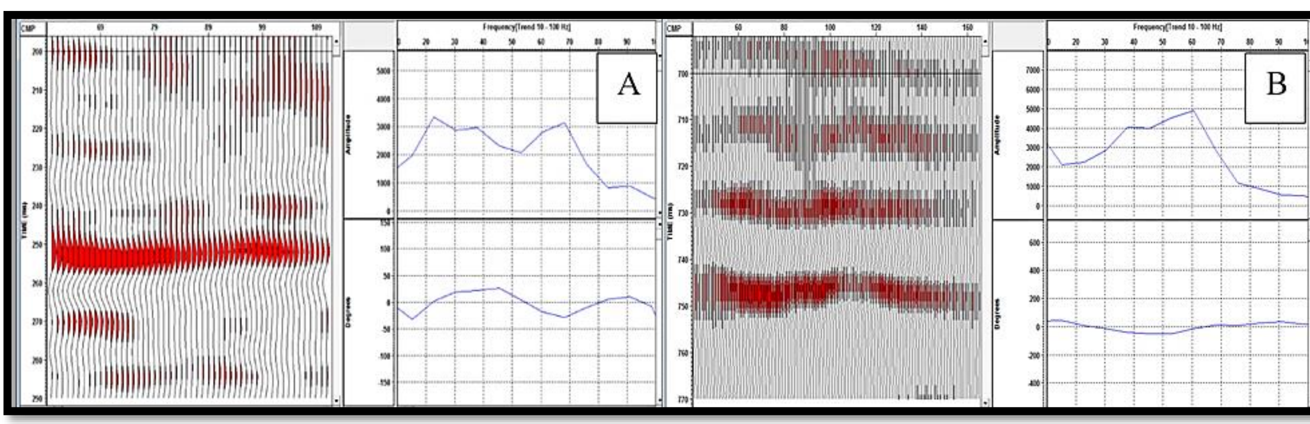

Figure 3-1. Frequency analysis: for the shallowest target (A) and the deepest targets (B)

3.6 Velocity-depth function

Well log data was used for compressional and shear wave velocity profiles, and Figure 3-2 shows the general relation between depth and velocity. For bin size and migration aperture estimation, it is possible to use constant or linear velocity function which can decrease the migration aperture size and acquisition area so that method can optimize the acquisition cost.

3.7 Bin size

Appropriate bin size can guarantee a data set acquisition without aliasing problem; small bin size can ensure unaliased data, but also can decrease S/N ratio (Cordsen et al., 2000). Here we directly use anti-aliasing bin size formula (Eq. 3-1) for the constant and linear velocity functions.

The project area is situated on a flat plain and no subsurface structure, and layers have a gentle dip angle less than 2 degrees. Figure 3-3 demonstrates the calculation result for the bin size by constant and linear velocity methods. The linear function for the velocity is calculating by the well log data as Figure 3-2. The bin size estimation by linear velocity method uses the velocity as a function of depth. The linear velocity concept is also useful in the migration aperture calculation. The dip angle is also relevant to migrating diffracted energy, even though the layers are nearly flat.

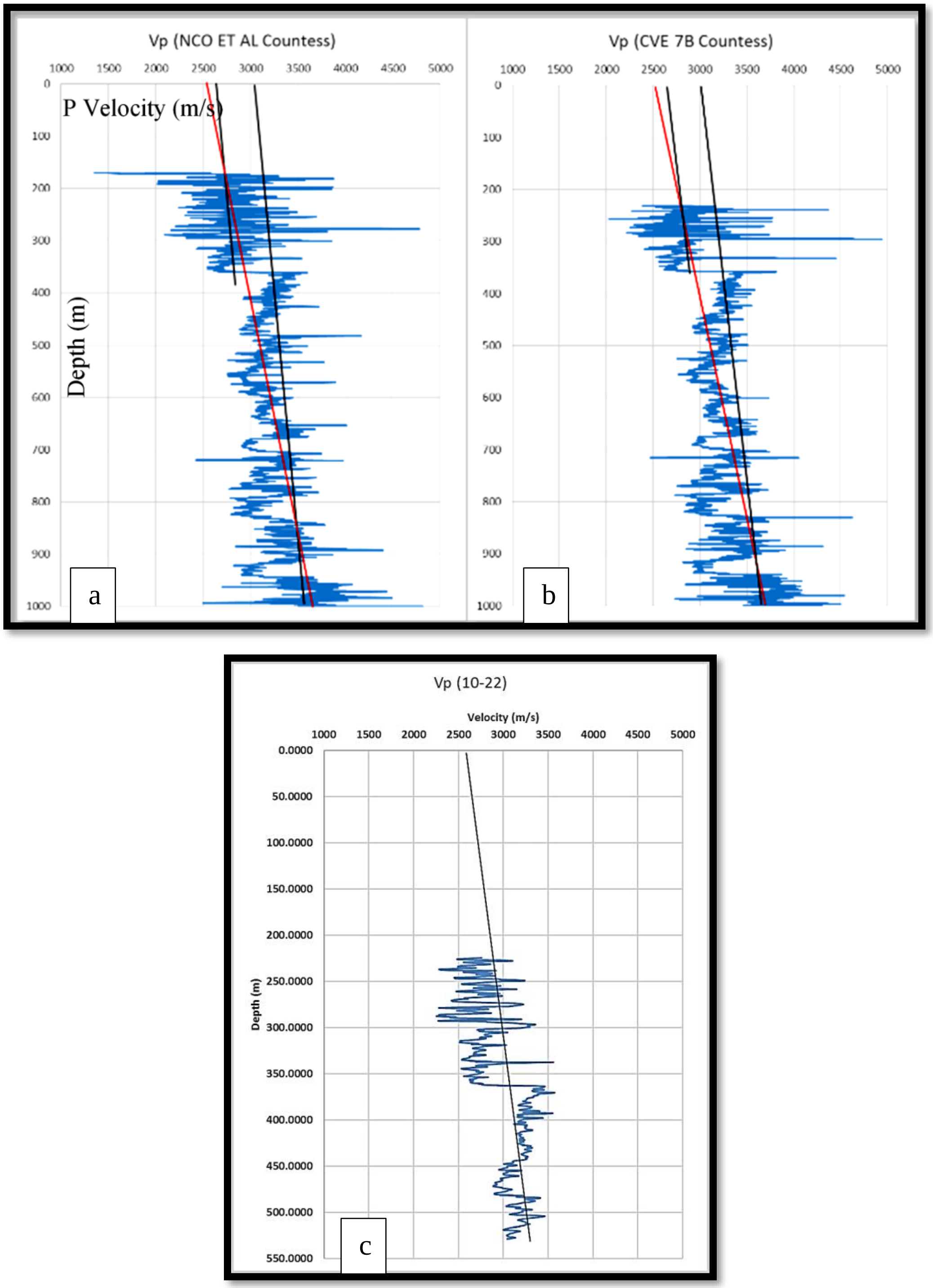

Figure 3-2. A linear function for velocity is used for calculation of bin size and migration aperture. Velocity function for FRS project regards to well log data (wells 11-22-17-16 (a) and 7-22-17-16 (b) and 10-22-17-16 (c)) is V=V0+kz=2650+z.

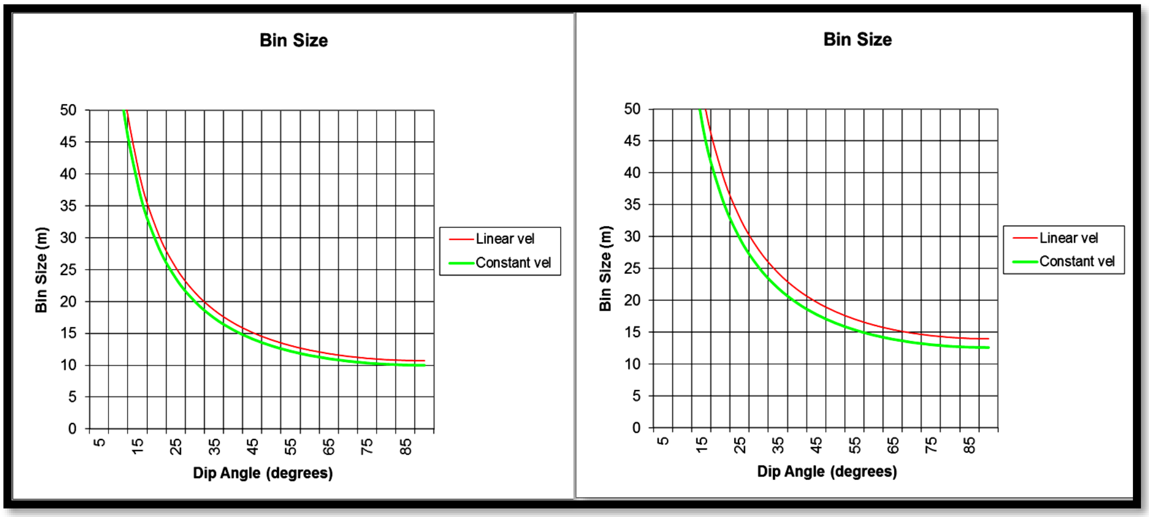

Figure 3-3. Bin size for the shallow target with 80Hz max frequency (left) and the deep target with 65Hz (right).

3.8 Box size and geometry

The box size (receiver line interval*shot line interval) and geometry can introduce the LMOS (largest minimum offsets) concept as an important parameter for the shallow target acquisition design. As mentioned, the target depth is from 300-700 m, and for acquiring data with the suitable fold on the target depth, LMOS should be smaller than the first target depth, because it results in a no data zone equal to the LMOS two-way time. Another problem that decreases fold at shallow depths is NMO stretch and mute so for the project, and this should be considered in the design.

3.9 Design option

Analysis and parameters calculation in the last section, and necessity to have a high-resolution seismic profile for the research purpose, led us to suggest a dense seismic survey. For the design quality control, the option was loaded and analyzed in OMNI (design and survey control software).

3.9.1 The acquisition parameters

The acquisition parameters are listed in Table 3-2. This option has a dense acquisition pattern in the middle part as shown in Figure 3-4. In this figure the red spots are shot points, and the red dots are receivers. The bin size for this option is 5m*5m and receiver and shot line intervals are both 50 m in the central part of the survey (500*500 m) and 100 m in the outer parts. The nominal fold is up to 185 in this central part. The acquisition parameters was designed for a high-resolution image for the shallow reservoir.

Table 3-2. The acquisition parameters.

Parameters	Main	Central part
Bin size (m)	5	5
Receiver interval	10	10
Receiver line interval	100	50
Shot interval	10	10
Shot line interval	100	50
Total Survey area	1000*1000	500*500
Maximum Offset	1407	
minimum offset	7	
Largest minimum offset (LMO)	134	
The highest fold (PP)	185	
Maximum inline offset	1000	
Maximum xline offset	1000	
Aspect ratio	100%	
Total shots	1434	
Total live geophones	1400	

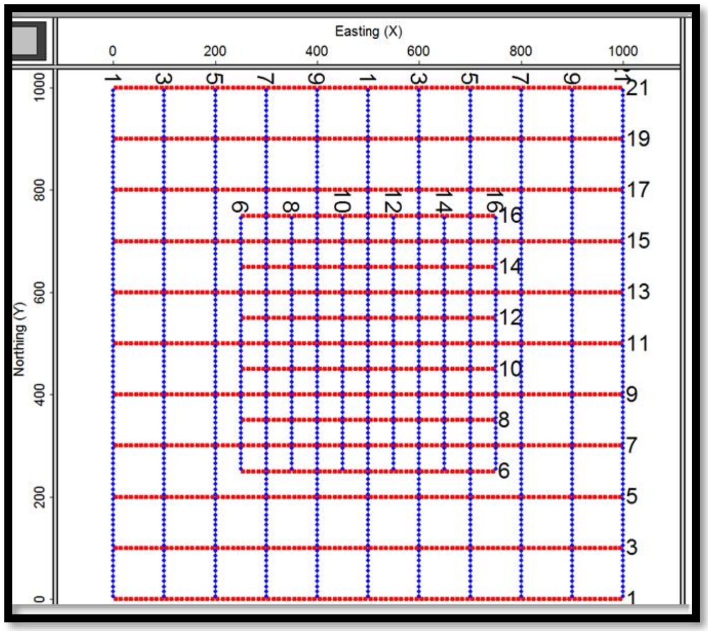

Figure 3-4.The survey geometry. The red points demonstrates shot points, and the blue ones are receivers. There are a dense shot and receiver points in the mid of survey with dimension equal to 500*500 m.

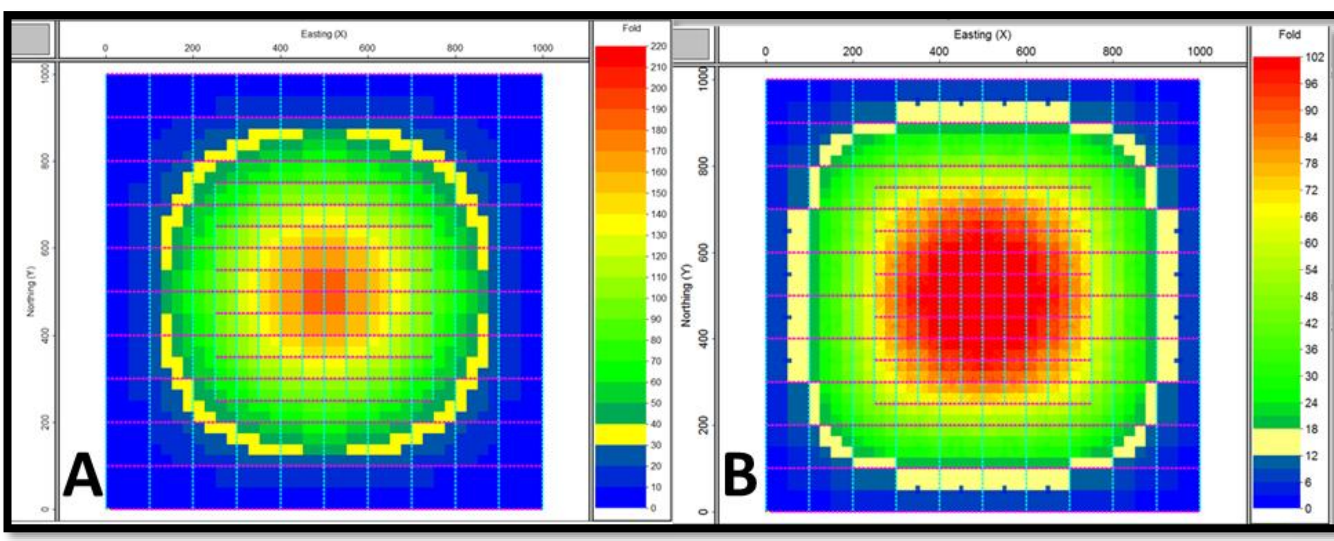

Figure 3-5. A. The fold map. The highest numerical range for the fold is 220 for both shown by the red color in the scalebar. The yellow circle shows the fold range between 30-40. B. The fold map for offset 0-700 m.

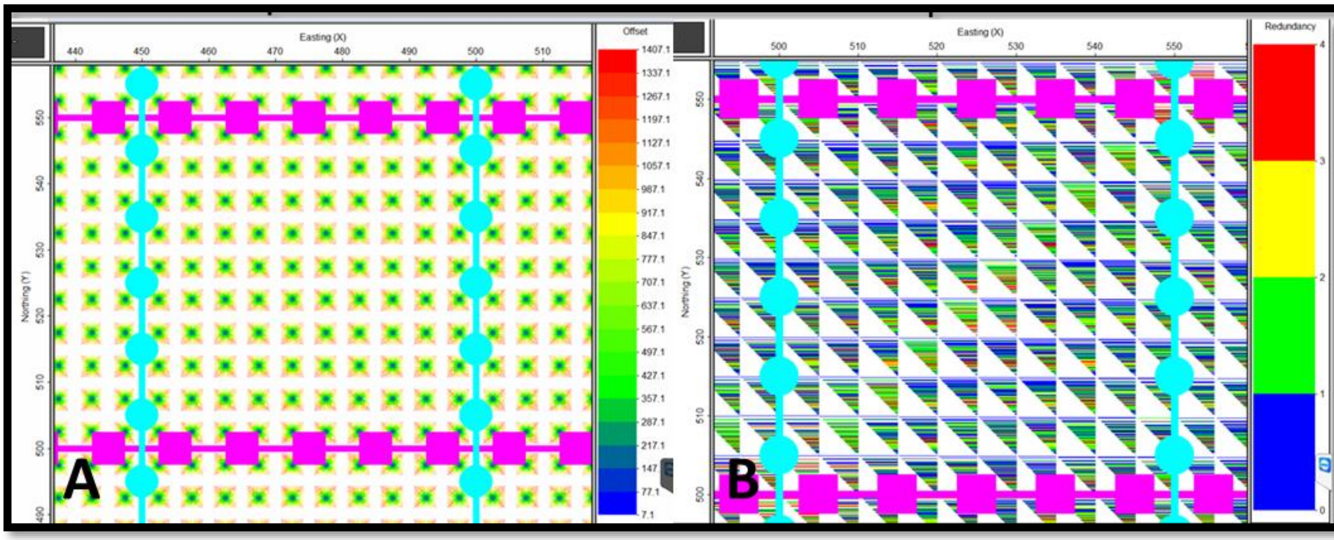

Figure 3-6. A. The azimuth distribution in the full fold zone. It shows a proper azimuthal coverage; the azimuth depends on the shorter offsets. B. The offset distribution in the full fold box. The acquisition covers full offset ranges.

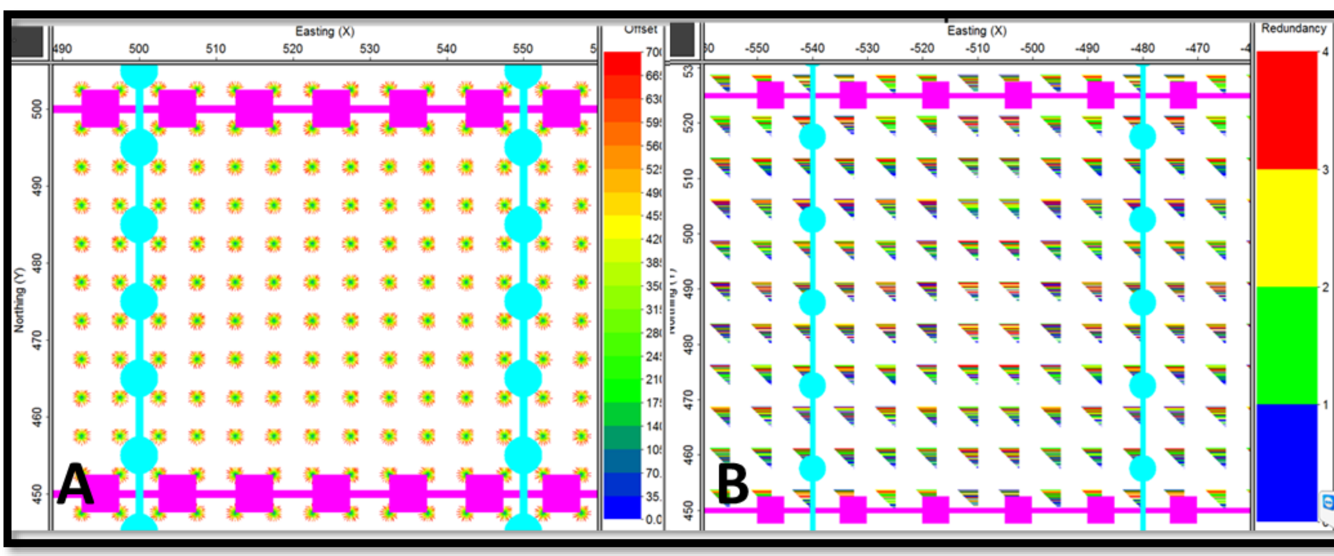

Figure 3-7. A. Azimuth distribution in the target range (0-700 m offsets). B. Offset distribution in the full fold box for 0-700 m.

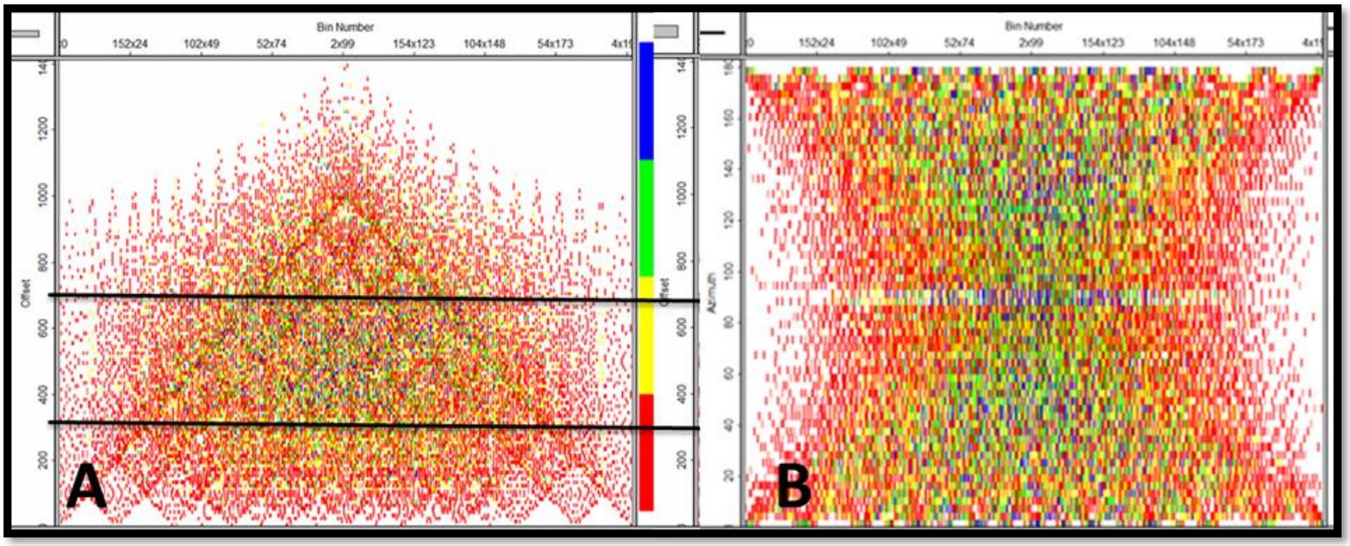

Figure 3-8. A. Offset redundancy, the target zone demonstrated by the black lines. B. Azimuth redundancy, the number of traces that fall in each section; gaps indicate missing azimuth

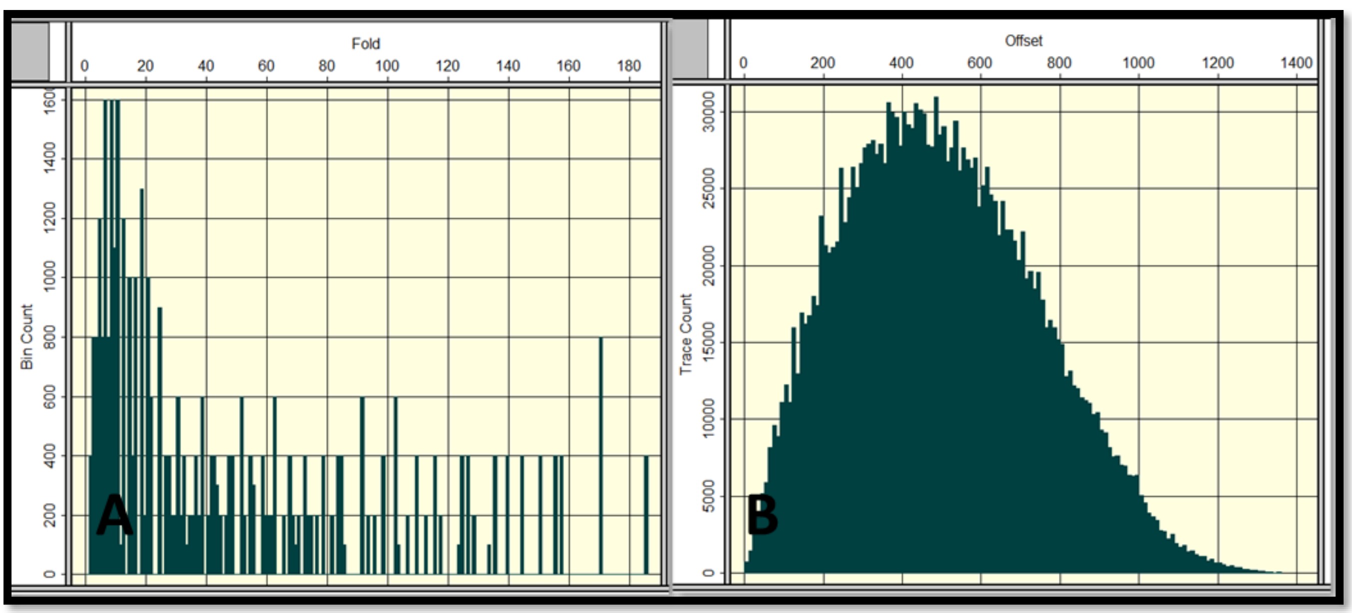

Figure 3-9. A. Histogram of Fold, the numbers of bins that fall in each range of fold values. B. Histogram of Offset, the number of traces that fall in each range of Offset values

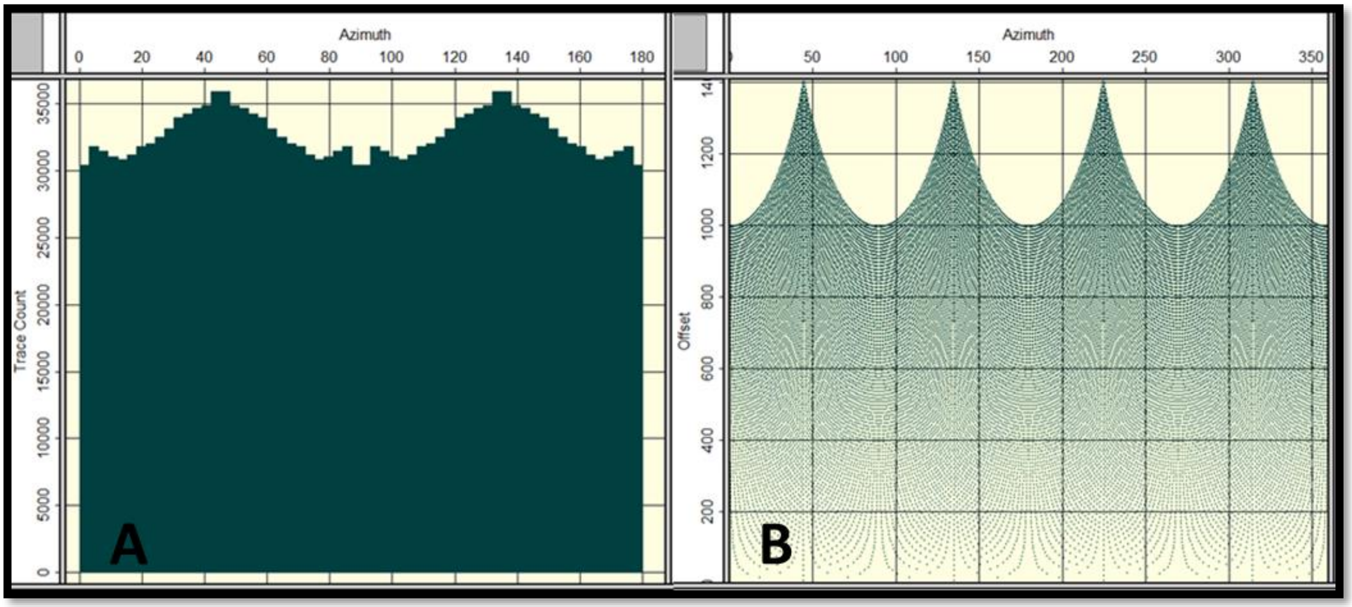

Figure 3-10. A. Histogram of azimuth, the number of traces that fall in each range of azimuth values. B. Offset versus azimuth diagram.

Figure 3-5 shows the fold map. Figure 3-5.A. is a nominal fold map that covers all acquisition offsets and azimuths. The yellow circle shows the fold range between 30-40 and out of this circle, the fold decreases less than 30. The fold at the well point is over 200. This fold distribution is normal for an area without any complexity in the geology with horizontal layers with no diffraction events. Figure 3-5.B. shows the fold for source-receiver offsets from 0 to 700m. The fold distribution in this range that can guarantee a suitable image at the target depth.

Figure 3-6 demonstrates offset (A) and azimuth (B) distribution. The distribution diagrams show a perfect offsets from 64-1407 m (they are LMOS and maximum offset) and azimuths from 0-360 degree.The offset and azimuth distribution are suitable for the shallow target range (Figure 3-7).

The offset and azimuth redundancy diagrams were determined for each bin of the survey (Figure 3-8). They show excellent response in the target range for offset redundancy (A) between the black lines with a perfect azimuth distribution (B). Figure 3-9 shows a statistical result for the fold versus bin count (left) and offset range versus trace count. As seen in the diagram, the offset coverage for the shallow to deep targets are suitable.

Figure 3-10 shows azimuth versus trace count and offset. Both diagrams demonstrate a proper distribution for the azimuth that can make a suitable database for amplitude variation with azimuth (AVAZ) study.

3.10 PS survey design

The base of PS designing is the concept of CCP (Common Conversion Point). In this chapter, a non-asymptotic method is used for determining fold and calculating other attributes. For the design attributes for the PS acquisition, a flat target is considered at 400 m depth.

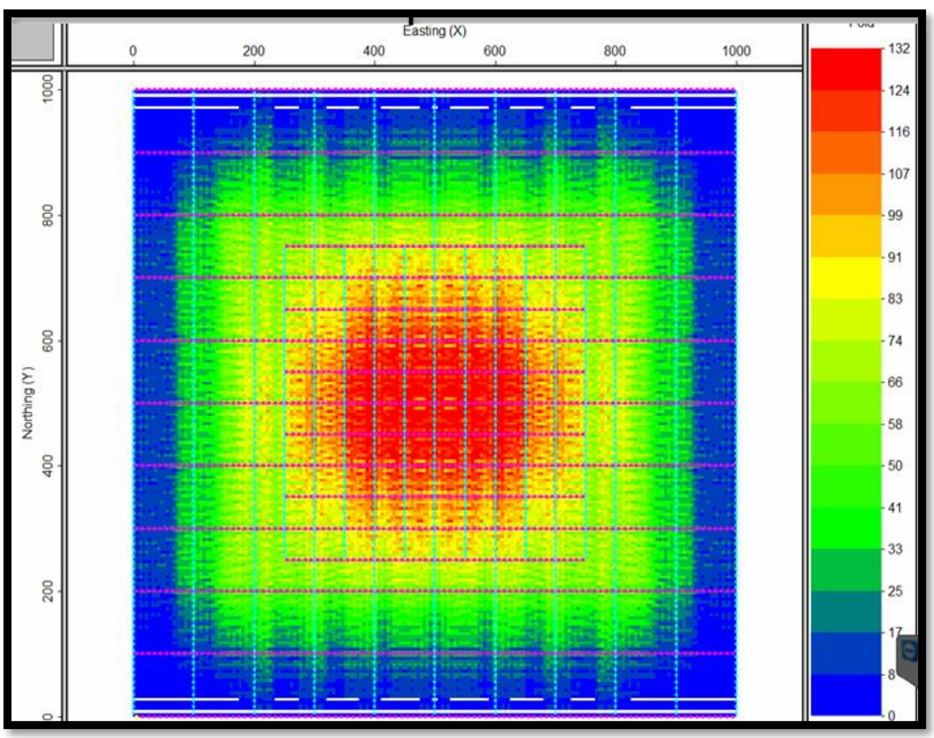

Figure 3-11. The PS fold map (non-asymptotic method) for a target in 400 m depth, Vp to Vs ratio is considered equal 2.

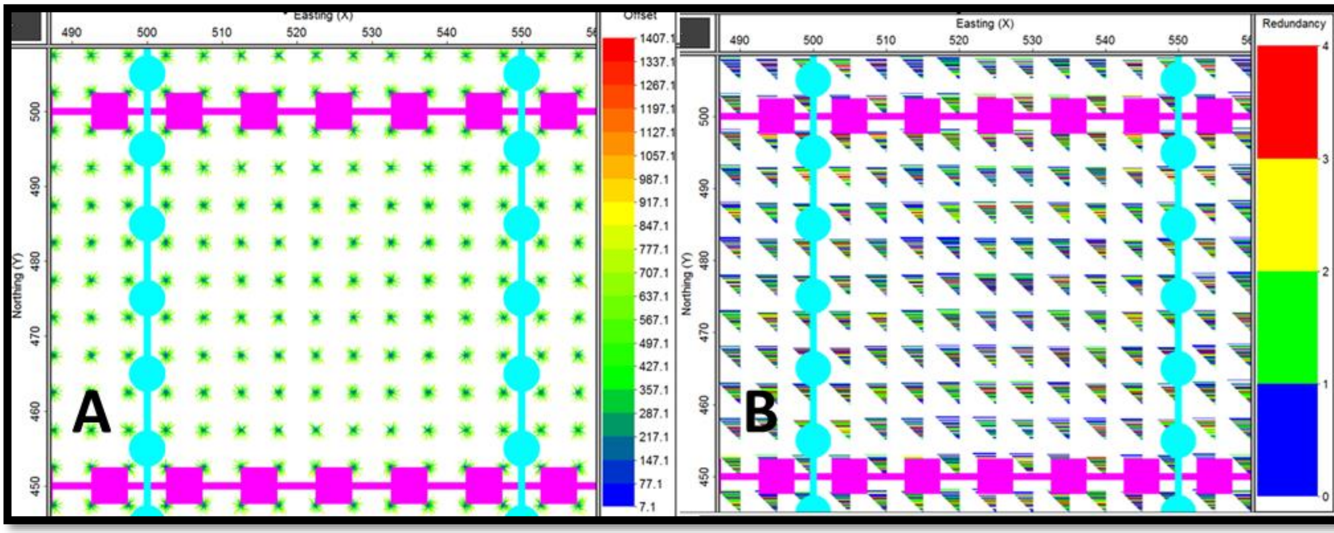

Figure 3-12. A. The PS azimuth distribution in the full fold boxes. B. Offset distribution for the PS wave.

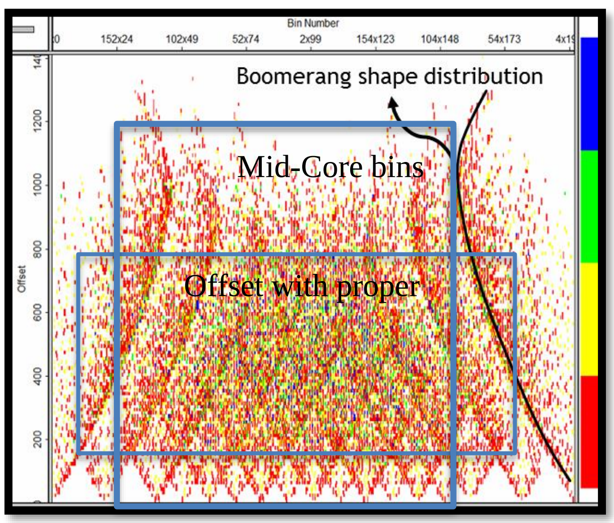

Figure 3-13. Offset redundancy for PS wave, the number of traces that fall in each section; gaps indicate missing offsets.The curve of boomerang shape distribution is a function of p to s wave velocities ratio.

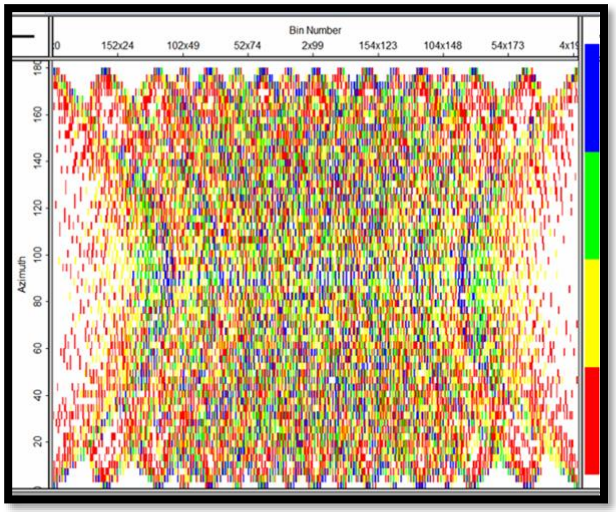

Figure 3-14. Azimuth redundancy for PS wave, the number of traces that fall in each section; gaps indicate missing azimuth.It shows a proper azimuth distribution.

The fold is concentrated mainly in the dense, central part and fold map reveals that just 50% of acquisition area will reach to the fold more than 30 (Figure 3-11). The maximum nominal fold is 185, and the mid-core high-density acquisition zone guarantees high fold as >100 for the offset 0-700 m. Because aspect ratio is 100% and box and patch are symmetric, azimuth and offset distribution maps show excellent design parameters. Azimuth-offset histogram indicates a good coverage for offsets less than 1 km and 360-degree azimuth, (also there are a lack of data for some azimuth for offsets greater than 1 km, but this part is not in our interest zone). The offset redundancy diagram, as expected, shows a zigzag pattern that is due to the orthogonal geometry. It shows a high redundancy for the offsets 300-700m.

For calculating PS fold, OMNI uses non-asymptotic PS conversion point between shot and receiver. It considers a flat target layer that is 400m for the project. The PS fold and offset; azimuth distribution maps (Figure 3-11, Figure 3-12, Figure 3-13 and Figure 3-14) show a good design attributes for the PS data acquisition.

3.11 A criterion for fold distribution

The fold is an important parameter in seismic design. Sufficient and uniform fold distribution in a survey is the priority that geophysicists deal with it in the parameter design. Prevention of striped fold pattern or lack of fold because of acquisition field barriers in PP-wave acquisition and smooth fold in PS acquisition are two challenges for designers. For an optimum fold condition and distribution in a 3D seismic survey, mathematically it can be described as a parameter with the lowest possible variance. For a discrete parameter as x_i, the variance (Var) and the expected value or average (μ) in a vector are demonstrated as Eq. 3-2 and Eq. 3-3:

$$Var\ (x) = \frac{1}{n}\sum_{i=1}^{n}(x_i - \mu)^2$$

Eq. 3-2

Where:

$$\mu = \boldsymbol{\frac{1}{n}\sum_{i=1}^{n} x_i}$$

Eq. 3-3

For a 3D seismic survey with totally m*n bins in x and y directions, (as two-dimension matrices), The fold in a i, j th cell is demonstrated by F_{ij}. So the variance of the fold for all bins can explain as following formula:

$$Var\ (F) = \frac{1}{mn}\sum_{i=1}^{m}\sum_{j=1}^{n}(F_{ij} - \mu)^2$$

Eq. 3-4

And the average can describe as Eq. 3-5.

$$\mu = \frac{1}{mn}\sum_{i=1}^{m}\sum_{j=1}^{n} F_{ij}$$

Eq. 3-5

Fold taper: in traditional design, fold taper is the area out of full fold zone. Formerly, the area out of full fold zone does not have a suitable fold amount for quantitative and qualitative interpretation. Now with improving acquisition techniques and increasing fold, geophysicists can work in the acquisition marginal zone because of reasonable fold value around the full-fold region. In a seismic survey with the high-fold acquisition, a new definition of fold taper is used and fold less than desired for interpretation will be considered as fold taper. In the current project, the suitable fold is >30 and bins with the fold less than 30 have been deleted for statistical analysis and variance calculations.

3.12 Improving PS fold coverage: randomize pattern

In this section, I attempt to improve the PS-fold coverage by changing the acquisition geometry. The patterns tested have randomized source or receiver points with a different configuration, and the criterion is the introduced variance test.

For the study purpose, I checked 12 different patterns as presented in Table 3-3. For each model the following variation were evaluated:

1- A movement direction was selected for each geophone. It can be a radial movement or in the cross-line or Inline direction.

2- The displacement distances are equal a bin size to half of receiver line interval.

3- The PS fold map was generated for each pattern and the high PS fold (or PP full fold area) zone selected for variance test.

4- The result of variance tests are demonstrated in Table 3-3.

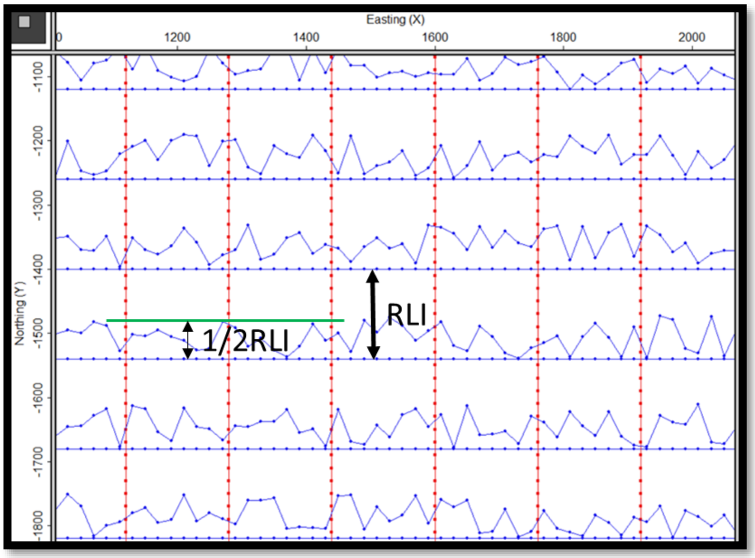

Figure 3-15.A sample of the suggested regular survey (rectangular box) and randomized receivers pattern.

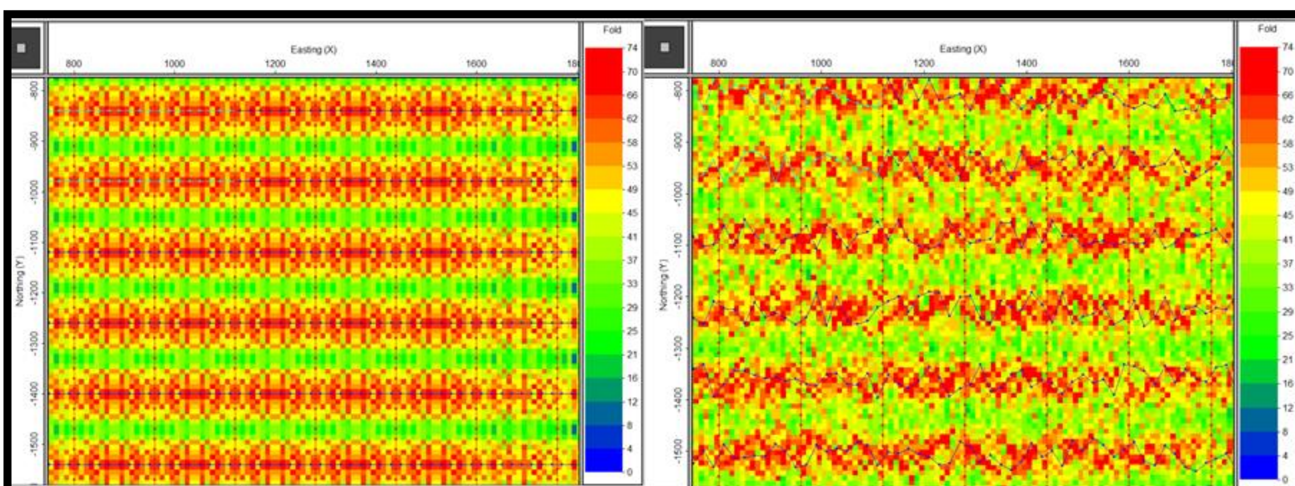

Figure 3-16. The fold map for regular rectangular box pattern (left) and randomized receivers pattern (right)

Table 3-3.The variance test result for 12 different acquisition pattern.

No	Type	Movement Direction	Receivers displacement	Var in full fold zone
1	PP	No	No	0
2	PP	Xline	20 (trace interval)	0.26
3	PP	Inline-Xline	10 (Bin Size)	0.15
4	PP	Inline	10	0
5	PP	Radial	10	7.34
6	PS	No	No	142.12
7	PS	Xline	20	142.88
8	PS	Inline-Xline	10	141.88
9	PS	Inline	10	141.84
10	PS	Radial	10	148.66
11	PS	Xline	70 (1/2RLI)	133.40
12	PS	Radial	70 (1/2RLI)	153.87

Figure 3-15. shows the survey configuration of randomly located receiver points up to half receiver line interval moved from the standard rectangular pattern. Figure 3-16 is the fold distribution map for the rectangular pattern and random pattern (Figure 3-15). The variance of PS-fold is 142.1 for the regular survey. Apparently, pattern number 11 (Figure 3-15) with cross-line movement direction and half receiver line interval displacement can improve the PS fold distribution.

Chapter 4. The baseline seismic data, interpretation and geomodel development

4.1 Introduction

The seismic acquisition parameters and the calculation method were introduced in the last chapter. Design option was approved and used for the 3D-3C data acquisition as baseline data. As mentioned in the introduction, the seismic field work was done in the summer (May) 2014 by Tesla Exploration. The recorded data sample rate was one ms. The source used was two mini vibrators with a linear sweep from 8 to 150 Hz and two sweeps of 16 s length per each point. INOVA-7 3C analog geophones was used as receivers in the survey.

The data were processed for PP-wave in two different versions with 2 ms sampling interval by CREWES (Isaac, 2015) and 1 ms sampling by Sensor Geophysical. Also for the interpretation and inversion purpose, a PS wave data processing was done in 2015 by CREWES. Post-stack migration method was applied for the both processing flows.

4.2 Field acquisition

The field is almost flat and accessible by truck and vibroseis. The only limitation are two pipelines that passing southwest to northeast as shown in Figure 4-1. For HSE purposes there is a 25 m setback from source points to the pipelines. The fold map and azimuth and offset distribution do not show any problems in fold or azimuth and offset distribution so we do not expecting any footprint of the field acquisition. The acquisition attributes for the actual acquisition are shown in

Figure 4-2 (PP fold), Figure 4-3 (offset and azimuth distribution) and Figure 4-4 (PS fold).The results are very similar to the design attributes that described in the previous chapter.

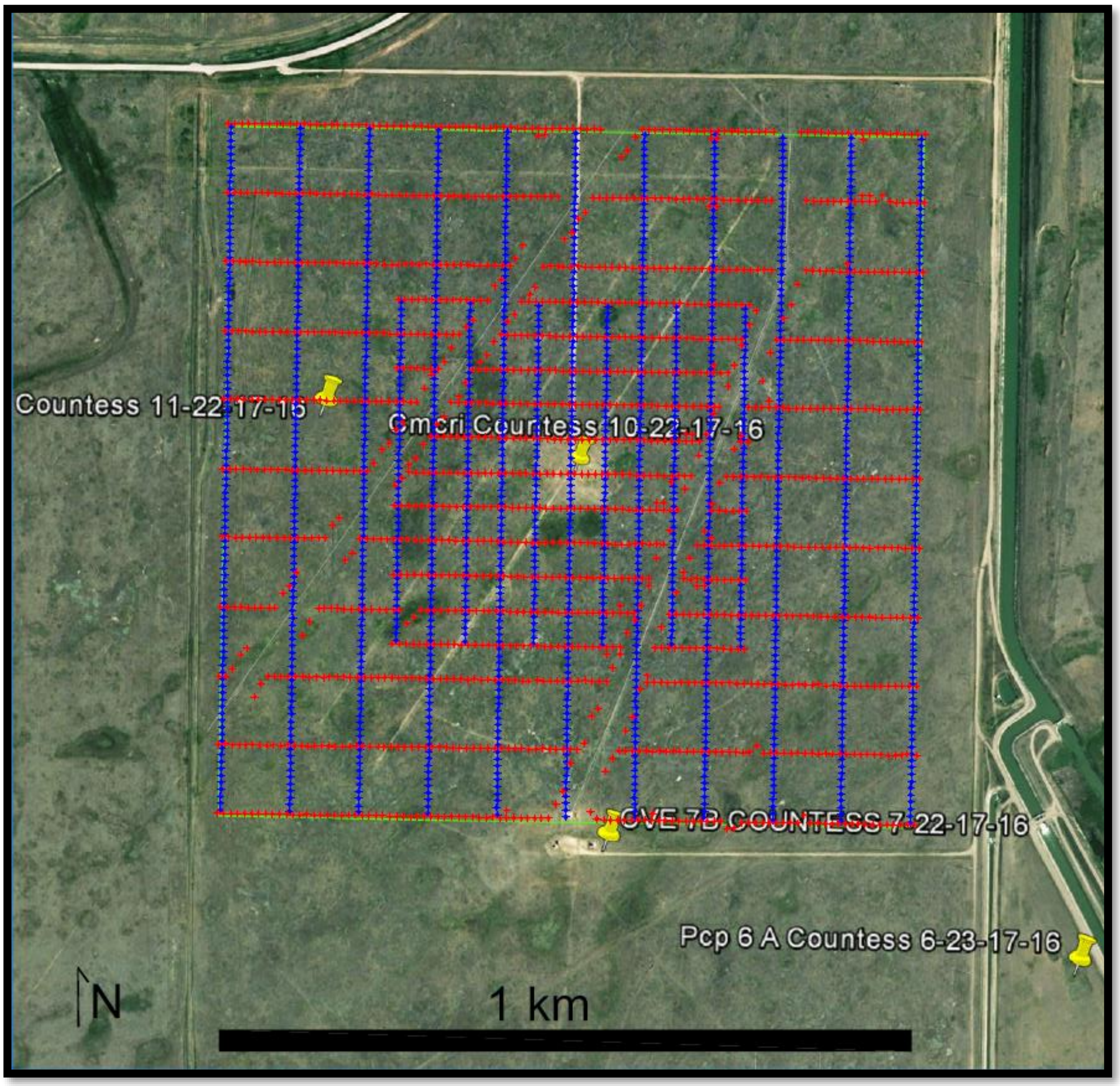

Figure 4-1. The seismic survey map of FRS project. The blue points are the receivers and red shows the sources. Two pipelines caused some change in the shot point coordinates. (Satellite image source: Google Earth)

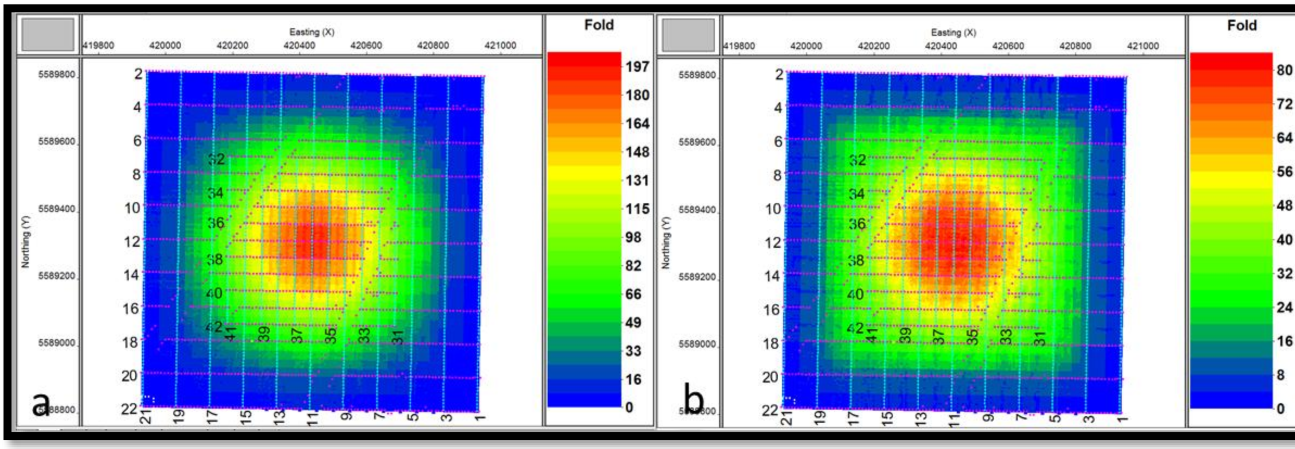

Figure 4-2.The PP-wave fold map for (a). total nominal fold and (b). 0-300 m source-receiver offsets.

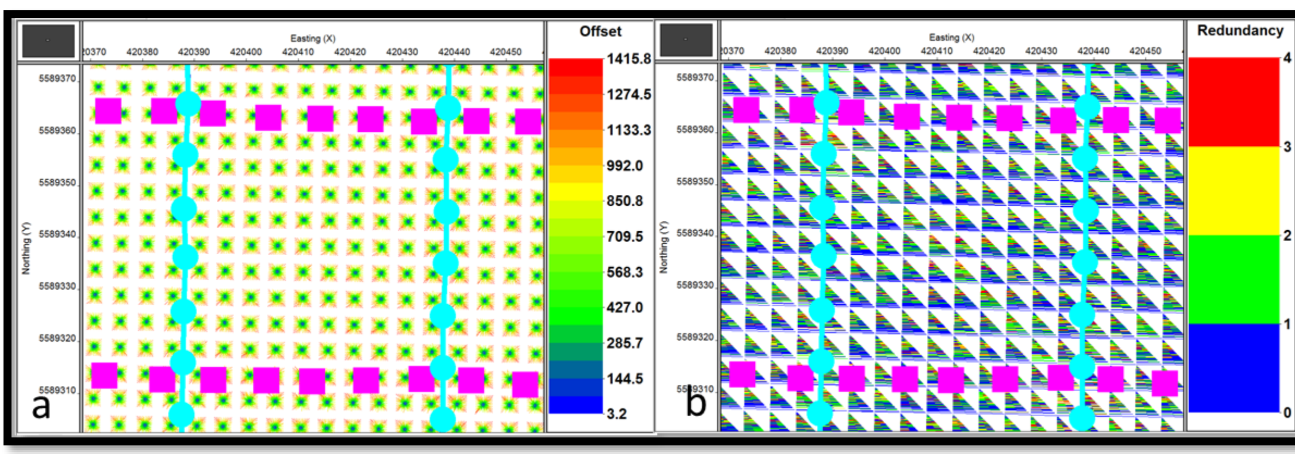

Figure 4-3. (a). Azimuth distribution and (b). Offset distribution

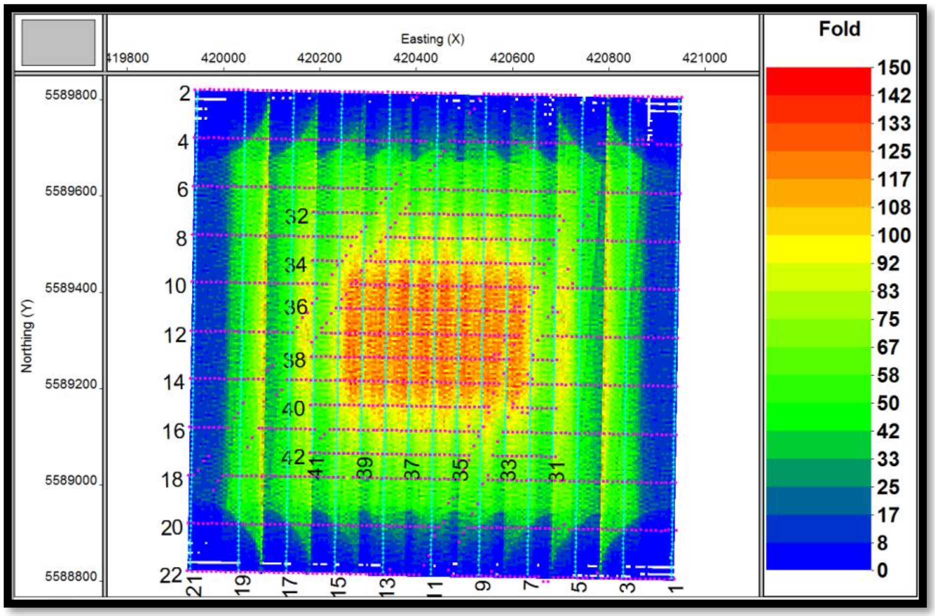

Figure 4-4. The PS-wave fold map for the target in the 300 m depth.

4.3 LMO effect and fold taper

Always there is the fold fluctuation came from the acquisition geometry in a seismic survey according to the layout limitation, seismic design, and processing flow. The fold taper and migration aperture effect in the outermost area of a seismic survey; e.g. LMO effects the very shallow target and the mute function effect in the deeper targets (Figure 4-5).

In the field, there are two pipelines that because of setbacks, the shot points were removed from this zone and some extra shot points were added to compensate for the dropped shots (Figure 4-1).

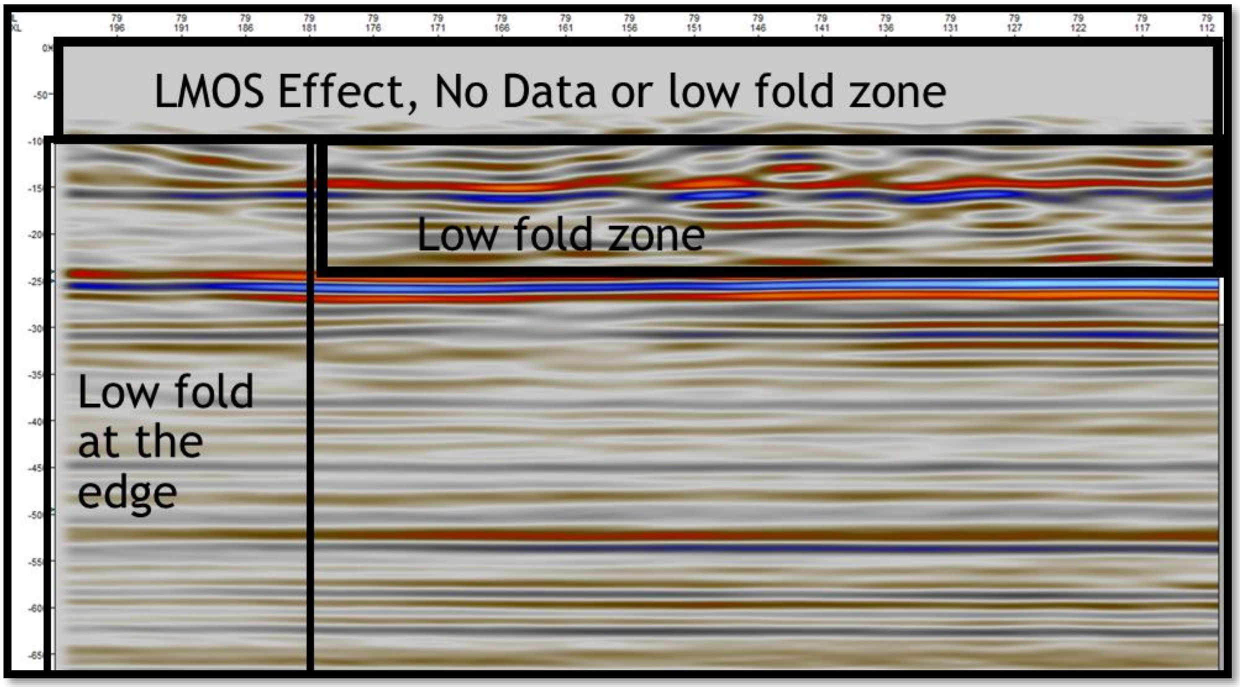

Figure 4-5.The low fold zone and acquisition on the acquired seismic data.

4.4 Seismic data resolution and coherency

Parameters was designed for a high-resolution dense central area that covers 500*500 m with source and shot line interval equal to 50 m. We checked the influence of the dense survey for data quality. For this purpose, we processed the seismic data, and in the second case, without the dense central area (Figure 4-6). For this purpose, all CMP points related to the dense zone were removed in the processing stage.

The results are shown in Figure 4-7 for PP-wave (inline no 101, that is in the middle of survey, an east-west line passed over the 10-22 well). The red rectangle shows the location of the dense source and receiver zone. Comparison of the results shows a better coherency in the shallow targets (750 ms and including the reservoir) that is pointed out by the green rectangle. The red arrows identify reflectors that have improved coherency with the denser acquisition grid. For a successful reservoir study, high resolution and high fold acquisition are vital for discriminating the small changes in reservoir CO_2 saturation. As we will see latter in the seismic modeling and imaging chapter, the resolution and coherency for the reservoir layer are crucial especially in the early years of the gas injection.

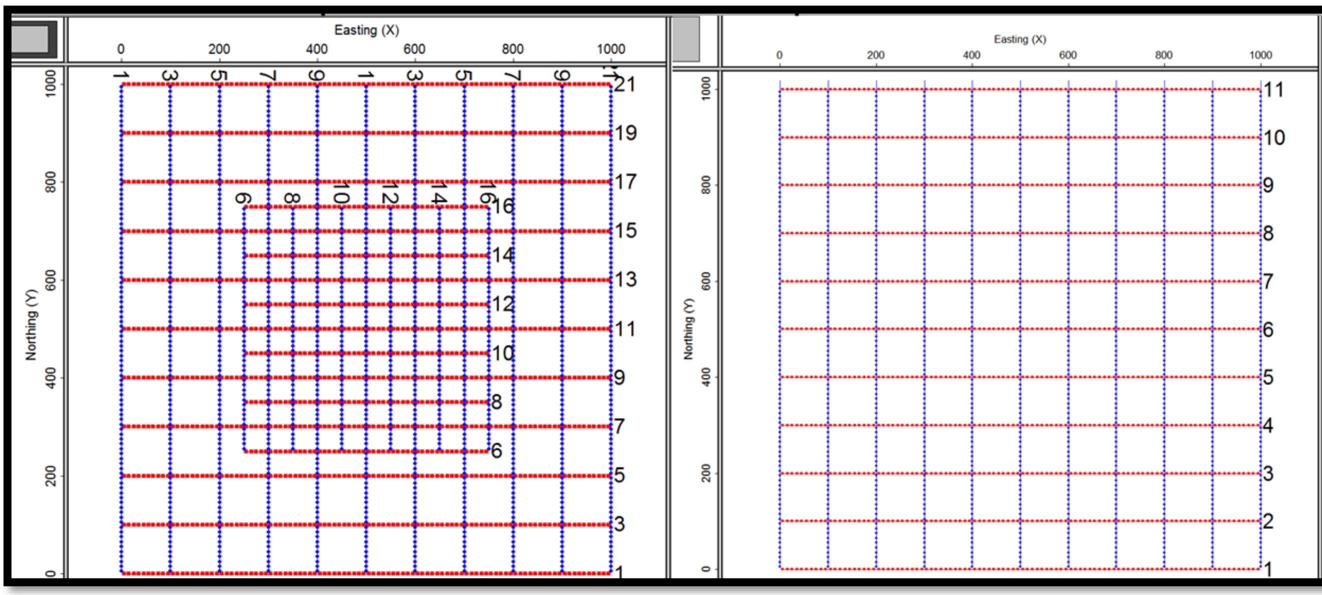

Figure 4-6.The configuration of acquisition were used for the processing. Left survey shows and right is the same survey after eliminating the dense center region.

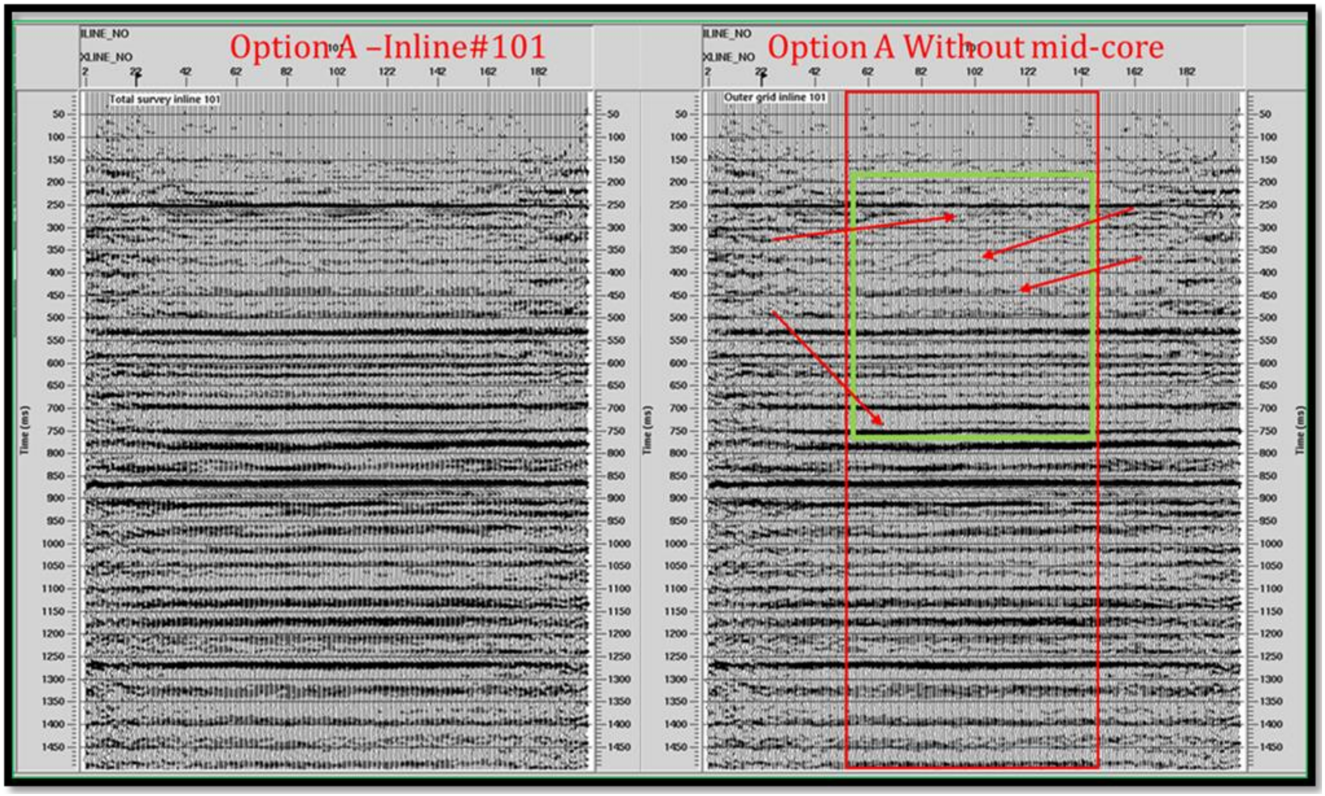

Figure 4-7. The result of processing for the acquired PP seismic data in (left) and after eliminating the dense source-receiver CMPs (right).The arrows show the main differences between two seismic sections.

4.5 Seismic PP and PS-wave data after processing

The acquisition method was 3D-3C, and so raw data of both PP and PS set were available. Figure 4-8 shows the PP and PS seismic data cubes and Figure 4-9 and Figure 4-10 illustrate 2D sections for the PP and PS-wave data that used for conventional analysis and the structural interpretation and geomodel development. The data quality is excellent for quantitative and qualitative interpretation. The two-way time conversion between PP and PS seismic sections is illustrated in Figure 4-11, that was calculated for the P and S-wave slowness logs in the 10-22 well.

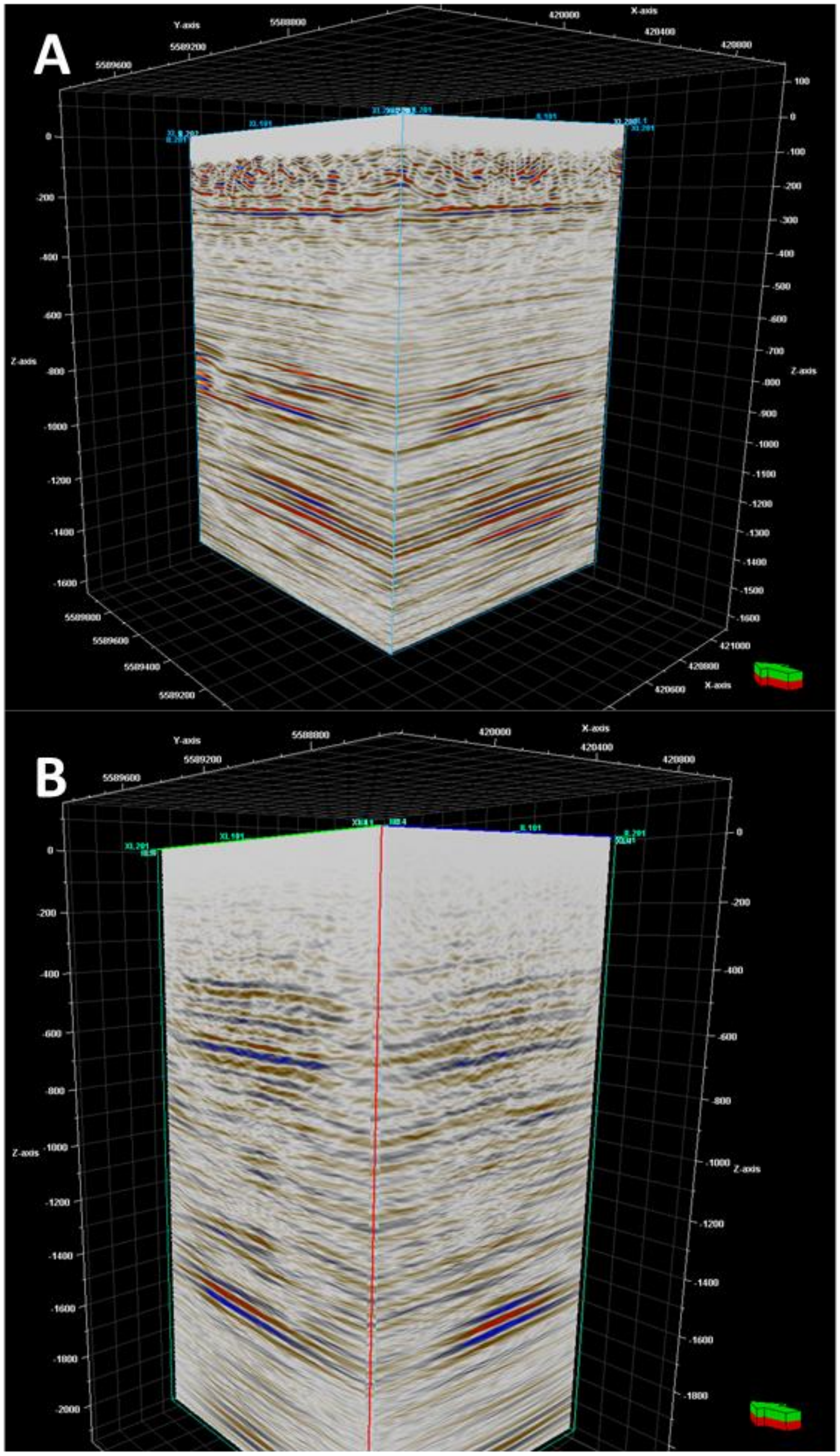

Figure 4-8. The seismic data, A. processed PP-wave data, B. processed PS wave data

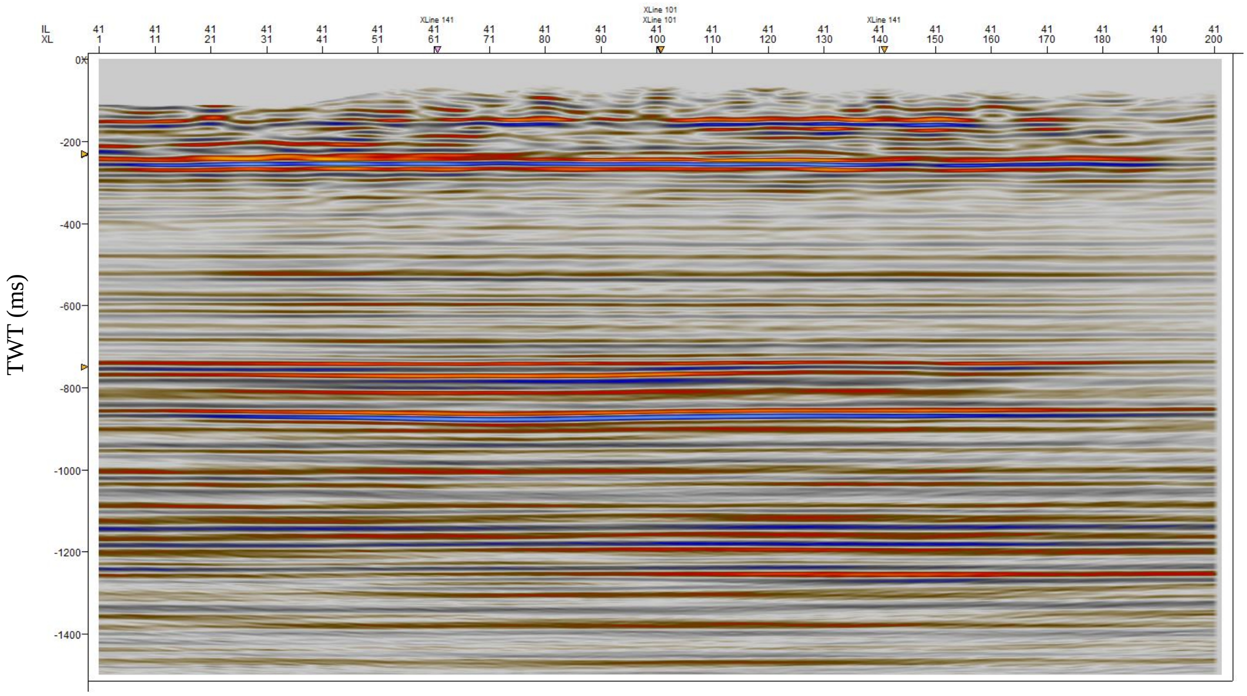

Figure 4-9. PP-wave migrated seismic section on inline 41

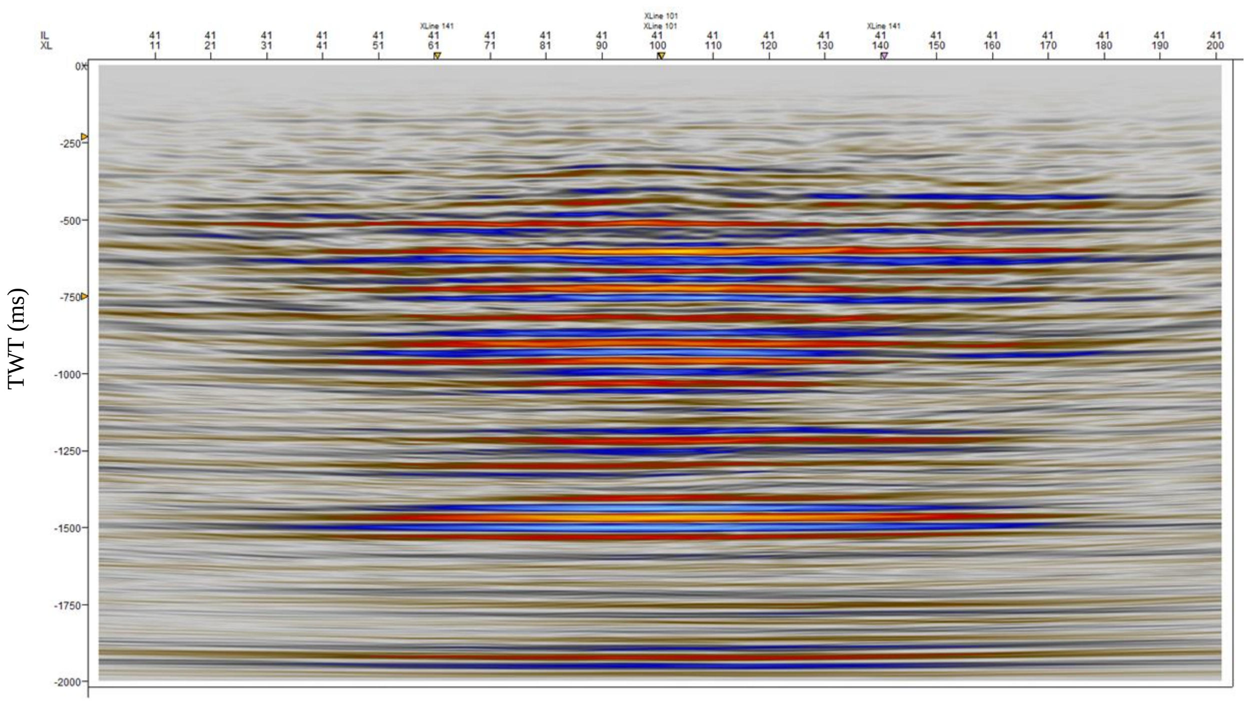

Figure 4-10. PS-wave migrated seismic section on inline 41

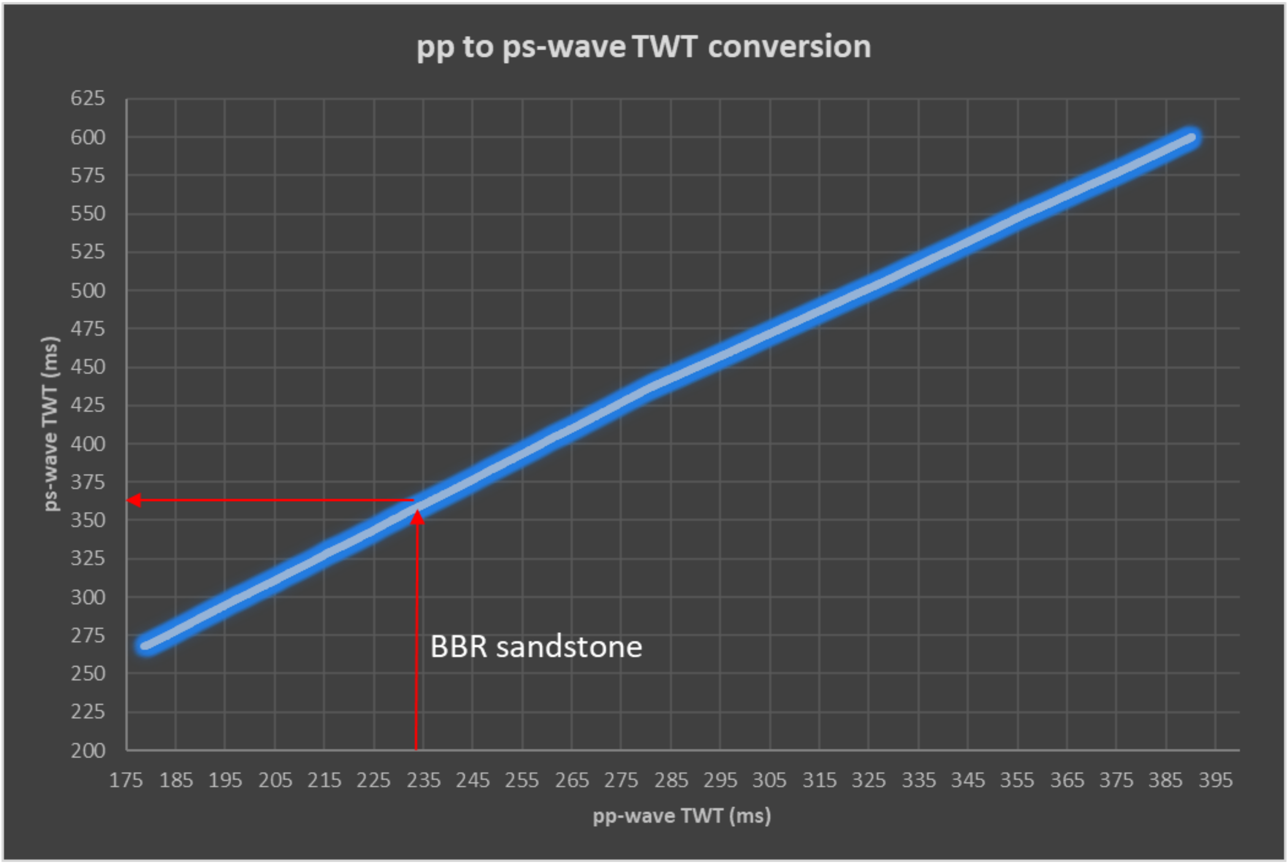

Figure 4-11.The TWT conversion diagram between PP and PS seismic sections. The injection target at 233 ms for PP time and 364 ms for PS time. It was calculated from the P and S-wave slowness logs. The velocity for no well log data zone calculated by the seismic analysis.

4.6 Seismic interpretation: The phantom horizons methods

The geometry of layers and faults are key inputs for the geomodel frame. In this chapter, two goals for the FRS project from the seismic interpretation were:

1- The geometrical form and discontinuities of the layers and formations (structural interpretation and fault study).

2- Interpretation of the homogeneity of the sediments in the reservoir horizon around the injection well.

In the seismic interpretation, we interpolate the well tops and log data between the wells with acceptable accuracy and geometry. A common structural interpretation framework is shown in Figure 4-12. The fault study was done by the seismic qualitative interpretation and attributes study. The selected horizons for the detailed interpretation and geomodelling are shown in Figure 4-16.

The well tops are the first information package for the layers' geometry assessment, and seismic data interpretation can reveal a better accuracy of the geometry in comparison to a well top interpolation method. The seismic data will help to find formations fluctuations in the area and mapped the discontinuities as faults.

For a better estimation and accuracy, intra-formation layers were also interpreted as phantom horizons. This information was used for making surfaces of the formation, sub-formation, layers, faults and fractures in the geomodel.

4.7 Well ties

The synthetic seismogram is a tool to correlate well tops with the seismic data. For reflectors match between synthetic seismogram and seismic data, a wavelet was derived from the seismic and the well log data (Figure 4-14 and Figure 4-15).The seismic data are in the time domain, and the well log data are in the depth domain, so to produce a synthetic seismogram, we need a depth to time converter that is coming from velocity log, check shot data or velocity analysis in the seismic processing or interpretation stages. The overburden thickness without well log data in the well (10-22-17-16) is 225 m, so for the seismic analysis, the P-wave velocity in this was selected 2550 m/s.

Finally, the selected wavelet was convolved with the derived reflection coefficient from the sonic log to generate the synthetic seismogram in the well site. The similarity of the seismogram and the migrated seismic data around the well, with the formation tops will present the markers for the interpretation purpose.

The following routine was used for generating a synthetic seismogram and well tie (also as explained in Figure 4-13):

1- Extract wavelet from seismic and well log data
2- Generate the reflection coefficient, acoustic impedance, and synthetic seismogram
3- Time shift and match events
4- Stretch-squeeze the synthetic seismic data

For the interpretation, the reservoir layers (Basal Belly River sandstone) mapped (Figure 4-17, Figure 4-18 and

Figure 4-19) and the other layers interpreted as phantom layers to an accurate analysis and geomodel structure and geometry.

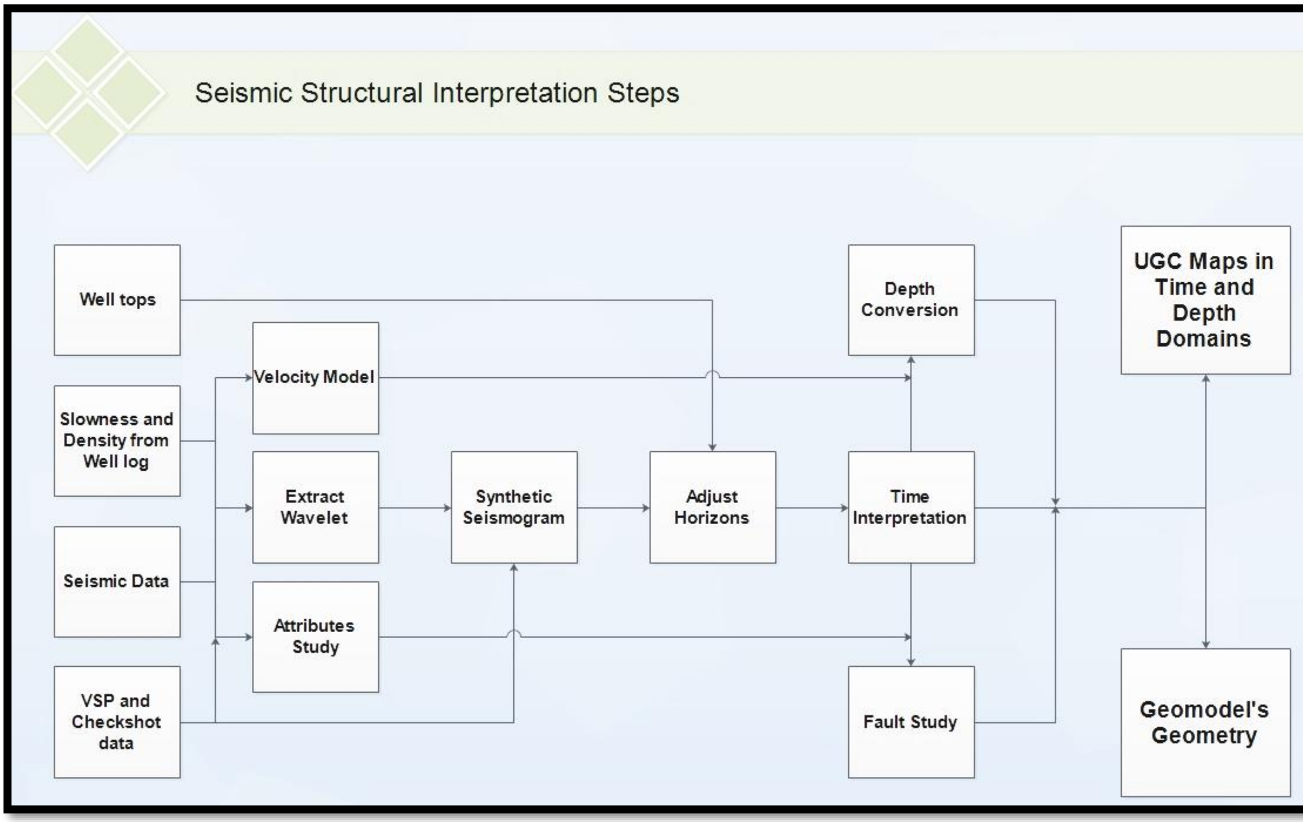

Figure 4-12. Flowchart that shows the simplified stages of work for a general structural interpretation.

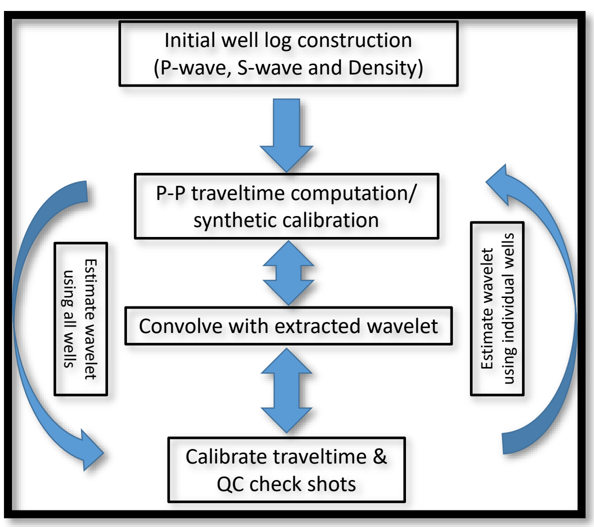

Figure 4-13: schematic of procedure used for well to seismic calibration

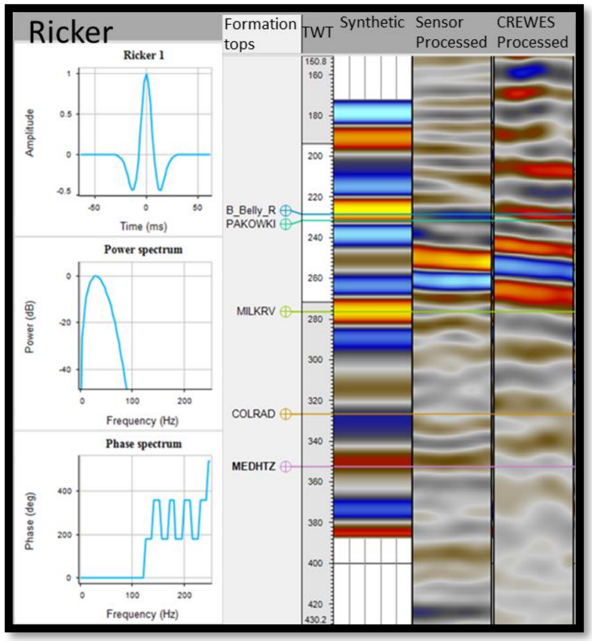

Figure 4-14. Ricker wavelet and the synthetic seismogram from well log data against processed seismic data.

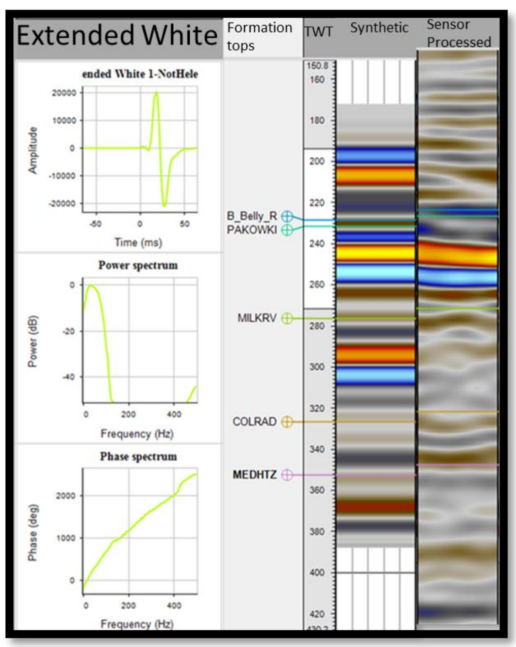

Figure 4-15.The wavelet calculated by extended white method for the Sensor processed data set. The reflectors correlation is acceptable in the 200-300 ms range.

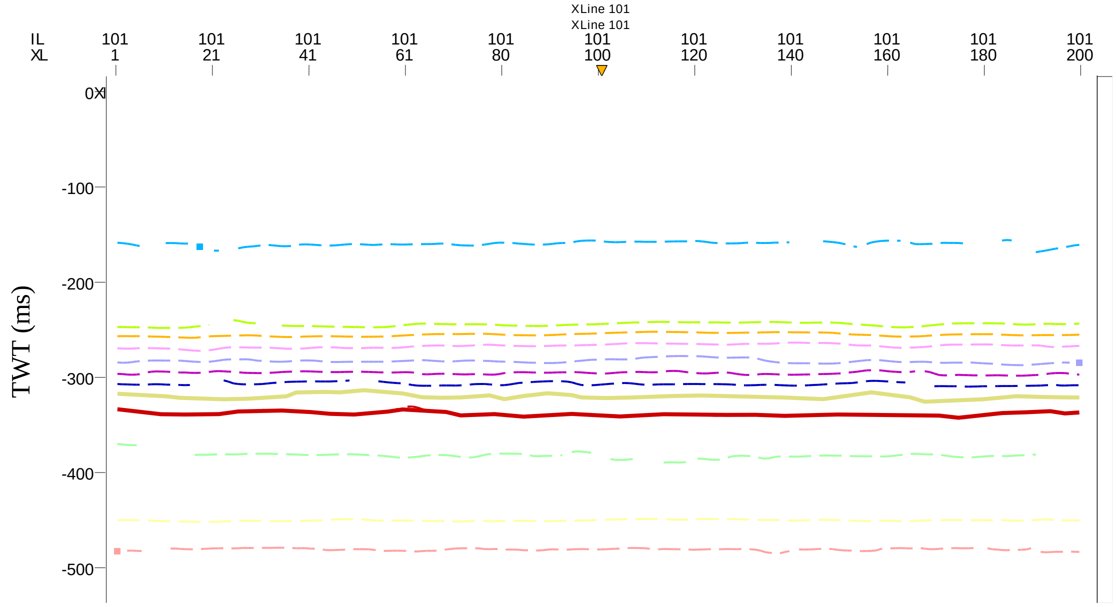

Figure 4-16. PP seismic interpretation in time domain including the main formations and phantom layers (time domain). The line is passing of the main well.

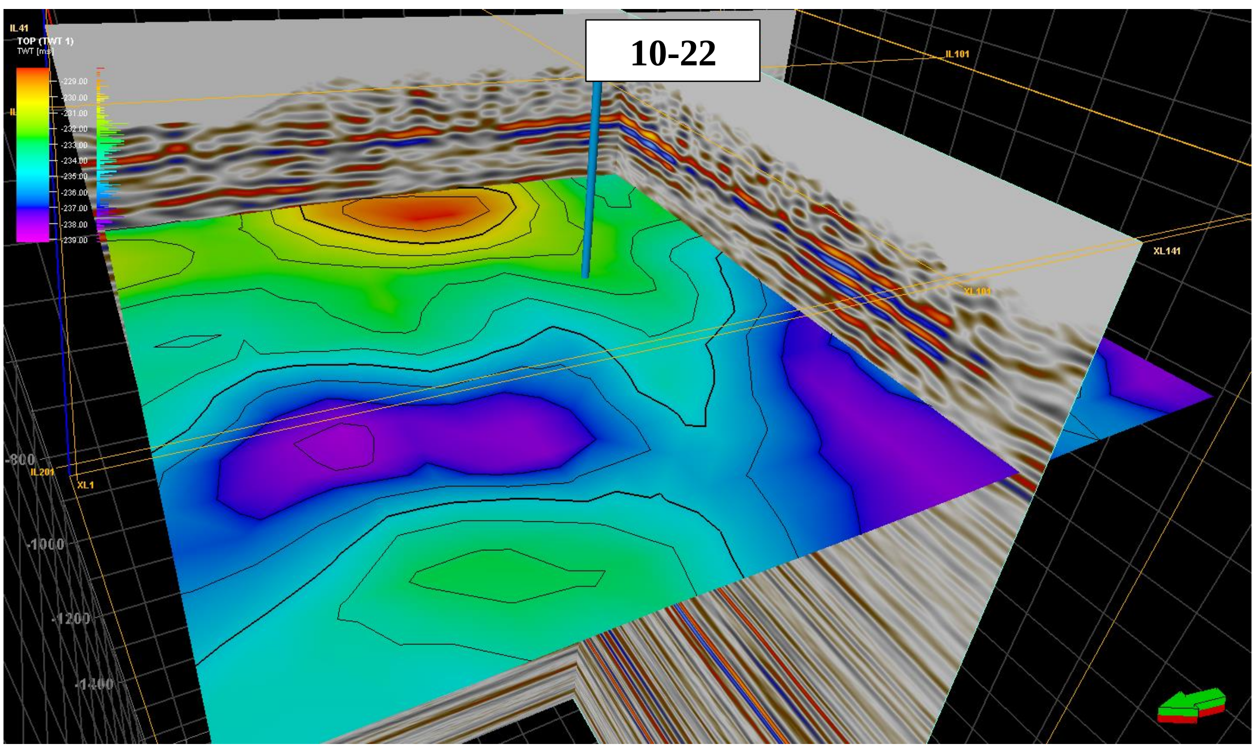

Figure 4-17. The top Basal Belly River sandstone as the top of the reservoir in the seismic cube in time domain.

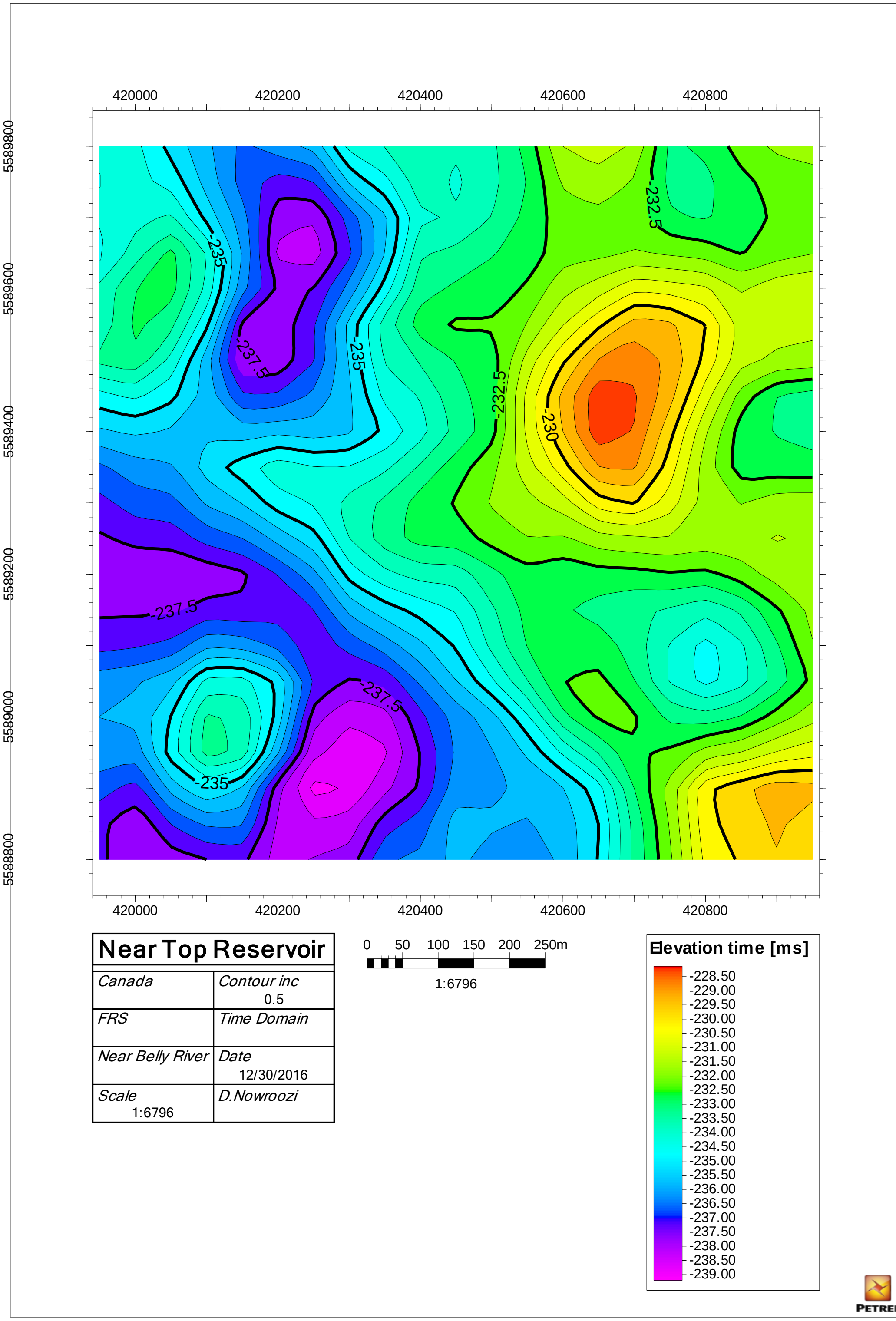

Figure 4-18. Time structure of the top of the Basal Belly River sandstone.

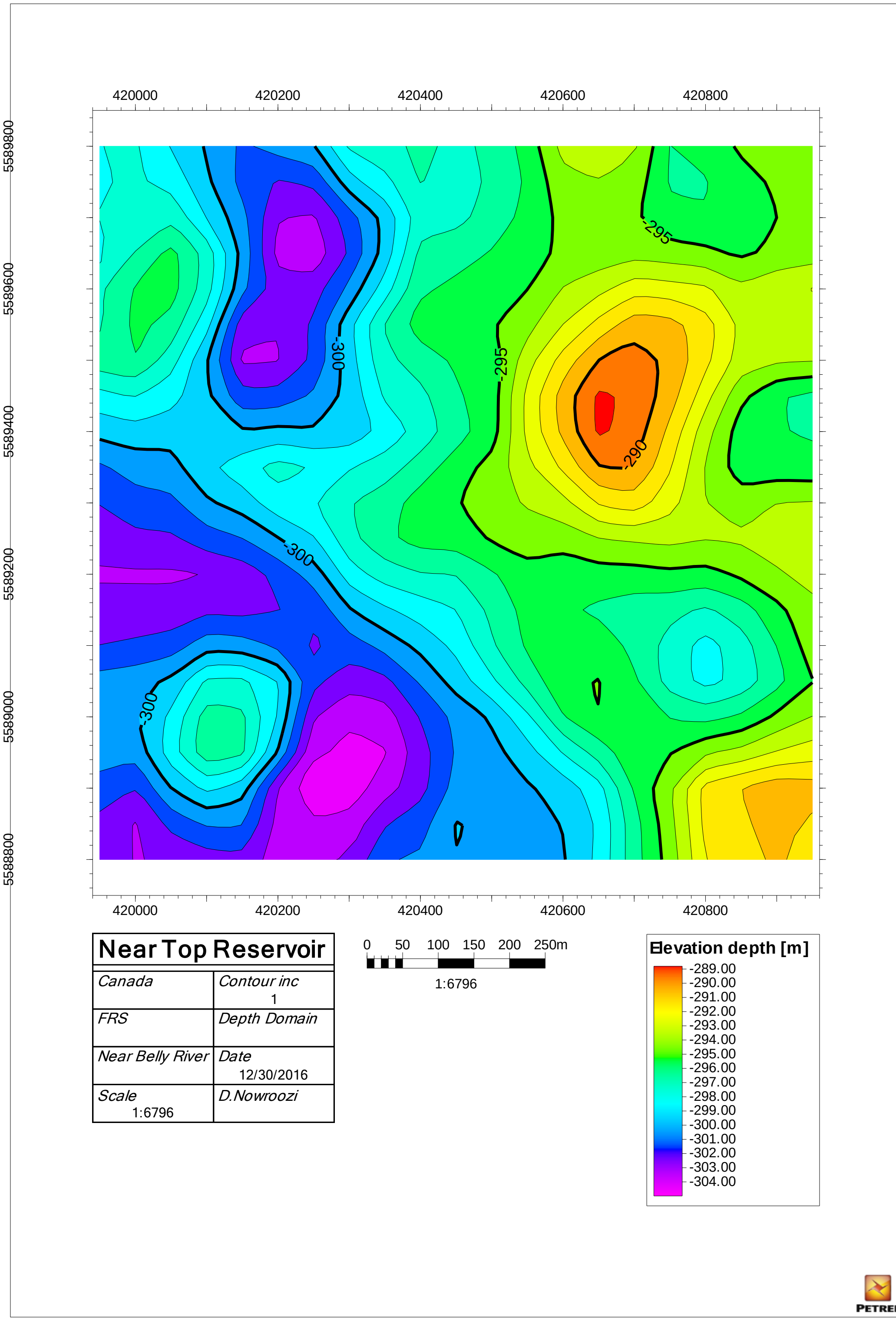

Figure 4-19. **Depth structure of the top of Basal Belly River Formation.**

4.8 Attributes study

Seismic attributes are parameters calculated from the seismic data based on time, amplitude, frequency and attenuation (Sheriff, 2002). They can reveal the structural properties, reservoir parameters or discontinuities and faults. In the next section, the attributes were used to certify any faults and the discontinuities and interpret the homogeneity of the reservoir layer.

4.8.1 Generic Inversion

Generic inversion is an attribute that correlates well data with seismic data to generate P-wave slowness, and it is demonstrated in Figure 4-20 for the seismic cube and Figure 4-21 for the top horizon layer. This attribute can show the channels, changes in the lithology, faults and dense fractured zones. However, in this integration, Figure 4-21(the slowness in the BBRS) shows a very smooth change in the reservoir layer near the well.

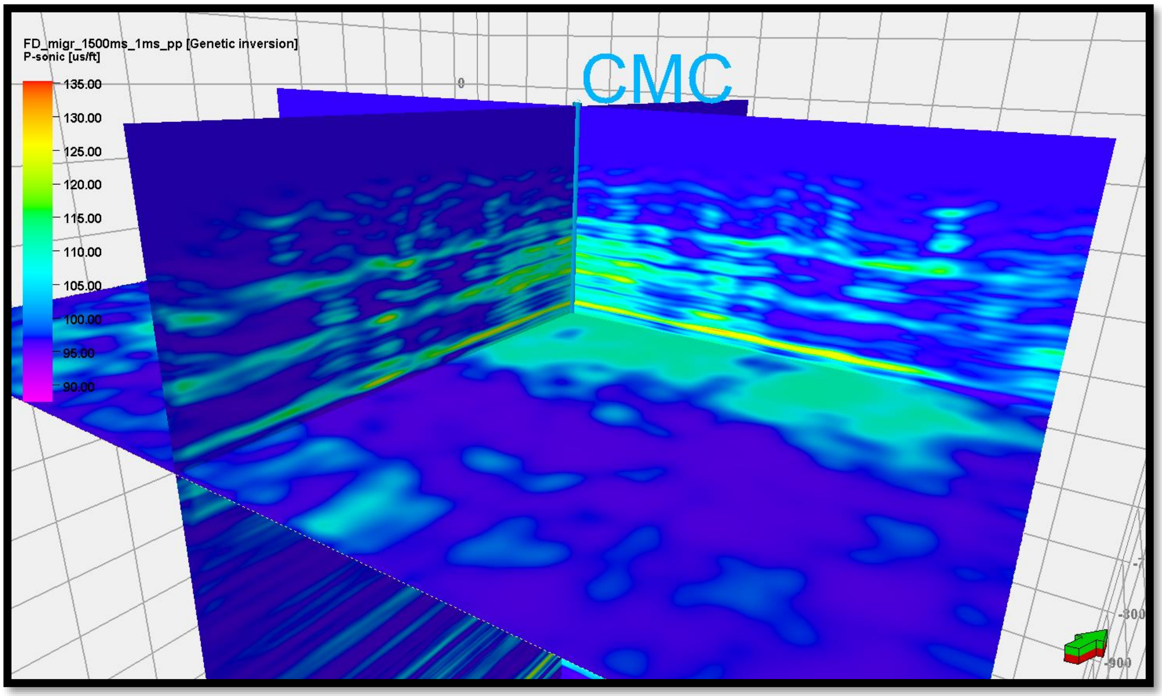

Figure 4-20.Genetic Inversion (time slice is 235 ms near the top of reservoir)

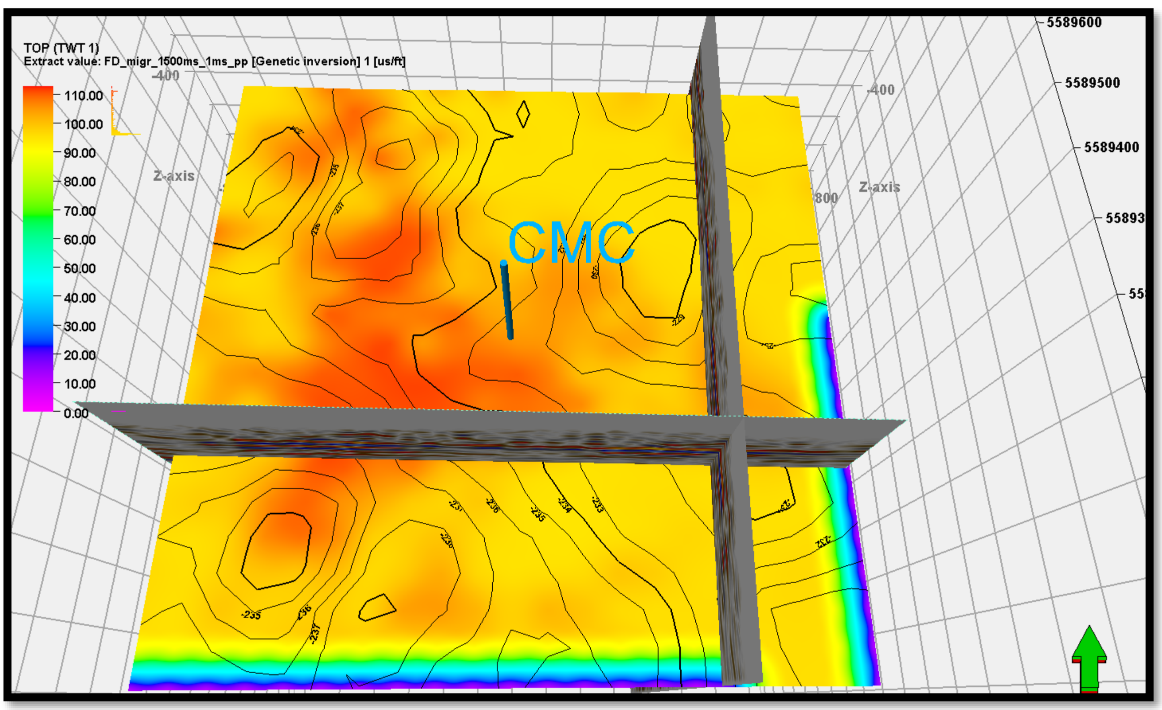

Figure 4-21.Genetic Inversion on the top reservoir surface

4.9 Fault detection attributes

Using single attribute and a combination of them were also used for possible fault and fracture recognition. The primary attributes used for fault detection were 3D curvature, variance and chaos attributes, which will show lineation of geological events some of which can be associated with the existence of faults. For accurate estimation, a combination of attributes was also used, as demonstrated in Figure 4-22. Software such as Petrel has some tools to assist extracting and mapping possible faults using introduced attributes.

Figure 4-23 to Figure 4-30 show the results of multi-attribute on the seismic data for fault detection.

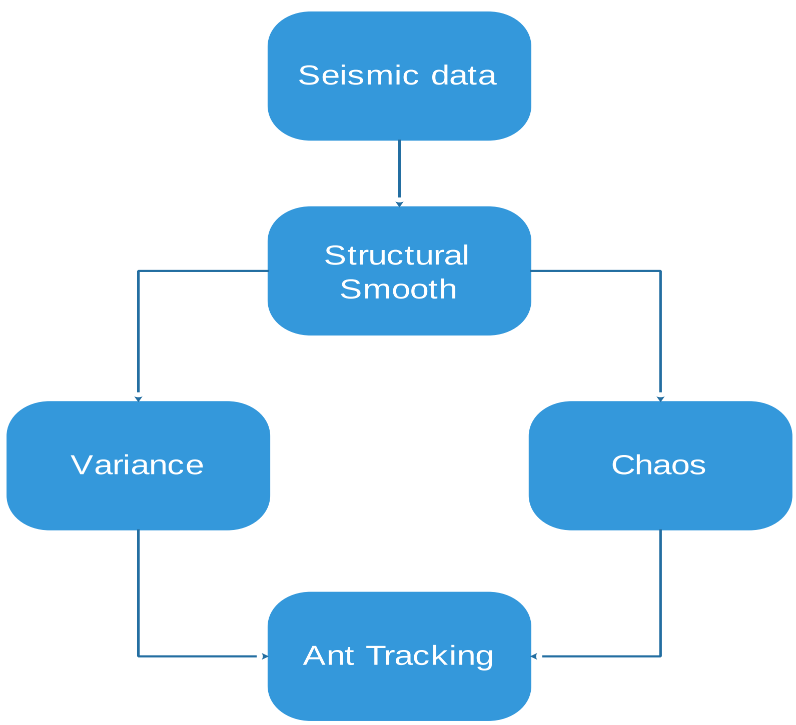

Figure 4-22. Fault detection using the multi-attribute method.

4.9.1 Structural smoothing

It can eliminate a local noise from the data set; through the use of a mean or median filters. Figure 4-23 shows overall pattern in the smoothed amplitudes for a time slice near the BBRS top.

4.9.2 Dip Deviation

This attribute maps edges and truncations, and it is useful for identifying faults (Figure 4-24). The attribute does not show any truncation events around the injection well.

4.9.3 Chaos

The chaos attribute can be described as Eq. 4-1 (Randon et al., 2000) as:

$$c_x = \frac{2\lambda_2}{\lambda_1 + \lambda_3} - 1$$

Eq. 4-1

Where λ_1 and λ_2 are the eigenvalues of the Gradient Structure Tensor (GST) matrices. Note that if $\lambda_1 >> \lambda_2$, the coherence is high and c_χ goes to –1. If $\lambda_1 \approx \lambda_2 \approx \lambda_3$, c_χ goes to 0. Finally, if $\lambda_1 \approx \lambda_2$, but $\lambda_3 \approx 0$ [Bakker's (2003) lineament attribute], c_χ goes to +1.

The result of chaos attribute on the structural smoothed cube are shown in Figure 4-25, for a time-slice of the mid reservoir level.

4.9.4 Variance

The variance attribute is another way to search faults. This attribute measures the dissimilarity of the seismic data. Figure 4-26 shows the variance attribute on the FRS seismic data. For a better result, a combination of attributes included variance were used for fault recognition.

4.9.5 Ant tracking

This attribute is useful for fault detection. The ant-tracking method was introduced and algorithm organized by Randen et al. (2001). By the algorithm, the coherency of the seismic data is probed by an iterative scheme (Chopra et. al, 2007). The input data for the ant tracking attribute are variance or chaos attributes. These two attributes can present an accurate result compared to the seismic data after ant tracking. Figure 4-22 shows the usage of multi attributes methods for the fault detection.

Figure 4-27 is a smoothed-chaos-ant tracking attributes study on the seismic cube (Figure 4-29 shows the BBR surface). Figure 4-28 shows smoothed-variance-ant tracking on the seismic data (Figure 4-30 shows the BBR surface). There is no evidence of any discontinuities near the 10-22 well at the reservoir level.

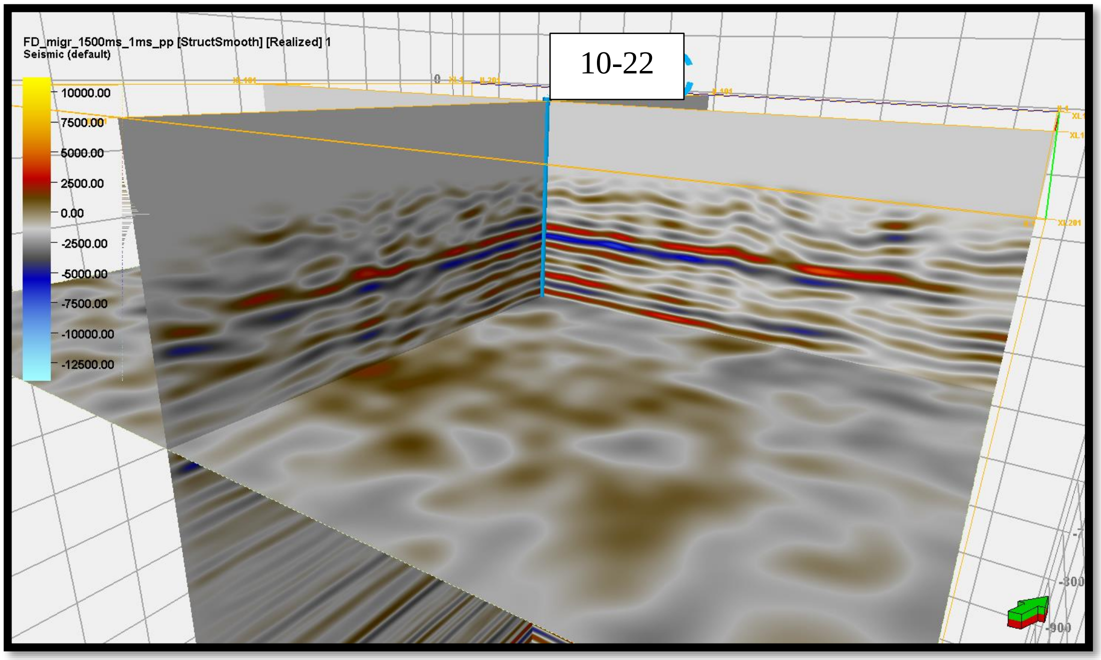

Figure 4-23.Smoothing attribute is the first step of the multi-attribute method for faults recognition.

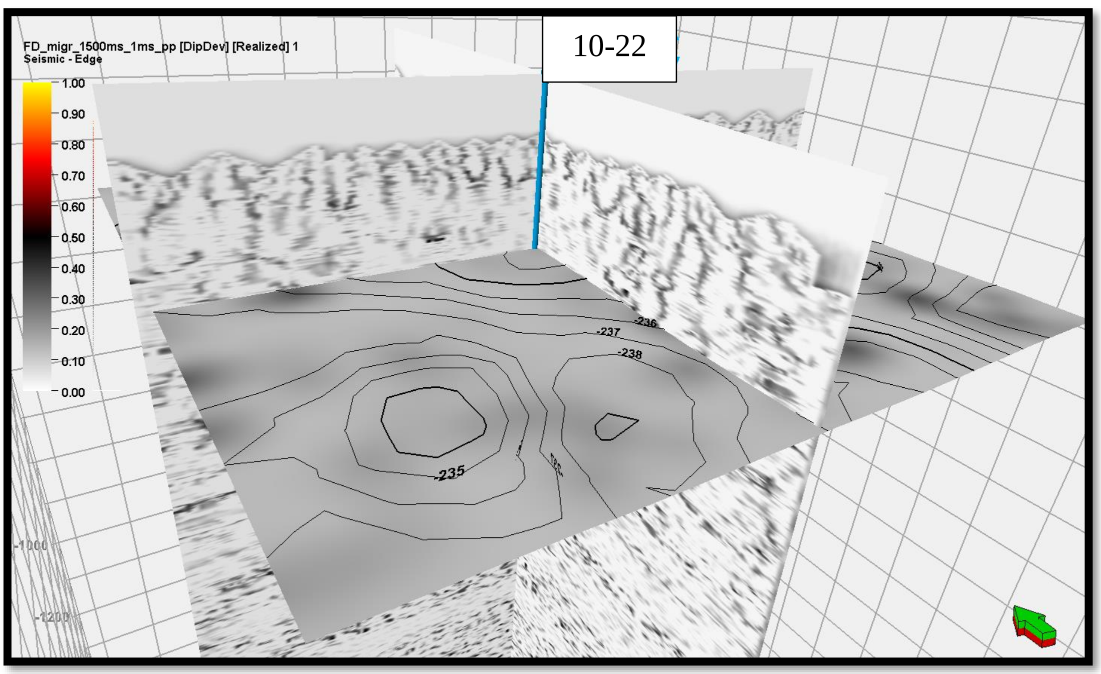

Figure 4-24.The single attribute study (dip deviation) for fault recognition.

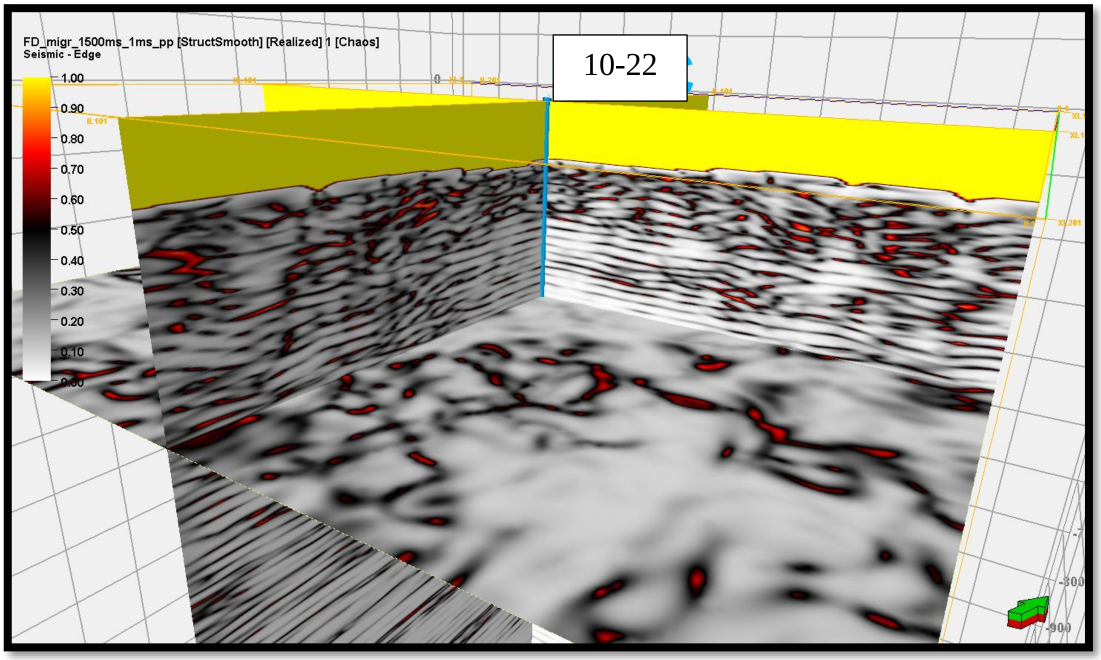

Figure 4-25.The chaos attribute applied to the smoothed data cube.

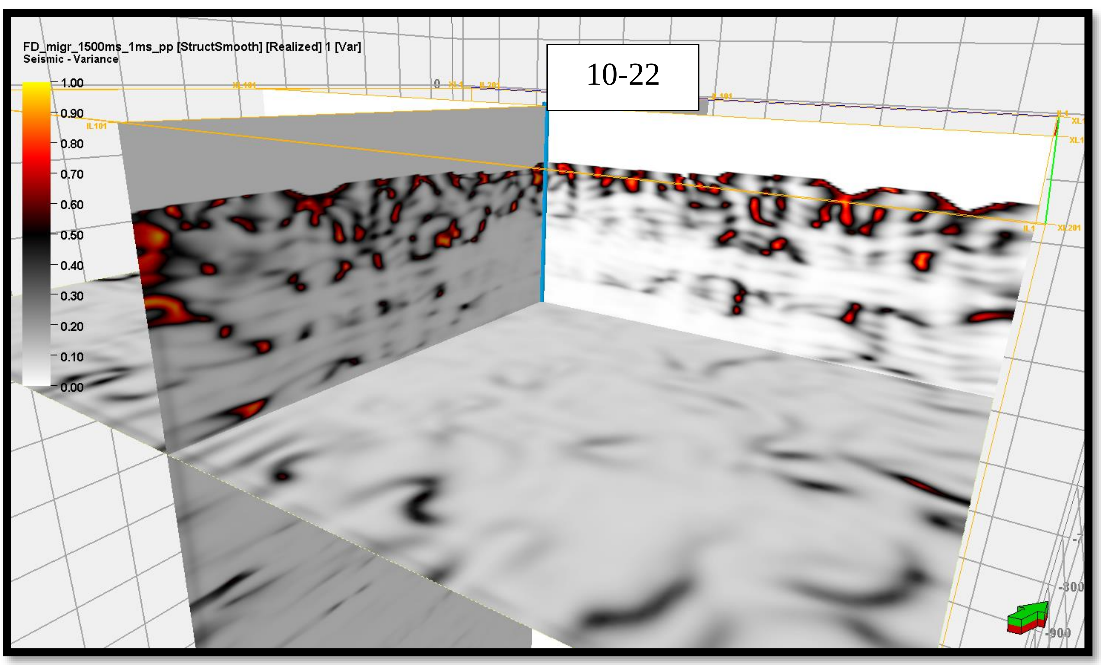

Figure 4-26. The variance attribute applied to the smoothed data cube.

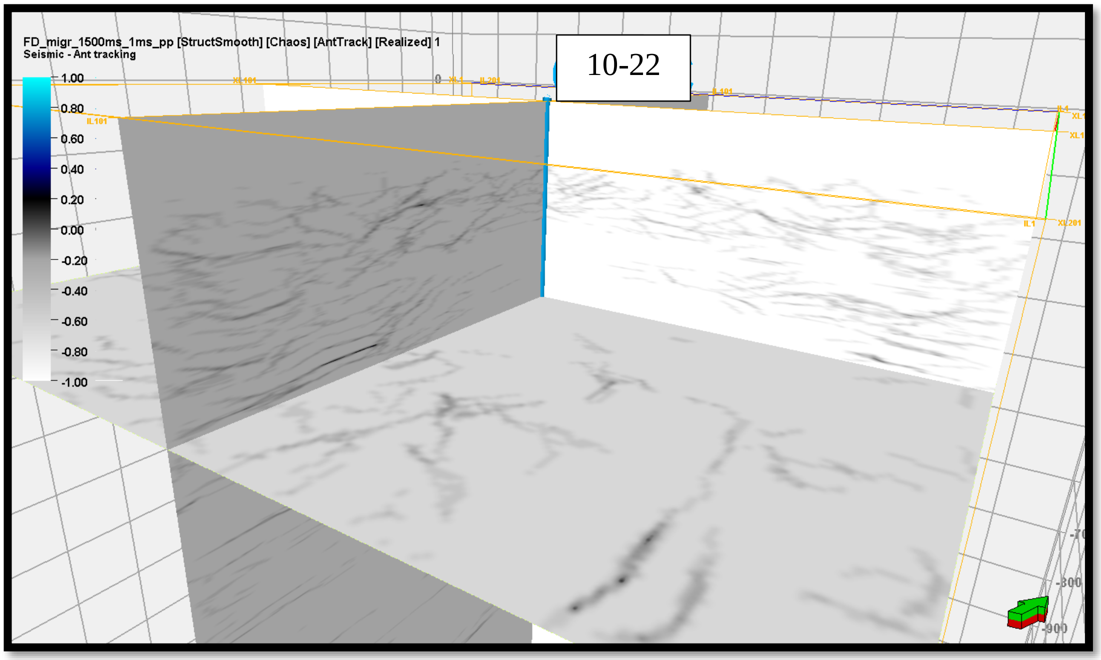

Figure 4-27. AntTrack attribute applied to the Smoothed Chaos data cube.

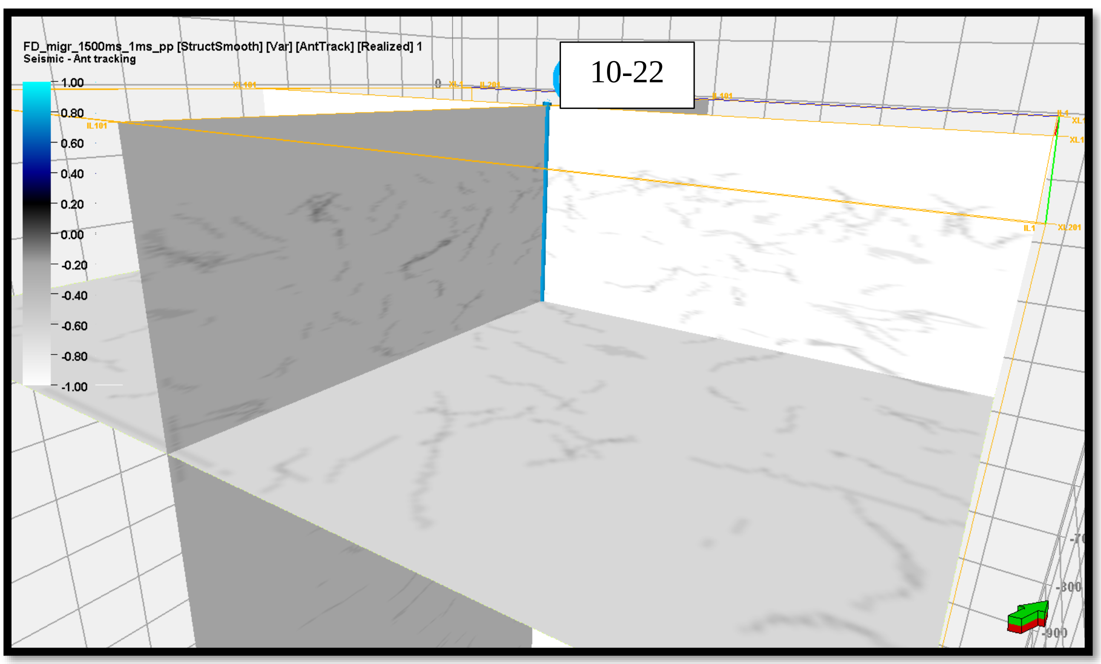

Figure 4-28. AntTrack attribute on the Smoothed Variance attribute result

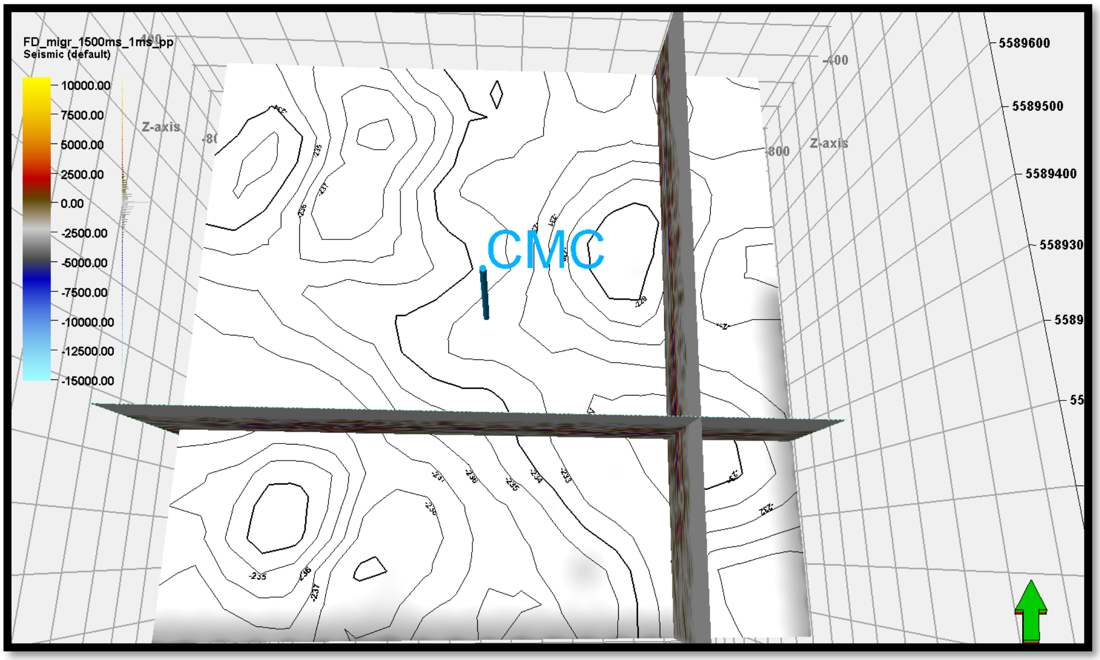

Figure 4-29.A multi-attribute map (Structural- Chaos – Ant track) for the fault discrimination.

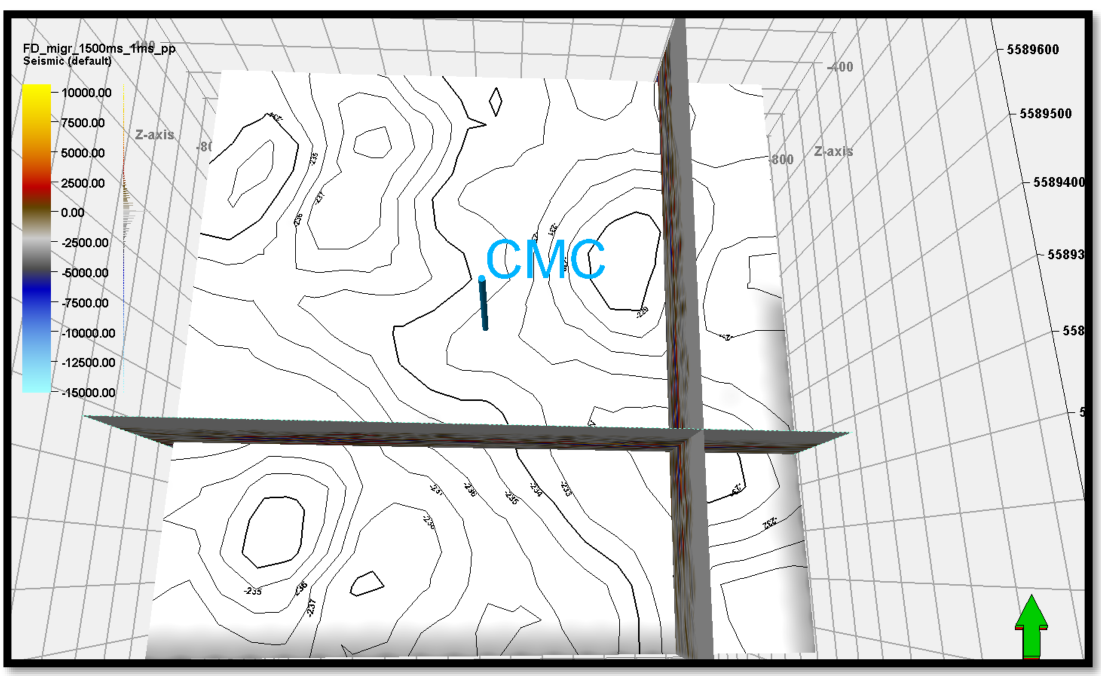

Figure 4-30. A multi-attribute map (Structural - Variance – Ant track) for the fault discrimination.

4.10 The velocity model

The velocity model generated was based on the seismic velocity analysis and well sinic log. For this purpose, the log of velocity in the 10-22 well defined as a first-degree linear function (Figure 4-31). The velocity over 225 m is calculated by the analyzing the first breaks from the seismic data (Isaac, 2015). Based on these picks, the velocity from the ground surface to 225 m depth found to be 2525 m/s.

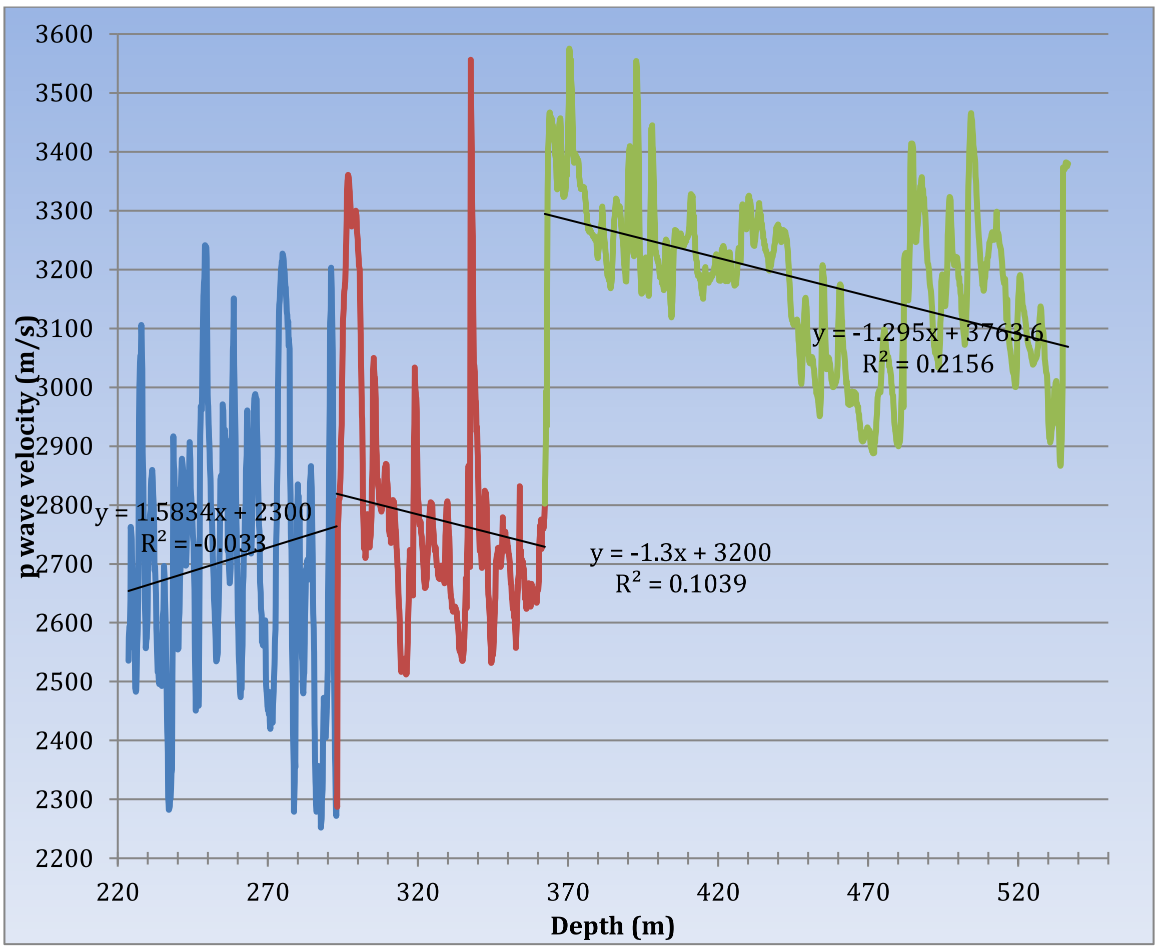

Figure 4-31.The P-wave velocity in the well 10-22 with simplified gradients for time to depth conversion

Figure 4-32 shows the time to depth conversion (or vice verse) for the PP, PS, and SS-wave arrivals calculated from the well log data. This data is used in the next section to change the domain from time to depth for building the geomodel.

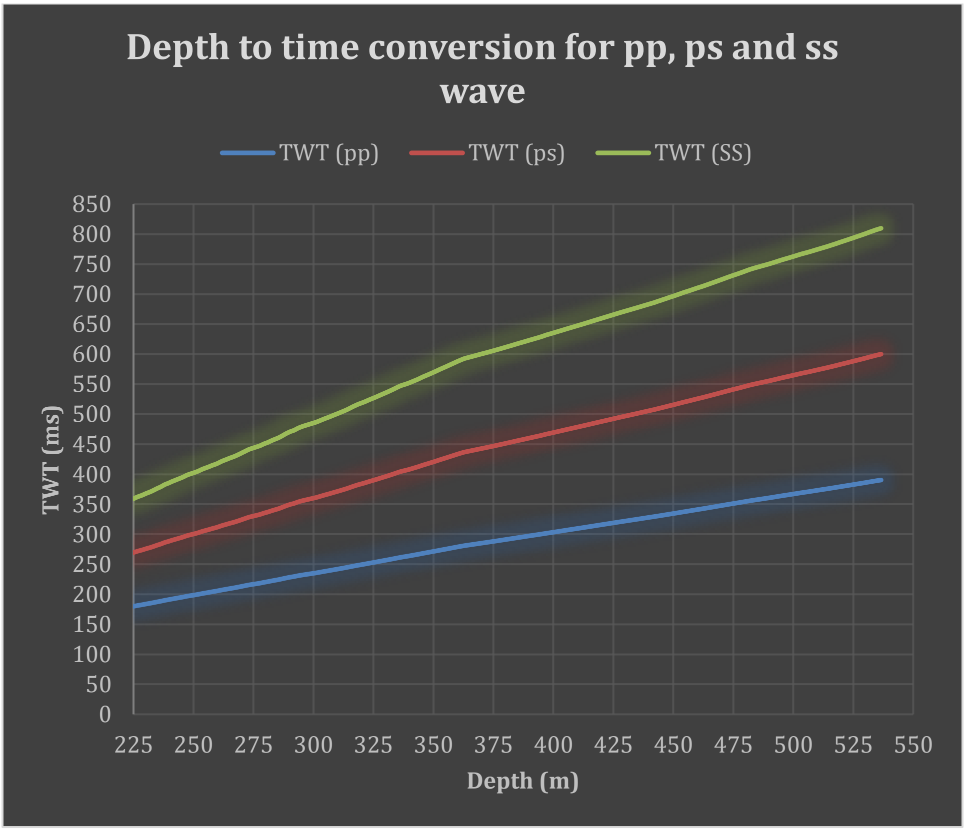

Figure 4-32.The time to depth conversion for the PP, PS and SS wave in the well 10-22.

4.11 Geomodel of the project area

A geomodel contains physical properties extended in 3D encompassing the reservoir. In a geomodel, the reservoir divided to the cells as a 3D matrix that oriented by the formation geometry. The model can be generated mainly based on well log data and seismic interpretation according to statistical or geostatistical analysis. For a better estimation, the results from qualitative interpretation of seismic data (like horizons and faults) and quantitative interpretation (pre-stack or post-stack inversion results) can be used.

The procedure to make a geomodel is shown in Figure 4-33.

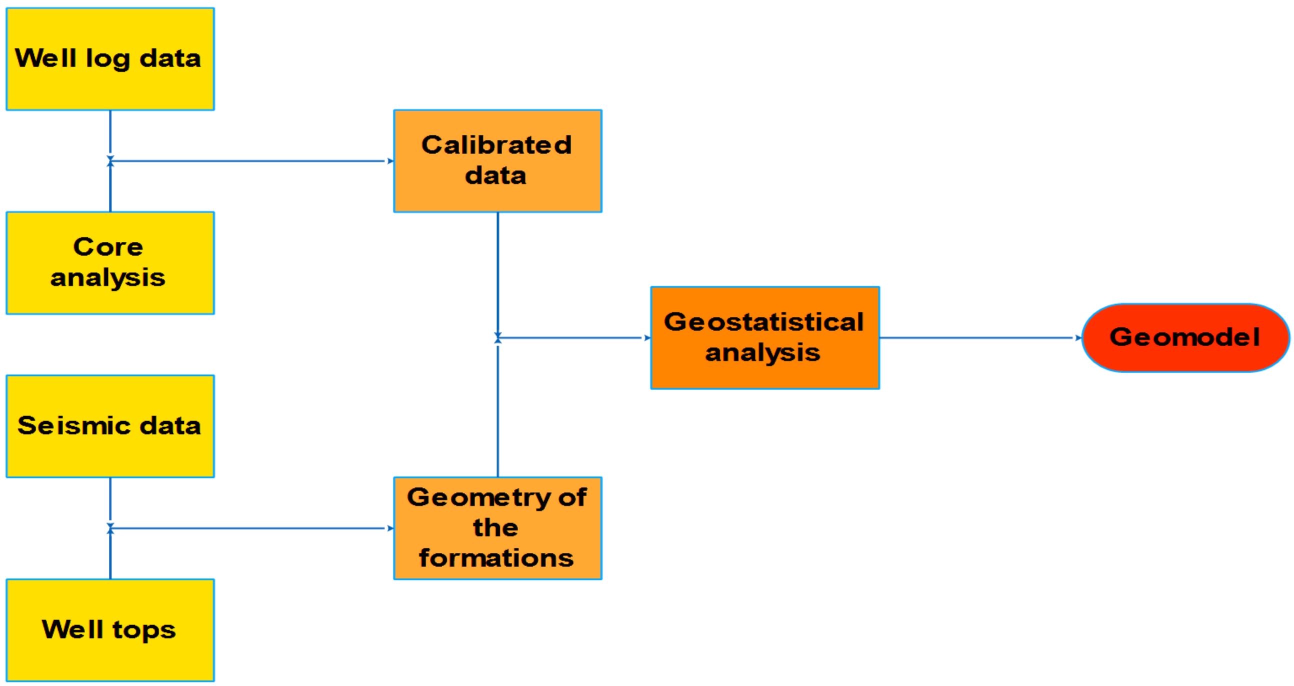

Figure 4-33: The procedure for producing a geomodel in the FRS project.

In the current research, the geomodel was used for three purposes:

1. Reservoir fluid simulation; the permeability (x, y, z directions) and porosity were determined.
2. Fluid substitution effects on the elastic modulus.
3. Seismic modeling and imaging (velocity and density or acoustic impedance).

Figure 4-34 shows the upscaled well log data in the initial stage of the geomodelling for the FRS project.

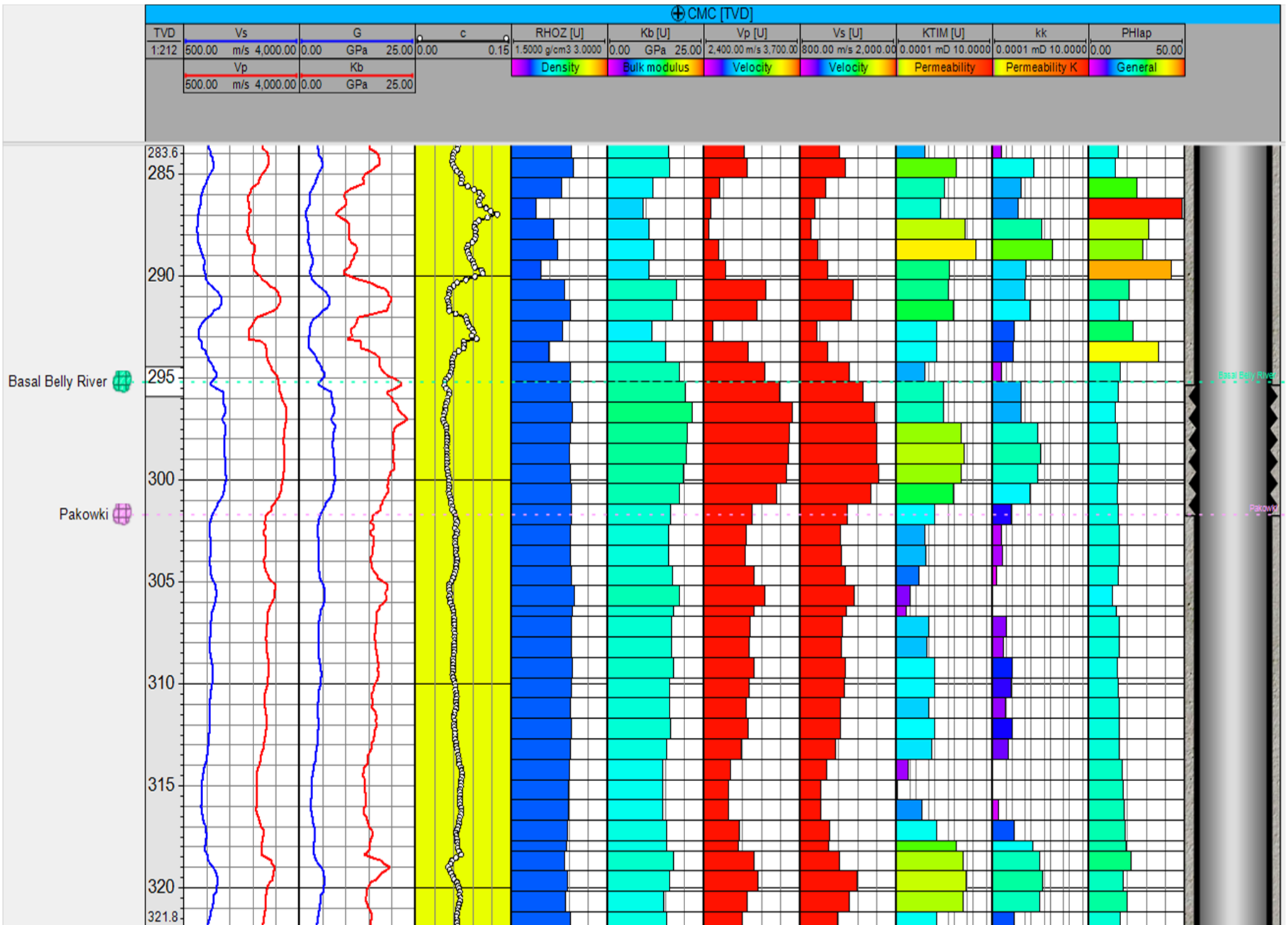

Figure 4-34. The upscaled well log data for building geomodel in well 10-22 before permeability calibration.

4.12 Introduction to Geostatistics:

4.12.1 Variogram:

A variogram is a tool to analyze the structural form of the spatial distribution of the variables in a statistical population. Eq. 4-2 and Eq. 4-3 are general forms of variogram formula.

$$\gamma(\mathrm{h}) = \frac{1}{2}\operatorname{var}\left(Z(\mathrm{s}) - Z(\mathrm{u})\right) = \frac{1}{2}\iint\left(Z(\mathrm{s}) - Z(\mathrm{u})\right)^2 f(\mathrm{s},\mathrm{u})\,d\mathrm{s}\,d\mathrm{u}$$

Eq. 4-2

$$\hat{\gamma}(\mathrm{h}) = \frac{1}{2N(\mathrm{h})}\sum_{i=1}^{N(\mathrm{h})}\left[z(\mathrm{s}_i) - z(\mathrm{s}_i + \mathrm{h})\right]^2$$

Eq. 4-3

γ (*h*): Semi-Variogram

Z(*s*): The variable (can be porosity, permeability, etc.)

f (*s*, *u*): the joint probability density function of *Z*(***s***) and *Z*(***u***)

h: the distance separating sample

N (*h*): the number of distinct data pairs

Note: The real data (as porosity and permeability) usually skewed and do not have Gaussian or normal distribution. For geostatistical analysis, the normal distribution of variables are needed. The normalization procedure can be done by logarithm transformation or Box-Cox method as skewed data distribution has a high impact on the variogram.

Definitions:

In a standard variogram, three parameters are recognizable as shown in Figure 4-35:

1- Nugget effect: The variable and variance change in its neighborhood. It is estimated from the empirical variogram at h = 0.

2- Sill – The asymptote volume in a variogram.

3- Range – The distance that a variogram reaches to the sill, it shows the range of influence of each point on the others. So, there is no correlation between samples with distance bigger than the range.

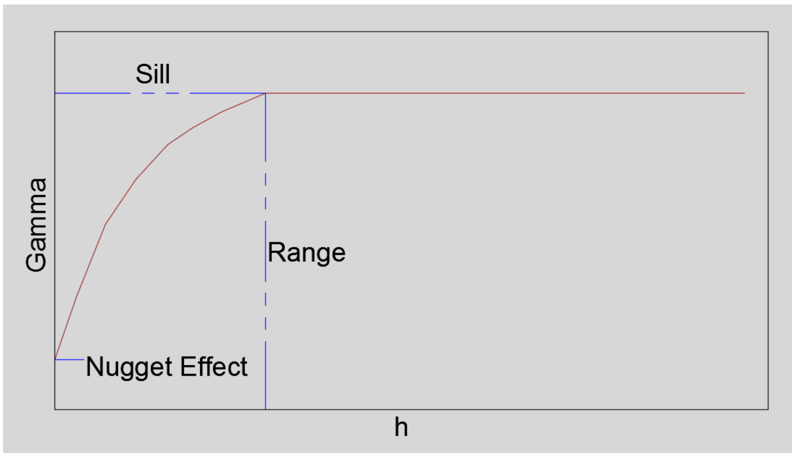

Figure 4-35: A typical Variogram diagram and main parameters.

4.12.2 Variogram models:

For kriging propose and estimate the value of the sill and range in an empirical variogram, the variogram models are fitted to the empirical models. Some models are as following:

1. Linear model
2. Spherical model
3. Logistic model
4. Cauchy model

5. Power model

6. Exponential model

7. Gaussian model

8. Matern model

For the current research, the most used model is spherical (Figure 4-36). The formulation of this model is:

$$\gamma(h) = c_0 + c_1\left(\frac{3}{2}\frac{h}{a} - \frac{1}{2}(\frac{h}{a})^3\right) \qquad 0 < h \le a \qquad \text{Eq. 4-4}$$

$$\gamma(h) = c_0 + c_1 \qquad h \ge a$$

C_0 is nugget effect and (C_0+C_1) shows the sill.

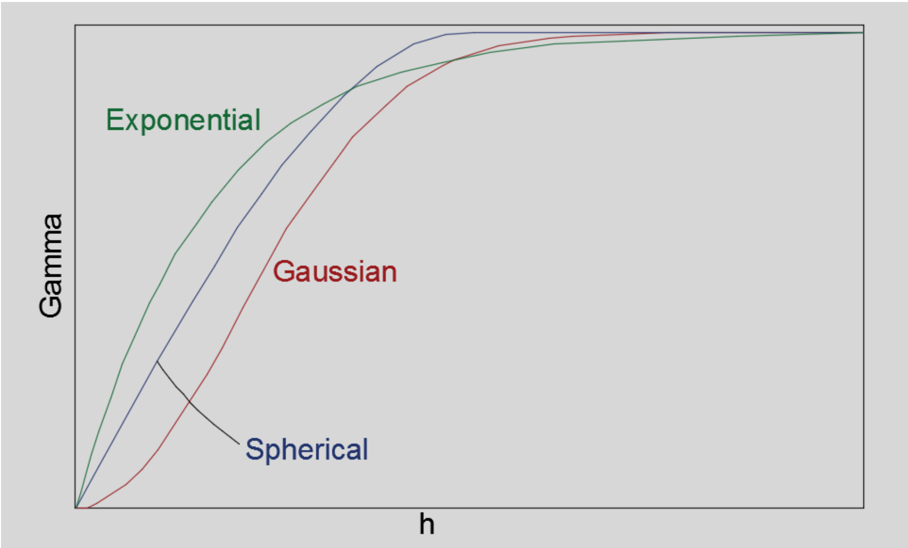

Figure 4-36: Three variogram models.

4.12.3 Anisotropies

The model and structure of variograms can change in the directions and different azimuth. For a detailed study and accurate interpolation by the Kriging method, the azimuthal variograms (X, Y, and Z directions) are needed. The anisotropy is a reflection of the sedimentation layering and geological lineaments (as fractures and faults). The different sill and range in the different azimuth can make an anisotropy ellipsoid, and the anisotropy is then considered in Kriging stage.

In the FRS project, the seismic study and geological condition of the area demonstrate a similar values in the X and Y direction and so it was considered a homogeneous variogram, but with a different structure of the variogram in the Z direction because of layering and it is calculated from the well log data (Figure 4-37).

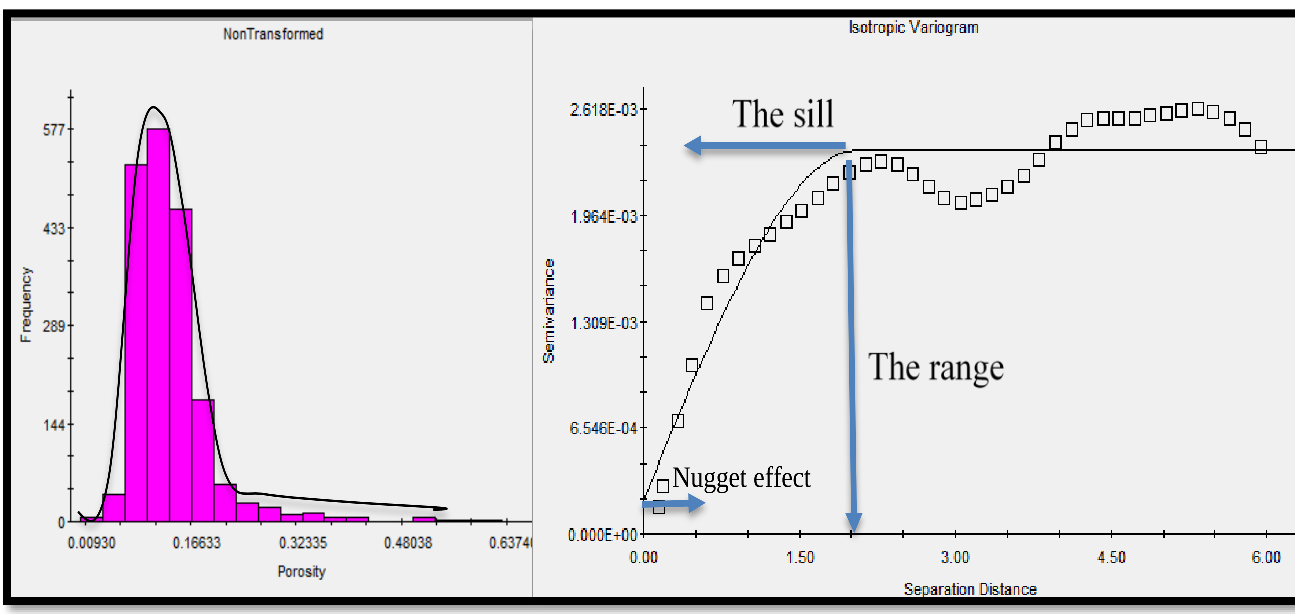

Figure 4-37: The histogram (to check the distribution type of the data) and semi-variance with a spherical model fitted for the density porosity variable (The nugget effect = 0.0002080, the sill= 0.0023660, the range= 2.0700 m for h=15 cm in the well direction).

4.12.4 Kriging:

In the final step of the geostatistical analysis, Kriging method was used for the interpolation purpose. It is a way to distribute permeability and porosity in the prepared geometry model and cells. Kriging (introduced by D. G. Krige) is a local estimation technic which provides the Best Linear Unbiased Estimator (BLUE) of the unknown characteristic studied (Journel,1991).

4.13 Primary models

The first tested geomodel has dimension of 3900*3000*473 m, and the grid sizes were fine near the 10-22 well and coarse grid sizes in the other part of the model as shown in Figure 4-38. The surfaces fixed by the seismic interpretation and well tops. The simulation time for this geomodel is long, and because we needed to test some features and properties for the simulation, we change it to smaller and simpler model, with dimension of 1000*1000*473 m.

This geomodel uses data from three wells and has a geometry derived from the interpreted horizons of the seismic data as shown in Figure 4-40.

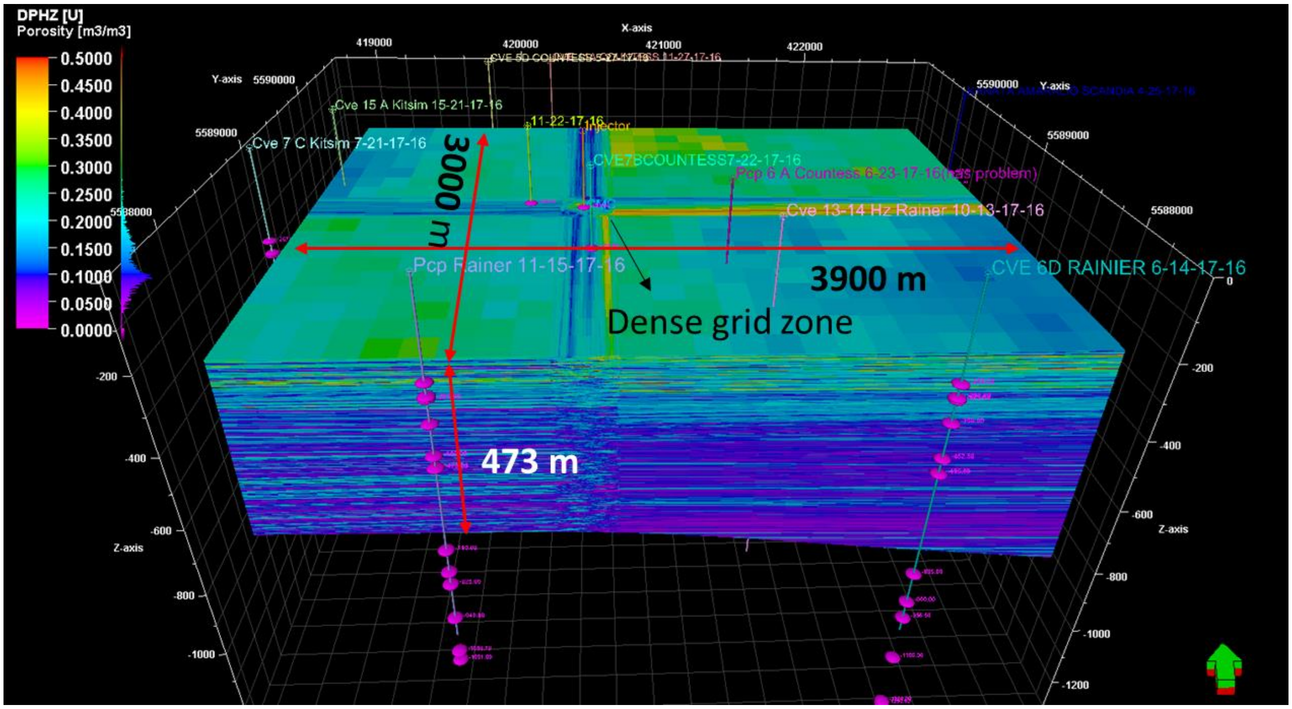

Figure 4-38. A geomodel made from 11 wells and a small cell size around the injection well. The dimension of geomodel is 3900*3000 m.

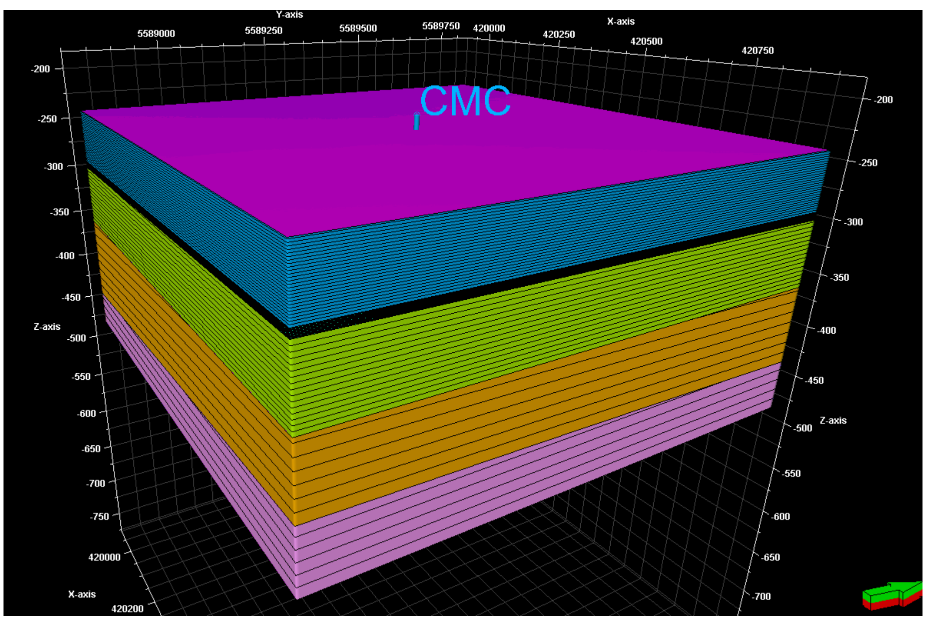

Figure 4-39.The geometry of layers in the geomodel from the seismic interpretation. Colors shows the main geological events and formations, dimension is 1000*1000 m

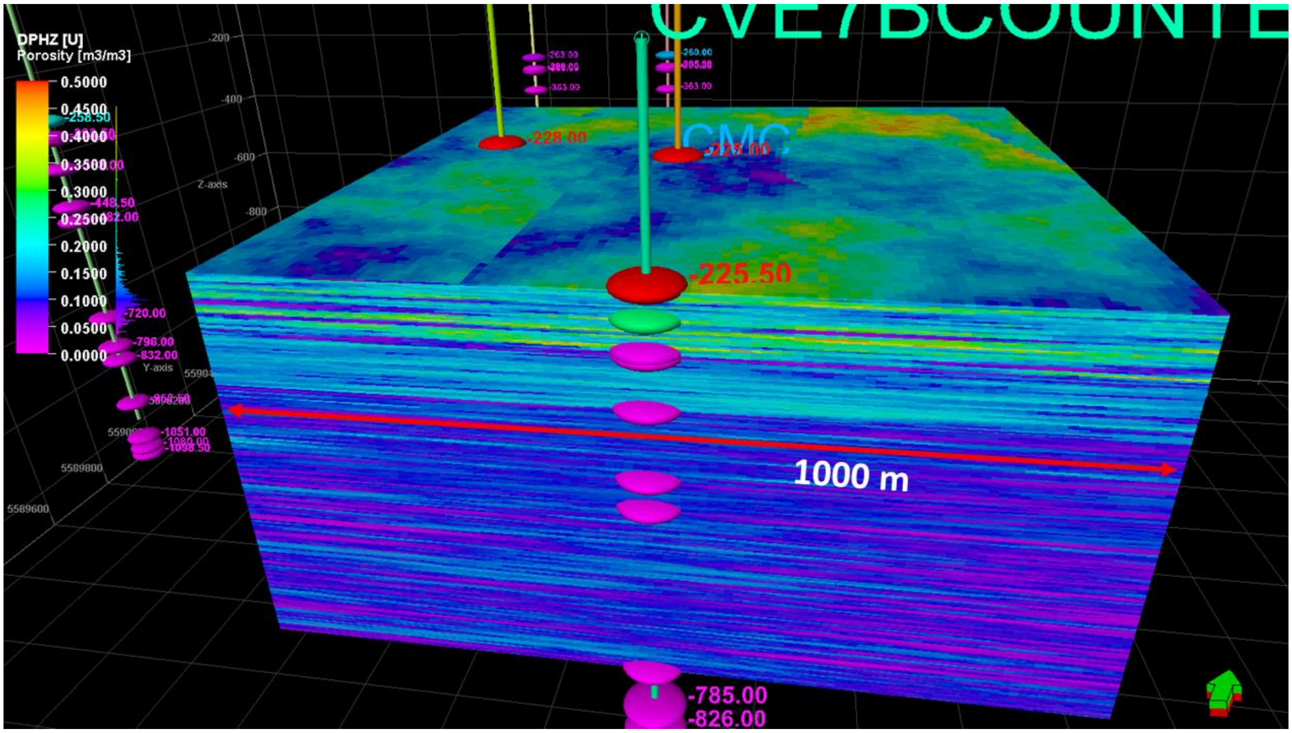

Figure 4-40.The revised geomodel derived from log data from three wells. The dimension of geomodel is 1000*1000 m.

4.14 The isotropic geomodel for fluid simulation

As mentioned, because the injection rate was found to be quite limited (Chapter 5), the geomodel that finally used for the simulation is used only the 10-22 well for geomodelling. The geometry is shown in Figure 4-39, and Figure 4-41 is a 3D figure of the geomodel showing porosity distribution and Figure 4-42, Figure 4-43 and Figure 4-44 are a 2D figures of geomodel showing vertical permeability and porosity, respectively near the injection horizon with more detailed information about the grid size.The permeability in Z direction considered as 10% of permeability in XY directions (personal discussion with Schlumberger reservoir expert).

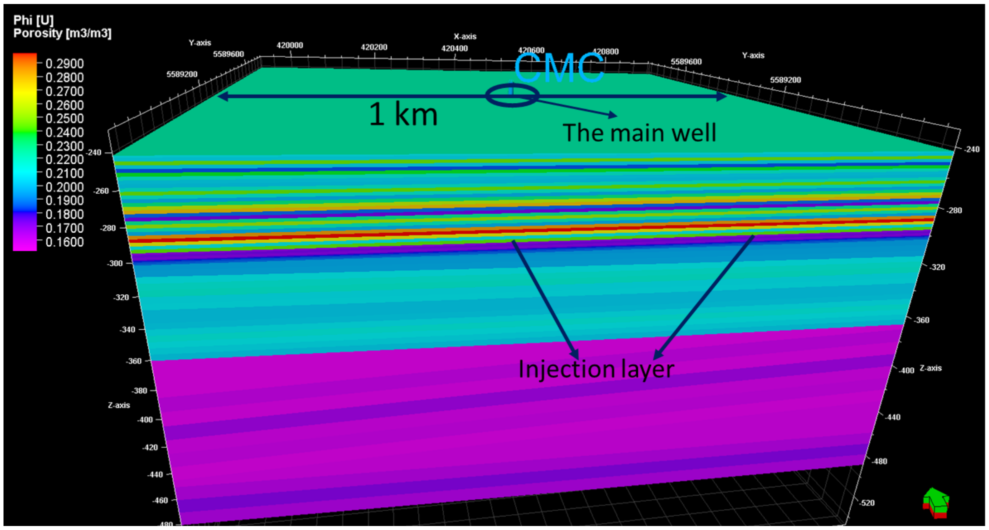

Figure 4-41.The porosity geomodel made up with the well log data. The geomodel size is 1000*1000*240 m.

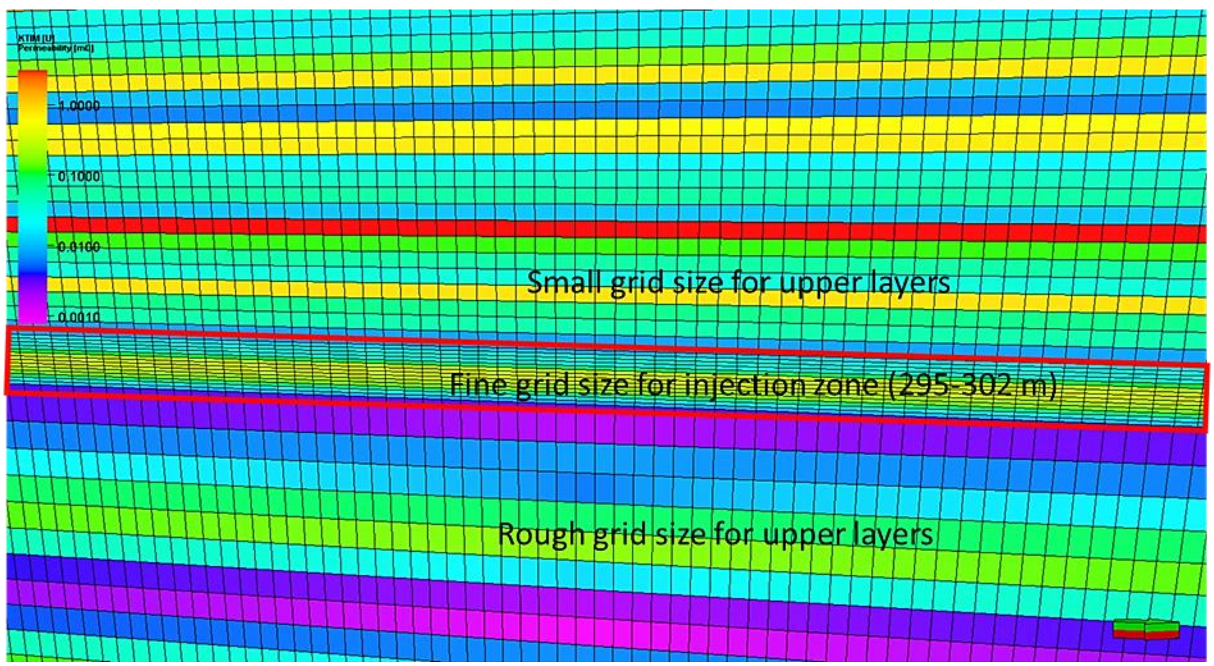

Figure 4-42. A section of the xy permeability geomodel shows the grid size in the injection layer and others. The red rectangle shows the injection layer (i.e. Basal Belly River)

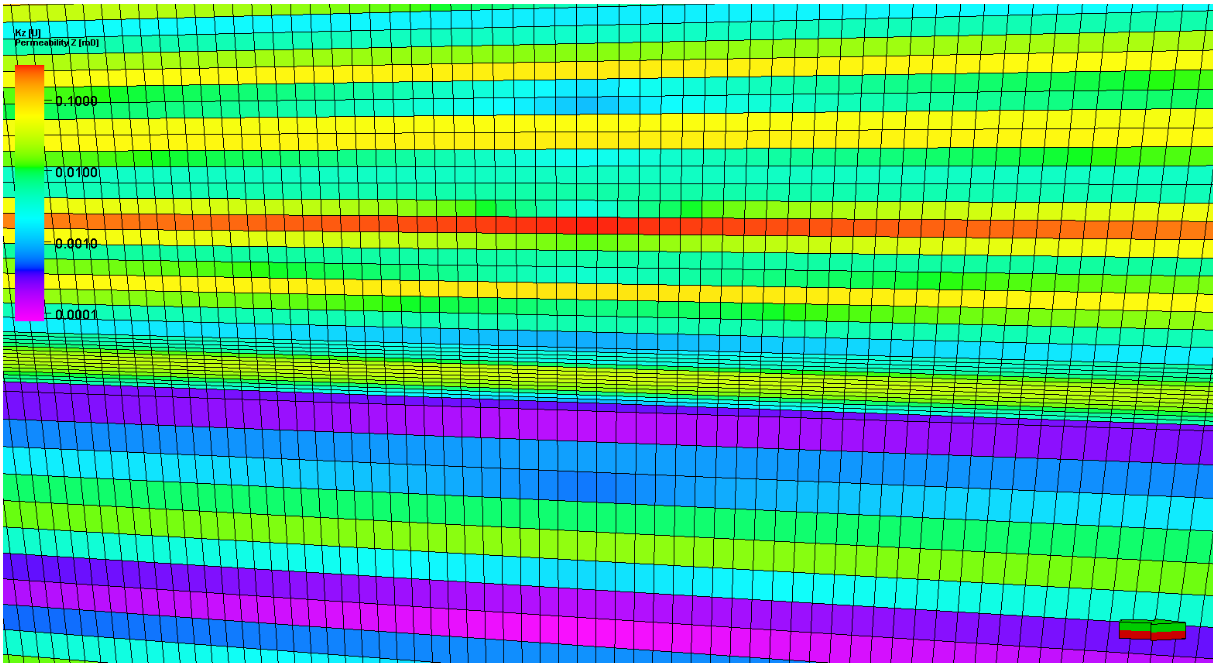

Figure 4-43. A section of geomodel for the permeability in z direction.

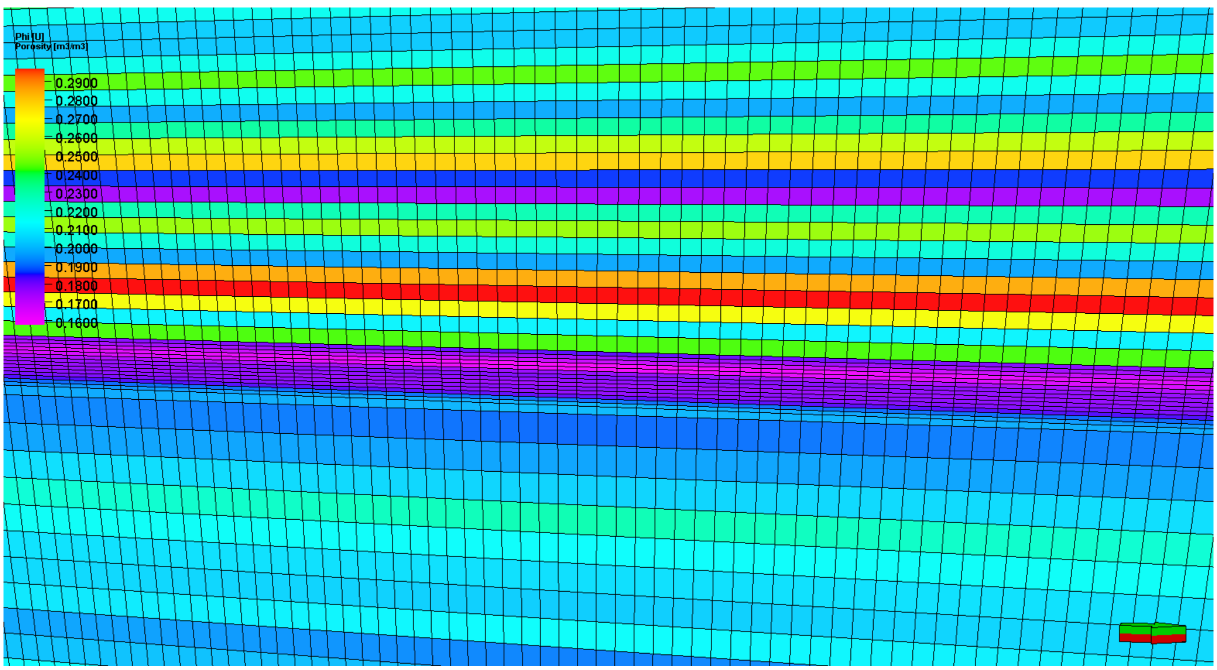

Figure 4-44. A section of geomodel for the porosity.

4.15 The geomodel for the seismic modeling and imaging

For seismic modelling using finite difference approach, the code is based on the equal grid sizes, and it is defined in the code by 2D matrices. In the next step, we need to import and convert the reservoir geomodel for input into the seismic code.

The cell size in the geomodel for the fluid simulation is variable from the injection zone to the rest of the formation. The cell size for the seismic modeling and RTM imaging code is small size as 1*1 m (Figure 4-45 (3D geomodel for Vp), Figure 4-46 (3D geomodel for density) and Figure 4-47 (2D geomodel for Vp)). The seismic code for part of the 2D seismic modeling and imaging, so it uses 2D geomodel, extracted from the 3D geomodel.

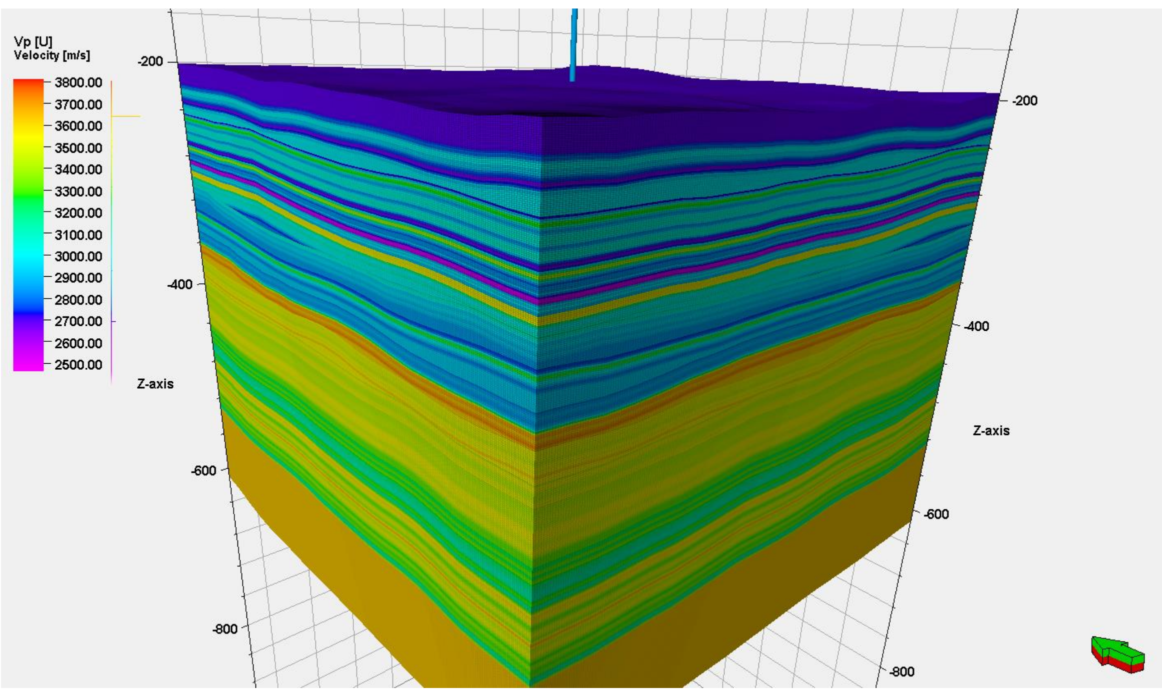

Figure 4-45.The P-wave velocity model. This model was used for the seismic imaging.

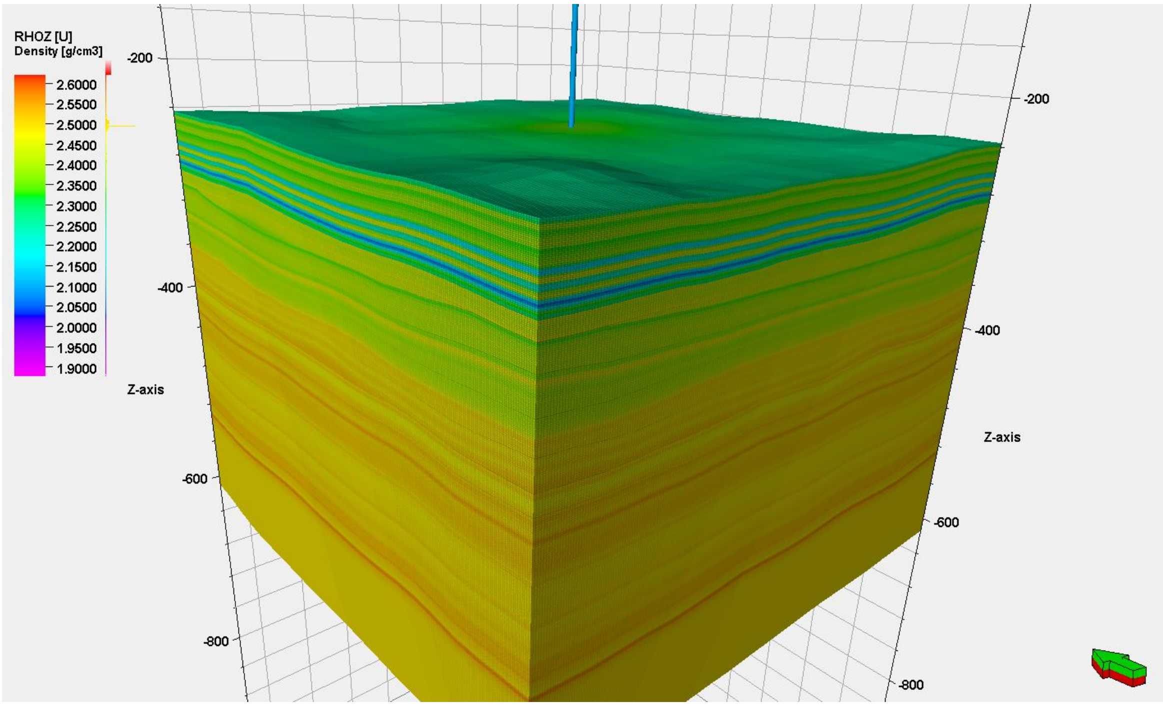

Figure 4-46. The density model used for seismic modelling.

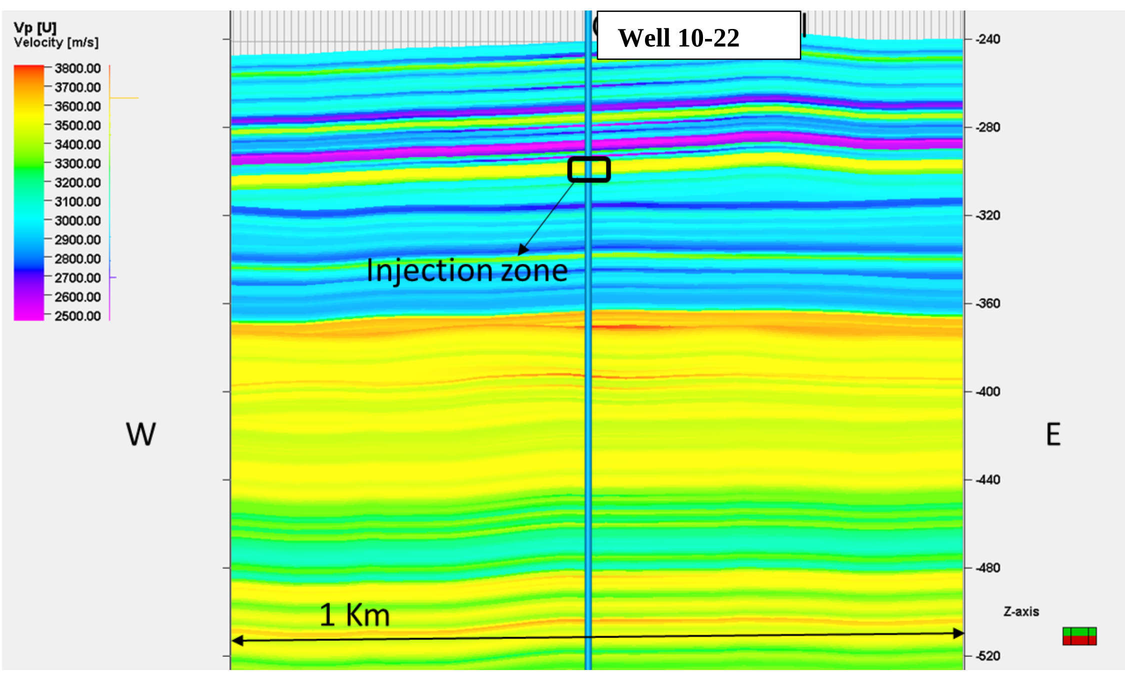

Figure 4-47: The P-wave velocity oriented by seismic layers (a 2D view of Figure 4-45 in a section passing of the 10-22 well). The section is W-E and view is to the North.

Chapter 5. Reservoir fluid simulation for FRS project

5.1 Introduction

Reservoir simulation is a direct numerical method to model fluid flow in a porous medium containing one or more fluids. Fluid simulation has the goal of managing production/injection rate and for optimizing the operational cost. For simulation purposes data from many other disciplines are gathered as shown in Figure 5-1.

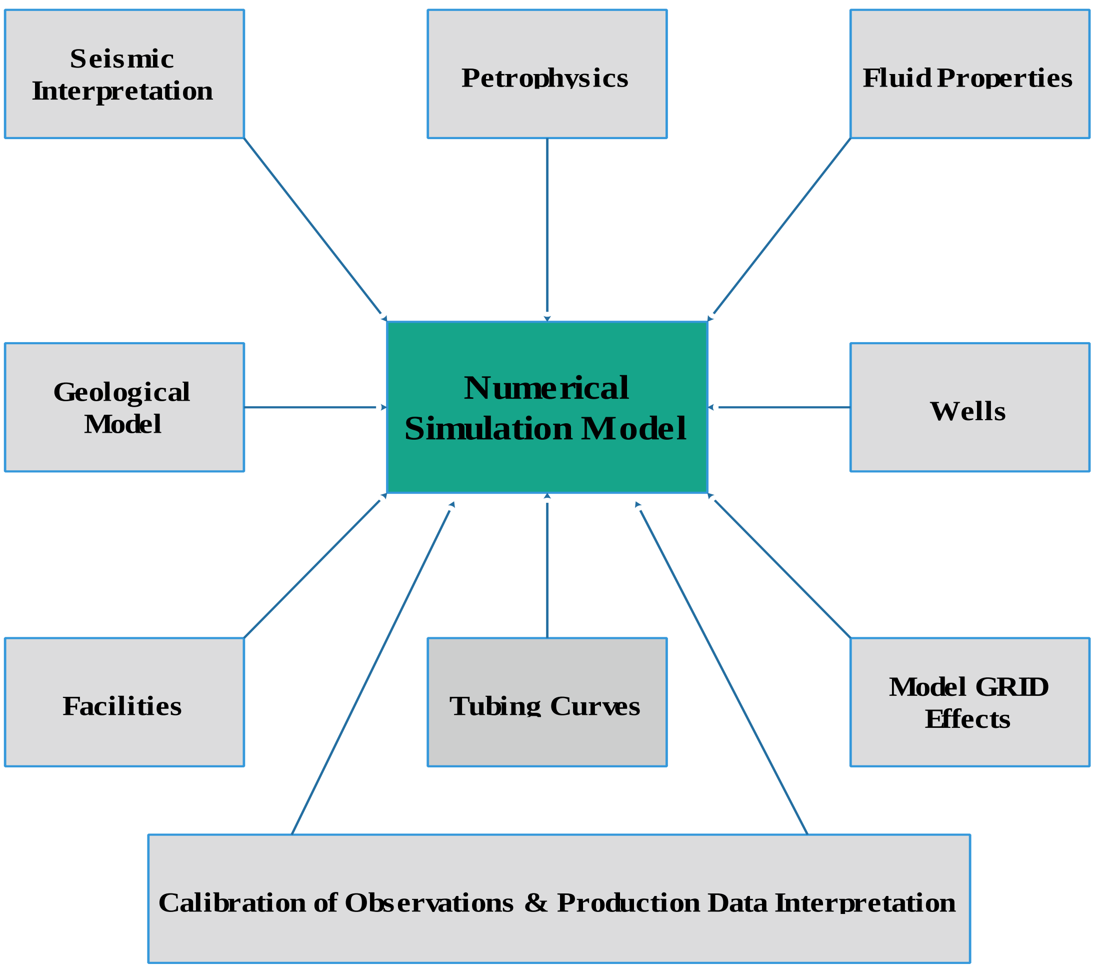

Figure 5-1. Disciplinary contributions to reservoir flow modeling (after Fanchi, 2006)

For a fluid simulation, one needs to have a geomodel with valid geometrical data of the reservoir with suitable grids and appropriate cell size. These grids make a 3D matrix such that each component such as porosity or permeability were estimated and interpolated by a geostatistical method. For this stage, the information and data are determined from petrophysics and well log data combined with the geological model and seismic interpretation results.

In this project, the objective is to simulate CO_2 gas injection in a shallow target (300 m) that is a low pressure and temperature reservoir, and predict the behavior of the gas in the reservoir. The results of the simulation are integrated with a rock physics study to translate the reservoir parameters to seismic properties for monitoring purposes. In this chapter, I calculate the static physical parameters of the reservoir to input in the simulation procedure, and the final output in this chapter will be dynamic parameters (saturation and pressure, with the CO_2 plume geometry).

In the previous section (4.11), I prepared a horizontally isotropic geomodel from the available well log data (10-22), seismic interpretation results and geological data as shown in Figure 4-41. The physical properties of the fluids (brine and carbon dioxide) are discussed in the next chapter (Chapter 6) using an Equation of State for CO_2 by Span and Wagner (1996) and formulas for the brine properties by Batzle and Wang (1992).

5.2 Initial state of the FRS reservoir

The first step of fluid simulation study is related to the physical and chemical properties of the reservoir. For the simulation purpose, the aquifer is considered a brine with 8000 ppm of salt. Also, the fluid phase is assumed to be isotropic, homogeneous and isothermal in the research. The temperature of the reservoir was measured to 13^{o}C, and it will be constant during the gas injection (isothermal). Figure 5-2 shows the hydrostatic and lithostatic pressure in the well 10-22. The lithostatic pressure was calculated from the density log with a primary density equal to 2200 kg/m^3 for the no data zone in the well shallower than 225m (depth of surface casing).Table 5-2 list the initial properties in the reservoir.

There are many methods and approaches for calculation of the physical properties of fluids in different phases. Batzle and Wang (1992) introduced approximations for density, viscosity and bulk modulus of oil, gas, and brine and this approach is usually used by geophysicists. Cho (1970) and Kestin et al. (1981) discussed other approximations for the physical properties of brine. In this dissertation, Batzle and Wang equations were used for density, compressibility (= 1/bulk modulus) and viscosity of the reservoir fluids. The calculation method is described in Chapter 6.

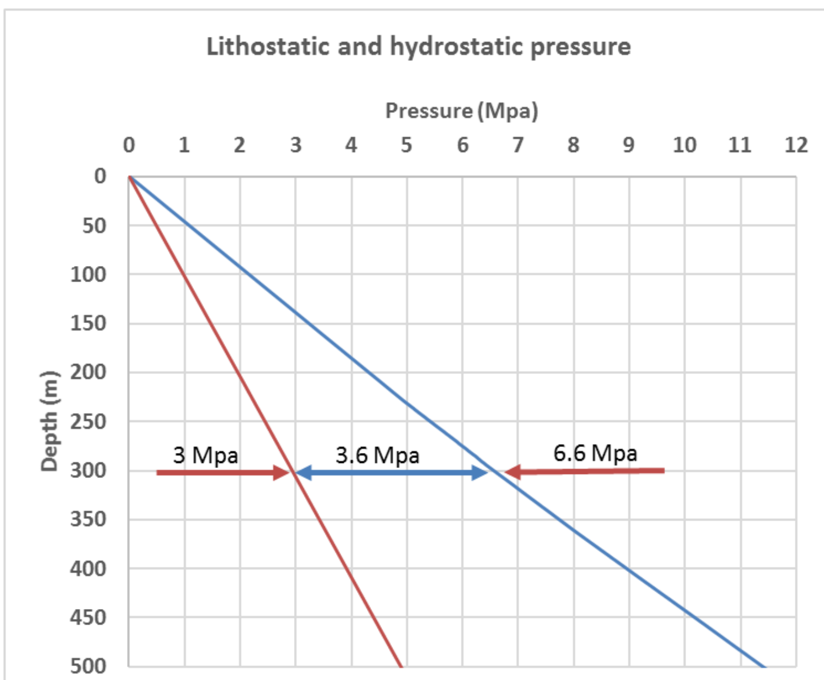

Figure 5-2.Hydrostatic and lithostatic pressure in the reservoir; the latter is calculated from the density log data.

Table 5-1.The initial properties of the injection target

Depth (m)	**295-302**
Thickness (m)	**7**
Lithostatic Pressure at aquifer top (MPa)	**6.6**
Temperature (ºC)	**13**
Permeability (md)	**0.1-2.0**
Porosity (%)	**14-18%**
Salinity of formation water (mg/l)	**8000**
Density of formation water (kg/m^3)	**1005.2**
The viscosity of formation water (centipoise)	**1.16**

5.3 The reservoir concepts and simulation methods

5.3.1 Relative permeability

When there is more than one fluid phase in a reservoir, the effective and relative permeability can play a significant role in the simulation. Effective permeability is a value for the conductance of a porous medium for a specific fluid phase when the reservoir has more than one fluid. Relative permeability can be explained by Eq. 5-1 and it is equal to effective permeability (k_i) normalized by the single phase absolute permeability (k).

$$k_r = \frac{k_i}{k}$$

Eq. 5-1

Models prepared by Brooks-Corey (1964) that rewrote for the CO2 injection case by Bachu (2013), were used for the relative permeability calculation in the current study (Eq. 5-2 and Eq. 5-3).

$$k_{rCO2} = k_{CO2}^{\max}\left(\frac{S_{CO2} - S_{CO2}^{C}}{1 - S_{CO2}^{C} - S_{b}^{irr}}\right)^{n}$$

Eq. 5-2

$$k_{rb} = k_{rb}^{\max}\left(\frac{1 - S_{CO2} - S_{b}^{irr}}{1 - S_{CO2}^{C} - S_{b}^{irr}}\right)^{m}$$

Eq. 5-3

Where: irr : irreducible, c : critical, S : saturation, max : Maximum, m , n : Corey's coefficient for both the drainage and imbibition cycles and S_{CO2}^{irr} is calculated by Eq. 5-4 as:

$$S_{CO2}^{irr} = \frac{S_{CO2}^{\max}}{1 + CS_{CO2}^{\max}}$$

Eq. 5-4

C is a coefficient related to the trapping efficiancy, and C=0 iff all CO_2 trapped and infinity if it is not trapped.

Studies about relative permeability in Alberta's sandstone and limestone formations by Burnside (2014), Bachu (2013) and Bennion (2010). Bachu (2013) studied Alberta's sandstone in different formations with a range of permeability. The permeability of the Belly River sandstone is between 0.1 to 2 mD. So, it is in low k value and based on the previous studies on the formations with sandstone lithology in Alberta; the trapping efficiency will be 49-55% (Figure 5-3), so it means the CO_2 saturation can be alike similar to the trapping efficiency range.

Finally, the relative permeability curve for the BBRS was calculated based on Corey's equation for the reservoir's sandstone as shown in Figure 5-4.

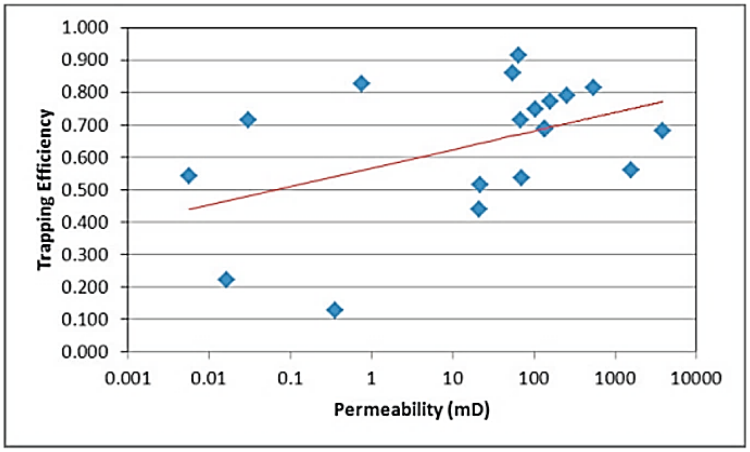

Figure 5-3. Trapping efficiency in sandstone based on previous work in Alberta (Bachu, 2013)

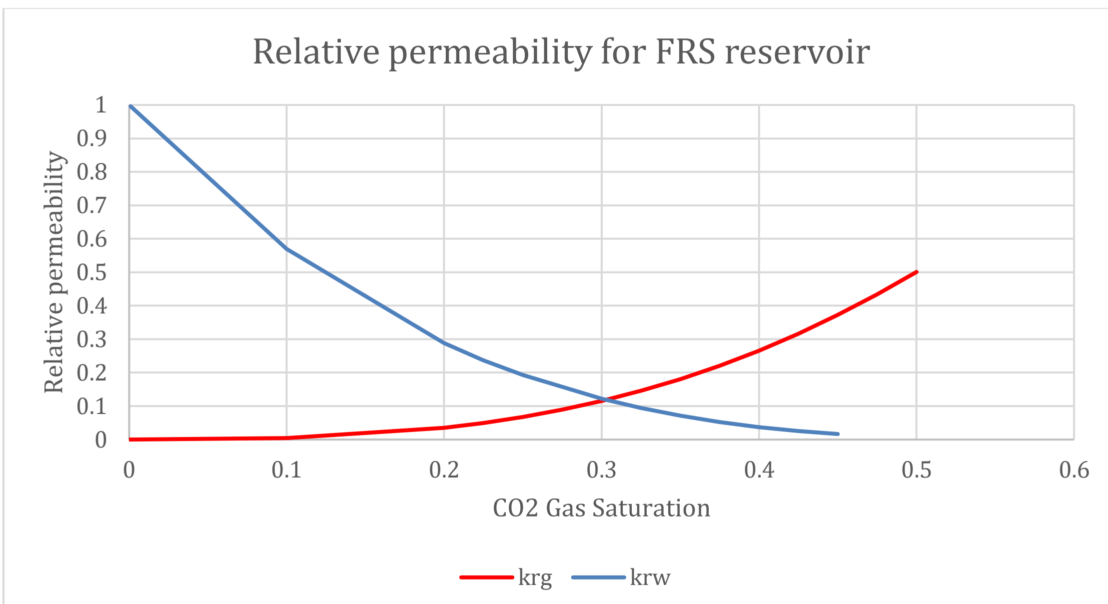

Figure 5-4. The relative permeability curve calculated for the reservoir.

5.3.2 Anisotropy of the permeability

Permeability is influenced by stratigraphy, and rock fabric. Usually, it has a higher value parallel to sedimentary layers compared to the perpendicular to the layers. Also, tectonic phenomena as faults, joints and fractures can play a dominant role in the formation's permeability through fracture orientation. The FRS reservoir does not have any evidence for significant faults, as determined from the seismic interpretation and attribute study.

For the current study, there is no measurement for permeability in the Z direction, and so by the industrial protocol, it was considered 10% of the permeability in X and Y directions.

5.3.3 Formation compressibility

This parameter is necessary to measure the change in pore volume due to a change in reservoir pressure. It can be expressed by Eq. 5-5.

$$c_f = -\frac{1}{V_\varphi}\left(\frac{\partial V_\varphi}{\partial p}\right)_T$$

Eq. 5-5

Where:

c_f is formation compressibility, V_φ is the pore volume of rock, p is pressure on the formation.

T as a subscript in the last term shows the isothermal process.

For the reservoir, the P and S-wave slowness and the density were determined from the 10-22 well log data. The velocity is calculated by the following formulas (Eq. 5-6):

$$V_p = \frac{1}{P-slowness}$$
$$V_s = \frac{1}{S-slowness}$$

Eq. 5-6

The elastic moduli have a direct relation with the density, P and S-wave velocity shown in Eq. 6-21 and this was used for the elastic modulus calculation. Figure 5-5 showing the result of calculation for the velocities, elastic modulus and compressibility.

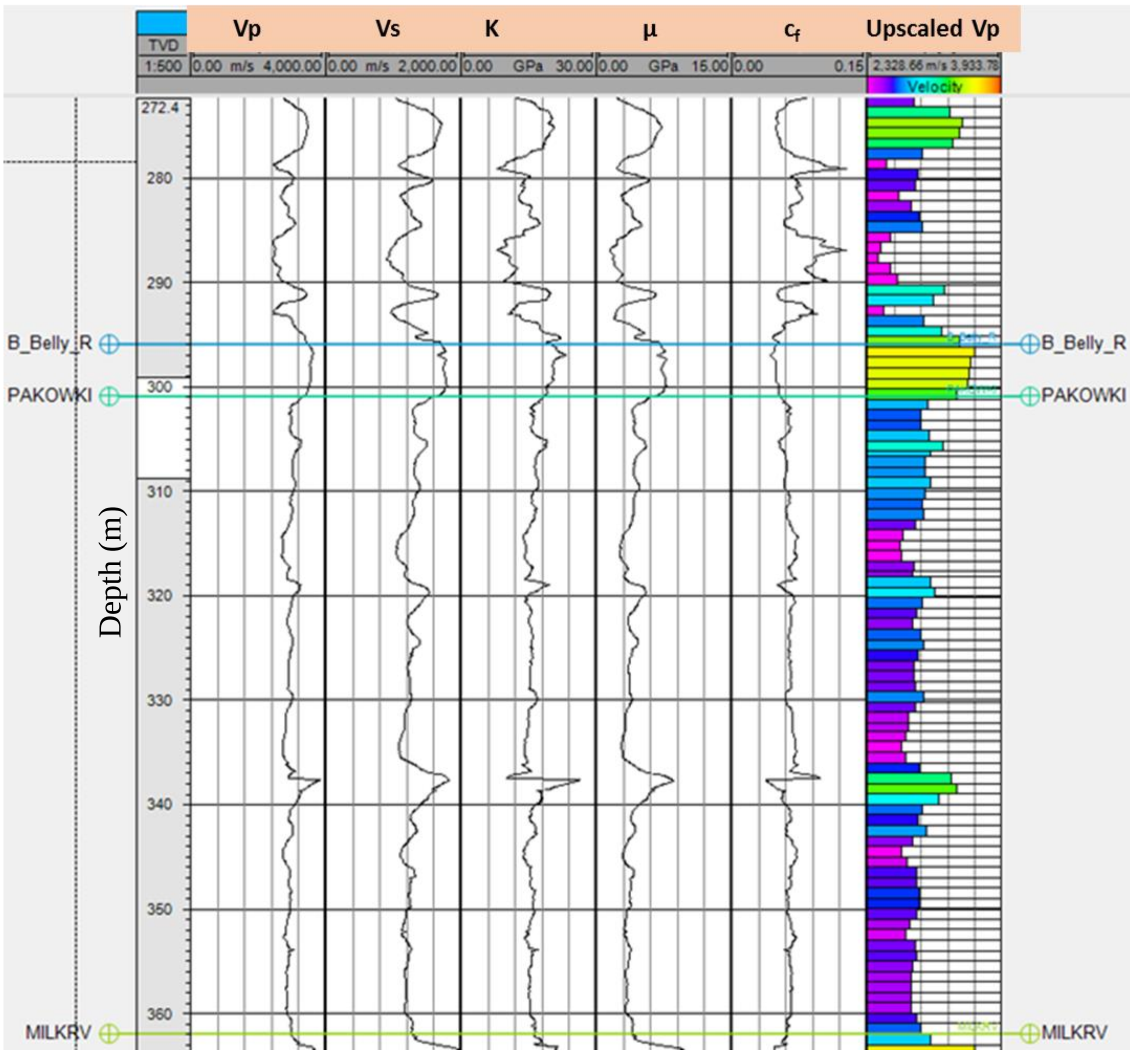

Figure 5-5.Geomechanical properties of the reservoir in the well 10-22-17-16. The compressibility was demonstrated by c_f (the unit is 1/GPa).

5.3.4 Darcy's law

The basis of reservoir simulation is the mass movement and its relation to the permeability and reservoir pressure. In a medium with a particular phase in it, Darcy's law can estimate the fluid flow rates as Eq. 5-7 and with absolute permeability value in existence of just one phase. Darcy's law in one dimension can be expressed as:

$$u = -\frac{k}{\mu}\frac{\partial P}{\partial x}$$

Eq. 5-7

For a medium, saturated by two phases (here: gas and oil) with considering effective permeability definition for each phase can be determined from Eq. 5-8 and Eq. 5-9.

$$u_g = -\frac{kk_{rg}}{\mu_g}\frac{\partial P_g}{\partial x}$$

Eq. 5-8

$$u_o = -\frac{kk_{ro}}{\mu_o}\frac{\partial P_o}{\partial x}$$

Eq. 5-9

Where

u_n = volumetric flow rate for a particular phase *n*

k_{rn} = *relative permeability of phase n*

μ_n = fluid viscosity for phase *n*

5.3.5 Simulation methods

Equations used in hydrocarbon simulation are based on the continuity equation. The conservation law in the reservoir (conservation of mass, energy, and momentum) is essential for mass balance and the continuity equation. In simple form, for each cell (Figure 5-6 and Figure 5-7) a combination of Darcy's law (Eq. 5-7), the material balance (Eq. 5-11) and flow equation are solved (Fanchy, 2006 and ECLIPSE course material, Schlumberger, 2016).

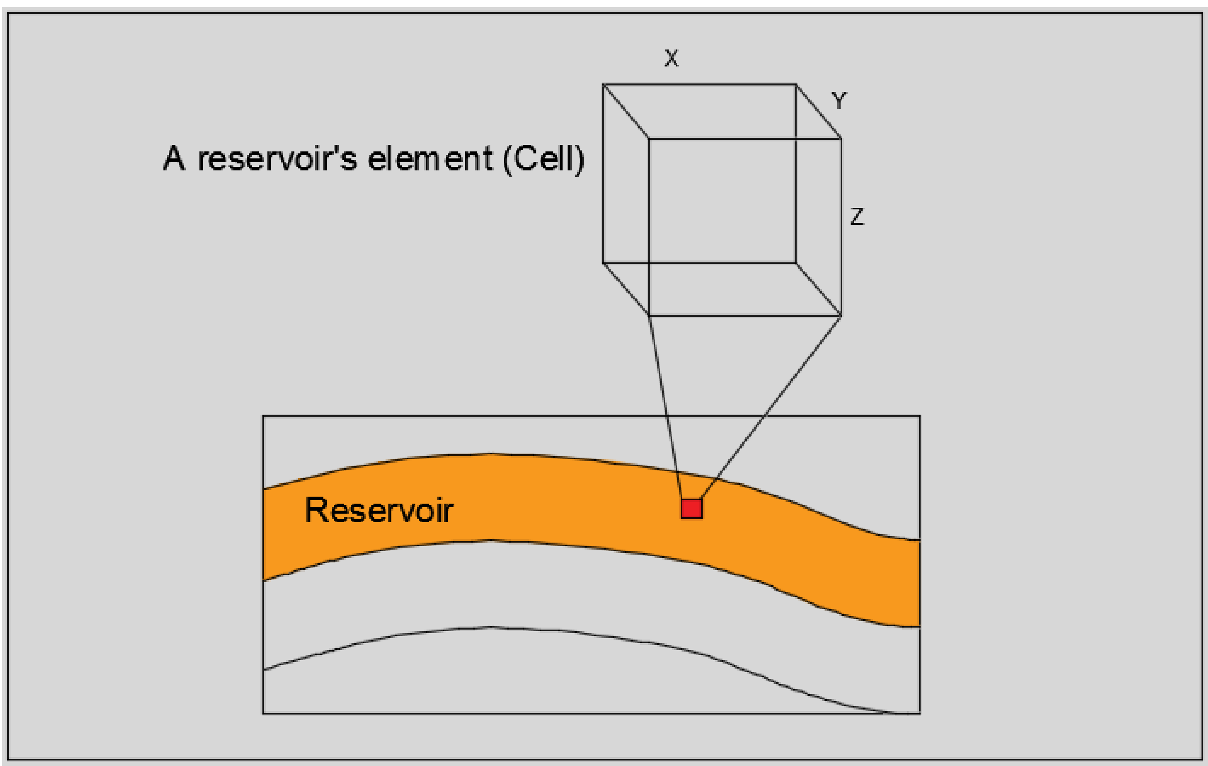

Figure 5-6. Volume elements or grid block in reservoir simulation.

Material Balance:

Mass flux =Accumulation + injection/production

$$\sum_{k=1}^{N_c} C_{kg} = 1 \quad \text{and} \quad \sum_{k=1}^{N_c} C_{ko} = 1$$

Eq. 5-10

Mass balance of component k in one dimension:

$$-\frac{\partial}{\partial x}\left(C_{kg}\rho_g u_g + C_{ko}\rho_o u_o\right) = \frac{\partial}{\partial t}\left[\varphi\left(C_{kg}\rho_g S_g + C_{ko}\rho_o S_o\right)\right]$$

Eq. 5-11

$$P_{cog} = P_g - P_o$$

$$P_{cow} = P_o - P_w$$

$$S_o + S_g = 1$$

With considering Darcy's law:

$$\frac{\partial}{\partial x}\left(C_{kg}\rho_g \frac{kk_{rg}}{\mu_g}\frac{\partial P_g}{\partial x} + C_{ko}\rho_o \frac{kk_{ro}}{\mu_o}\frac{\partial P_o}{\partial x}\right) = \frac{\partial}{\partial t}\left[\varphi\left(C_{kg}\rho_g S_g + C_{ko}\rho_o S_o\right)\right]$$

Eq. 5-12

For a reservoir's element and in three dimensions it can be explained as:

$$-\frac{\partial J_x}{\partial x} - \frac{\partial J_y}{\partial y} - \frac{\partial J_z}{\partial z} - q = \frac{\partial C_1}{\partial t}$$

Eq. 5-13

or:

$$-\nabla \cdot M = \frac{\partial}{\partial t}\left(\varphi\rho\right) + Q$$

Eq. 5-14

$-\nabla \cdot M$ is the mass flux, $\frac{\partial}{\partial t}\left(\varphi\rho\right)$ is the accumulation and Q is injection/production term (ECLIPSE black-oil reservoir simulation, Schlumberger, 2009).

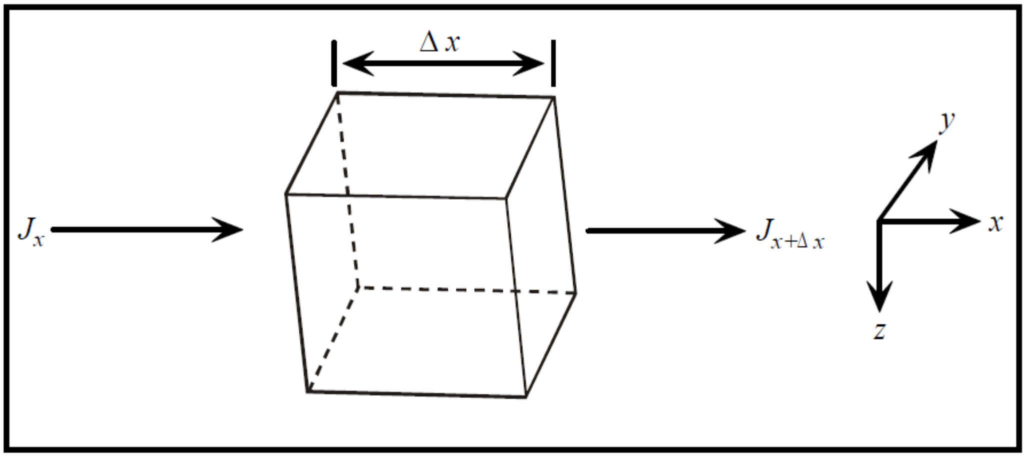

Figure 5-7.Reservoir gridblock, coordinate and directions

Black-oil and compositional simulators are two methods for undertaking reservoir fluid simulation. The Black-oil simulator is suitable for three components (oil, gas, and water) and properties of the three phases as a function of pressure. It is usable for cases with recovery mechanics not sensitive to composition changes in the reservoir fluids such as primary recovery, solution gas drive, gravity, drainage, gas cap expansion, water drive, water, and gas injection without mass transfer. The density of each phase is necessary for material balance equation. The density also relates to pressure and temperature. PVT properties are required to estimate and convert the volume of phases in a different environment as reservoir condition or production part. The principal assumptions in the black-oil simulation are:

1. Darcy's law governs the velocities of the fluids.
2. The void porous is filled by water/oil and gas
3. Capillary pressure = gas pressure – oil pressure
4. Phase mobility = phase permeability / phase viscosity

A Compositional Simulator can support multi-component and multi-phase reservoirs based on the Equation of State (EoS). Also, it can model the simulation and mass movement when a new component was created because of chemical reactions. The Compositional method is expensive and takes more time compared to black-oil Simulator methods.

For a Black Oil simulation, the parameters needed are (a) geometry, (b) matrix properties, (c) fluid property and (d) well production/injection plan. Geometry and properties are input into grids and cells with size and static properties for each of them (permeability and porosity). The fluid properties are needed for the simulation, and they include viscosities, the solution gas-fluid (here CO_2 and water) ratio (R_s) and relative permeability curve for drainage and imbibition conditions. The production/injection schedule and strategy are the final part to complete the simulation data sequence, as the effect of production or injection will enter to simulation as our last term of the material balance or simulator flow equations.

Briefly, as shown in Figure 5-8, the compositional simulator is suitable for oil and gas reservoirs when the thermodynamical condition is near the critical point. The Black-Oil and following requirements can help to select the right simulator:

5.3.6 Black-oil simulator

The black-oil simulator is useful for the following cases:

•Three-phases (oil, gas, and water)

•Three components (oil, gas, and water)

•When all fluid properties are functions of pressure

Suitable for black-oil simulators are cases with recovery mechanics not sensitive to composition changes in the reservoir fluids such as primary recovery, solution gas drive, gravity, drainage, gas cap expansion, water drive, water injection and gas injection without mass transfer.

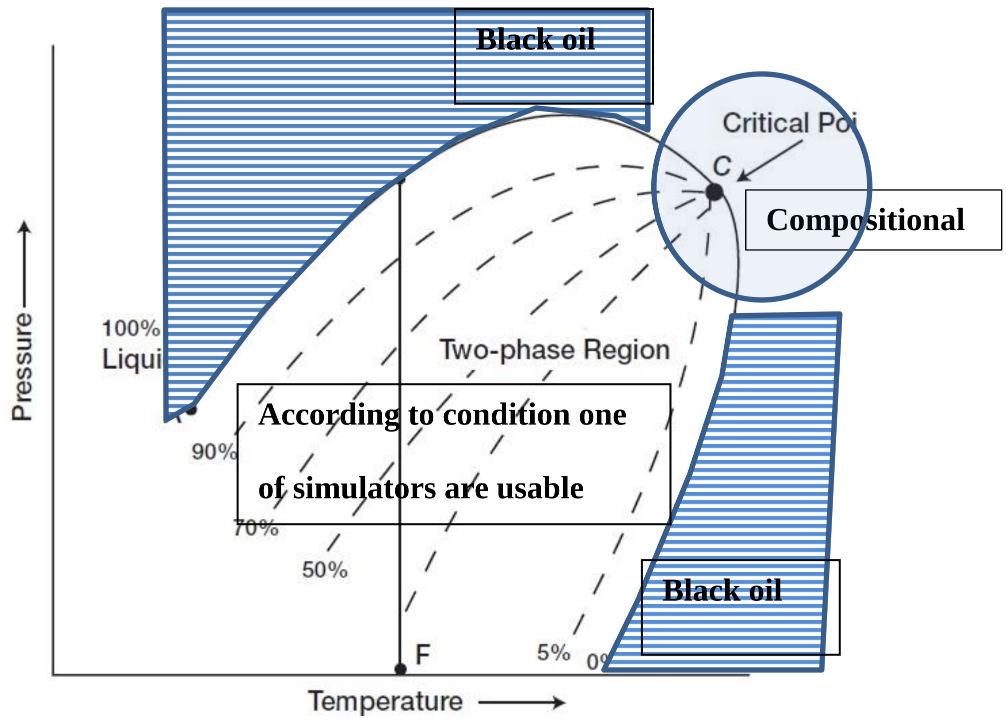

Figure 5-8. Appropriate situation for Compositional and black-oil and compositional simulators for oil and gas phases (ECLIPSE course material, 2016).

5.3.7 Specifications and Advantages of Compositional Simulator

Multi-component and multi-phase reservoir simulators are based on EoS modeling. Suitable for compositional simulation are cases sensitive to compositional changes in reservoir fluids such as primary depletion of volatile oil, gas condensate reservoirs and pressure maintenance in such reservoirs. Also multiple contact miscible gas injection, CO_2 and N_2 injection.

5.4 The result of the reservoir simulation

The FRS reservoir is at shallow depth with low pressure and temperature. The temperature of the formation is 13°C in the target zone, and the pressure is 30 bar. At this temperature, the injected CO_2 will change from gas to the liquid phase at a pressure equal to 49 bar. The goal of the research is to inject CO_2 in gas phase, and so the strategy will be a constant bottom hole pressure equal 49 bar for five years. After five years, the injection will be stopped, and the monitoring will continue for a decade. According to the reservoir's PVT table, simulation has been chosen to be undertaken by the compositional simulator (Figure 5-9) for CO_2 injection in the gas phase. The result of simulations for the gas saturation and pressure are outlined in Figure 5-11.

The compositional simulation is a complex and time taking procedure compare to the black-oil simulator. The black-oil simulator has been used in the WASP project, that CO_2 were injected in the supercritical condition (see WASP reservoir simulation by the black-oil method, Nowroozi, 2013). Figure 5-9 shows the phase diagram for the CO_2 and the FRS project condition. Figure 5-10 is a detailed phase diagram for T= 0 to 30 °C and P=0 to 80 bar (8 MPa).

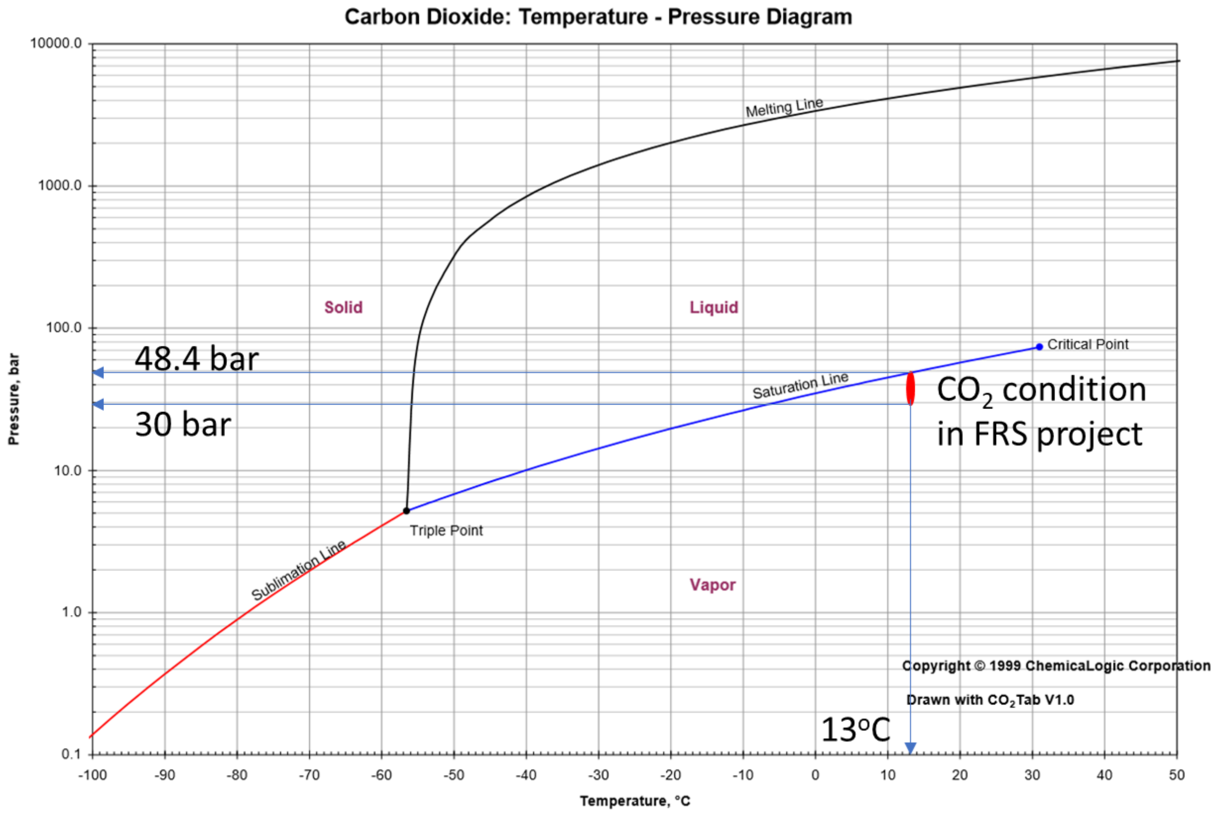

Figure 5-9: The phase diagram of carbon dioxide and pressure and temperature condition in the FRS project (Phase diagram from ChemicaLogic Corporation).

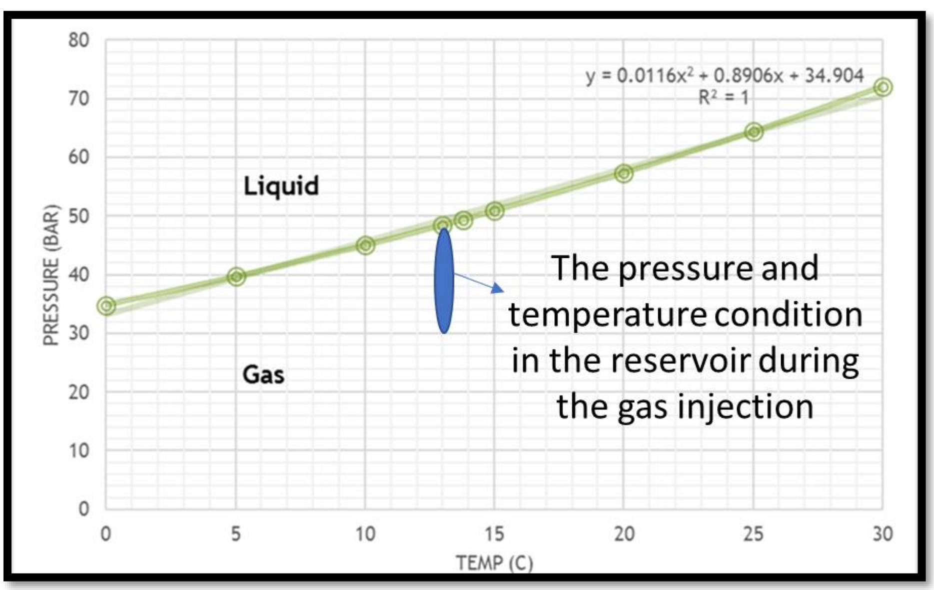

Figure 5-10. The phase diagram of CO_2 for the reservoir condition. This figure is a magnified image of Figure 5-9 near the reservoir condition.

5.5 Simulation results

As explained previously, the simulation was undertaken using a compositional method. As mentioned, the injection is in 10-22-17-16 well, with BHP~4.9 MPa for a five-year period. The geomodel has 1 km*1 km dimension, so the boundary of the geomodel was considered to be as unlimited and open boundary for a reliable and accurate results of the simulation. In the unlimited and free boundary, the pressure increase due to injection may transfer out of geomodel without any effect inside the reservoir.

Figure 5-11 (pressure during injection) and Figure 5-12 (gas plume during the injection) are the result of the simulation. The plume size after five-year injection is 184 m*10.6 m.

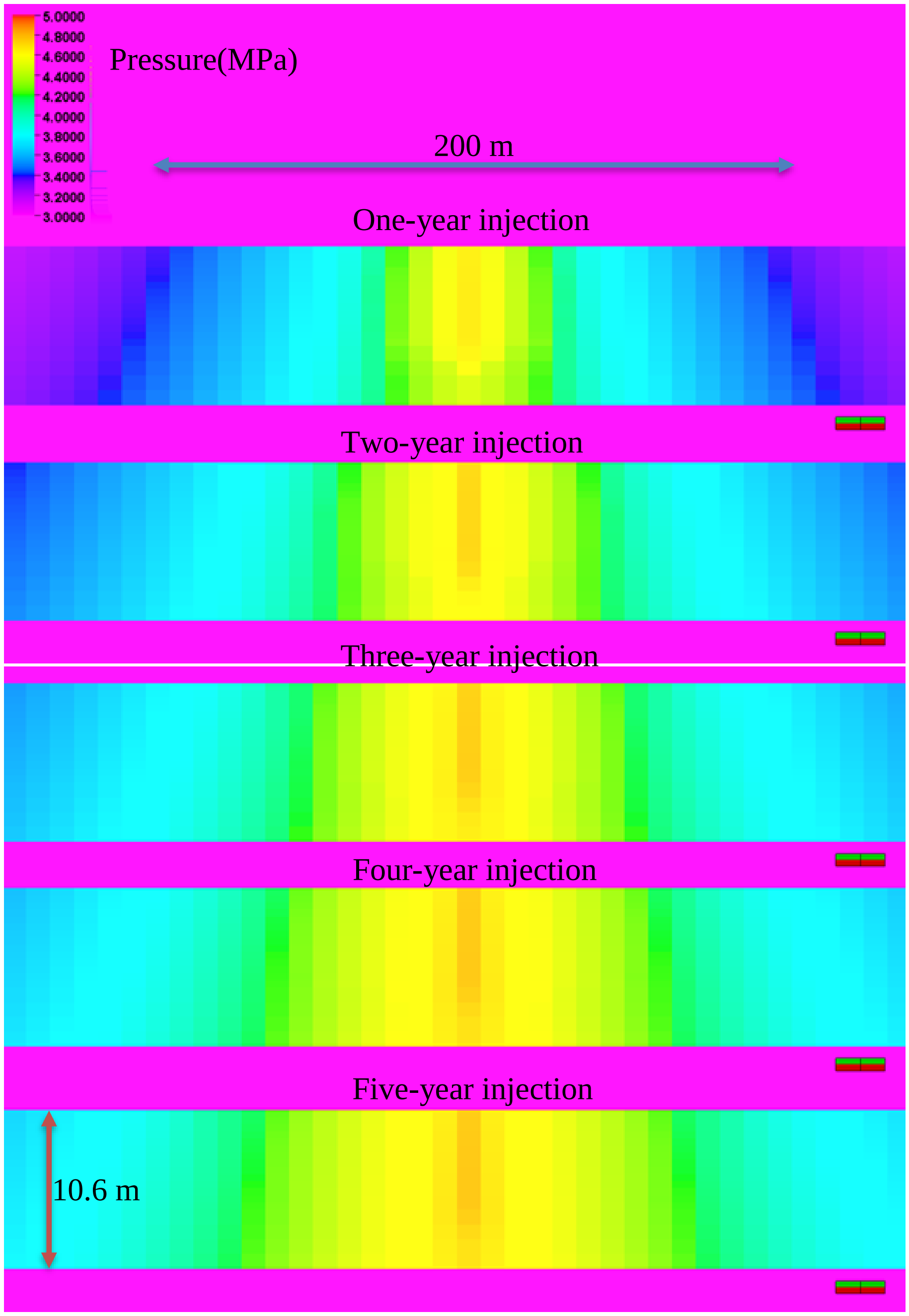

Figure 5-11.The simulation result for the reservoir pressure by the CO_2 injection for five years with BHP=4.9 MPa. The scale is same as Figure 5-12.The unit for the pressure is MPa.

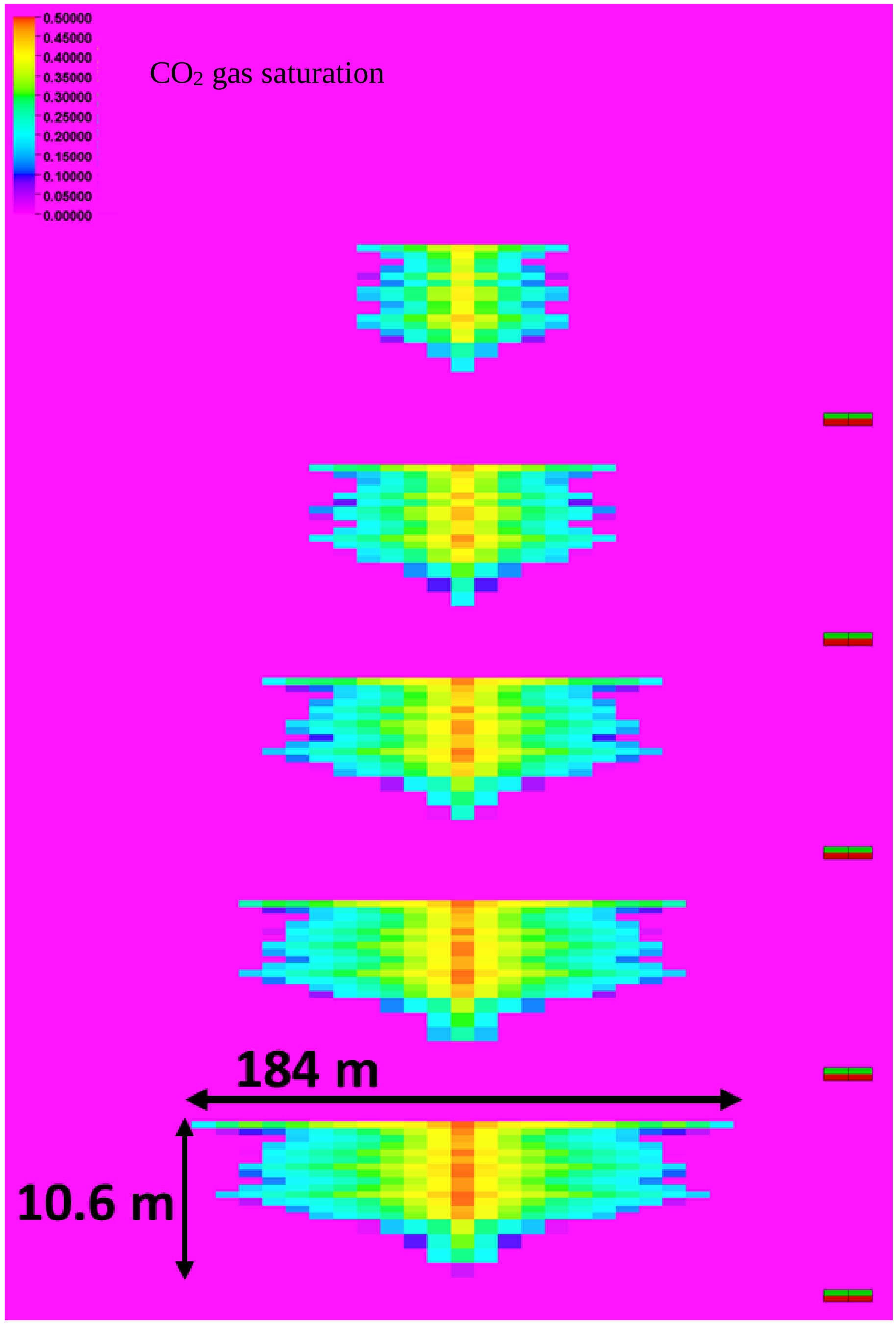

Figure 5-12. The CO_2 gas saturation for the five-year injection by BHP=49 bar (4.9 MPa)

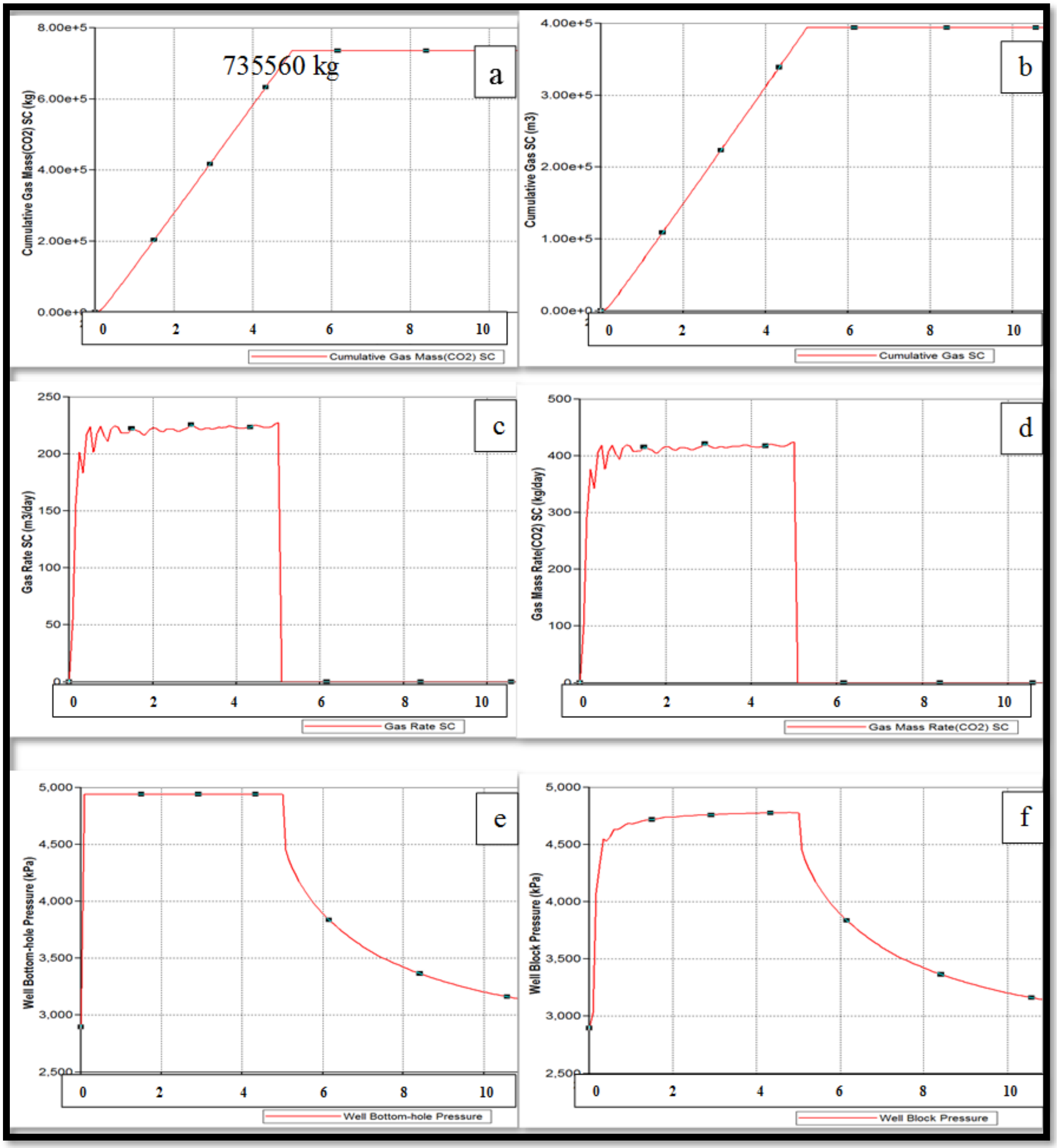

Figure 5-13: Diagrams showing the result of injection for BHP=49 bar for five years (the x-axes show the year of injection) a. Cumulative gas mass (kg), b. Cumulative gas volume (m^3), c. Daily volume (SC) injected gas rate (m^3/day), d. Daily mass injected gas rate (kg/day), e.Well bottom hole pressure (kPa), f. Well block pressure (kPa), (SC stand for Standard Condition - 15ºC and 1 bar).

5.6 The CO_2 gas injection effect on fluid phase in the reservoir

CO_2 gas injected into the brine can have some effects in the reservoir. The mechanisms that may occur during the injection include:

1- Evaporation of brine into the CO_2. The evaporation can increase salinity in the water and make a new phase in the reservoir (vapor water phase). Also, this effect can decrease the value of the immiscible water near the injection zone.

2- In a brine with a high amount of dissolved salt a desiccation can convert salt to a crystalline form. It can reduce the porosity and permeability and so the injectivity (Figure 5-14).

The drying-out effect can change the simulation parameters during the injection process. The simulation software does not consider the alteration of the parameters in the drying-out zone. For controlling the permeability loss due to salt precipitation near the well, injecting a slug of fresh water before the commencement of CO_2 injection can be a solution (Karsten et al. 2009).

Figure 5-14.Results of visual inspection of the brine+CO_2-reacted sample; deposits of NaCl crystals (salt precipitation) and calcite dissolution textures at the outer surface of the sample in a lab test (Rathnaweera et al., 2016).

The gas injection also causes a pressure change in the reservoir. The pressure can have a direct effect on the permeability of the gas (Rathnaweera et al., 2016). For a high-pressure change in the reservoir, the CO_2 permeability variation during the injection procedure is not negligible, and so it should be considered in the fluid simulation.

5.7 Injection with different BHP

In this section, the behavior of the CO_2 plume is studied for different injection pressures.For this purpose, the BHP equal to 48, 51.41, 53.42 bar were simulated.Due to the fast pressure changes in the reservoir, it can be possible to inject the of CO_2 in liquid phase, and by decreasing the pore pressure, the phase change from liquid to gas will happen.However, the current simulation software does not support the phase change conditions at low pressure and temperature so the simulation results may be biased. Figure 5-15 shows the five-year injection for the BHP=4.8 MPa (48 bar). As a result, the cumulative gas mass in each case were obtained and it introduced an exponential function between cumulative mass and BHP as shown in Figure 5-44.

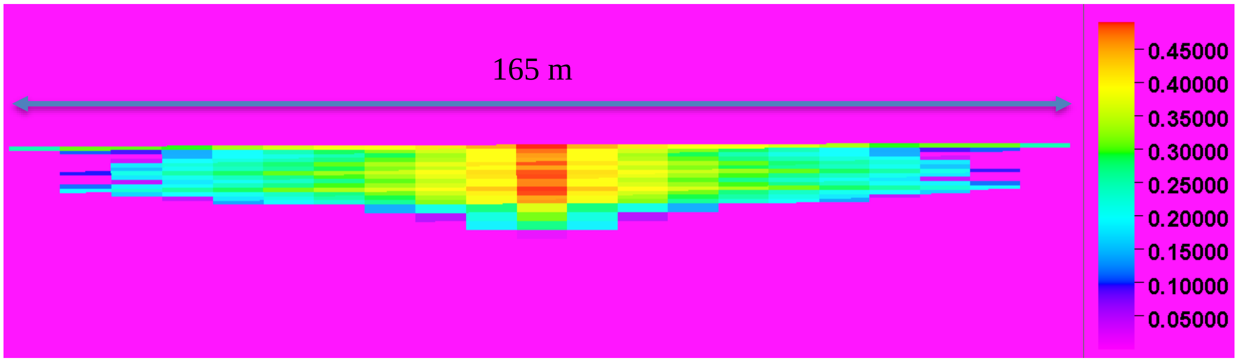

Figure 5-15. Gas saturation after five-year injection with BHP=48 bar.

5.8 Long-term prediction

The reservoir modelling process was continued for a century to observe the CO_2 plume behavior (after stopping the injection). As the expectation, during the monitoring, the gas plume migrates to the top of the reservoir and it makes a high saturation plate in the top layer (saturation can reach up to the reservoir efficiency value that is equal 0.5 in this type of sandstone (Bachu,2013)). The results of the fluid simulation are demonstrated in Figure 5-16 through Figure 5-23 for up to 100 years post-injection. Figure 5-24 is the pressure variation for a long-term prediction. It shows the reservoir pressure reduces to the initial value after 28 years from the first injection day. The pressure will fall after stopping injection, and after 23 years, it will decrease to the initial reservoir pressure.

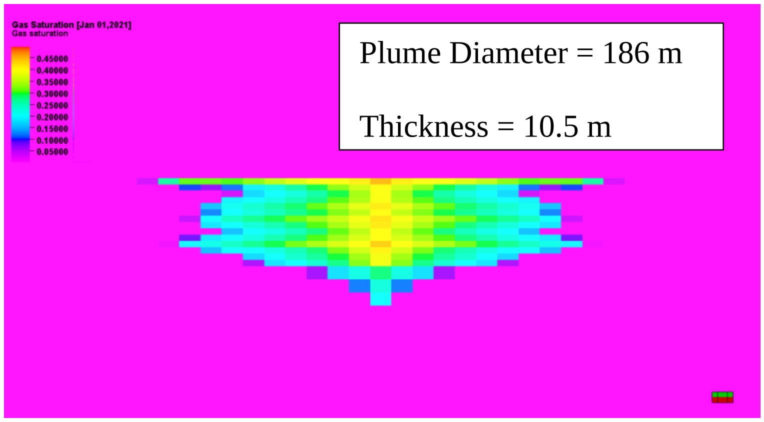

Figure 5-16.The saturation after five-year injection by constant BHP.

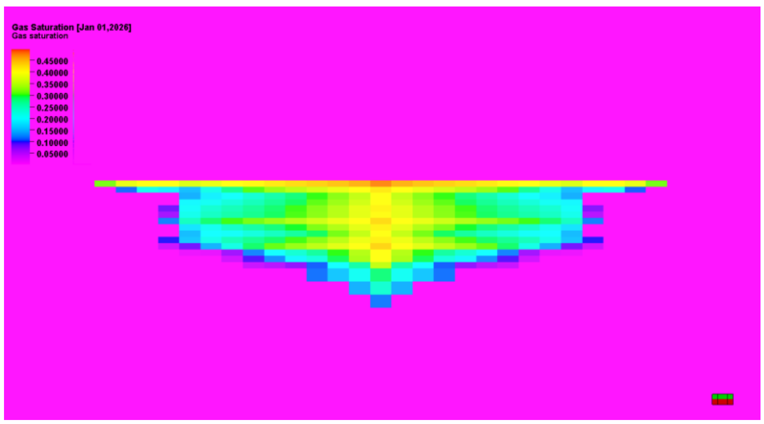

Figure 5-17. Predicted CO2 saturation five years after discontinuing the injection

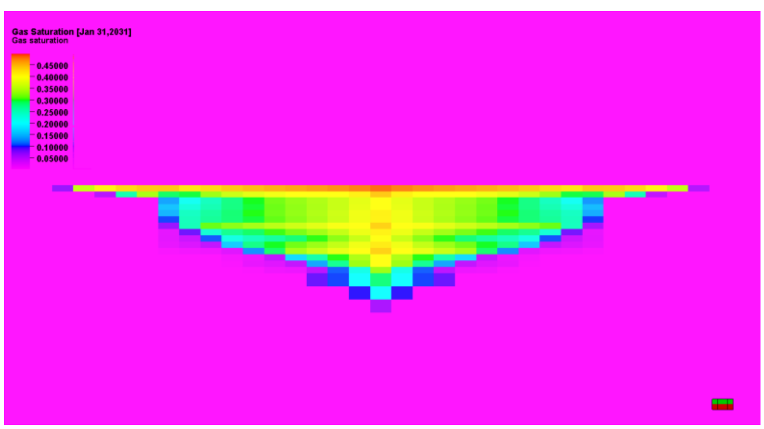

Figure 5-18. Predicted CO2 saturation ten years after stopping the injection

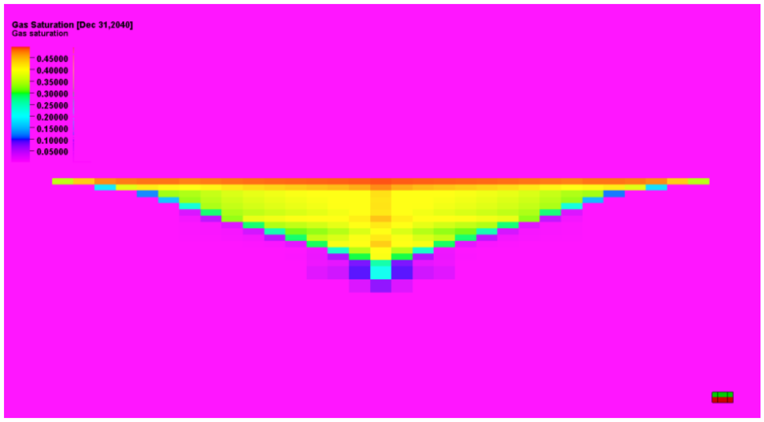

Figure 5-19. Predicted CO2 saturation 20 years after stopping the injection

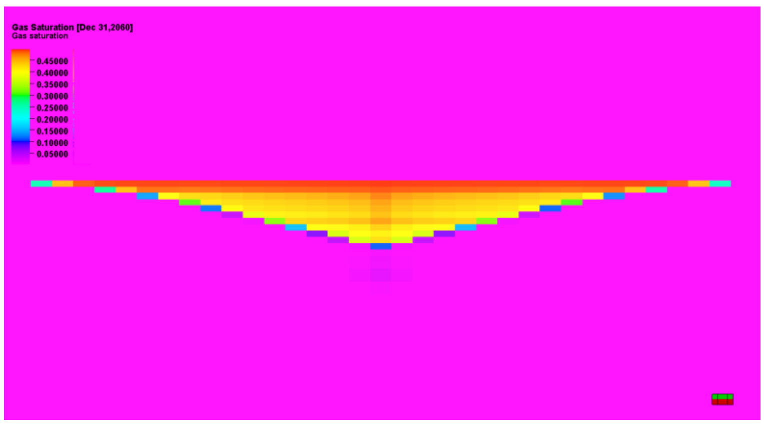

Figure 5-20. Predicted CO2 saturation 40 years after stopping the injection

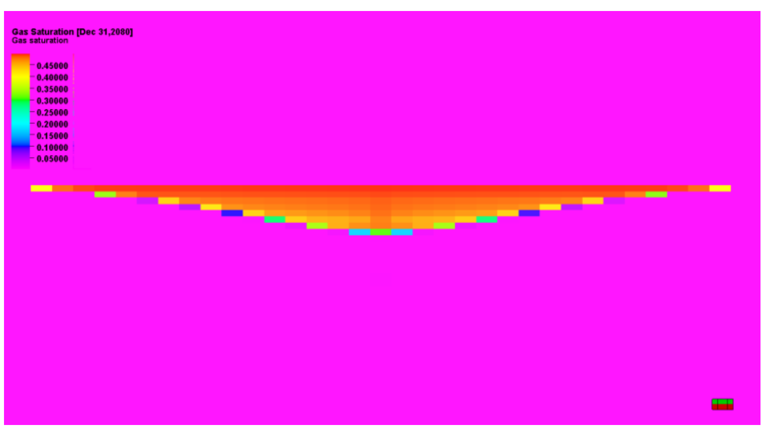

Figure 5-21. Predicted CO2 saturation 60 years after stopping the injection

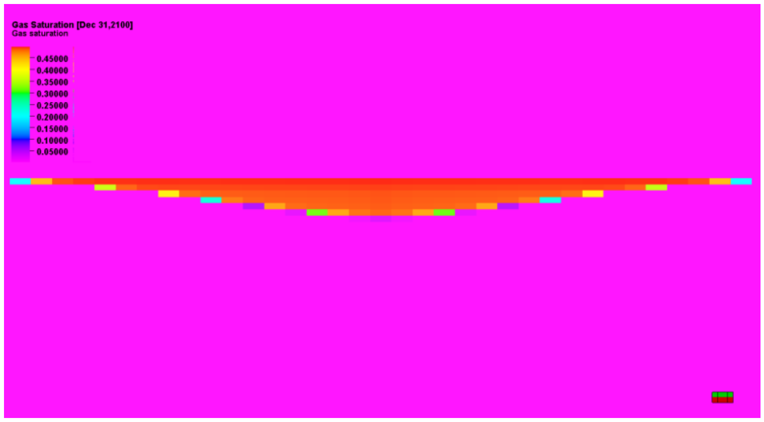

Figure 5-22. Predicted CO2 saturation 80 years after stopping the injection

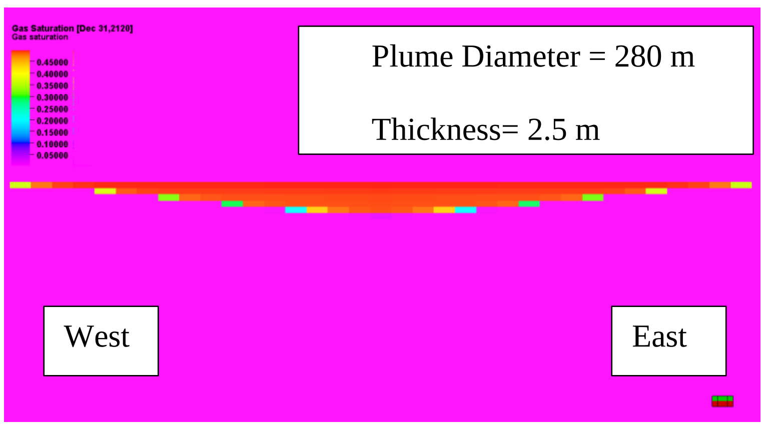

Figure 5-23. Predicted CO2 saturation 100 years after stopping the injection

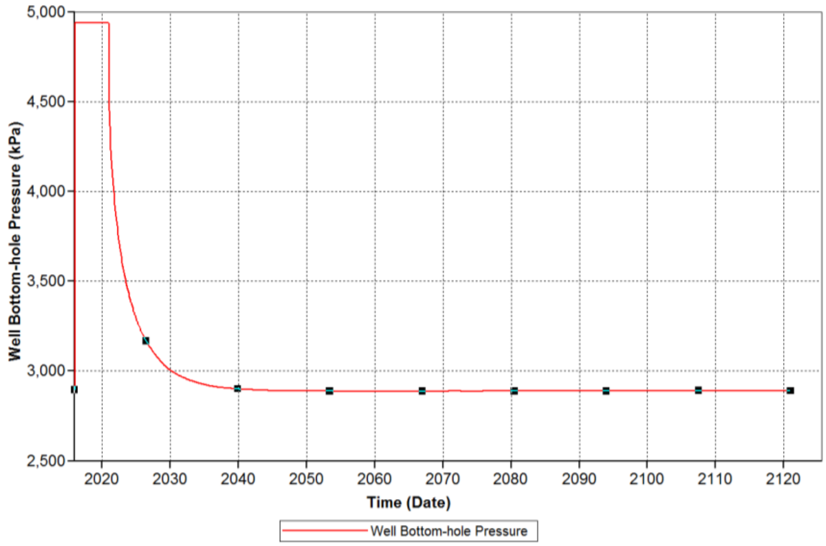

Figure 5-24. The Bottom-hole pressure changes over a century. The pressure will be equal to initial reservoir pressure after the year 2044 (28 years after beginning the injection process).

5.9 Conservation of CO_2 mass after stopping the injection

After five years' injection, the mass of CO_2 will be constant in the reservoir. If the injected CO_2 mass is considered to be equal M, so based on the cells porosity, saturation and the pressure of the reservoir, it can be explained using the following formula:

$$C_t = \sum_{i=1}^{n} M_i(t)$$

Eq. 5-15

That M is CO_2 mass in a cell as a function of time (t), and n shows the cells number with CO_2 saturation more than zero and C is a constant value.

For a cell, M_i be explained as:

$$M_i = \varphi_i s_{iCO_2} V_i \rho_{CO_2}$$

Eq. 5-16

Moreover, so for the entire reservoir:

$$C_t = \sum_{i=1}^{n} M_i = \sum_{i=1}^{n} \varphi_i s_{iCO_2} V_i \rho_{CO_2}^{(T,P)}$$

Eq. 5-17

Where: $V_i = x_i y_i z_i$ and x, y and z are the three dimensions of each cell.

This formula can help to predict the expansion of CO_2 plume in a sealed reservoir after stopping the injection procedure (if the gas solution in the brine and chemical reaction between minerals, CO_2, and carbonic acid is ignored). The prediction will be near the real fluid simulation result after a long time (stabilization time). This time is a function of pressure, temperature, and permeability.

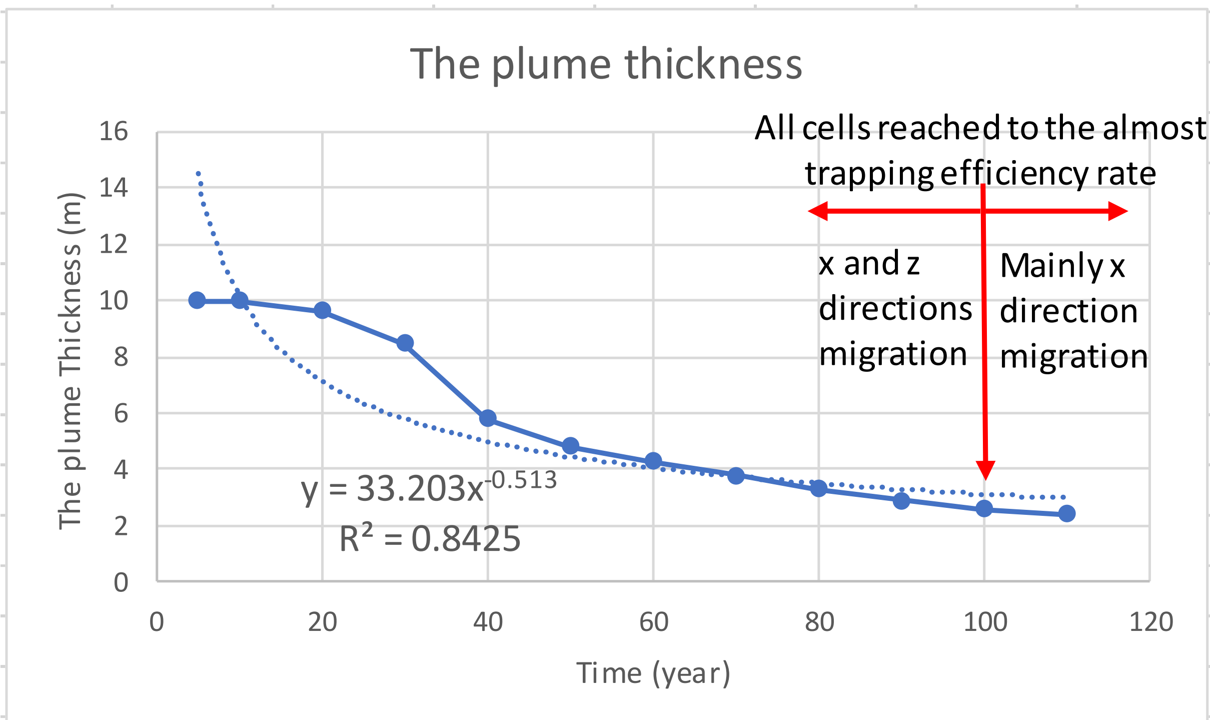

Figure 5-25.The thickness of the plume in the injection point after stopping the injection. After 100 years, all cells in the plume show a saturation rate around the trapping efficiency, and so continued gas migration will change to a mainly horizontal direction.

As mentioned previously, the plume size is a function of the permeability vector in the xy and z directions. The plume thickness at the injection point decreases after stopping the injection as the gas migrates to the higher levels in the reservoir. This decreased rate after stopping the injection is an exponential function of time that is unique for each reservoir. For the FRS reservoir in the Basal Belly River sandstone zone, it is illustrated in Figure 5-25 that shows a good fit after 40 years. The form of the CO_2 gas plume is like an inverted cone because of gas density and gravitation effect. So, the average thickness of the plume can be explained as half as the central thickness. The relation between time and the plume thickness is an exponential function.

$$
\begin{aligned}
Z_a &= \frac{Z_{center}}{2} \\
Z_{center} &= 33.2 * t^{-0.513} \\
Z_a &= 16.6 * t^{-0.513}
\end{aligned}
$$

Eq. 5-18

that Z_a is average thickness and Z_{center} is the thickness of the plume in the injection point, and t is time after stopping the injection.

To test the equations Eq. 5-15 to Eq. 5-18, I simulated the fluid behavior for injected CO_2 for 233 years. The result is shown in Figure 5-26**.** The central thickness of the plume after 233 years of the injection day can be determined by the function fitted to the curve in Figure 5-25 and Eq. 5-18 is 2 m, and the average plume thickness is 1 m.

V= 32 m^3 (the size and volume of each cell in the reservoir)

φ = 16 % (for the top layer, the porosity is the same in all cells in a layer)

S= 52% (the maximum possible CO_2 saturation by considering the trapping efficiency)

ρ_{CO_2} =69.555 kg/m^3 (@13^{o}C and 30 bar) (after stopping the injection the pressure drops to the reservoir's natural pressure that is around 3 MPa (Figure 5-13.e)).

$\sum_{i=1}^{n} M_i = M_t$ = 735560 kg (see Figure 5-13.a.)

So, for similar cells size Eq. 5-17 can be explained by Eq. 5-19:

$$\sum_{i=1}^{n} M_i = \sum_{i=1}^{n} \varphi_i S_{iCO_2} V_i \rho_{CO_2}^{(T,P)} = N\varphi S_{CO_2} V \rho_{CO_2}^{(T,P)}$$

Eq. 5-19

That N shows the number of uniform cells.

With the available data in this project, Eq. 5-19 can be used to calculate number of cells with CO_2 gas inside:

32*0.16*0.52*69.555*N = 735560

Finally, the CO_2 will spread in N=3972 cells. If we consider the plume thickness equal to 1 m, the coverage area is a=124006 m^2, equal to 397 m in diameter. It is similar to the simulation result that shows the plume diameter at 376 m.

CO_2 is not completely free gas in the reservoir. The first absorbance is the capability of the CO_2 solution in brine. It is a function of the physical condition of the reservoir and can be described as:

$$M_1=g\ (P, T)$$

The chemical reaction between carbonic acid and the minerals can absorb CO_2 into a solid phase. The amount of this mass is a function of time that can be explained as:

$$M_2=f(t)$$

For a long-term plume size fate, this two absorbance factors should be considered for a better estimation as:

$$\sum_{i=1}^{n} M_i = \sum_{i=1}^{n} \varphi_i S_{iCO_2} V_i \rho_{CO_2}^{(T,P)} - (M_1 + M_2)$$

Eq. 5-20

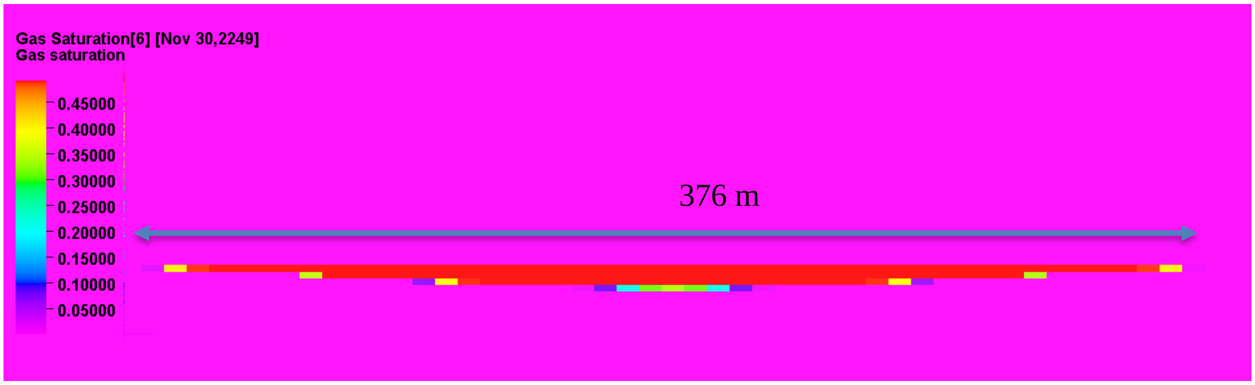

Figure 5-26. The result of long-term monitoring for the gas saturation after 233 years from the start of injection. The maximum plume thickness is 2 m.

5.10 An injection/production pattern for improved gas phase injection

The purpose of the injection in the previous section was the gas phase injection that should not exceed of 49.41 bar @13 ^{o}C (reservoir temperature). Decreasing the pore pressure in the reservoir can increase the mass injection into the porous medium. A brine production plan in a pattern of wells around the injection well can reduce the pore pressure under a phase change condition.

A production well that produces brine from the reservoir level, decrease the pore pressure in the reservoir. Figure 5-27 and Figure 5-28 show the pressure and plume size in the area based on the fluid simulation results for the 10-22 well. Figure 5-29 shows four production wells at a specific distance X meter from the injection well. The plume shape with these production wells will be a function of production rate and the location of the wells.

For increasing the injection rate in the gas phase, a plan could be drill four production wells that remove the brine out of the BBRS aquifer; they can reduce the pore pressure up to 6.5 bar in the reservoir if they locate in 50 m distance of well (10-22). The maximum injection pressure could then increase up to 5.6 MPa (56 bar) in the gas phase. Another advantage of these production wells is estimating real permeability in the directions of the wells. The permeability estimation in four directions could show the possible anisotropy in permeability or fractures around the injection well.

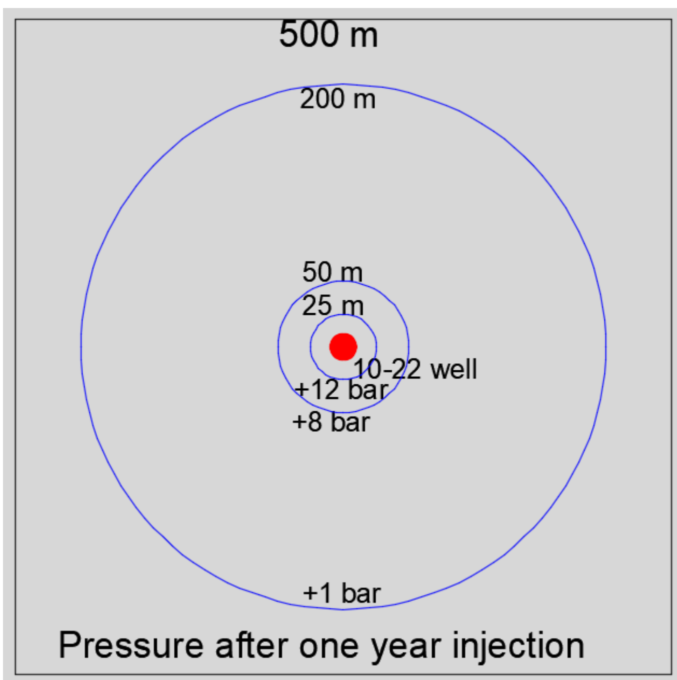

Figure 5-27.The pressure condition in 25,50 and 200 m distance of injection well after one-year injection.

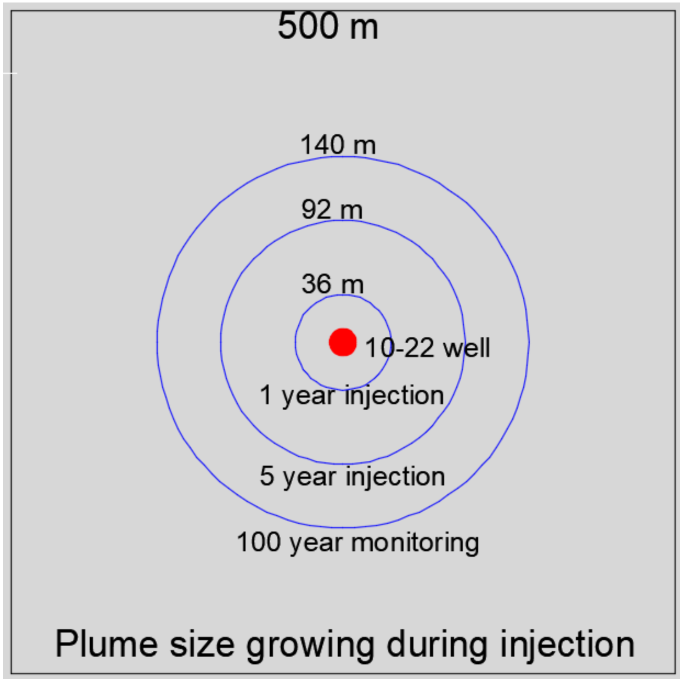

Figure 5-28.The plume size after 1 and 5-year injection and 100-year post-injection.

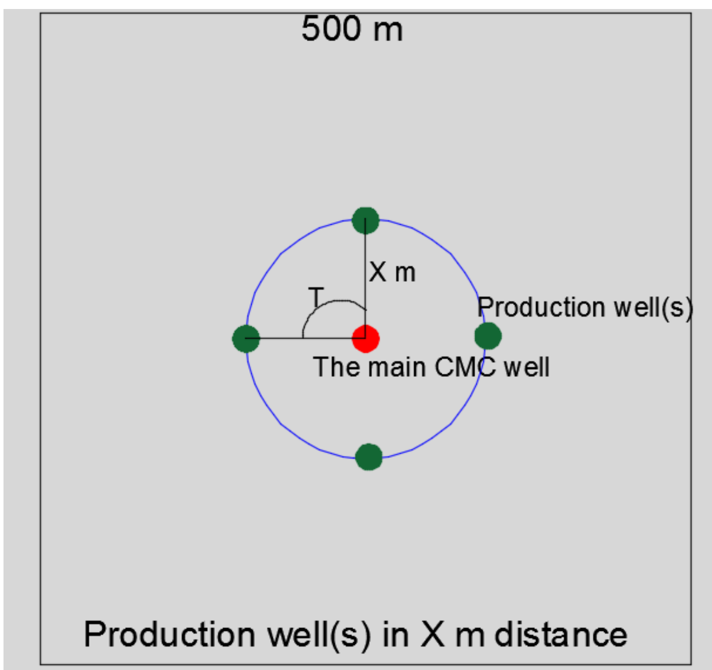

Figure 5-29. The production well(s) in X m distance to decrease the reservoir pressure, it can help to inject more mass in the gas phase. T is the angle between the wells. X, T and the number of wells are variable.

5.11 Injection at higher BHP

As mentioned, the simulation software (ECLIPSE and CMG) do not support a phase change from gas to liquid (it was tested with both software packages). Thus, it is not possible to simulate the CO_2 behavior through a phase change from gas to liquid. The research is just in the gas phase, and for the testing upper pressures, we changed the physical properties to stay in gas phase. For this part, we considered a higher reservoir temperature of 20°C, as makes it possible to increase the BHP to 57.3 bar. The pressures examined were 5.141, 5.341, 5.541 and finally 5.73 MPa at 20°C. This maybe the case of the reservoir temperature around the well is increased by heating the CO_2. The results are described in the following pages as Table 5-2.

Table 5-2. The different BHP and related figures.

BHP(bar)	Plume After a year injection	Plume After 5-year injection	Plume After ten years of stopping injection	The Cumulative Gas Mass	The Cumulative Gas Volume
51.41	Figure 5-30. a.	Figure 5-30. b.	Figure 5-30. c.	Figure 5-32.	Figure 5-33.
53.41	Figure 5-34. a.	Figure 5-34. b.	Figure 5-34. c.	Figure 5-35.	Figure 5-36.
55.41	Figure 5-37. a.	Figure 5-37. b.	Figure 5-37. c.	Figure 5-38.	Figure 5-39.
57.3	Figure 5-40. a.	Figure 5-40. b.	Figure 5-40. c.	Figure 5-41.	Figure 5-42.

Figure 5-31 shows the reservoir pressure simulation result for the BHP=5.141 MPa. The pressure drops after stopping the injection (Figure 5-43). Also, Figure 5-44 shows the final summary of the cumulative mass injection for the different BHP @20°C. An exponential function explains the mass injection value as a function of BHP in the FRS project as predicted by Eq. 5-21.

$$\text{Total injected } CO_2 \text{ Mass} = 24.613e^{0.0689BHP}$$

Eq. 5-21

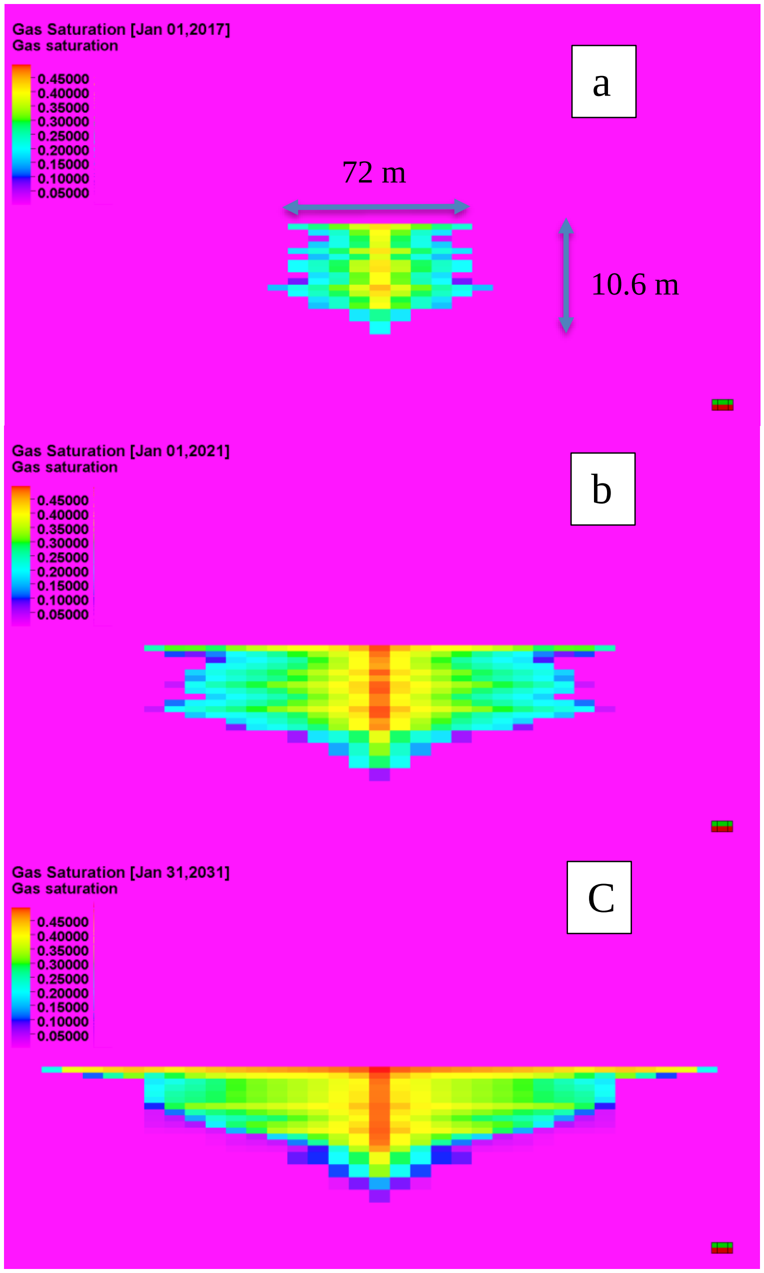

Figure 5-30. CO_2 saturation at pressure of 51.41 bar @ 20°C. (a). after one-year injection(2017), (b). after five-year injection(2021), (c). after ten years of stopping the injection(2031).

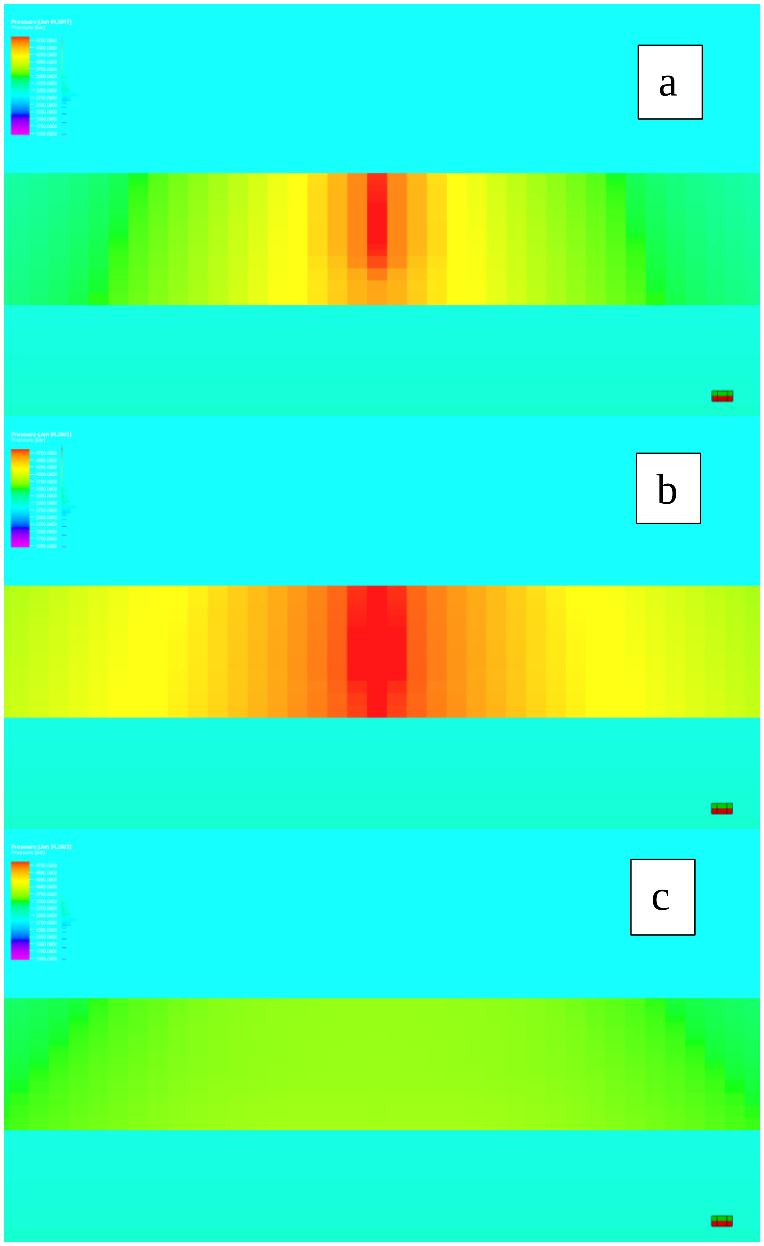

Figure 5-31.The pressure change in the reservoir for BHP=51.41 bar and temperature =20^{o}C, (a). one year after injection, (b). Five-Year injection, (c). Two years after stopping the injection.

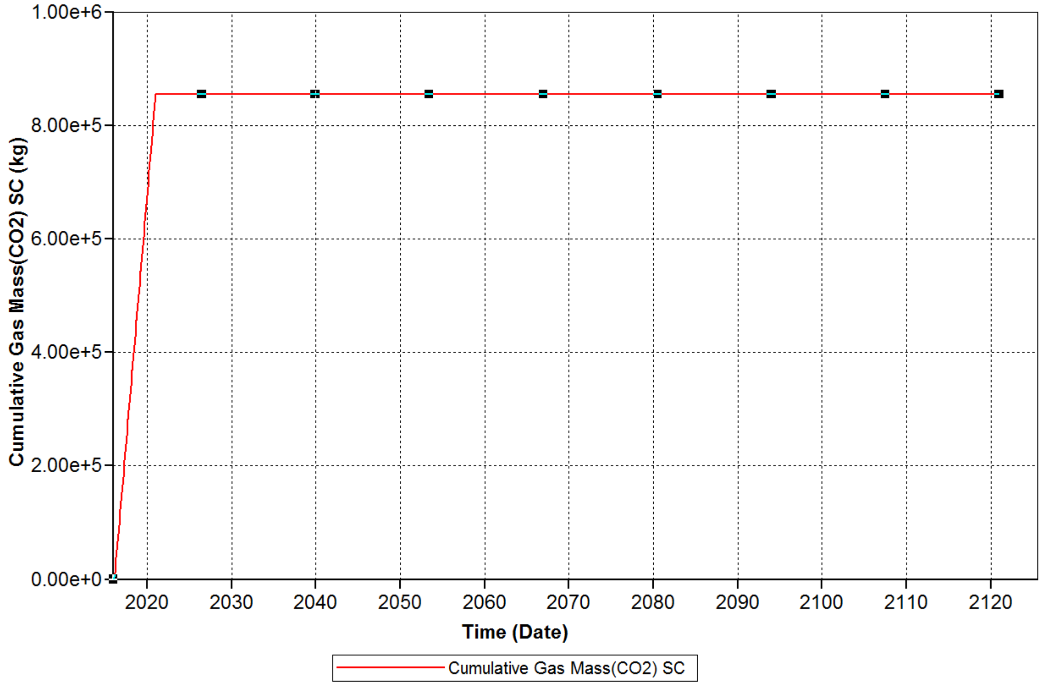

Figure 5-32.The cumulative gas mass (kg) injected at the constant BHP=51.41 bar.

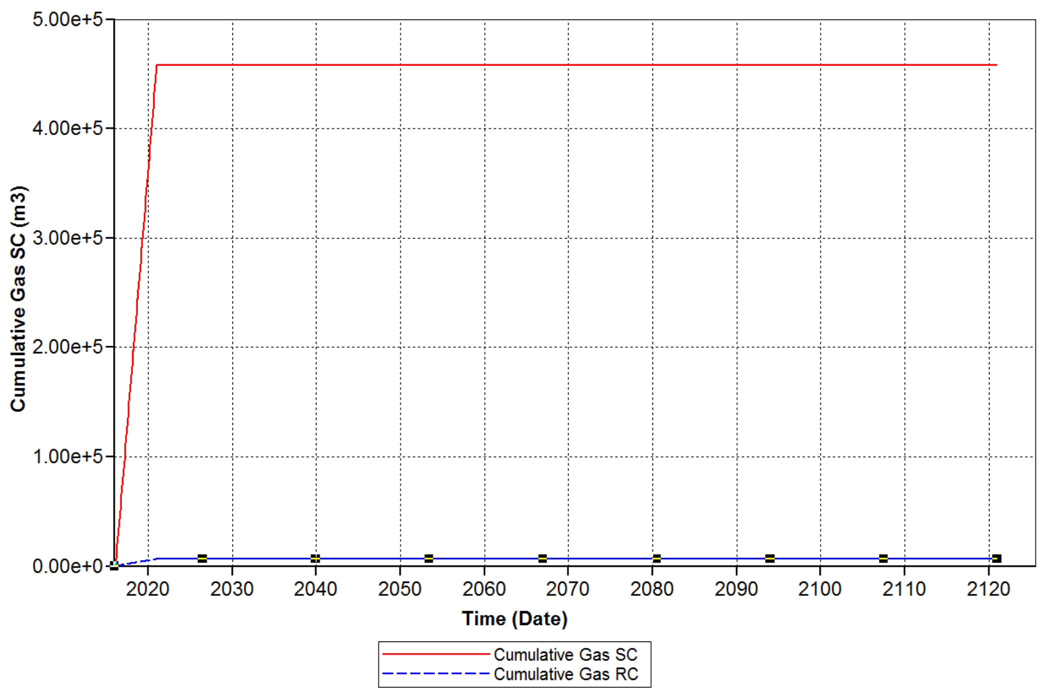

Figure 5-33.The cumulative gas volume (m^3) in the standard condition (red graph) and the reservoir condition (blue graph) injected at the constant BHP=51.41 bar.

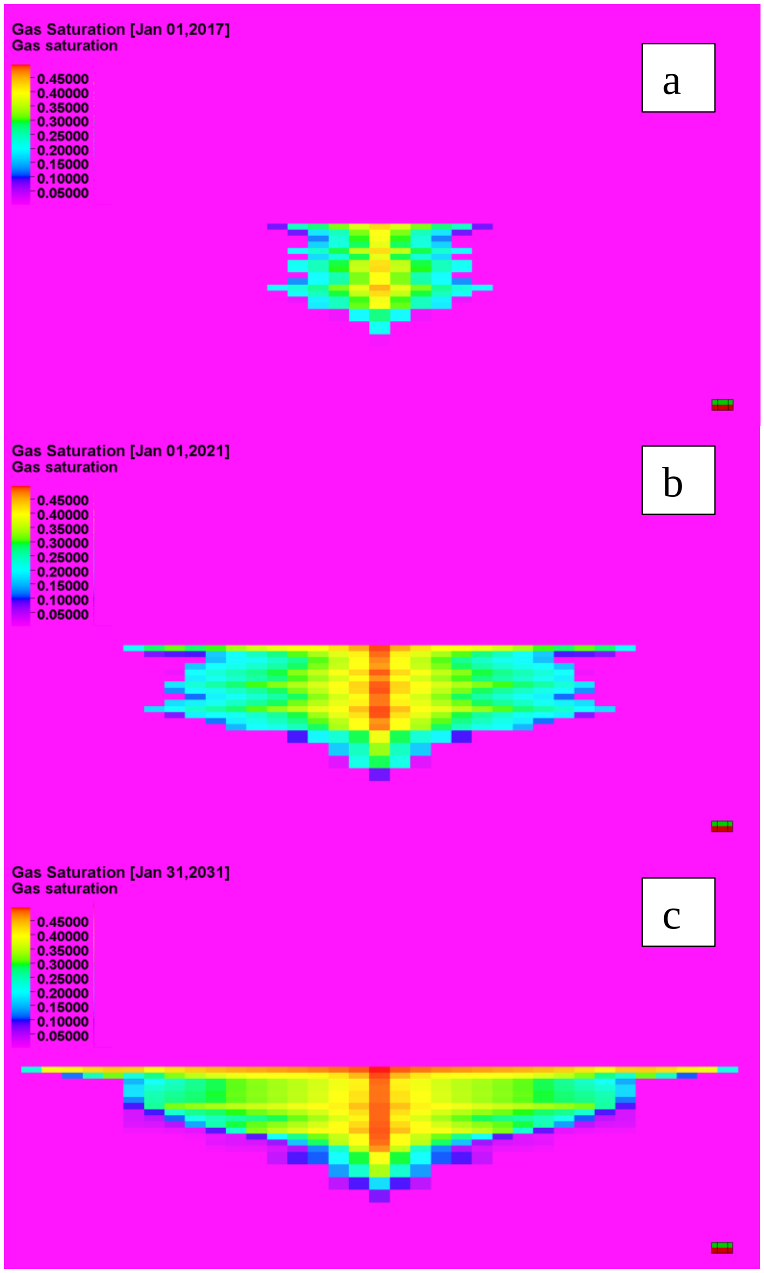

Figure 5-34. CO_2 saturation at pressure of 53.41 bar @ 20°C. (a). after one-year injection(2017), (b). after five-year injection(2021), (c). after ten years of stopping the injection(2031).

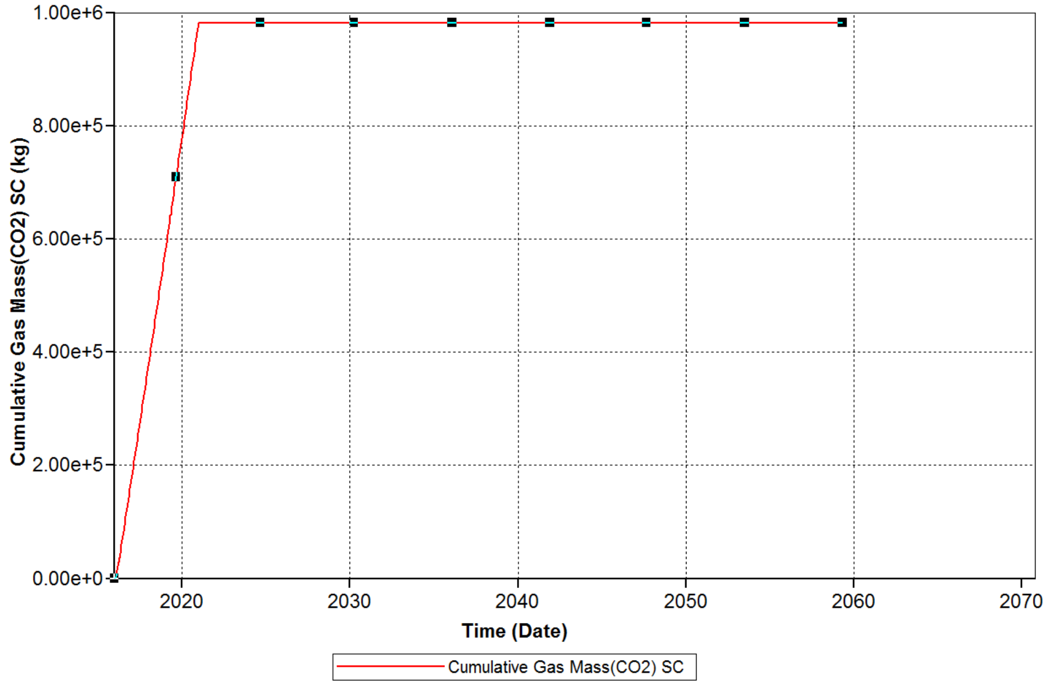

Figure 5-35. The cumulative gas mass (kg) injected at the constant BHP=53.41 bar

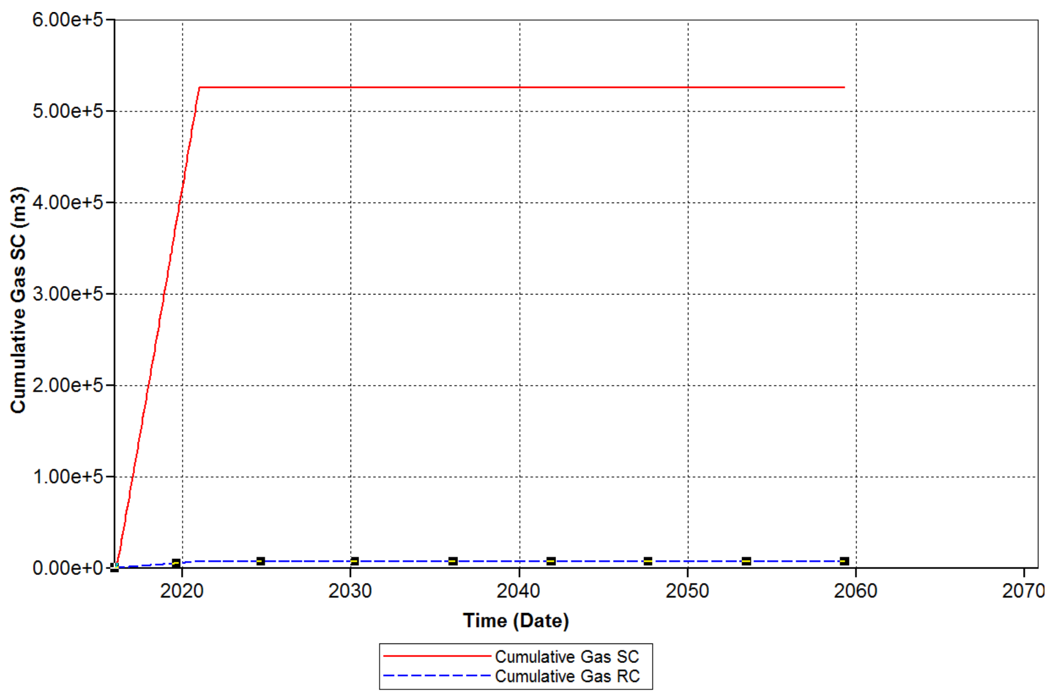

Figure 5-36. The cumulative gas volume (m^3) in the standard condition (red graph) and the reservoir condition (blue graph) injected at the constant BHP=53.41 bar

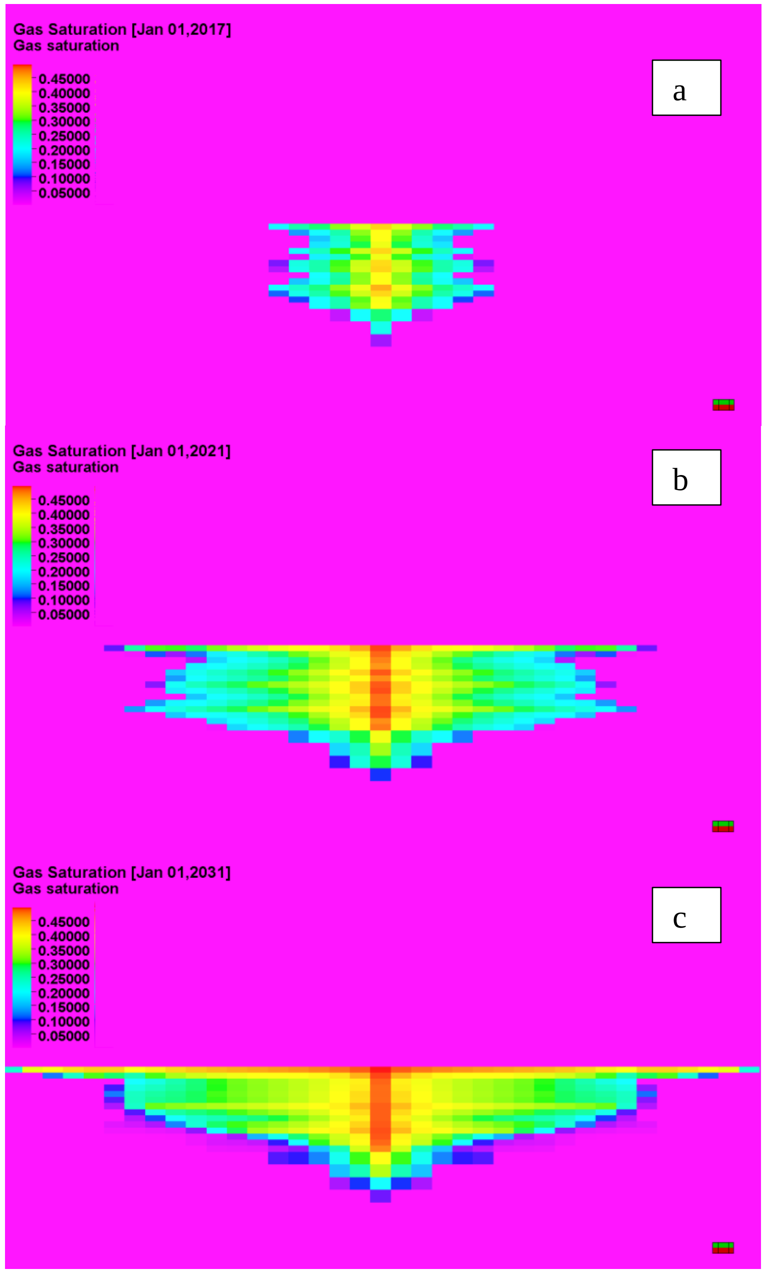

Figure 5-37. CO_2 saturation at pressure of 55.41 bar @ 20°C. (a). after one-year injection(2017), (b). after five-year injection(2021), (c). after ten years of stopping the injection(2031).

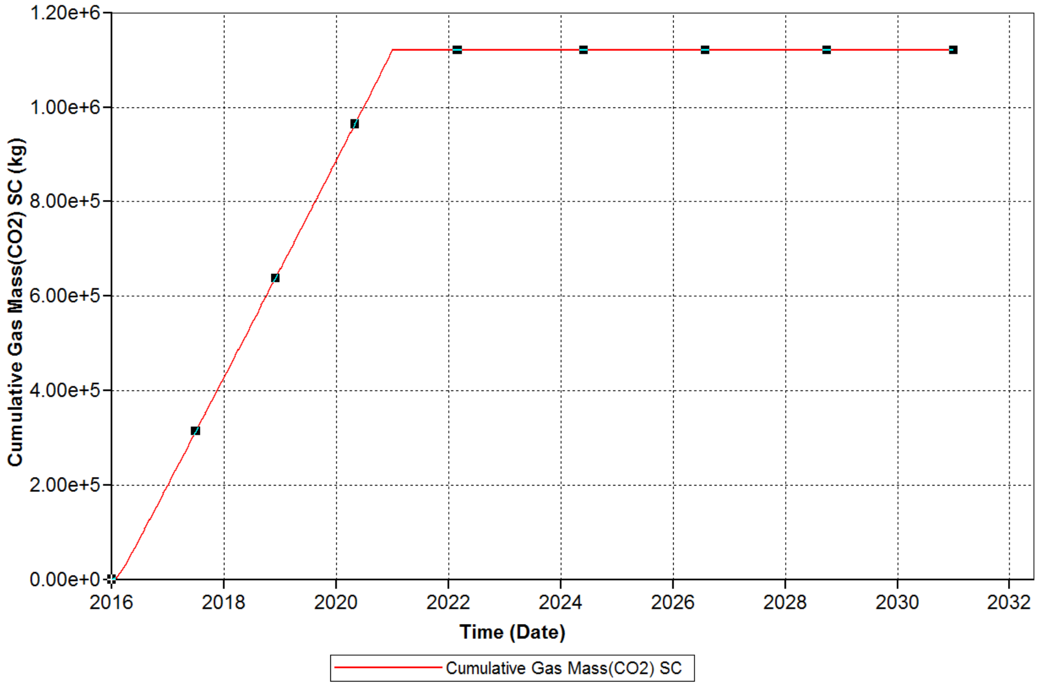

Figure 5-38. The cumulative gas mass (kg) injected at the constant BHP=55.41 bar

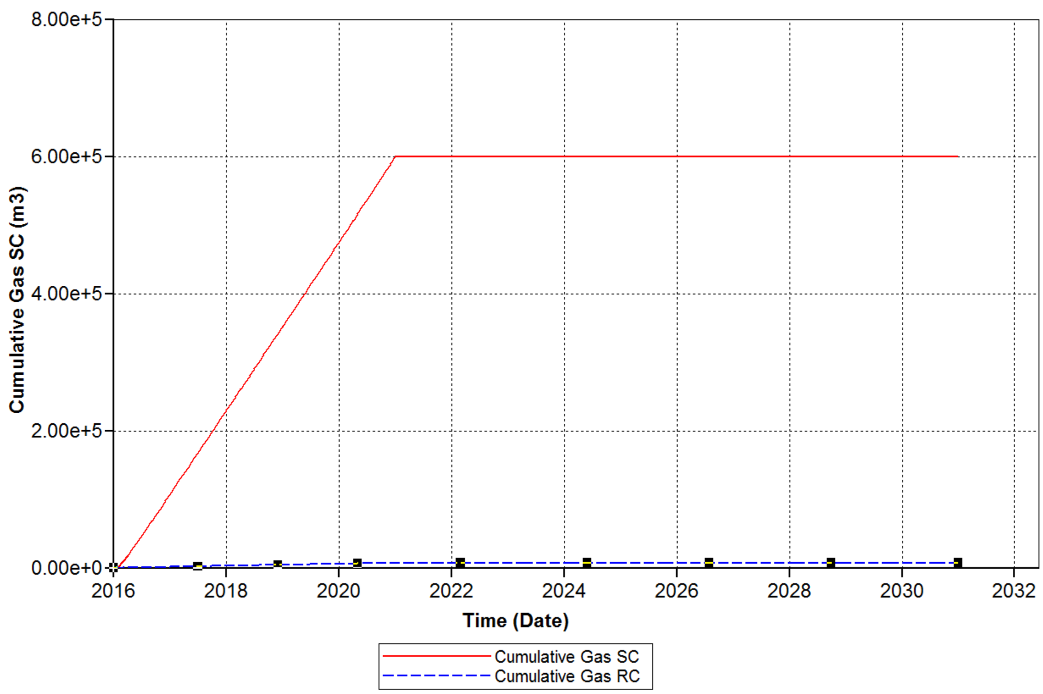

Figure 5-39. The cumulative gas volume (m^3) in the standard condition (red graph) and the reservoir condition (blue graph) injected at the constant BHP=55.41 bar

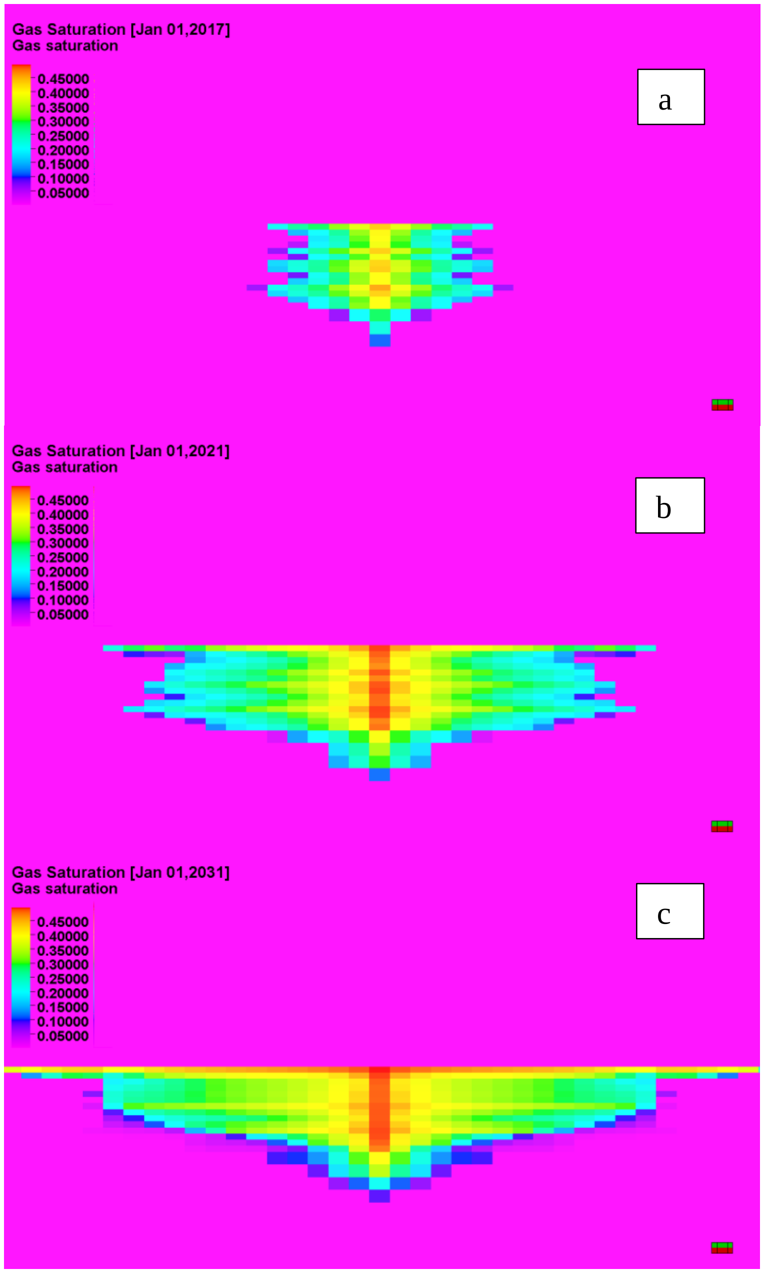

Figure 5-40. CO_2 saturation at pressure of 57.41 bar @ 20°C. (a). after one-year injection(2017), (b). after five-year injection(2021), (c). after ten years of stopping the injection(2031).

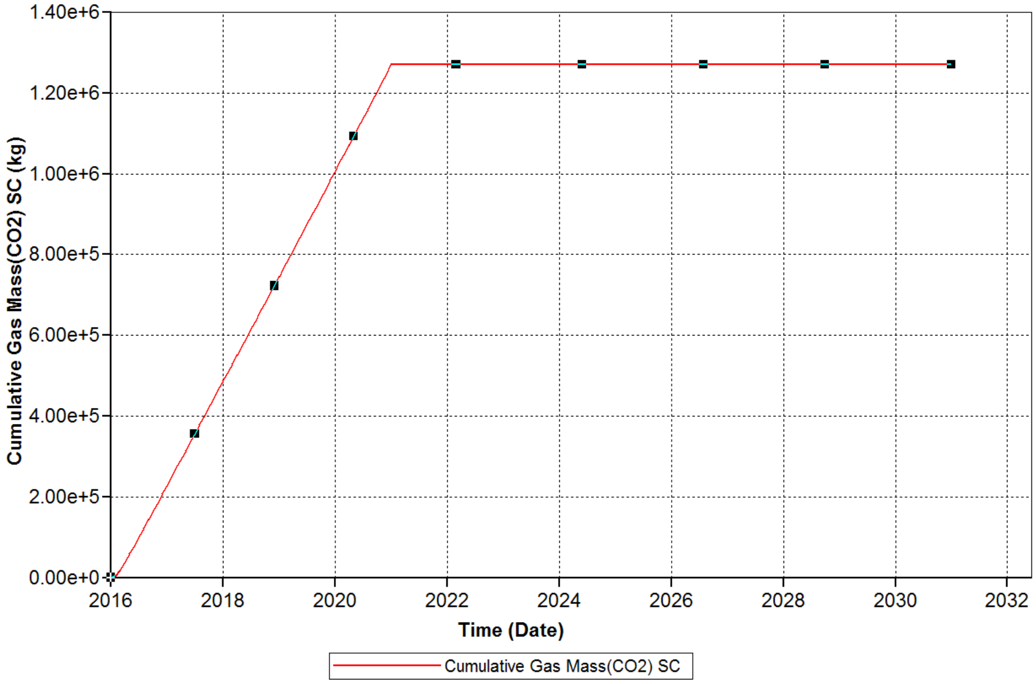

Figure 5-41. The cumulative gas mass (kg) injected at the constant BHP=57.3 bar

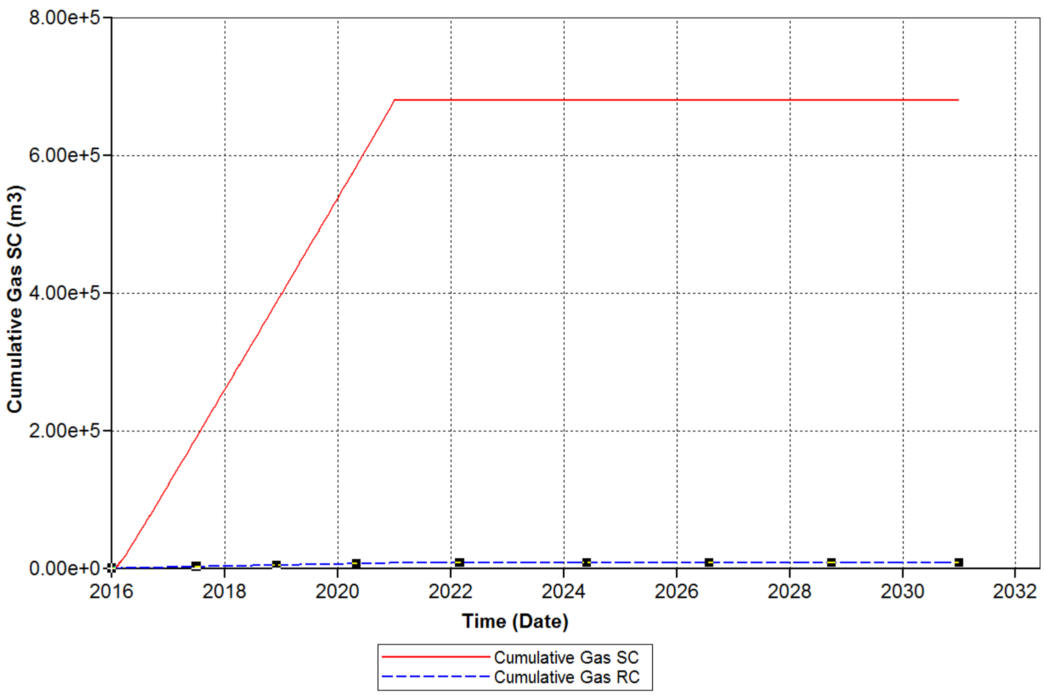

Figure 5-42. The cumulative gas volume (m^3) in the standard condition (red graph) and the reservoir condition (blue graph) injected at the constant BHP=57.3 bar

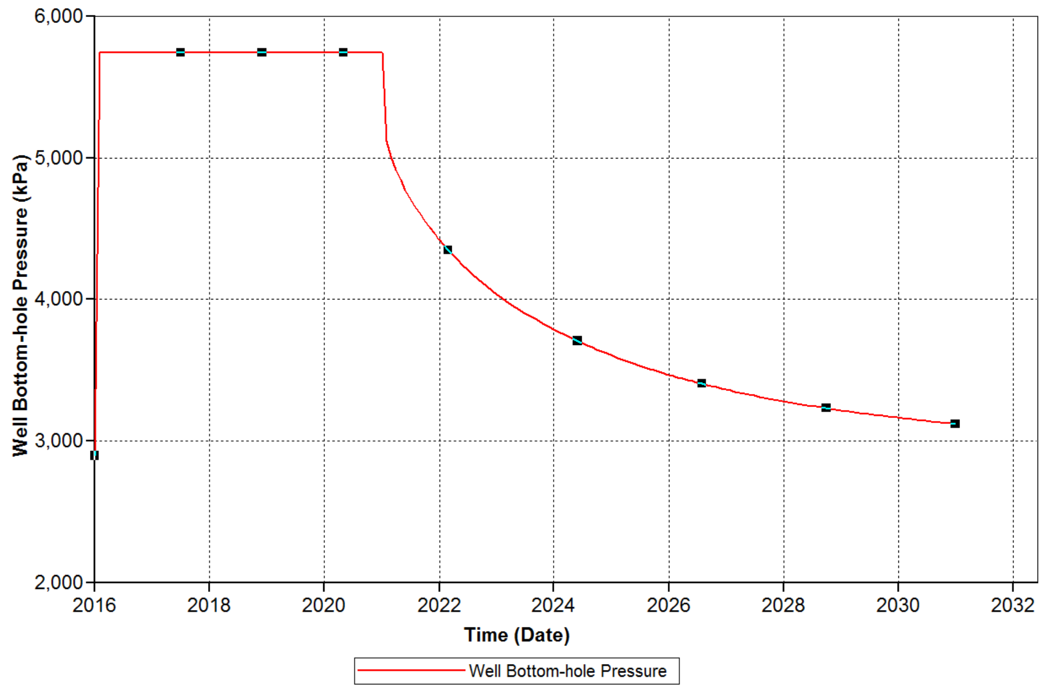

Figure 5-43. The pressure over 5 years of injection at BHP=57.3 bar (5.73 MPa), and 10 years after injection.

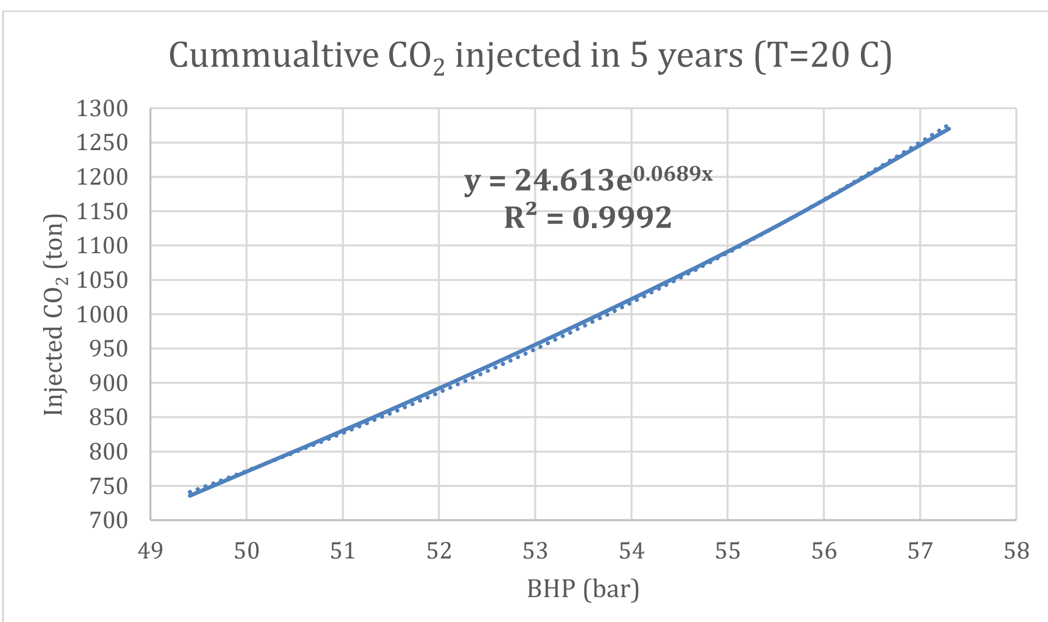

Figure 5-44. Cumulative CO_2 mass for different BHP for a five-year injection plan. An exponential function describes the relation between BHP and injected gas mass.

Chapter 6. Rock physics study for the FRS project

6.1 Introduction

This chapter engages rock physics to calculate physical parameters of the formation, the fluid and rock matrix in the reservoir due to CO_2 injection into the aquifer. Rock physics is a bridge between seismic data and reservoir properties that integrate geological uncertainties. The output and the primary results of reservoir simulation are the distribution of pressure and saturation. Fluid substitution formulas and Gassmann's equation are a part of rock physics studies about the effects of fluid changes on the bulk modulus and consequently on the seismic velocity in the formation. It was first introduced and discussed by Gassmann (1951), and provides a base equations of fluid substitution in rock physics.

The density and seismic wave velocities in a fluid is a function of the pressure and temperature. For the physical properties of CO_2, work by Span-Wagner (1996) was used and, Batzle and Wang (1992) provided the physical properties of the brine. In the reservoir, the fluid is a mix of various fractions of CO_2 and brine, and the velocity of the formation is a function of the CO_2 saturation value and the mixed fluid condition of brine and the gas. Finally, the seismic velocity variation in the reservoir is determined from the different mixed fluids.

Gassmann's equations were used for estimating the saturated bulk modulus in the formation after injecting the CO_2 gas. As the CO_2 gas saturation is obtained from the reservoir simulation, the velocity of each cell in the reservoir model is determined from the rock physics calculations, so each cell has physical properties as a function of the pressure and the injection time.

The workflow for the seismic parameter estimation over the injection period are:

1. Reservoir fluid simulation for CO_2 injection at constant bottom hole pressure rate in the target formation, using a compositional simulation method.

2. Input all property values (depth, porosity, saturation,) from log data, geomodel, and fluid simulation results.

3. Calculate the initial mineral bulk modulus with the different mineral composition for the target sandstone in Belly River sandstone. The detailed mineralogy study as described previously in section 2.5.

4. Use Batzle-Wang and EoS equations to calculate bulk modulus and density for brine water and CO_2 and mix fluid in each cell.

5. Calculate the initial bulk modulus (K_{sat}) for saturated rock (before injection) by using log data and P-wave velocity data.

6. Estimate the saturated bulk modulus and P-wave velocity for each cell during injection.

Figure 6-1 is a brief flowchart shows the work flow for the velocity and density estimation in the formation after the gas injection, described in this chapter.

6.2 The complexity of a solid or fluid

Rocks and fluids in nature are not homogeneous, isotropic and mono component. Figure 6-2 is a polarizing microscopic image of sandstone in which each color represents a different mineral. It shows a mixing medium of minerals that formed the rock. In the reservoir characterisation, we need to have a realistic estimation of physical properties of the mixed fluid and solid part and together as the formation properties. For calculating the physical properties (such as elastic modulus) of a mix (in solid or liquid phase), some methods and equations are introduced.

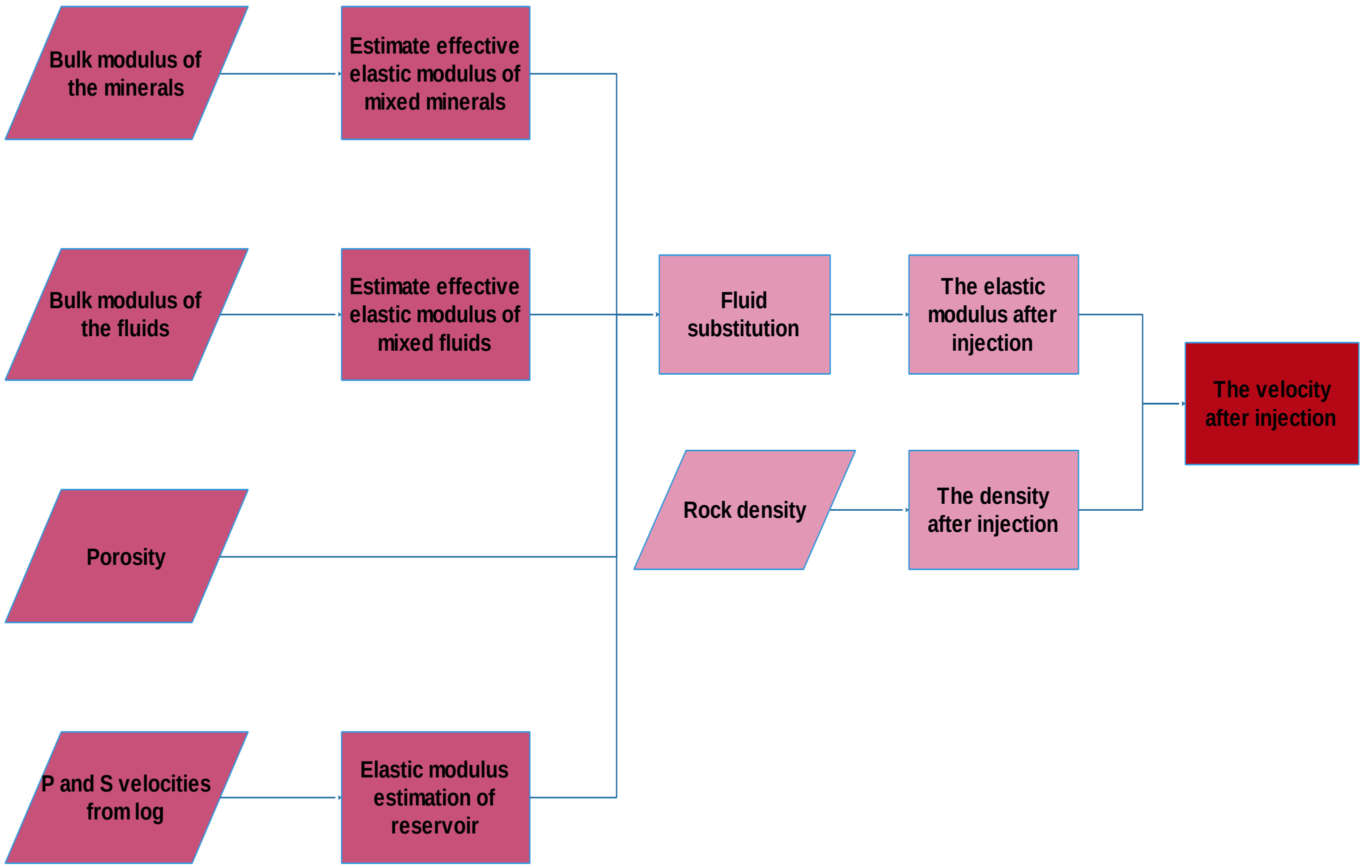

Figure 6-1. The fluid substitution procedure used in this chapter.

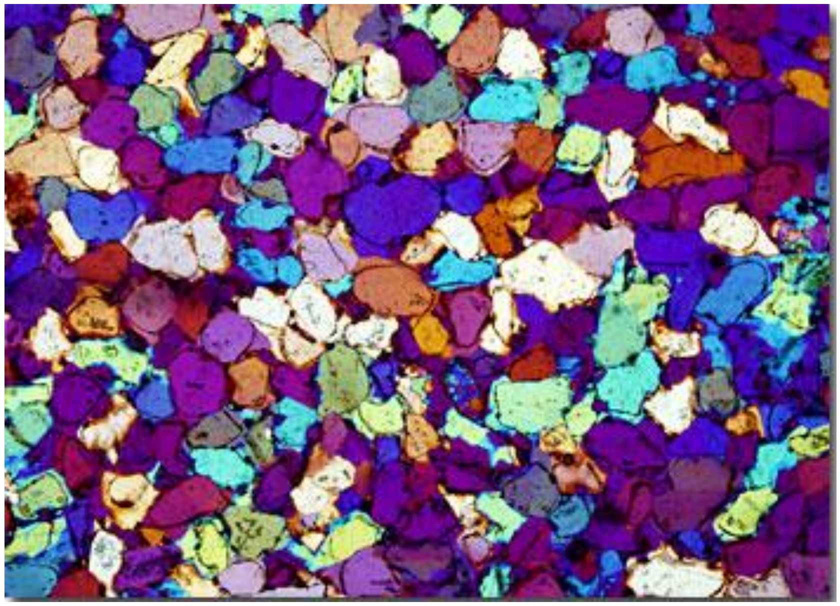

Figure 6-2. A microscopic thin section of sandstone in the polarization microscope. It demonstrates a variety of minerals in a rock (source: micro.magnet.fsu.edu).

To estimate a physical property of a substance that is made of mixed material (solid and liquid), the physical properties of the components individually (such as elastic modulus and density), the volume fraction, and components arrangement and geometry.

Precise estimation can be determined when all defined parameters described in the last paragraph are available, but there is always some uncertainties due a lack of data. Effective medium theory makes it possible to define upper and lower bounds of the property. It helps to have knowledge about the maximum and minimum limits of the physical parameters (as bulk modulus or velocity). In this section, the main challenge is determining the bulk modulus and density of the formation in the reservoir before and after the gas injection.

Commonly three methods are used for calculation of density and bulk modulus for reservoir fluids at different pressure and temperature:

1. Calculated from equation described and derived by Batzle and Wang, (1992).

2. Measurements of the fluid, that are recovered from the reservoir or formation.
3. The equation of state (EoS) is the best method for calculating the fluid properties. (McCain, 1990; Span and Wagner, 1996; Danesh, 1998).

6.3 The physical properties of the mix phases

Some physical properties are related to the geometrical distribution of the components in the medium, and some are not. For example, the density is a simple property that is not related to the distribution form and homogeneity of the mixture. For this kind of properties, we can explain an average value by Eq. 6-1.

$$M_{Average} = \sum_{i=1}^{n} f_i M_i$$

Eq. 6-1

Where: M is a physical property, f_i is fraction of i th component, and n is number of components.

This formula is the Voigt average that will be explained in the following sections (Figure 6-13). Some properties are sensitive to the components geometry distribution or homogeneity and isotropic specification in the mass. The velocity and elastic modulus are properties in this category. In the next section, we examine average properties for these parameters.

6.4 Voigt and Reuss average

There are many methods for calculating a physical property of a mixed phase (such as mineral’s bulk modulus). The Reuss lower bound and Voigt upper bound can be described through average by Eq. 6-2:

$$K = \sum_{i=1}^{n} (f_i K_i^m)^m$$

Eq. 6-2

Where n is the number of components, *i* is component's number in the mixed phase and f_i is fraction of *i* th component. If m= -1 it is Reuss average and if m=1 it defines the Voigt average. Voigt-Reuss-Hill (VRH) average (Eq. 6-3) is an approximation that uses Voigt and Reuss estimation as:

$$K_{VRH} = \frac{1}{2}(K_{Voigt} + K_{\mathrm{Re}uss})$$

Eq. 6-3

Figure 6-3 shows a sample of bulk modulus calculation for a mix of sand (plagioclase) and water, solved by Reuss and Voigt averages and the physical concept of them. The Voigt average is a formula for an iso-strain model and Reuss is an average that solves an iso-stress model. When the water saturation is over 60%, effects of suspension are important. It is usual in rocks that are not compacted and not cemented in environments with a high-water content.

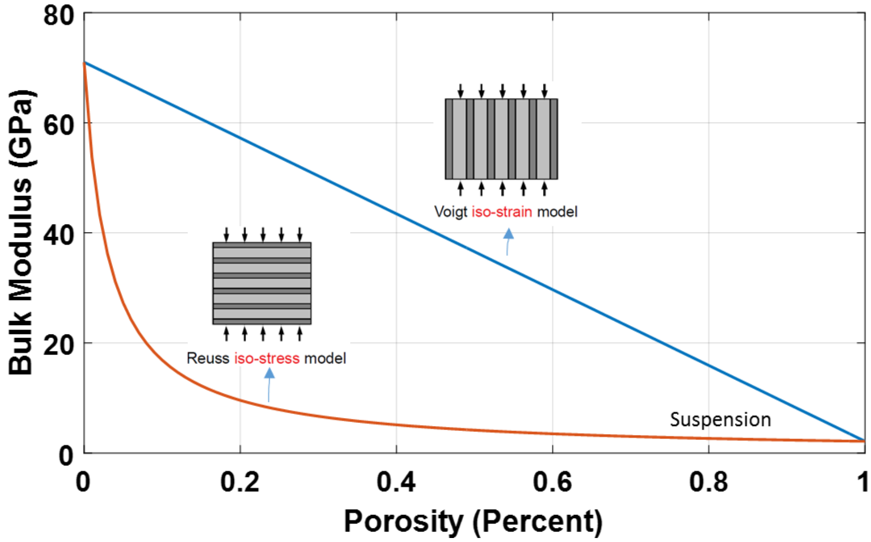

Figure 6-3: The bulk modulus for the mix of a porous sand with 100% plagioclase (as immature sand) and water.

6.5 Brie's average for fluid mix

Brie's average is an empirical fluid mixing law, introduced by Brie (1995) and can be explained by Eq. 6-4 :

$$K_{Brie} = (K_{liquid} - K_{gas})(1 - S_{gas})^{e} + K_{gas}$$

Eq. 6-4

Where K_{liquid} is the bulk modulus of the liquid phases calculated from the Reuss average (for the mixed case) in the reservoir, K_{gas} is the gas bulk modulus and S_{gas} is gas saturation. As mentioned previously, the Voight bound is appropriate for a patchy mixed fluid condition, but this occures rarely, so technically, the Brie's average is preferred to be considered as the upper bound for a mixed fluid.

For the velocity estimation after fluid substitution, the fluid properties need to be calculated. Figure 6-14 shows the bulk modulus of the mixed fluid (brine+CO_2) with a different fraction of CO_2 calculated by Voigt, Reuss, VRH and Brie's average methods.

6.6 Hashin-Shtrikman (HS) Bounds

The Voigt-Reuss bound introduces a wide range in average physical properties (Figure 6-3). The Hashin-Shtrikman bounds are a better way to make the narrower bounds for a property (such as the bulk modulus) estimation. Figure 6-4 shows the distribution and geometry of two components in the Hashin-Shtrikman bounds calculation. For the maximum and minimum HS boundary, the position of the minerals were changed in the calculation. Eq. 6-5 and Eq. 6-6 are for calculation bulk and shear modulus in the HS average method.

$$K^{HS\pm} = K_1 + \frac{f_2}{(K_2 - K_1)^{-1} + f_1 (K_1 + \frac{4}{3}\mu_1)^{-1}}$$

Eq. 6-5

$$\mu^{HS\pm} = \mu_1 + \frac{f_2}{(\mu_2 - \mu_1)^{-1} + 2 f_1 [\frac{(K_1 + 2\mu_1)}{5\mu_1 (K_1 + \frac{4}{3}\mu_1)}]^{-1}}$$

Eq. 6-6

Where K_i is the bulk modulus and μ_i is the shear modulus of the material with f_i fraction.

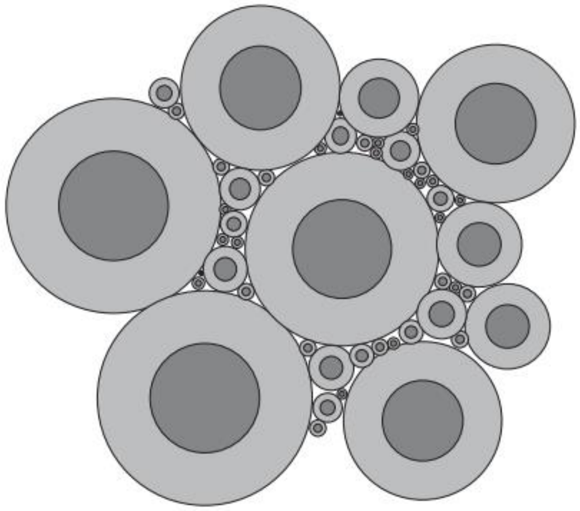

Figure 6-4.Two phase material in the Hashin-Shtrikman bounds.

For the upper boundary (HS+) calculation, the hard material is considered as the first component (K_1, μ_1), and for the lower boundary (HS-), the softer material is selected as the first component.

Walpole (1966) introduced a new form of the Hashin-Shtrikman approach called the Hashin-Shtrikman-Walpole method, as Eq. 6-7 and Eq. 6-8 (after Mavko, 1998):

$$K^{HS\pm} = K_1 + \frac{f_2}{(K_2 - K_1)^{-1} + f_1(K_1 + \frac{4}{3}\mu_m)^{-1}}$$

Eq. 6-7

$$\mu^{HS\pm} = \mu_1 + \frac{f_2}{(\mu_2 - \mu_1)^{-1} + f_1[\mu_1 + \frac{\mu_m}{6}(\frac{9K_m + 8\mu_m}{K_m + 2\mu_m})]^{-1}}$$

Eq. 6-8

Where subscript m refers to the maximum bulk and shear modulus values for the upper bound and minimum for the lower bound calculation. A general form of Hashin-Shtrikman-Walpole equations for more than two-phase material (Berryman (1995)):

$$K^{HS+} = \Lambda(\mu_{max})$$
$$K^{HS-} = \Lambda(\mu_{\min})$$

Eq. 6-9

$$\mu^{HS+} = \Gamma(\zeta(K_{\max}, \mu_{max}))$$
$$\mu^{HS-} = \Gamma(\zeta(K_{\min}, \mu_{\min}))$$

Eq. 6-10

Where:

$$\Lambda(z) = \langle \frac{1}{K(r) + \frac{4}{3}z} \rangle^{-1} - \frac{4}{3}z$$

$$\Gamma(z) = \langle \frac{1}{\mu(r) + z} \rangle^{-1} - z$$

$$\zeta(K, \mu) = \frac{\mu}{6}(\frac{9K + 8\mu}{K + 2\mu})$$

The brackets indicate an average over the medium, which is the same as an average over the constituents weighted by their volume fractions.

Figure 6-5 shows the bulk modulus calculated for a mix of calcite and quartz by using the Voigt, Reuss, VRH and HS averages. As can be seen, the VRH average approximately is equal to the HS bounds, and HS+ is near to HS- in this sample for two minerals. Figure 6-6 is another sample of mixed minerals (quartz and wet clay) for which the bulk modulus was calculated by the Voigt, Reuss and VRH average methods. For two mixed fluids (shear modulus of fluids is zero), the HS+ and HS- are Reuss averages.

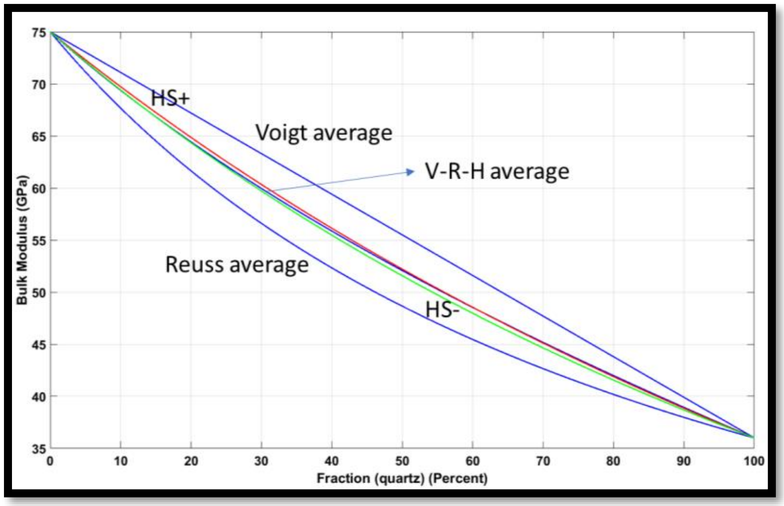

Figure 6-5.The average bulk modulus for a mixed case of quartz and calcite. The blue curves show Voigt, Reuss and VRH averages. The red curve is HS+ and green is HS-. The VRH is very near to Hashin-Shtrikman averages.

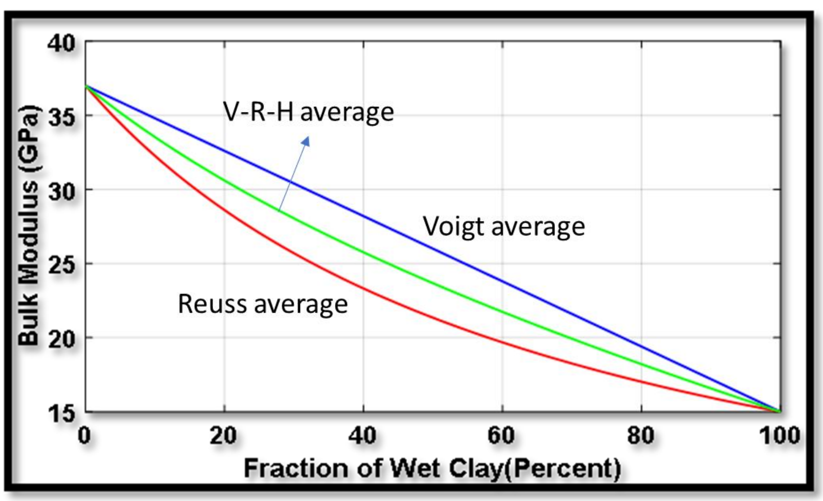

Figure 6-6. Matrix Properties calculated by Voigt (blue), Reuss (red) and VRH (green) methods for a mix of pure quartz and wet clay.

6.7 Fluid properties

During the injection or production, the pressure changes in the reservoir due to the injection. Also, if the injected fluid's temperature is not equal to the formation's temperature, it will be affected. As mentioned in the Chapter 5, the aquifer salinity can change locally by CO_2 injection around the injection point. A secondary effect of these changes can affect the seismic velocity and formation density and consequently seismic responses. In the project, there is assumed to be no temperature change during the injection.The pressure increases a little during the injection (from 3 to 5 MPa). In this section, I discuss the fluid phases properties and the mixing case.

6.7.1 Brine

Water has high capability to dissolve salt and ions. Like other liquids, the pressure and temperature changes have an effect on the physical properties of the water. For seismic modeling of the reservoir, I calculate the bulk modulus, seismic velocities and density of the brine. There are some approaches for this purpose, and for a geophysicist, Batzle-Wang (1992) equations are the well-known method. Also, another alternative introduced by Rowe and Chou (1970) for the brine density and bulk modulus.

As mentioned, the density of pure water is a function of temperature and pressure. By a polynomial (Batzle-Wang, 1992) it is possible to calculate the density of water in the various temperatures (T) and pressures (P) as Eq. 6-11.

$$\rho_w = 1 + 10^{-6}\left(-80T - 3.3T^2 + 0.00175T^3 + 489P - 2TP + 0.016T^2P - 1.3\times10^{-5}T^3P - 0.333P^2 - 0.002TP^2\right)$$

Eq. 6-11

For the brine, salinity is another parameter that should be considered in the density calculation. So, the density of brine can be represented as Eq. 6-12:

$$\rho_b = \rho_w + S\left\{0.668 + 0.44S + 10^{-6}\left[300P - 2400PS + T\left(80 + 3T - 3300S - 13P + 47PS\right)\right]\right\}$$

Eq. 6-12

In Eq. 6-11 and Eq. 6-12, ρ_w and ρ_b are water and brine density in g/cm^3, P is pressure in MPa, T is the temperature in Celsius and S is the weight fraction of salt (NaCl) in (ppm/1000000).

The bulk modulus of the brine is predictable by a simplified function as Eq. 6-13 (Chen et al., 1978):

$$V_B = V_w + S(1170 - 9.6T + 0.055T^2 - 8.5\times10^{-5}T^3 + 2.6P - 0.0029TP - 0.0476P^2)$$
$$+S^{1.5}(780 - 10P + 0.16P^2) - 820S^2$$

Eq. 6-13

Where V is the velocity of P-waves in the brine (V_B) and water (V_W). The water velocity can be estimated by Eq. 6-14 up to 100°C and about 100 MPa (Wilson, 1959):

$$V_W = \sum_{i=0}^{4}\sum_{j=0}^{3} w_{ij} T^i p^j$$

Eq. 6-14

Where the coefficients (w_{ij}) are:

$w_{00} = 1402.85$	$w_{50} = 1.524$	$w_{02} = 3.437\times10^{-3}$	$w_{03} = -1.197\times10^{-5}$
$w_{10} = 4.871$	$w_{11} = -0.0111$	$w_{12} = 1.739\times10^{-4}$	$w_{13} = -1.628\times10^{-6}$
$w_{20} = -0.04783$	$w_{21} = 2.747\times10^{-4}$	$w_{22} = -2.135\times10^{-6}$	$w_{23} = 1.237\times10^{-8}$
$w_{30} = 1.487\times10^{-4}$	$w_{31} = -6.503\times10^{-7}$	$w_{32} = -1.455\times10^{-8}$	$w_{33} = 1.327\times10^{-10}$
$w_{40} = -2.197\times10^{-7}$	$w_{41} = 7.987\times10^{-10}$	$w_{42} = 5.230\times10^{-11}$	$w_{43} = -4.614\times10^{-13}$

Figure 6-7 and Figure 6-8 show diagrams for density, bulk modulus and velocity of brine (salinity=8000 ppm in BBRS reservoir) and pure water. These properties are a function of pressure in Figure 6-7 and temperature in Figure 6-8. The relation between the properties are nearly linear with the pressure between 2 to 8 MPa.

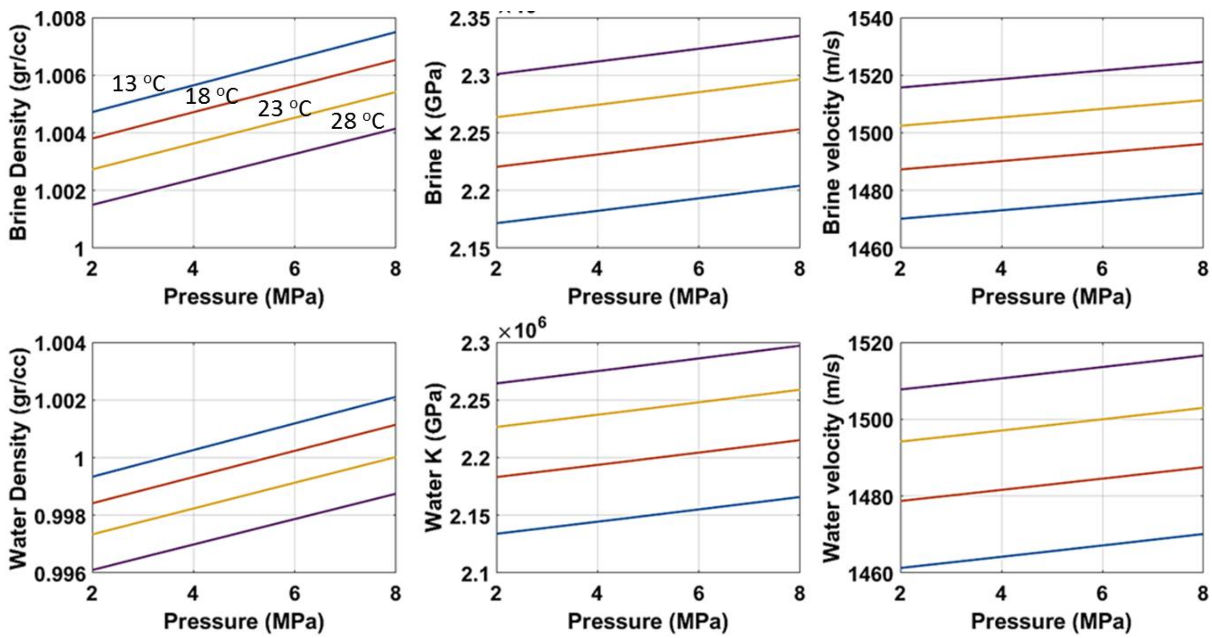

Figure 6-7. The density, bulk modulus and P-wave velocity of brine and water temperature from 13 to 28 °C (with 5 °C steps) and salinity equal to 8000 ppm from 2 to 8 MPa.

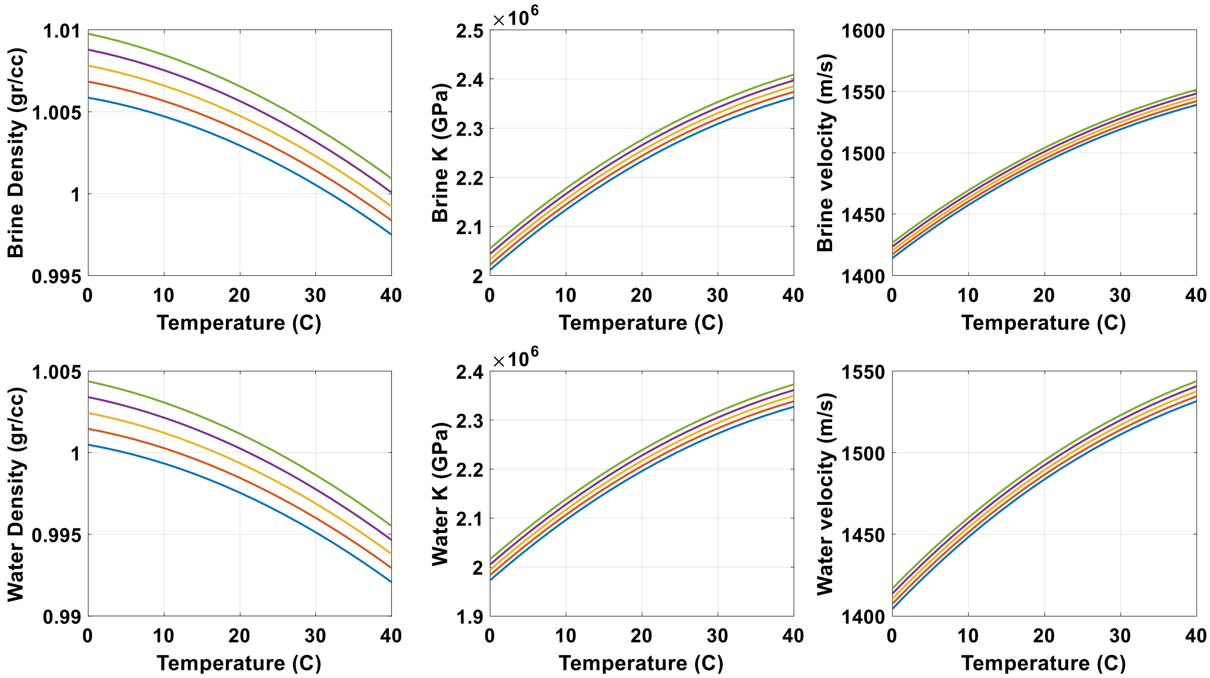

Figure 6-8.The density, bulk modulus and P-wave velocity of water and brine (salinity=8000 ppm) as a function of temperature. Each curve belongs to the pressure from 1 to 10 MPa in steps of 2 MPa.

The viscosity of brine is also a necessary parameter for the fluid simulation. Kestin et al., (1981) derived a formula for the brine viscosity:

$$\eta = 0.1 + 0.333S + (1.65 + 91.9S^3)exp\{-[0.42(S^{0.8} - 0.17)^2 + 0.045]T^{0.8}\}$$

Eq. 6-15

Where T is temperature and S is salinity. The pressure effect is negligible for the viscosity change in water and brine, so there is no influence of it in the formula. Figure 6-9 shows the viscosity of the brine as a function of temperature. The blue arrow in Figure 6-9 indicates the viscosity for the FRS aquifer.

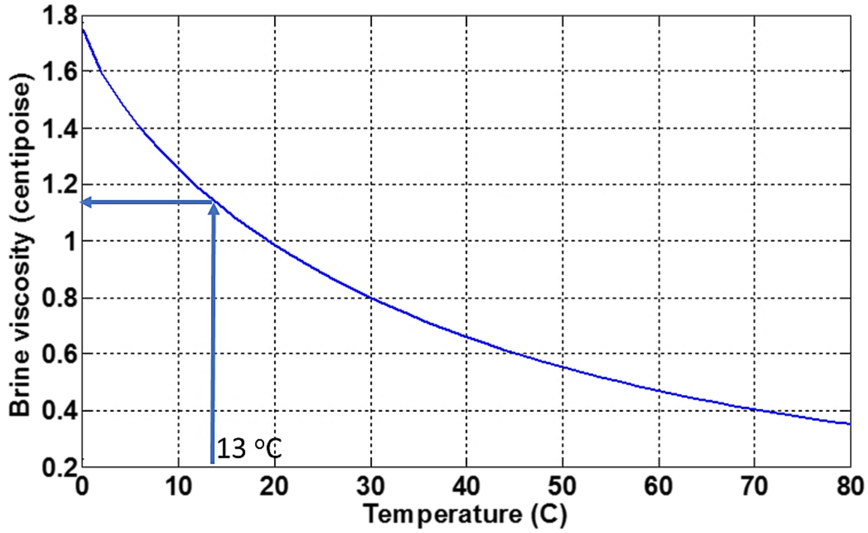

Figure 6-9. The viscosity of brine (based on Batzle-Wang (1992)), the pressure does not have a significant influence on the brine viscosity.

6.7.2 Carbon dioxide

The equation of state for carbon dioxide can predict actual physical parameters for it at different temperatures and pressures. Span and Wagner (1996) described a very detailed formulation for CO_2 properties from using the equation of state (EoS) that were used in this research. Other articles introduced the CO_2 properties using simple calculation methods (e.g. Vargaftik (1975) and Sun (2009)). Two diagrams in Figure 6-10 demonstrate the bulk modulus and density of carbon dioxide as the function of pressure and temperature. In the FRS project, the reservoir temperature is 13°C. To inject CO_2 in gas condition into the reservoir at a higher BHP, some simulations were tested for a higher temperature as 20°C in the last chapter. The reservoir pressure changes from 3 MPa to 5.5 MPa. Figure 6-11 and Figure 6-12 show the density and P-wave velocity respectively at reservoir conditions.

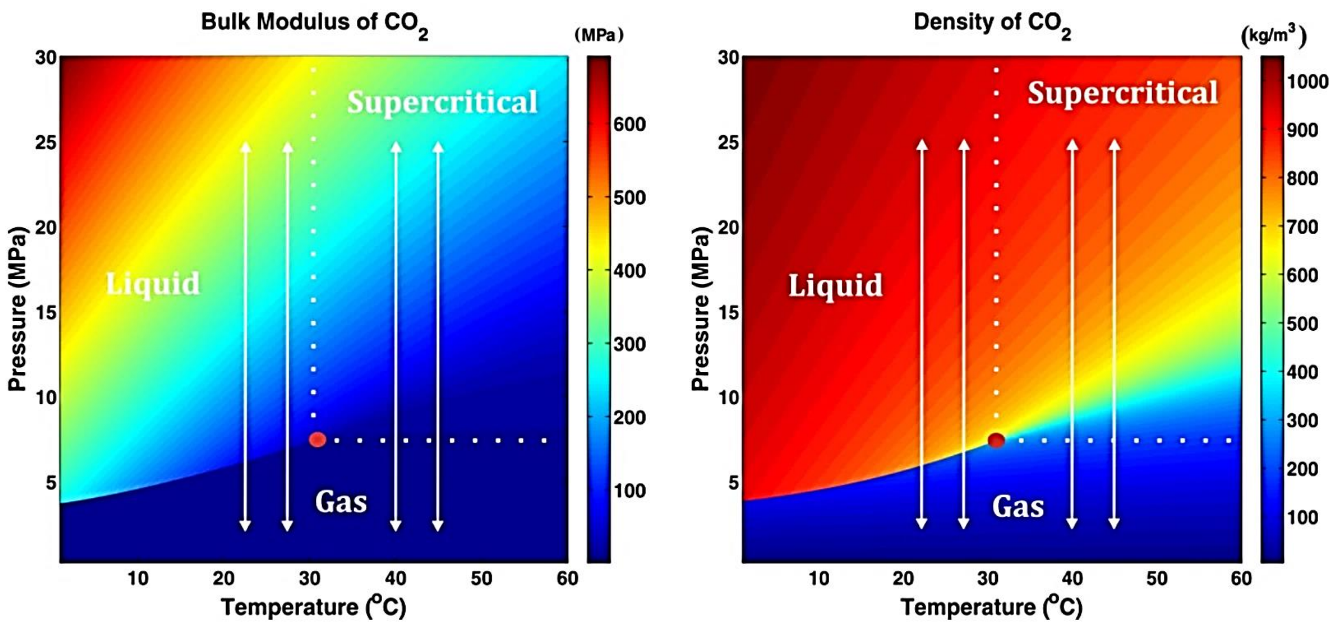

Figure 6-10.The bulk modulus and density of CO_2 at different pressures and temperatures. EoS described by Span and Wagner (1996) were used to generate the diagram (drawn by Yam,2011).

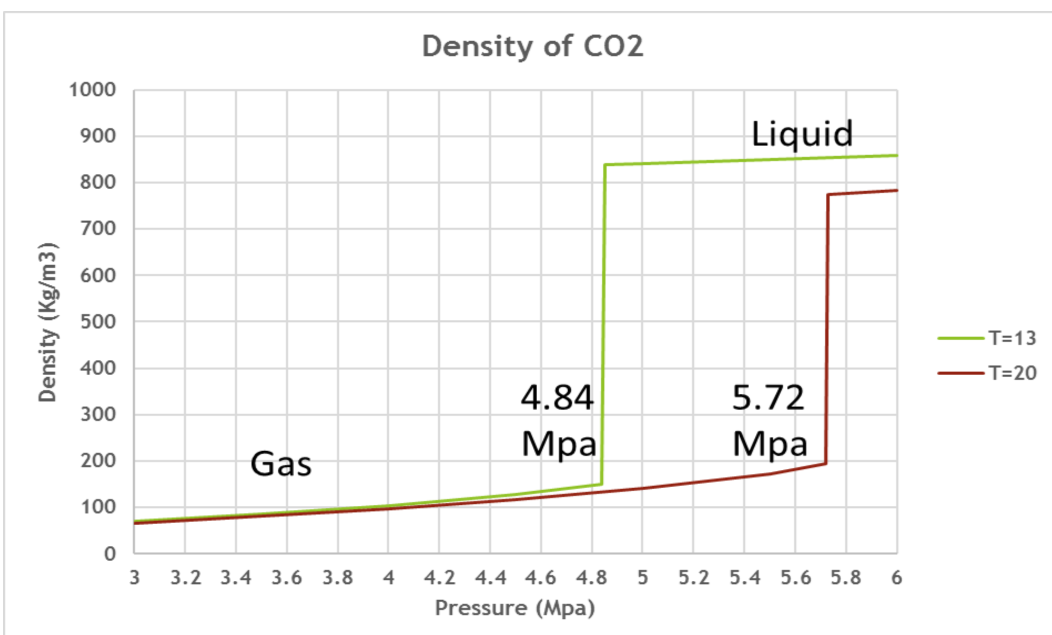

Figure 6-11. Density of CO_2 for 13 and 20ºC and 23<p<57 bar.

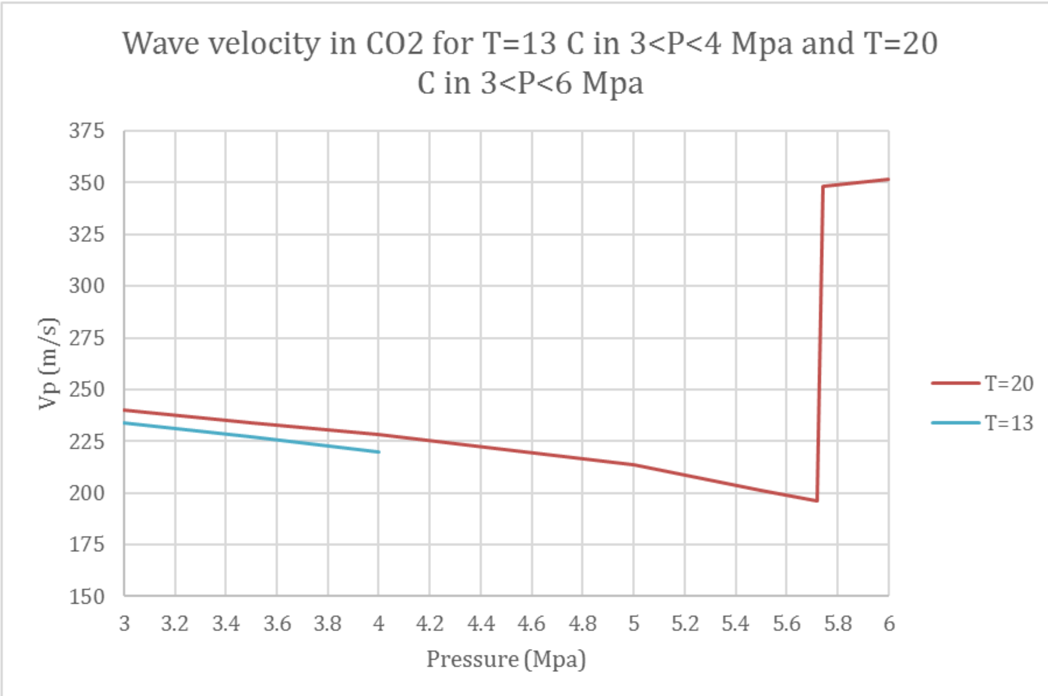

Figure 6-12. P-wave velocity of CO_2 versus pressure at T= 13 and 20 ^oC (the velocity calculated upper than 4 MPa at T=13 ^oC was unstable)

6.8 Mixed fluid properties

A mixed fluid of brine as a liquid and carbon dioxide in the gas phase will decrease the density and bulk modulus as a function of the CO_2 saturation. The mixed condition of brine and carbon dioxide (that can be fine mixed, semi-patchy or patchy mixed condition) has a significant effect on the P-wave velocity and bulk modulus (see sections 6.3, 6.4, 6.5 and 6.6).

Garcia (2001) reported a density increase equal 2-3%, when CO_2 dissolves in the water (or brine). In this research, the effect of the CO_2 solution in the brine is ignored. The bulk modulus and the density of fluid phase are calculated in this section to estimate the P and S-wave velocity and density at the formation. Also, the all possible fluids mixed patterns (from fully patchy to fine mixed) are considered for the 4D seismic modeling. The phases properties (for brine and CO_2)

generated previously (from Batzle-Wang equations and CO_2 Equation of State formulation) by using the different averages (as Voigt, Reuss, VRH and Brie) were used to calculate the mixed fluid properties shown in Figure 6-13 through Figure 6-16.

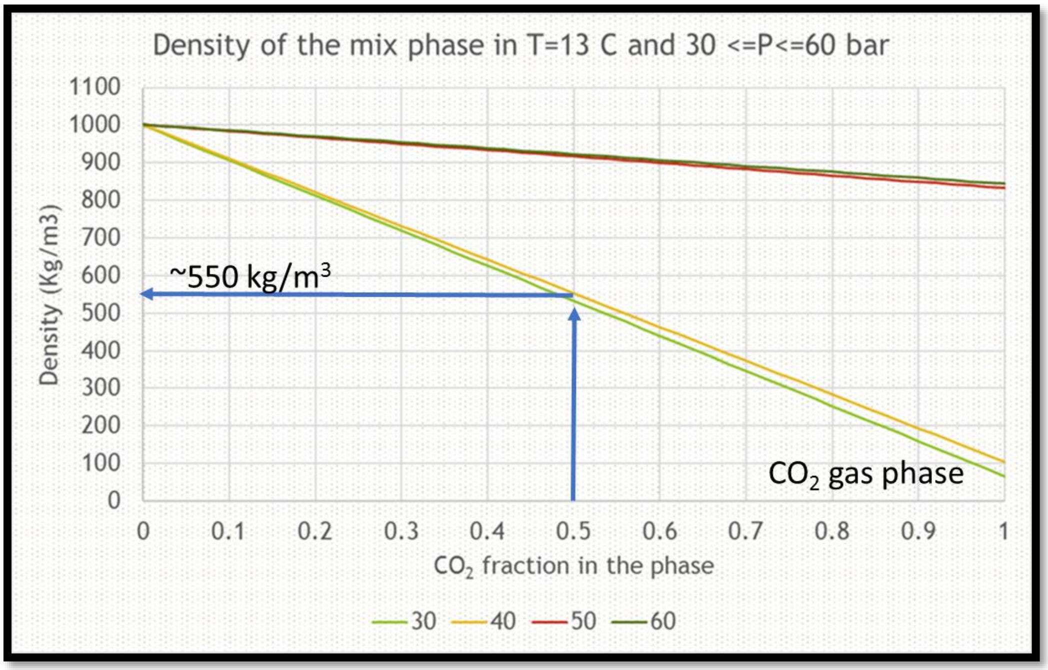

Figure 6-13. The density of the mixed fluid in T=13.8ºC and pressure from 30 to 60 bar (3 to 6 MPa).

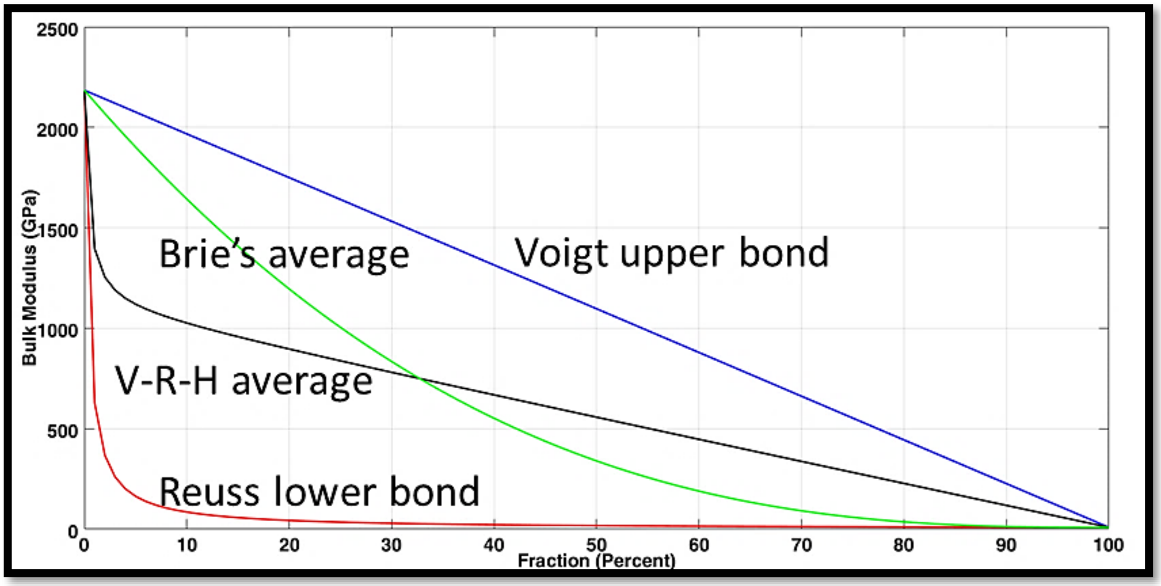

Figure 6-14. The bulk modulus for the mix of brine with 8000 ppm salinity and CO_2 in 13 ^{o}C and 4.5 MPa (45 bar). In the mixed fluid condition (as CO_2 and brine), the Hashin-Shtrikman averages (upper and lower bounds) are using the Reuss Average.

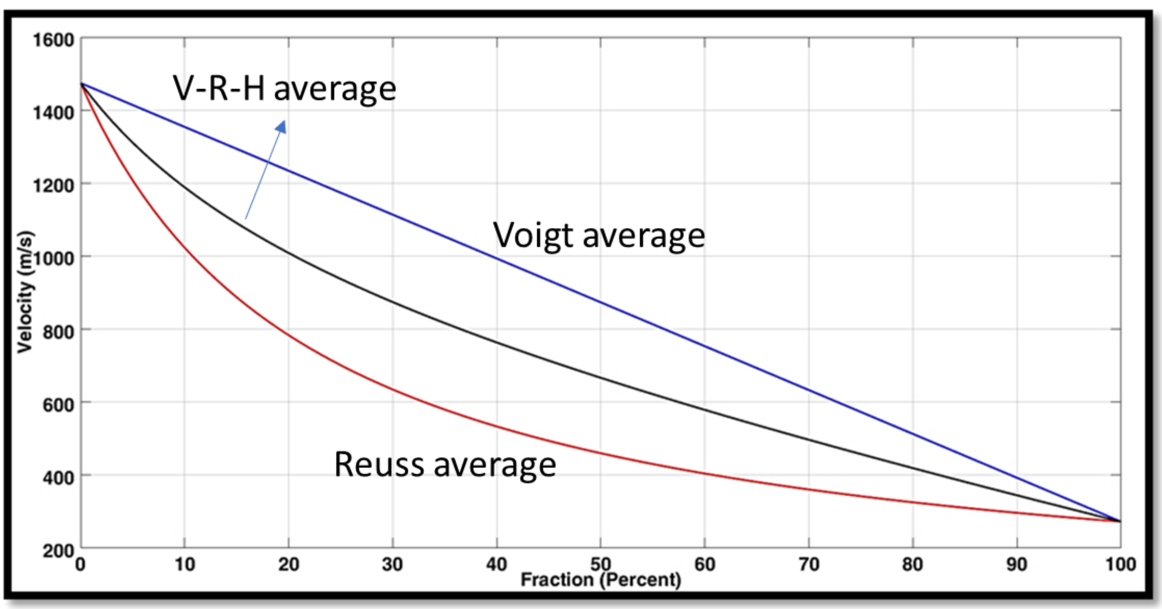

Figure 6-15. The P-wave velocity in the mixed fluid of the brine (8000 ppm salinity) and CO2 in T=13 oC and P=4.5 MPa (the reservoir condition during the injection procedure).

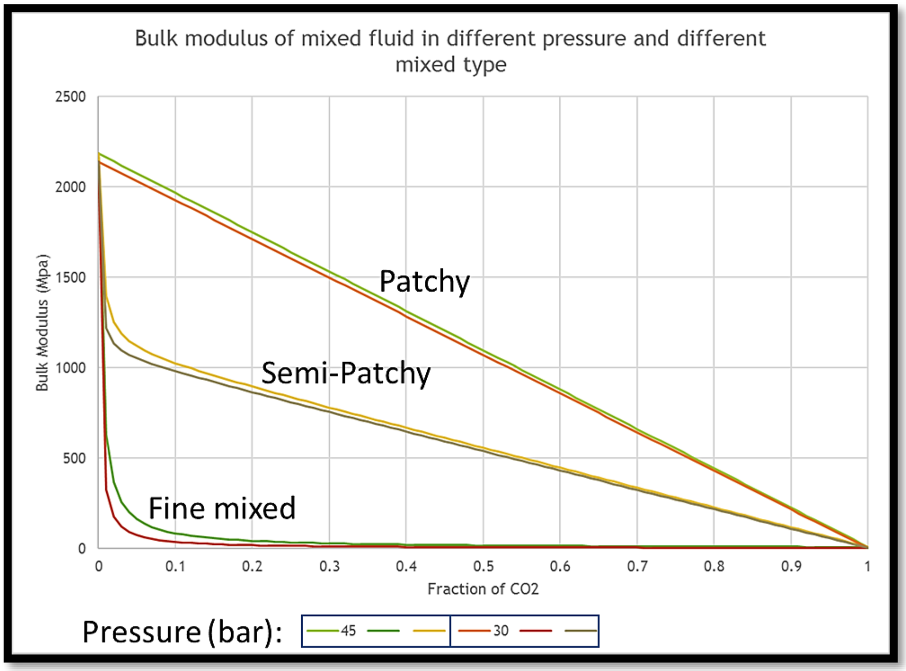

Figure 6-16. The bulk modulus of the mixed fluid with a different fraction of CO_2 and different mixed condition in P=30 bar (3 MPa) and 45 bar (4.5 MPa).

6.9 Effect of pore pressure on seismic velocity

For a gas (as CO_2) the pressure has a significant effect on the velocity and density (Figure 6-11 and Figure 6-12). Figure 6-17 demonstrates the influence of the pressure on the velocity of mixed fluid with a different fractions of CO_2 and brine. The pressure change in this example is for the maximum case from 3 to 4.5 MPa (equal to a 1.5 MPa change) that will increase velocity between 3-7% (Figure 6-17). As we demonstrated in the last chapter, the pressure in the reservoir will decrease after ceasing the gas injection and it will return to the initial reservoir pressure after nine years.

In the reservoir system, CO_2 flooding has an effect on seismic velocity by changing the pore or effective pressure. Higher pore pressure directly impacts the effect of CO_2 injection on the seismic velocities, as lab experiences show a 2-6.9% decrease in Vp for a maximum 12 MPa increase in the pore pressure (Wang et al., 1998). For the FRS project the injection has low BHP, so the velocity change due to the pressure change is negligible. However, a basic calculation on the pressure change effect on the fluid phase velocity in the reservoir was undertaken and the result is demonstrated in Figure 6-17. The velocity (or bulk modulus) change in the fluid shows big variation with a large pressure change (Figure 6-18) or in the CO_2 change in phase.

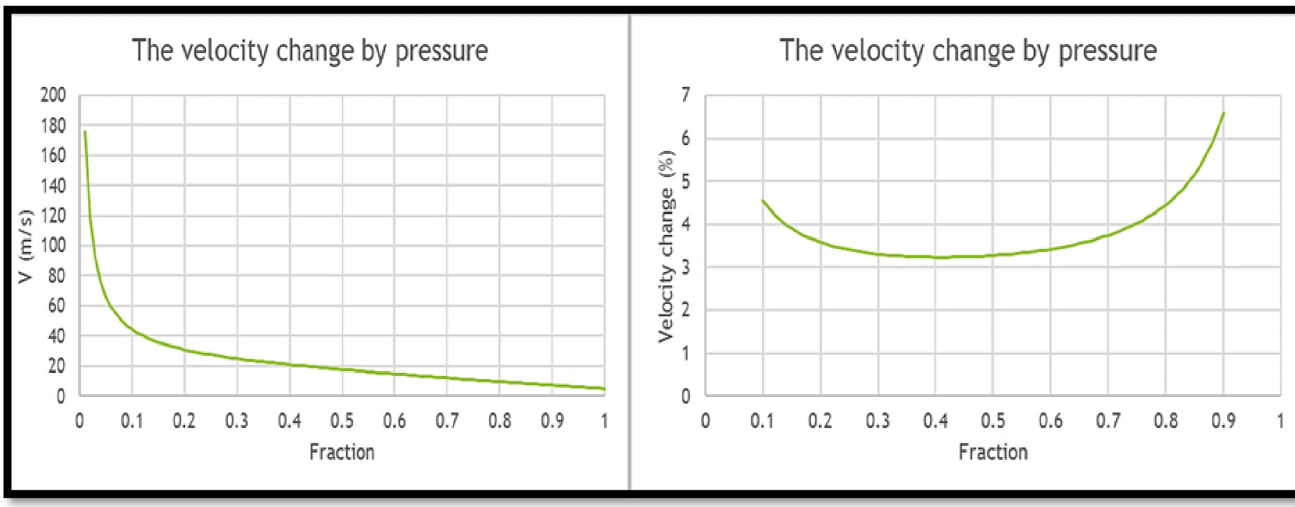

Figure 6-17. The velocity change in the fluid phase of the reservoir (brine+CO_2) for a semi-patchy mixed fluid by pressure. The pressure increased from 3 to 4.5 MPa.

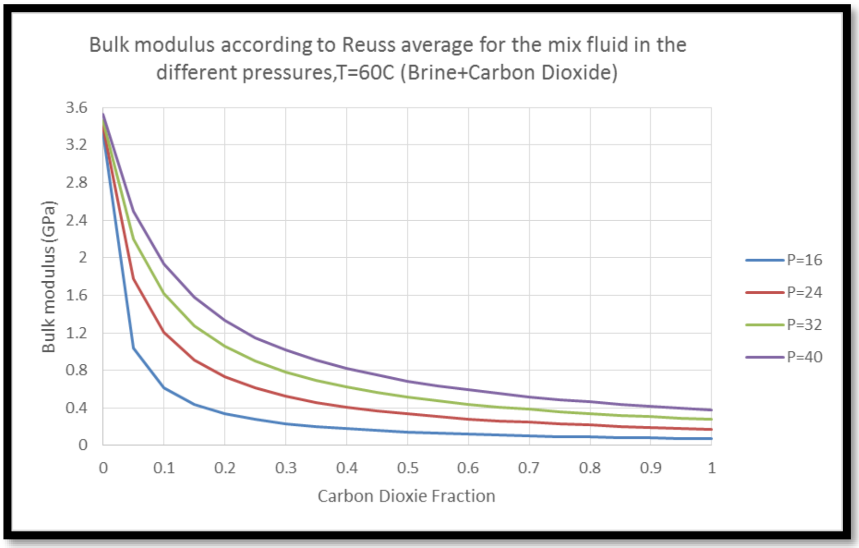

Figure 6-18: Bulk modulus estimation for different fraction of fluid mix by Reuss average (fine mixed fluids) in T=60 C and different pressures (16 to 40 MPa) (P and T for Nisku aquifer condition, WASP project; Nowroozi, 2014)

6.10 The physical properties in the matrix

For the P-wave velocity calculation after the gas injection (by Gassmann's equation), we need the bulk modulus of the minerals. For this purpose, mineral components of rock should be distinguished. Some laboratory technics as X-ray diffraction or Fourier transform infrared analysis are possible when core sample is accessible. Another method as well logging and Clay value analysis are suitable. As mentioned in the section 2.5, the well log data was used for mineral discrimination. The final result of the mineralogical study were demonstrated in Figure 2-12 and Table 2-1.The modulus and density of the mineral are introduced in Table 6-1. The elastic modulus of a combination of minerals was calculated in Table 6-2 by Voigt, Reuss and VRH average methods.

Table 6-1. The fraction of the minerals in the reservoir based on the well log data analysis.

Mineral	Fraction	Bulk Modulus (Gpa)	Shear Modulus (GPa)	Density (gr/cm^3)
Quartz C	40%	37.4	41.14	2.65
K Feldspar	4%	65.41	27.54	2.64
Albite	8%	55.94	30.17	2.61
Kaolinite	15%	46.01	23.89	2.439
Chlorite	7%	165.02	52.1	2.839
Illite-Smectite	11%	35.72	17.8	2.546
Siderite	15%	116.01	48.06	3.75

Table 6-2.The mixed minerals bulk and shear modulus calculated by three average methods.

Average Method	Bulk Modulus (Gpa)	Shear Modulus (Gpa)
Voigt Ave.	61.84	36.37
Reuss Ave.	48.09	32.52
VRH Ave	54.96	34.44

The average density value is calculated by the Eq. 6-1, and it is equal 2.87 gr/cc for a zero-porosity sample. For the average 15% porosity in the reservoir, the formation bulk density is 2.439 gr/cc.

For quality control of the mineral discrimination, the bulk density was derived based on the mineral study and porosity(density) well log and compared with the density from log data. The result is shown in Figure 6-19. It shows the difference between density calculated by the well log data and mineral discrimination study and the overestimation of density can be because of higher percentage estimation of heavy minerals (as siderite).

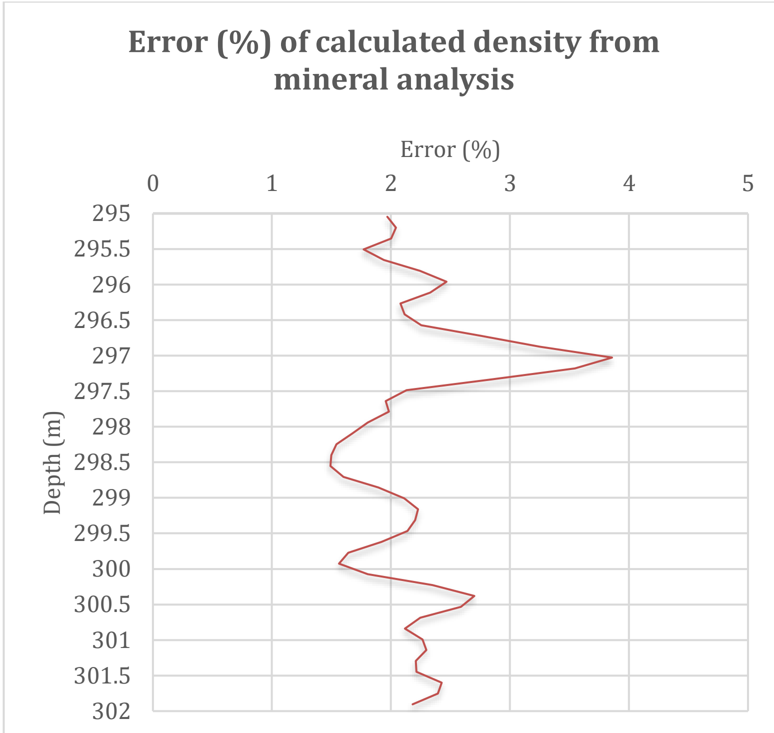

Figure 6-19. The error in density calculated by the mineral discrimination method and well log data in the injection horizon.

6.11 Fluid substitution

Gassmann's equation is a theoretical approach that relates saturated bulk modulus to bulk modulus of the mineral matrix (mono mineral), bulk modulus of the fluid, bulk modulus of the porous rock frame and porosity. The first introduction of Gassmann's equation can explain as Eq. 6-16.

$$K_{sat} = K_{dry} + \frac{(1 - \frac{K_{dry}}{K_{\min}})^2}{\frac{\varphi}{K_{fl}} + \frac{1-\varphi}{K_{\min}} - \frac{K_{dry}}{K_{\min}^2}}$$

Eq. 6-16

Where:

K_{sat} = The saturated bulk modulus (undrained of pore fluids)

K_{dry} = The bulk modulus of the dry porous rock = frame

K_{min} = The bulk modulus of the solid rock matrix material

K_{fl} = The bulk modulus of the fluid saturating the porous rock

φ = The porosity of the rock.

6.12 Model Assumption

There are some considerations for successful use of Gassmann's theory. These assumptions are:

1. The porous rock is homogeneous and isotropic. It means frame must be formed of one mineral or if the frame has more than one mineral, they should have a near elastic stiffness (Berge, 1998).
2. The pores are interconnected (no isolated pores). The pore space is completely connected, and fluid should be moveable, and fluid pressure must be uniform. It considers one pores type, and more types of pore need to use more complex model (Berryman and Milton, 1991).
3. Skeleton grains, fluids obey Hooke's law (stress is proportional to strain), and the pore fluid is frictionless (low-viscosity fluid).
4. Relative motion between fluid and solid during the passage of an elastic wave is negligible (low frequencies only)
5. The pore fluid does not interact with the solid material (the matrix elastic moduli are unaffected by fluid saturation).

6. The system should be closed, and no fluid leaves the rock volume. No cavitation occurs, no separation at contact boundaries.

p and s-wave velocities are controlled by shear (μ) and bulk modulus (K) as Eq. 6-17 and Eq. 6-18.

$$v_p = \sqrt{\frac{K + \frac{4}{3}\mu}{\rho}}$$

Eq. 6-17

$$v_s = \sqrt{\frac{\mu}{\rho}}$$

Eq. 6-18

For two last formulas, if velocity is km/s and density in gr/cc, K and G will be in Gpa.It is assumed that in the fluid substitution procedure, the shear modulus of the formation stays constant as the fluids shear modulus are always zero.Another form of Gassmann's equation is useful for the direct velocity calculation for the fully fluid saturated porous rock is as Eq. 6-19 and Eq. 6-20 (for Vs) (Gerritsma, 2005):

$$v_P = \left[\frac{K_{dry} + 4\mu_b/3 + n^2 M}{\rho_{sat}}\right]^{1/2}$$

Eq. 6-19

$$v_S = \left[\frac{\mu_b}{\rho_{sat}}\right]^{1/2}$$

Eq. 6-20

Where:

$$n = \left(1 - \frac{K_{dry}}{K_{\min}}\right) \quad \text{and} \quad M = \frac{1}{\dfrac{\varphi}{K_{fl}} + \dfrac{1-\varphi}{K_{\min}} - \dfrac{K_{dry}}{K_{\min}^2}} \ ;$$

in which

K_{dry} , $K_{\min}$ or $K_{\min eral}$, K_{fl} , φ were described above (Eq. 6-16)

$\mu_{dry} = \mu_{sat} =$ the shear modulus of the dry porous rock

ρ_{sat} = ρ_b = the density of the saturated rock; $\rho_{sat} = \varphi\rho_{fl} + (1-\varphi)\rho_m$

ρ_{fl} = the density of the fluid saturating the porous rock

ρ_m = the density of the solid matrix material.

6.13 Practical usage of the Gassmann's equation

The first parameters for a successful and correct usage of Gassmann's equation are the wave velocities (Vp and Vs) and density. These three parameters lead us to the shear and bulk modulus calculation (Eq. 6-21) with a variable displacement in Eq. 6-17 and Eq. 6-18 as:

$$\mu = \rho V_s^2$$
$$K = \rho(V_p^2 - \frac{4}{3}V_s^2)$$

Eq. 6-21

As we know, shear modulus for fluids are zero, and it remains constant during fluid substitution (Eq. 6-22).

$$\mu_{fl} = 0$$
$$\mu_1 = \mu_2$$

Eq. 6-22

Figure 5-5 shows the result of modulus calculation by the well log data in the reservoir zone. K_{dry} is a parameter that is unknown. To solve Gassmann's equation, we need to remove this term. Gassmann's equation can be revealed as Eq. 6-23.

$$\frac{K_{sat}}{K_{\min eral} - K_{sat}} - \frac{K_{fl}}{\varphi(K_{\min eral} - K_{fl})} = \frac{K_{dry}}{K_{\min eral} - K_{dry}}$$

Eq. 6-23

In this equation, the last term is a combination of K_{dry} and $K_{mineral}$. It is supposed that K_{dry} and $K_{mineral}$ are constant during fluid substitution procedures, so the last term remains constant within the fluid substitution procedure. This point can help us to explain Eq. 6-23 as Eq. 6-24 that is easily applicable for the fluid substitution.

$$\frac{K_{sat1}}{K_{\min eral} - K_{sat1}} - \frac{K_{fl1}}{\varphi(K_{\min eral} - K_{fl1})} = \frac{K_{sat2}}{K_{\min eral} - K_{sat2}} - \frac{K_{fl2}}{\varphi(K_{\min eral} - K_{fl2})}$$

Eq. 6-24

So, with this simple equation, the p wave velocity is available by calculation of new saturated bulk modulus. The bulk density before the injection is known with log data, and it is a combination of mineral and fluid (here brine) density as:

$$\rho_{fluid}\varphi + \rho_{\min eral}(1-\varphi) = \rho_{bulk}$$

Eq. 6-25

Moreover, mineral density is calculable by using porosity and density log data, and brine density for the initial reservoir condition (P=30 bar, T=13^{o}C) explained in the section 0.

6.14 The CO_2 gas injection effect on the formation velocity in the field and lab test

In this section, I review the results of velocity change due to CO2 injection from lab test (Figure 6-20 (Smith,2003), Figure 6-22 (Alemo et al., 2011) and Figure 6-23 (Wang, 2001)), time-lapse result from a field work(Figure 6-21 (Lumley, 2010)) and the velocity variation by Gassmann's equation (Figure 6-20and Figure 6-21) in the previously published papers. I use and compare our result for the FRS project with these research results. The velocity calculation is possible by three different methods:

1- Fluid substitution equations as Gassmann's method (Smith, 2003).
2- In field estimation by injection CO_2 in the real reservoir and seismic test (Lumley, 2010).
3- The lab experiences on CO_2 injection on core samples (Alemo et al., 2011).

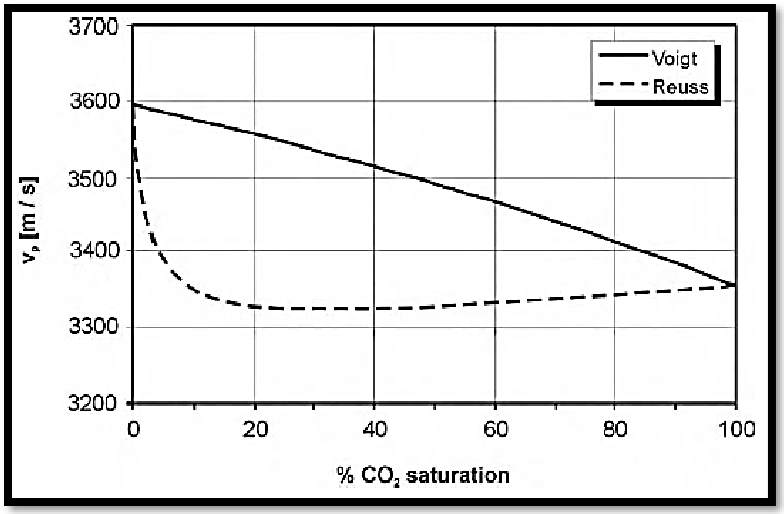

Figure 6-20. The influence of mixing method on the P-wave velocity. Reuss average is suitable for a fine mixed fluid, and the velocity change, in this case, is very dramatic in the low saturation of CO2.Over 15% of CO_2 saturation there is a slight increase in the velocity of the formation (a test with the low-frequency laboratory data). The Voigt average is for a patchy mixing, and the velocity change is almost a linear decrease with saturation (a test with the high-frequency laboratory data) (Smith, 2003).

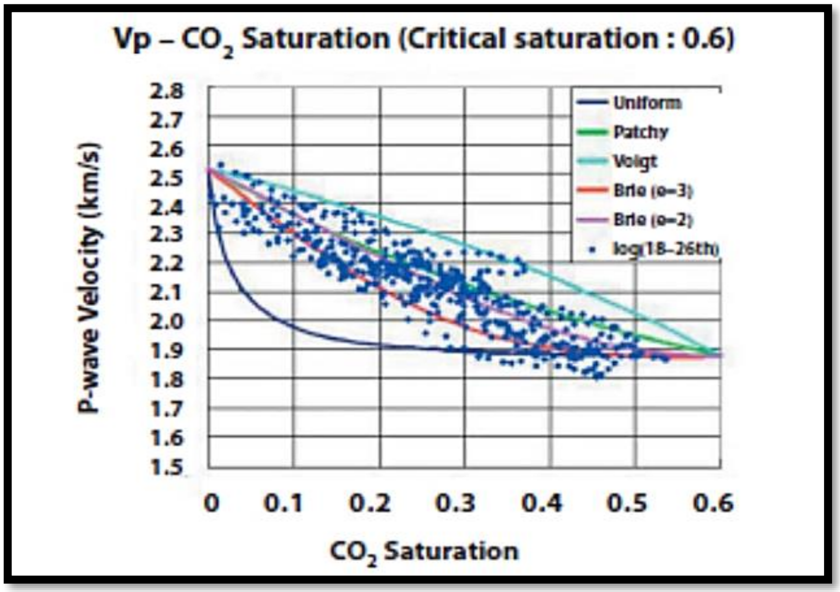

Figure 6-21. P-wave velocity versus CO_2 saturation from a field study. The blue dots show the field data measurements from time-lapse well logs at the Nagaoka site in Japan (Lumley, 2010).

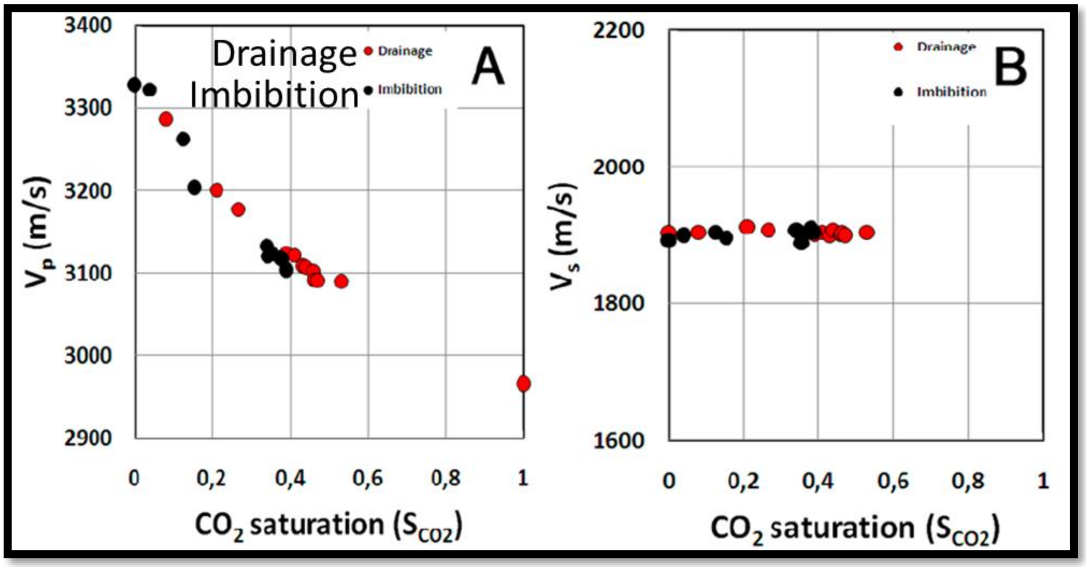

Figure 6-22. Results of lab test for the CO_2 injection into a sandstone (Alemo et al., 2011)

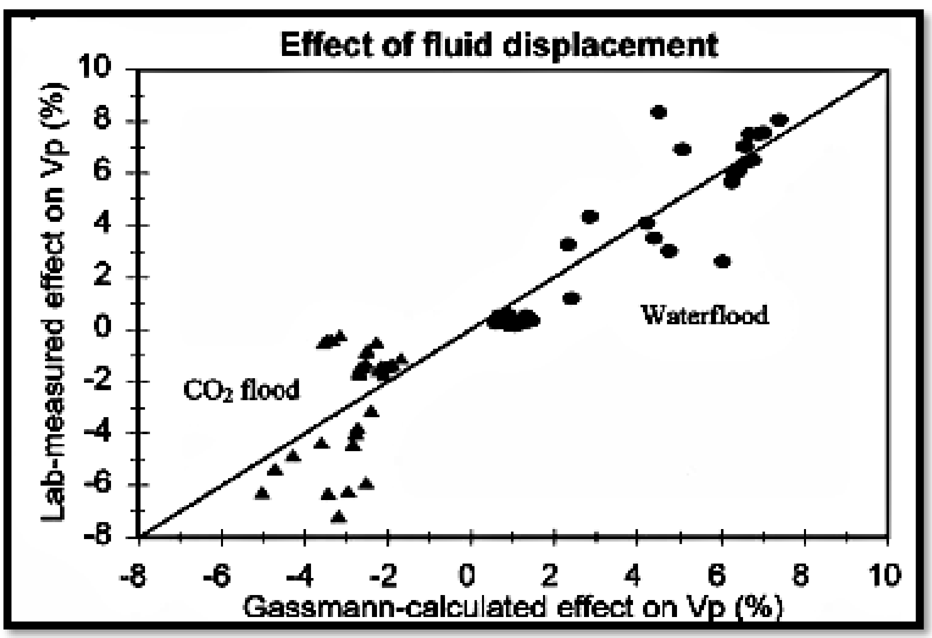

Figure 6-23. Laboratory and theoretical experiences for CO_2 and a water flood effect on the P-wave velocities (Wang, 2001).

The results of the field time-lapse and lab test show a P-wave velocity change due to CO_2 injection near to VRH or Brie's averages (in the 0-10% CO_2 saturation range it is the lower boundary, see Figure 6-21) that shows a semi-patchy mixed fluid type (Lumley, 2010), (Wang, 2001), (Alemo et al., 2011). So, in the FRS time-lapse seismic estimation, it is expected to see a semi-patchy mixed type in the reservoir according to the research. For the synthetic seismic models, we considered all mixed models for the P-wave velocity. Comparing the acquired field 4D seismic data with the synthetic seismic data in the various mixed conditions can reveal a realistic fluid mix type in the reservoir.

6.15 Time delay caused by the injected fluid

As it was demonstrated in the last section (as Figure 6-22), the P-wave velocity decreases with the CO_2 injection in the reservoir with brine content initially (except over 50% CO_2 saturation for the fine mixed fluid). The time delay for a P-wave passing from the reservoir horizon can explain as Eq. 6-26.

$$\Delta T = Z\left(\frac{V_2 - V_1}{V_2 V_1}\right)$$

Eq. 6-26

Where Z is the thickness of the injection target, V_1 is the initial velocity of the formation and V_2 is the formation velocity after injection. For a reservoir with n horizons (or cells) can be described as a summation of Eq. 6-26 as Eq. 6-27 (i is the number of the horizon).

$$\Delta T = \sum_{i=1}^{n} Z_i\left(\frac{V_{2i} - V_{1i}}{V_{2i} V_{1i}}\right)$$

Eq. 6-27

The time delay caused by the CO_2 injection in the below levels of the FRS reservoir is clearly demonstrated in Figure 7-27.

6.16 The formation velocity and density after CO_2 injection in the FRS reservoir

The injection of the CO_2 can change the acoustic attributes. The compressional wave velocity is decreasing by two effects: a- The bulk module of the injected CO_2 is lower than the primary pore fluid (brine). b- The effective pressure has a reverse relation with the velocity; CO_2 injection can decrease the effective pressure and velocity.

The bulk density of the fluid and consequently the formation decrease after gas injection. This change in the density can cause a slight increase in the shear wave velocity. The density calculation method is based on the well log density and porosity and calculated fluid density. Figure 6-26 shows the variation of the density and Vs by the injection as a function of CO_2 saturation (fraction). The diagrams that demonstrate the result of the fluid substitution by Gassmann's method is in Figure 6-24 for Voigt average and Figure 6-25 for the four average methods. Based on the upper and lower boundaries (Voigt and Reuss) it is possible to estimate the maximum and minimum velocity of the formation versus the gas saturation. Also, we calculated two models in the middle of the Reuss and Voigt boundaries (VRH and Brie) in this section, and we will introduce the 2D model for Vp in each year based on the mixed fluid type (Reuss (fine mixed) as lower boundary, VRH, Brie, and Voigt (patchy) as the upper boundary).

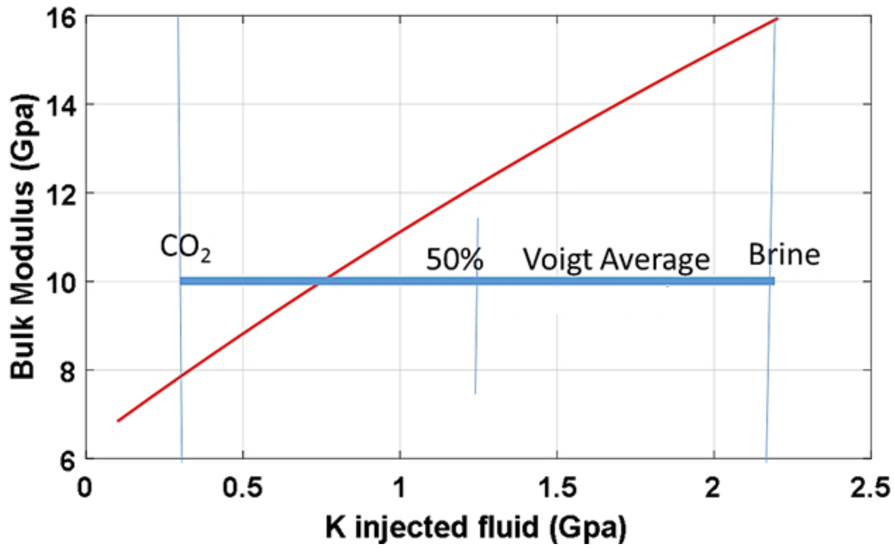

Figure 6-24: Bulk modulus for CO_2 and brine mixed phase.

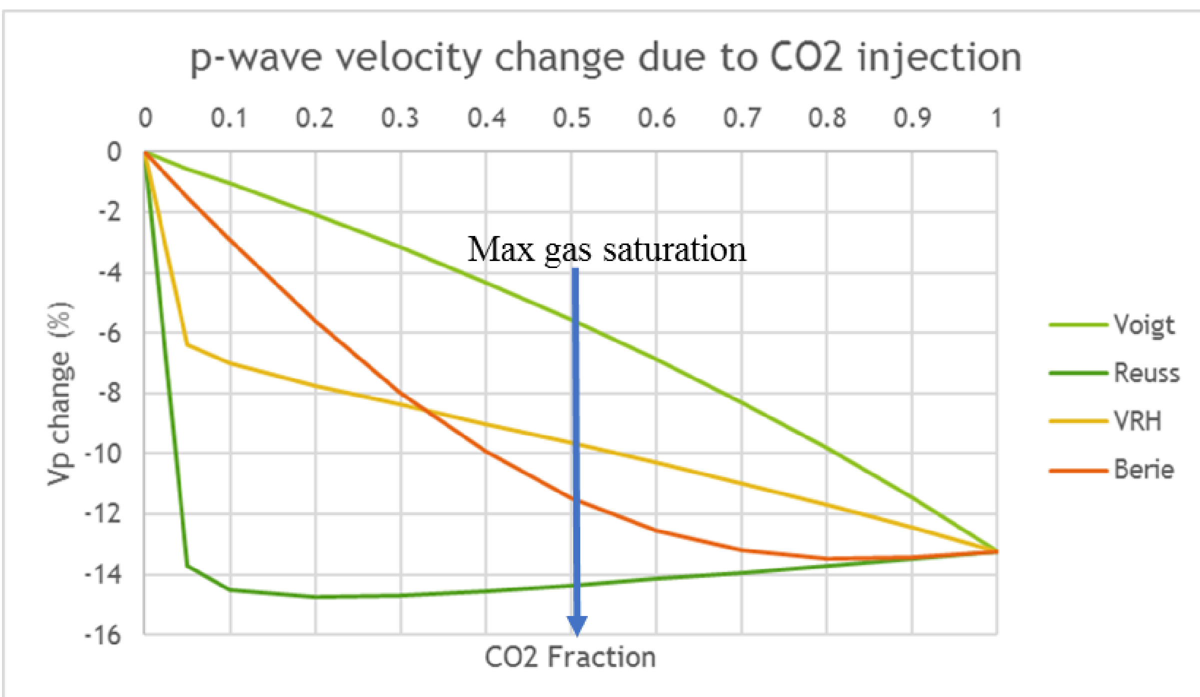

Figure 6-25. P-wave velocity after CO_2 injection in the reservoir calculated by Gassmann's equation, the shape of Vp diagram is a function of an average method for the fluid mix (CO_2+brine) properties calculation. The maximum possible CO_2 gas saturation in the FRS reservoir can reach to 50%.

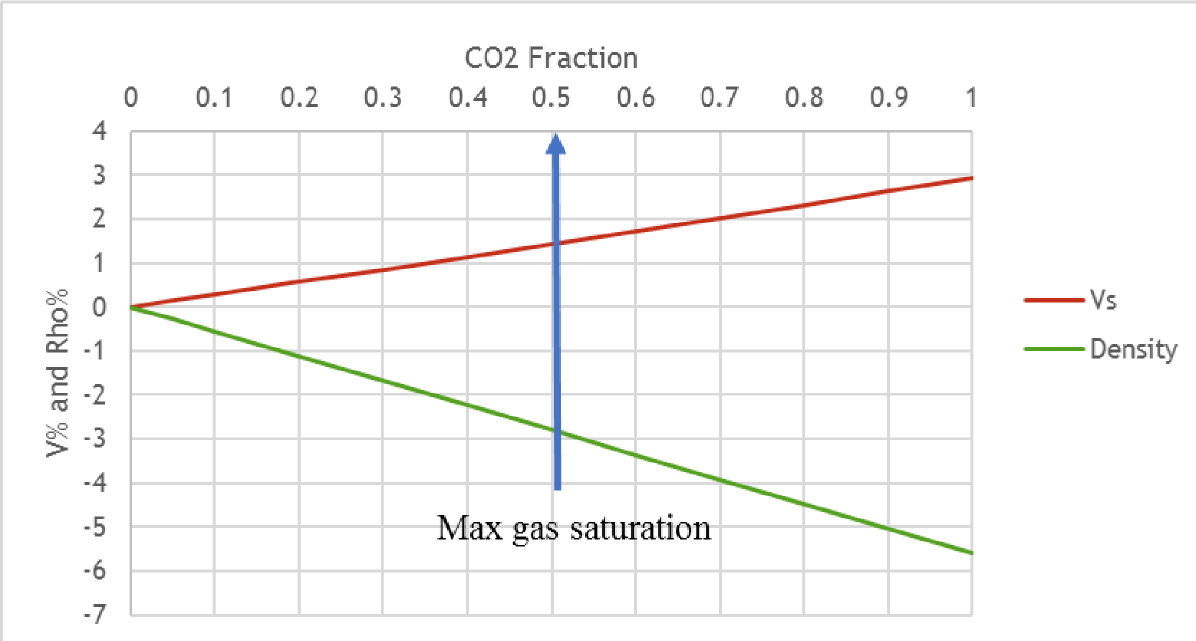

Figure 6-26: The physical properties (S-wave velocity and density) change as a linear function of the CO_2 saturation in the reservoir condition in FRS project.

6.17 The velocity and density model based on the rock physics study

The dynamic parameters of the fluid simulation were calculated in the last chapter. The result of the rock physics study can help us to translate the gas saturation and pressure in each cell to the seismic related physical parameters (velocity and density). The density was estimated by a linear function, and s-wave velocity is a secondary parameter that fluctuates with the density change. The gas injection in the reservoir can decrease the density up to 2.9% so that the shear wave will increase up to 1.5% in the gas saturation equal to 50%. The shear wave velocity and density change in the plume (after 1 to 5-year injection) were demonstrated in Figure 6-27. For this purpose, we used a linear converter as Figure 6-26 (for the density and Vs) on the matrices from fluid simulation procedure that shows the gas saturation in 2D dimension.

The P-wave velocity has a different calculation method that introduced in section 6.16. For each kind of fluid mix and average method, a P-wave velocity model was calculated (Figure 6-28 for the fine mixed (Reuss average), Figure 6-29 and Figure 6-30 for the semi-patchy mix (Brie and VRH average) and finally Figure 6-31 for the fully patchy mix (Voigt average)). As mentioned in the last section, the type of fluid mixture (can be patchy or fine mixed) has a huge effect on the P-wave velocity. The maximum range of P-wave velocity change by the CO_2 injection in the Basal Belly River sandstone is up to 15%, in the fine mixed type (fine mixed) for the 20% gas saturation. This condition for the fully patchy condition is about 2% variation in Vp for a gas saturation equal to 20%. As motioned in the last section, Lumley (2010) demonstrated a semi patchy condition with the CO_2 injection in Nagaoka field (Figure 6-21), so the field result shows that Vp is near to VRH and Brie's average. However, in this research for an accurate estimation, all mixed conditions will be tested in the next chapter for time-lapse seismic modeling and imaging.

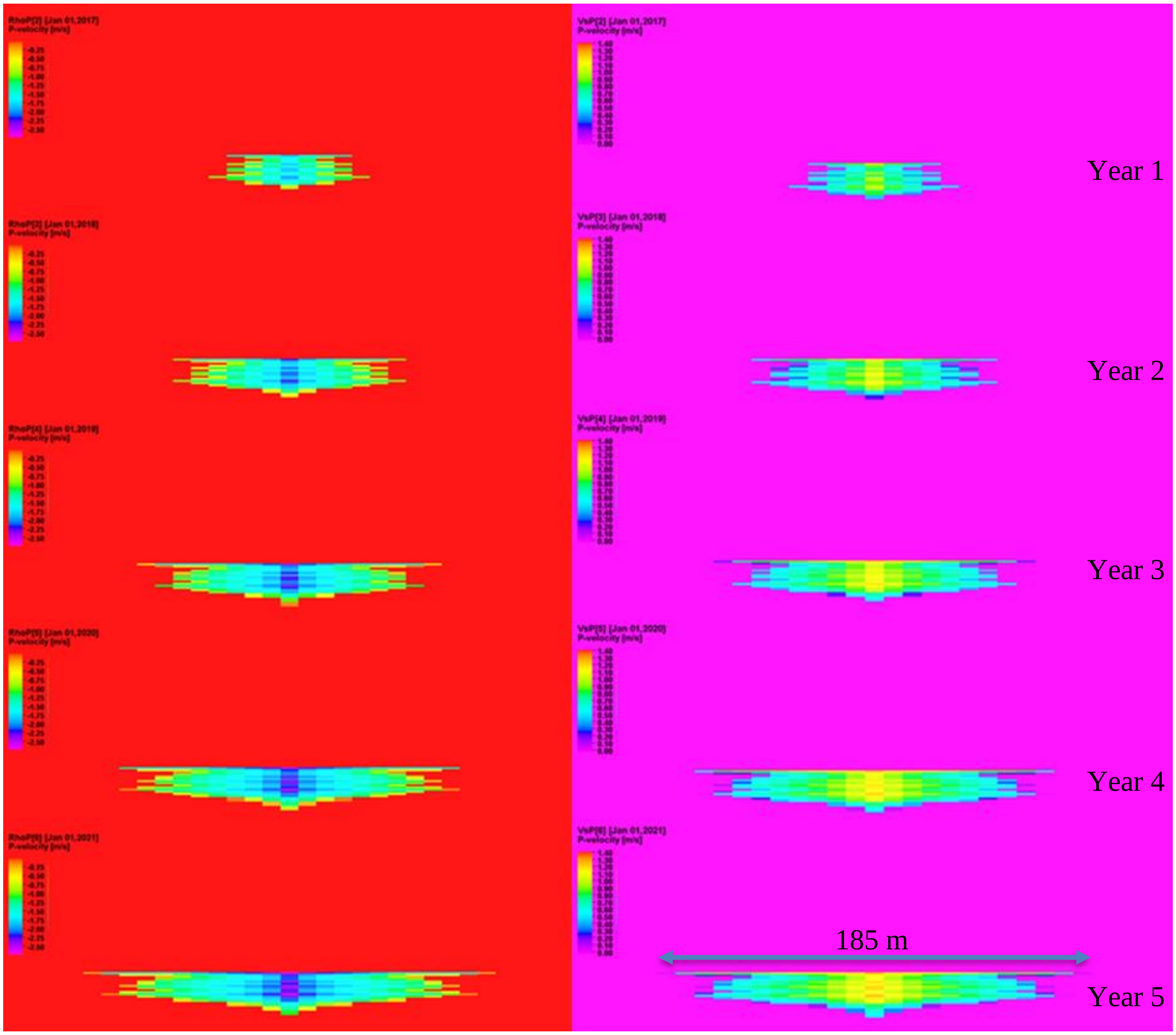

Figure 6-27: The density, and shear wave velocity change during the gas injection by the constant bottom hole pressure (49.4 bar for five-year). The shear modulus remains constant after injection, but decreasing in the density can make a small increase in the Vs value.

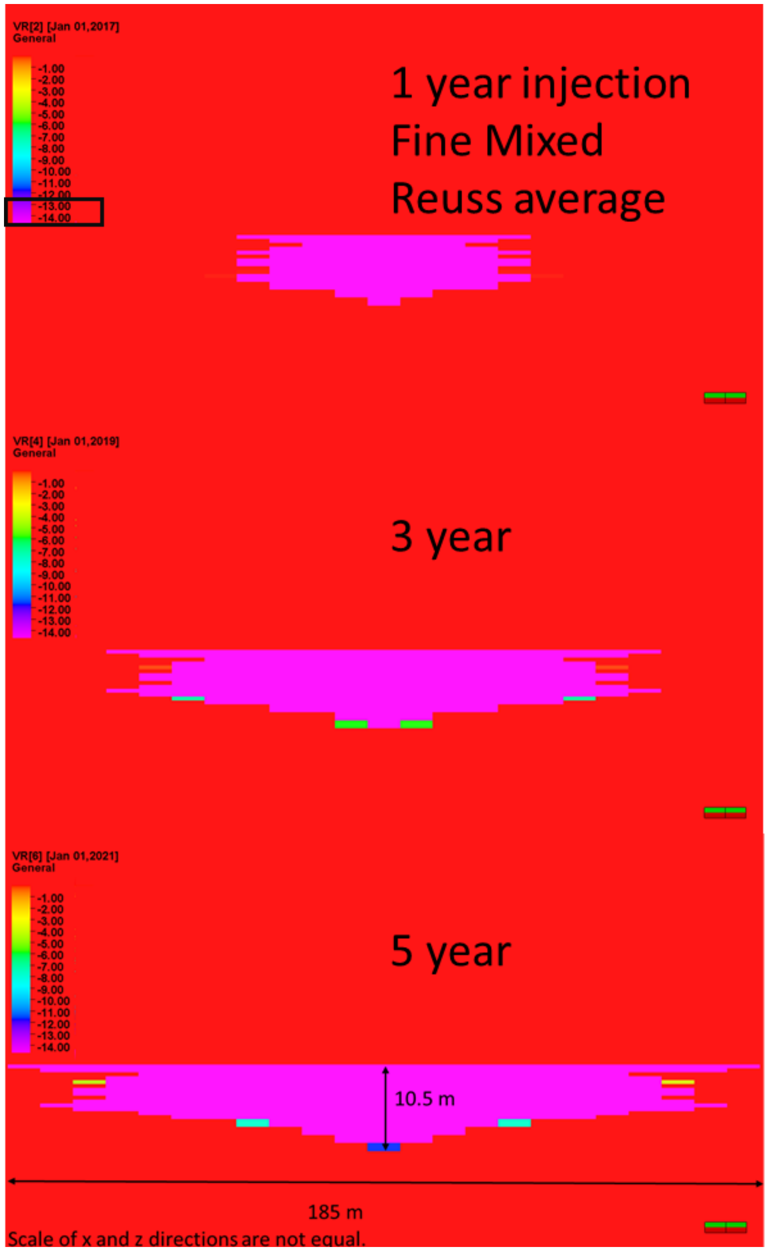

Figure 6-28. The P-wave velocity model based on the Reuss average method that shows a fine mixed fluid type after 1, 3 and five years' injection. This model shows a uniform velocity change in the reservoir volume.

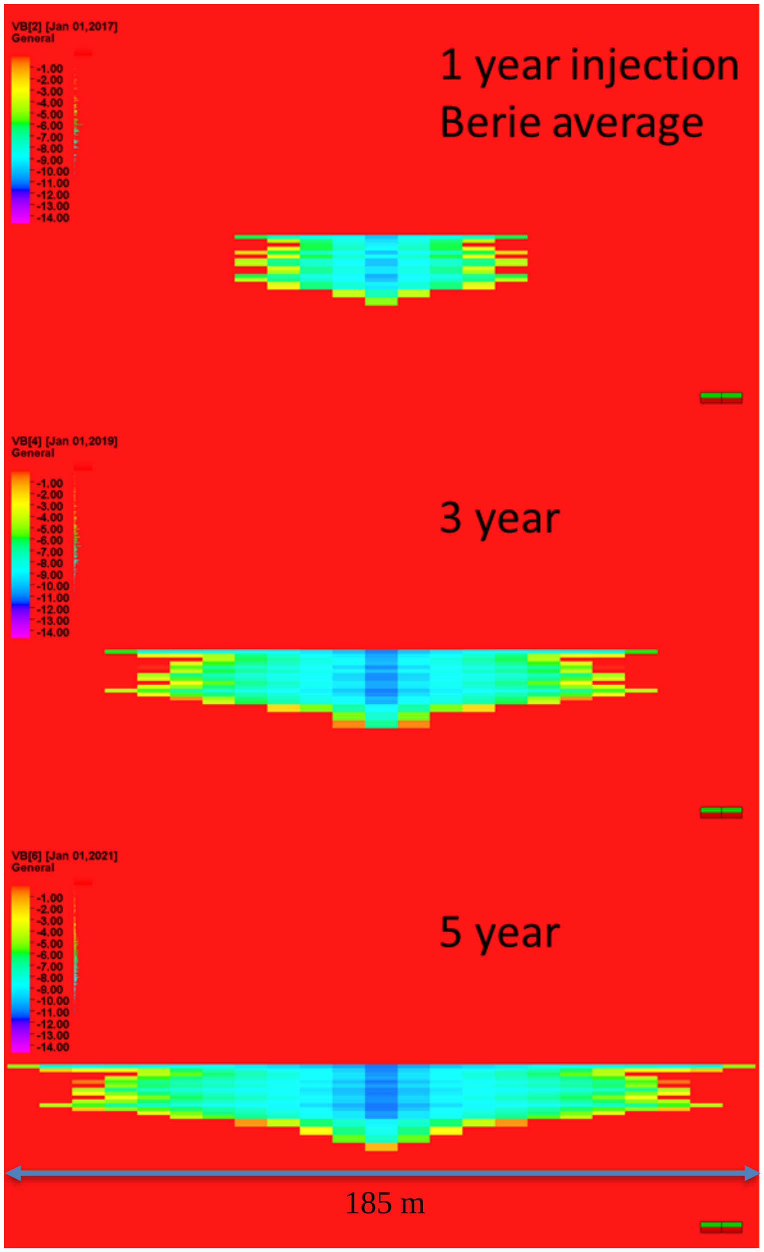

Figure 6-29. The P-wave velocity model based on the Brie's average method that shows a semi-patchy mixed fluid type after 1, 3 and five years' injection.

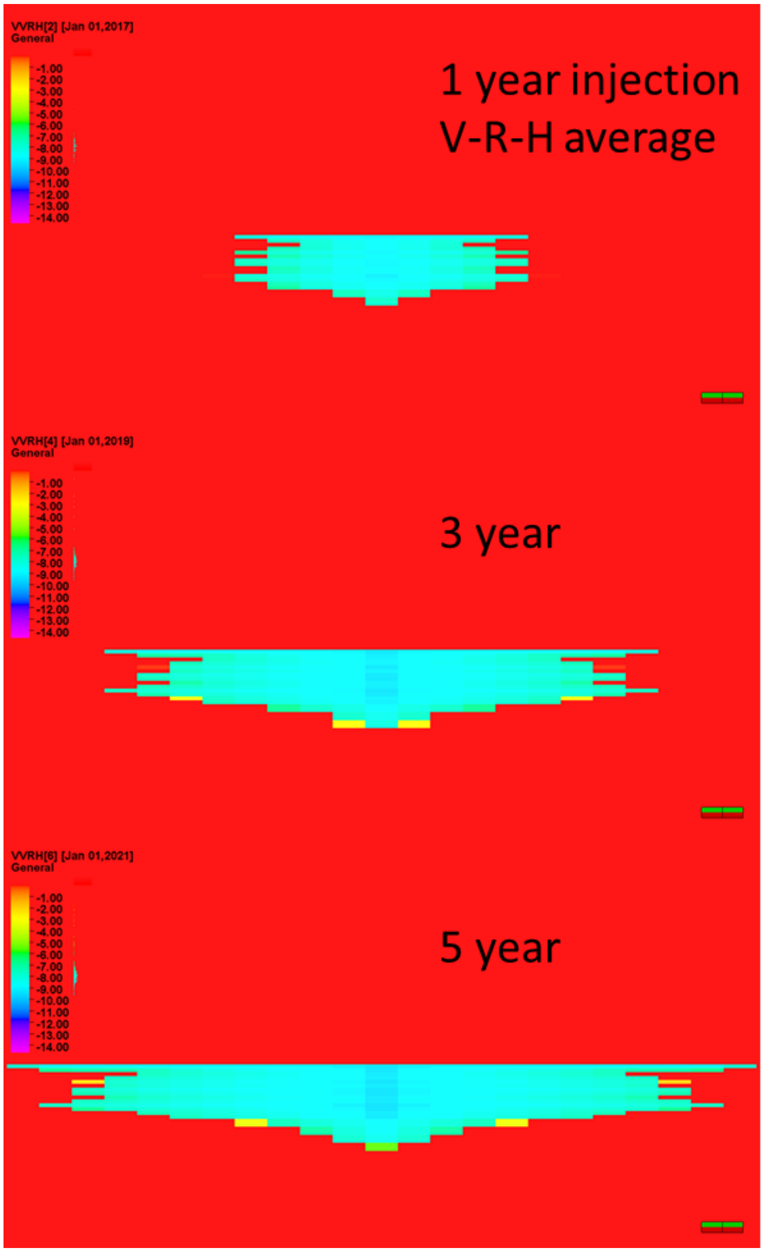

Figure 6-30. The P-wave velocity model based on the VRH average method that shows a semi-patchy mixed fluid type after 1, 3 and five years' injection.

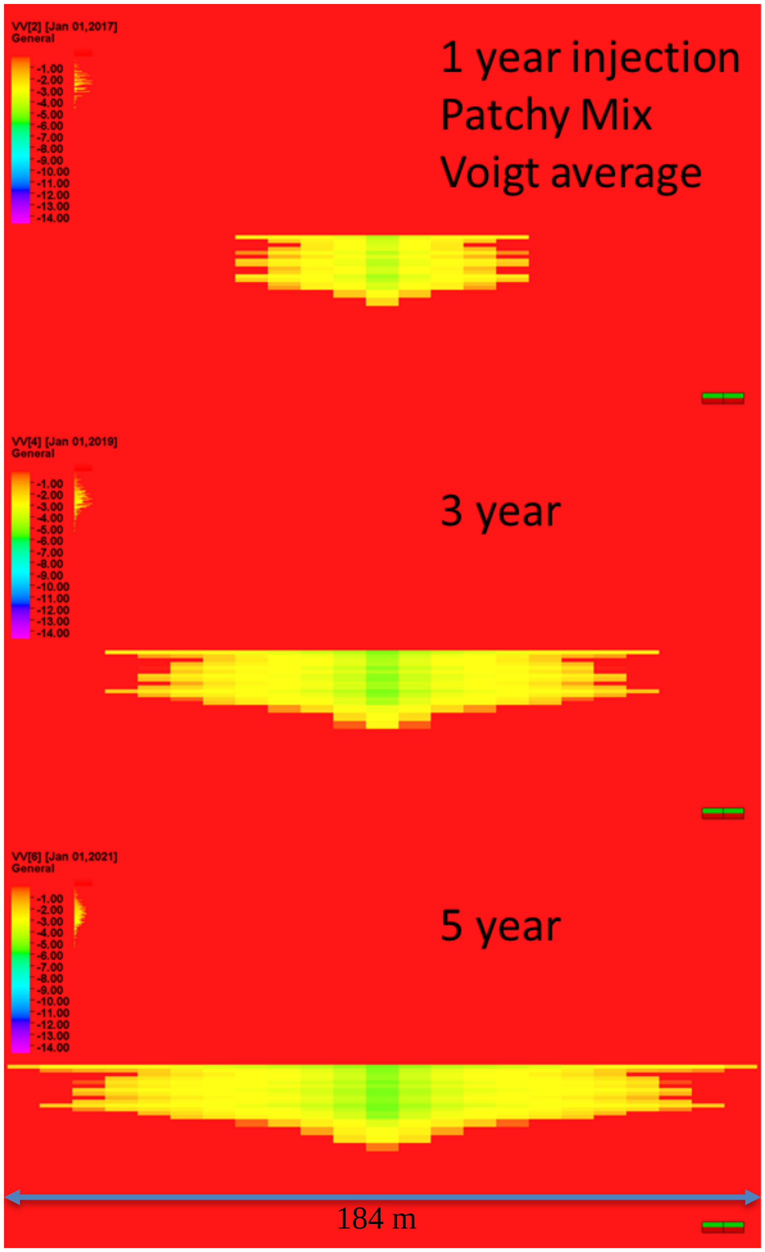

Figure 6-31. The P-wave velocity model based on the Voigt average method that shows a fully-patchy mixed fluid type after 1, 3 and five years' injection.

Chapter 7. SEISMIC IMAGING

7.1 Introduction

The goal of the seismic studies in the last century was the exploration and imaging for predicting promising structures to drill production wells in the low-risk location. Currently, the reservoirs mostly have been explored, and they are in the production stage. Now the seismic studies can help to characterize the reservoir parameters and time-lapse variation of the reservoir's dynamic parameters during production/injection.

We now focus on the interpretability of seismic study with considering dynamic parameters of the reservoir and plume size and geometry. Also, we examine the influence of the acquisition configuration including surface seismic, VSP and Cross Well surveys. In the dissertation, I used advanced methods for the seismic modeling and imaging included acoustic forward modeling and Reverse Time Migration (RTM). For this purpose, I improved finite difference Matlab codes for modeling and RTM, and made it possible to have flexible source and receiver locations. The code makes it possible to control and check the influence of the acquisition geometry on the seismic response of a reservoir for a successful time-lapse program. Also, code was developed to import geomodel data from Petrel and simulation data from ECLIPSE. By this code, the velocity (P-wave velocity by Gassmann's equation) and density were calculated and located in the corresponding cells. We used synthetic velocity models to make seismic model and to image and compare seismic responses of a reservoir with different CO_2 saturations, pressure, and the plume size for various saturation types and for a different kinds of acquisition geometry.

The content and research topics in this chapter will include:

1- Introduction to the forward modeling and RTM.

2- The seismic response for the different plume size and saturation in a reservoir.

3- The acquisition configuration influence in a time lapse study.

4- The seismic time-lapse models for the FRS project with various types of mixing of the reservoir fluids.

5- The reservoir dynamic parameters for time lapse studies and seismic models.

6- The elastic response of the reservoir.

7.2 The research method

In this chapter, the forward seismic modeling and RTM methods, the problems and noise associated with the RTM algorithem and some methods for noise reduction are described. The seismic modeling and analysis of the reservoir were assessed by seismic finite difference time domain (FDTD) modeling based on an acoustic velocity-stress staggered leapfrog scheme. The FDTD is second order in time and fourth order in space within a Central Finite Difference (CFD) framework. The boundary conditions are stablished at all edges of the input model except at the surface, based on a Perfectly Matched Layers (PML) approach.

Based on the synthetic models, there is an amplitude change in the reservoir and a time delay in the deeper levels because of velocity changes that result from CO_2 injection. The effect of the time delay is removed after depth migration with an accurate velocity model. As mentioned, the seismic models include surface seismic, VSP and cross well surveys. The well seismic surveys show high amplitudes due to gas injection, and because of lower noise content in these methods, we expect to map the reservoir properties in the early injection step (even in the patchy mixed condition) by well seismic acquisition. The surface seismic models show lower amplitudes than the well seismic methods after injection. The source of the main noises as traffic, wind, electricity lines are on the surface.So the monitoring by surface seismic methods may not give a proper result in the first years of injection (for a low-velocity variation in the reservoir due to CO_2 injection) when saturation and plume size are small, but we will demonstrate that the surface seismic can generate better images of a reservoir compare to well seismic.

7.3 Acoustic forward modeling strategy

The 2D acoustic wave equation can be expressed by Euler's equation and the equation of continuity (e.g., Brekhovskikh, 1960 and Zakaria et al., 2000). A system of first-order differential equations regarding the particle velocities and stresses is given by Eq. 7-1.

$$\left.\begin{aligned} \frac{\partial v_x}{\partial t} &= -\frac{1}{\rho}\frac{\partial p}{\partial x}, \\ \frac{\partial v_z}{\partial t} &= -\frac{1}{\rho}\frac{\partial p}{\partial z}, \end{aligned}\right\} \qquad \textit{Euler}$$

$$\frac{\partial p}{\partial t} = -\rho {v_P}^2\left(\frac{\partial v_x}{\partial x} + \frac{\partial v_z}{\partial z}\right), \qquad \textit{Continuity}$$

Eq. 7-1

Where p is the pressure, v_x and v_z are particle velocities in lateral x and vertical z directions respectively. The parameters ρ and v_p are density and the P-wave velocity and t is the time. The numerical solution is based on the FDTD of the staggered grid in a leapfrog scheme. The FDTD is 2nd order in time and fourth order in space on Central Finite Difference (CFD). The

Perfectly Matched Layers (PML) boundary condition of Zhou (2003) is used for all edge of the model except the surface.

7.4 RTM migration strategy

The RTM include three simultaneous imaging conditions given by Eq. 7-2:

$$I_u(\vec{x}) = \int_0^{T_{\max}} S_u(t,\vec{x}) R_u(t,\vec{x})\,dt,$$

$$I_v(\vec{x}) = \int_0^{T_{\max}} S_v(t,\vec{x}) R_v(t,\vec{x})\,dt,$$

$$I_p(\vec{x}) = \int_0^{T_{\max}} S_p(t,\vec{x}) R_p(t,\vec{x})\,dt,$$

Eq. 7-2

Where $I(\vec{\boldsymbol{x}})$ is the migrated image in the subsurface coordinate $\vec{\boldsymbol{x}} = (x,y,z)$, T_{max} is maximum recorded time, $S(t,\vec{\boldsymbol{x}})$ is the forward propagated source and $R(t,\vec{\boldsymbol{x}})$ is the backward propagated receivers. The subscripts p, u and v correspond to three images for pressure and displacements obtained by the imaging conditions. Note that here, the Einstein summation convention is not used for repeated indices. The imaging condition of the RTM algorithm is a cross-correlation of forward propagation sources and backward propagating receivers (Whitmore et al., 2012):

$$I(X) = \frac{1}{A(X)} \int S(X,t) R(X,T-t) dt$$
$$X = (x, y, z)$$

Eq. 7-3

The RTM method is a robust migration method for imaging complex geology conditions (see section 7.17).

In this chapter, I demonstrate the seismic model results with abbreviation *SM*. For example, the seismic model of the baseline and after two-years do injection will be defined as *SM*(base) and *SM*(m2). Also, the migrated data by RTM method will be demonstrated with *RTM*(*SM*(base)). Figure 7-1 shows the abbreviations that used for the seismic modeling and RTM.

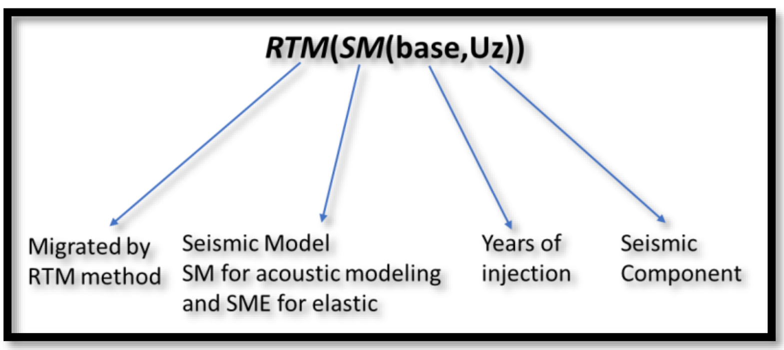

Figure 7-1. Description of the abbreviations.

7.5 Boundary Conditions

Boundary conditions are crucial in a synthetic modeling code that solves PDE numerically. The ordinary boundary can reflect the energy inside the model, and the result will be noisy data for the seismic processing stage. For the purpose of noise reduction because of the recursive wave, the Perfectly Matched Layer (PML) were include for the three internal boundaries of the model. Moreover, the upper boundary of the medium is free surface bound in the modeling code (see Figure 7-2).

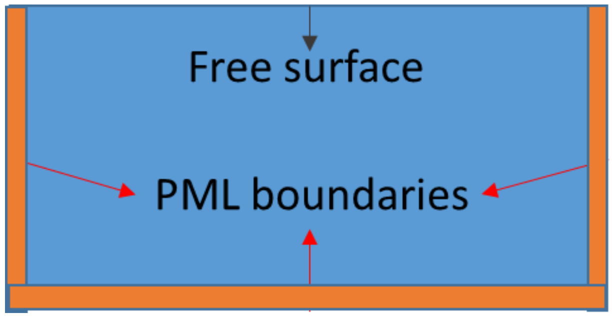

Figure 7-2.The Boundary condition in the seismic model. The orange rectangles show the internal boundaries.

7.5.1 The Perfectly Matched Layer (PML)

The first study of the PML boundary type dates back to (Berenger, 1994) in electromagnetics computation. PML boundary condition is referred to an absorbing layer or boundary for different kinds of the wave equation. It can make a mathematically infinite space for the wave to avoid the wave radiating back inside the model. Thus, it can have a simulated medium condition as open internal boundaries without any recursive waves. In the current modeling code, the absorption procedure begins at 20 cells from the boundary. It is an optimum size to make a near zero amplitude content for the wave in the internal boundaries.

The importance of usage PML boundary condition in the seismic modeling is related to the decreasing noise in the migration step. The RTM migration code can not support and eliminate the noise of the boundaries, so for an ideal result, the noise should be removed from seismic data before migration.

The formulation of split PML method (SPML) was used for this chapter. In this approach, the wave field was split into two components (Carcione et al., 2002) as (Eq. 7-4).

$$p = p_x + p_z$$
$$\frac{\partial p_x}{\partial t} = v^2 \frac{\partial v_x}{\partial x}$$
$$\frac{\partial p_z}{\partial t} = v^2 \frac{\partial v_z}{\partial z}$$
$$\frac{\partial v_x}{\partial t} = \frac{\partial p}{\partial x}$$
$$\frac{\partial v_z}{\partial t} = \frac{\partial p}{\partial z}$$

Eq. 7-4

by adding the decaying coefficient d(u)=(d(x), d(z)) the Eq. 7-4 can be reworked as Eq. 7-5 (Collino and Tsogka, 2001):

$$p = p_x + p_z$$
$$\frac{\partial p_x}{\partial t} + d(x)\,p_x = v^2 \frac{\partial v_x}{\partial x}$$
$$\frac{\partial p_z}{\partial t} + d(z)\,p_z = v^2 \frac{\partial v_z}{\partial z}$$
$$\frac{\partial v_x}{\partial t} + d(x)v_x = \frac{\partial p}{\partial x}$$
$$\frac{\partial v_z}{\partial t} + d(z)v_z = \frac{\partial p}{\partial z}$$

Eq. 7-5

Where d(x) and d(z) can define Absorbing Boundary Condition (ABC) coefficients as shown in Figure 7-3.The ABC coefficients can be represented by Eq. 7-6 (Collino and Tsogka, 2001):

$$
\begin{aligned}
&d(u) = d_0 \left(\frac{u}{L}\right)^2 \\
&d_0 = -\frac{3v}{2L}\ln(R) \\
&u = x, z
\end{aligned}
\qquad \text{Eq. 7-6}
$$

L indicates the thickness of PML boundary and R is usually chosen between 10^{-3} to 10^{-6}. SPML is applicable also for the elastic medium as well (Collino and Tsogka, 2001). A sample of SPML for the elastic medium and the P-wave source was tested in the MATLAB, and the result is demonstrated in Figure 7-4.

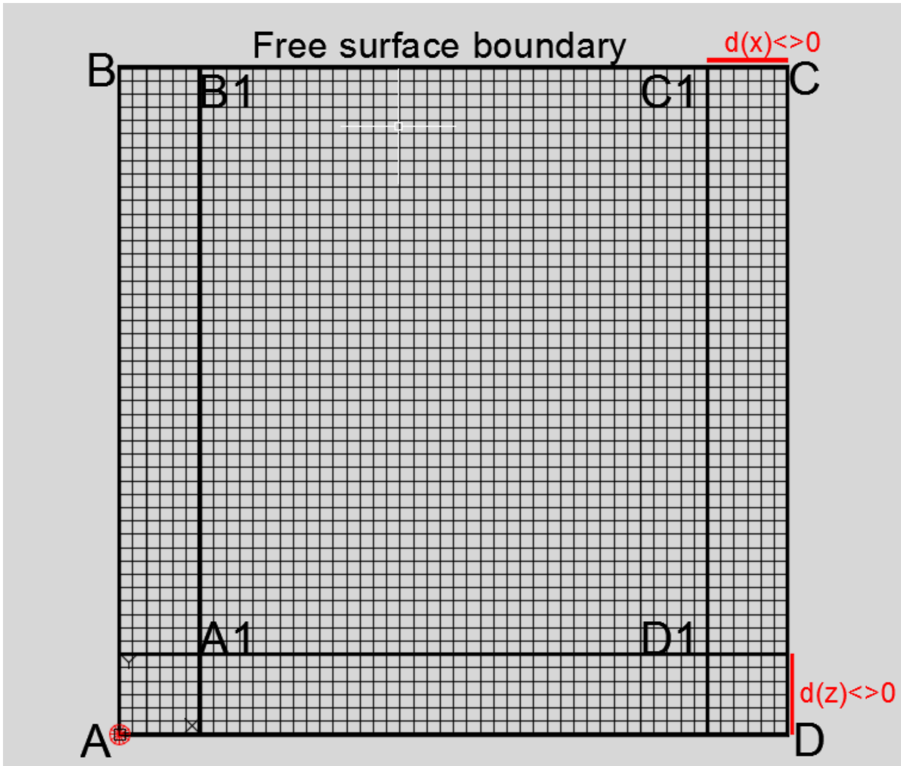

Figure 7-3. The model boundary is shown by ABCD. AB, CD, and AD have a SPML boundary condition, and BC is a free surface boundary.

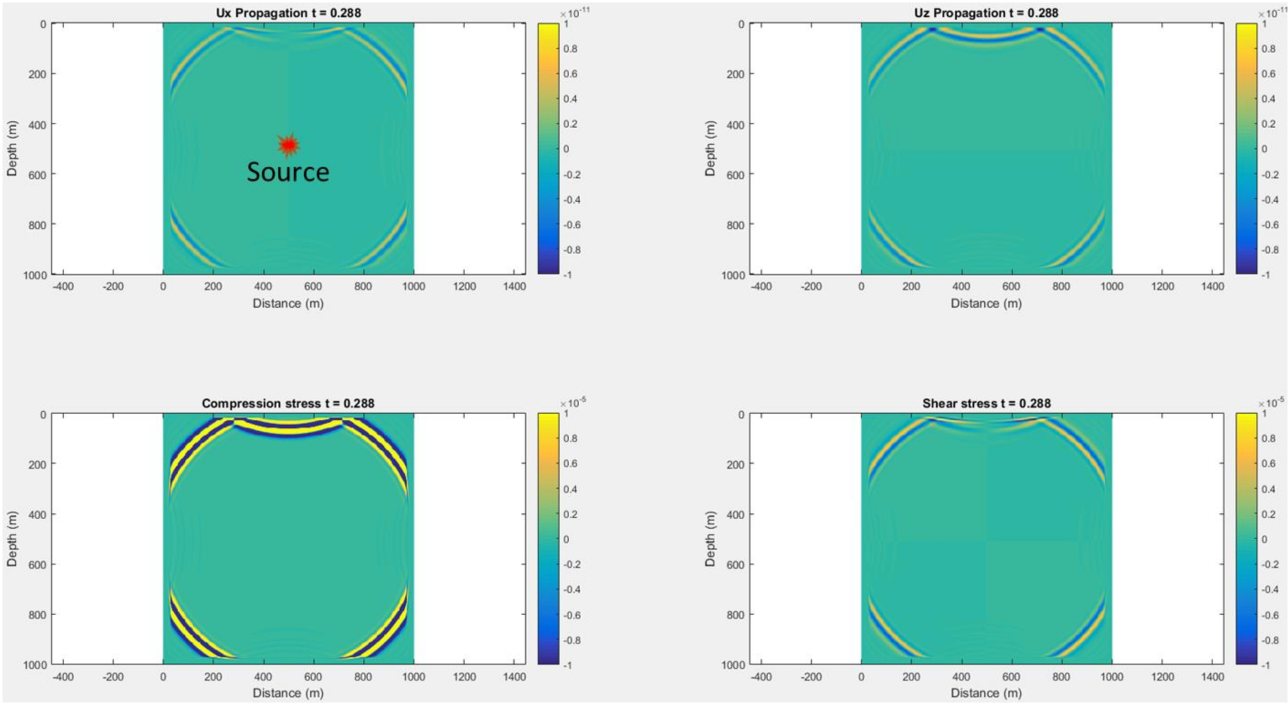

Figure 7-4. The different components of the wave at the PML absorption boundaries for a P-wave source in an elastic homogenous medium.

7.6 Low-frequency noise due to RTM procedure

The RTM algorithm can generate various type of noise (Khalil et al., 2014). Low-frequency noise is one of artifacts that can be recognized in high-velocity contrast zones. After time reversal of the receiver wavefield, the artifacts of the RTM occur where the two wavefields are traveling in the same direction; the inverse scattering imaging condition attenuates low wavenumber noise (Whitmore et al., 2012). Also, the Laplacian filter is used for low-wavenumber noise reduction (Liu et al., 2010) and (Martinez, 2016).

In this research, we use subtraction of monitor seismic model and the baseline with the first order derivative for the noise reduction. The work procedure is:

1- Construct the seismic model including the reservoir of interest.

2- Construct a baseline without any fluid substitution, and a monitor model after fluid substitution.

3- Make a seismic model and RTM image of both velocity models

4- The difference between the seismic models as RTM(SM(m))-RTM(SM(baseline)) can decrease the noise. This method is used in the current research for the noise reduction without any effect on the seismic data quality.

5- A derivation of the RTM result can decrease the low-frequency noise effect. This method can reduce the amplitude of the seismic result. This function is available in the MATLAB software. Figure 7-14 and Figure 7-15 later in this chapter show the result of (diff) function that used on the RTM result. The (diff) can be explained as (from MATLAB help):

    diff(X), for a vector X, is [X (2)-X (1), X (3)-X (2), ... X (n)-X (n-1)].

    diff(X), for a matrix X, is the matrix of row differences, [X (2: n, :) – X (1: n-1, :)].

7.7 Condition for successful 4D study

Seismic inversion can provide us four acoustic attributes including: Vp, Vs, density and Q (Mavko, 2010). For the reservoir study, one needs to have an ideal estimate for converting acoustic attributes to the reservoir's static and dynamic parameters. In a time-lapse study, an interpretation is possible by calculating the difference of seismic images during production. The first step is acquiring seismic data before any injection called the baseline survey. The repeated seismic acquisition and difference of the data should be interpretable. For interpretability, we need to address two parameters in the seismic data, the amplitude change reflectivity, and time delay because of the velocity change in the reservoir area. The parameters change the acoustic properties are plume size, pressure, and saturation.

A time-lapse (4D) study needs a 3D repeatable acquisition, so for this purpose the receivers and source points should be exactly in the same place. It means a successful 4D study needs specific CMP points for baseline acquisition. The FRS 4D seismic design is described in chapter 3.

The factors for a successful 4D study are (Johnston, 2013):

1- Integrate reservoir data with the 4D seismic interpretation.

2- Understanding of the rock physics behind the production or injection procedures.

3- Low-noise and repeatable seismic data.

4- Accurate reservoir characterization.

5- Optimal timing of repeat surveys.

7.8 Interpretability of an event

For quantitative seismic interpretation, the amplitude and coherency of data is important for an interpreter. An seismic event such as a reservoir or a structural shape can be interpretable by the phase change and visible amplitude variation, and a 4D seismic data change can be represented by:

$$\text{4D seismic change} = (\text{Monitor data} + \text{ERROR}_m + \text{Noise}_m) - (\text{Base data} + \text{ERROR}_b + \text{Noise}_b)$$

Acquisition footprint and noise can mask a weak seismic response of changes in a reservoir in a time-lapse study. In real field acquisition, amplitude can be affected by source, receivers, physical properties of the earth and environmental noises including:

1- The source and the recording system (arrays, type, and coupling)

2- All kinds of noise in the field (road and traffic noise, electricity line, wind)

3- Reflection coefficients of the formations and layers

4- Absorption of the formations

5- Multiples and ghosts.

In this chapter, I consider a noise-free data set for a primarily technical research about the seismic responses of the reservoir. In the next section, the influence of the plume size and formation saturation is tested by seismic forward modeling.

7.9 Plume size and velocity variation

The reservoir imbibition/drainage always cause a change in the fluid content and pore pressure of the formation. The secondary effects of the fluid substitution are the velocity and density variations. The halo of the velocity change in a reservoir is a function of the plume size and the CO_2 saturation (and the plume size is a function of the porosity and permeability). So, the velocity change is a function of such parameters as:

$$\mathit{\Delta} K = f\left(\varphi\ , \Delta\rho,\ \ \mathit{\Delta} K_f\right)$$

Eq. 7-7

$$\mathit{\Delta} V = g(\mathit{\Delta} K, \mathit{\Delta}\rho)$$

Eq. 7-8

$$\text{Plume size} = \ \mathrm{h}(\mathrm{k}, \mathrm{Q})$$

Eq. 7-9

Where:

k: The permeability

$\mathit{\Delta} K$: The bulk modulus variation in the formation due to fluid substitution

$\mathit{\Delta} K_f$: the difference of bulk modulus between initial and the secondary fluid in the reservoir

Φ: The porosity

$\Delta\rho$: The density change in the reservoir by the fluid substitution, this parameter is a function of the phase saturation and porosity.

Q: A term for the production/injection strategy

7.10 A diffusive and solid velocity model

In the reservoir, through injection/production (fluid substitution), the saturation of CO_2 changes spatially. During fluid substitution procedure in a reservoir model the velocity and density variation of the cells in the reservoir network are a function of phase saturation. For this test, I considered a typical model of a reservoir. As the result of the previous chapter (Chapter 6), a velocity change in a reservoir can possibly result in two different versions of P-wave velocity anomalies. The "solid" velocity model is equivalent to the fine mixed fluid saturation for which the P-wave velocity is calculated by the Reuss average (non-linear). The “diffusive” velocity model is a result of patchy or semi patchy mixed type saturation that is calculated by a linear conversion of the saturation to the P-wave velocity (as Voigt or VRH average). I generated two different velocity models to test the seismic response, as shown in Figure 7-5. I considered that the fluid can diffuse semi-homogeneously in x and y-directions (the permeability in the y direction is seen to be lower than x direction) in the model. The gravity effect was not considered in the fluid injection in the diffusion model.

As mentioned above, the “solid” velocity pattern (Figure 7-5, right diagram) is made by a non-linear function as the Reuss average (or fine mixed fluid type) because the velocity of reservoir cells drop immediately after a low gas injection volume. The left diagram in Figure 7-5 is a “diffusive” velocity model that as mentioned, velocity decreases from the center to the ellipsoid boundary in a linear gradient.

In this section, the objective of all tests are for the diffusive and solid velocity models with different size (plume size) and velocity/density variations.

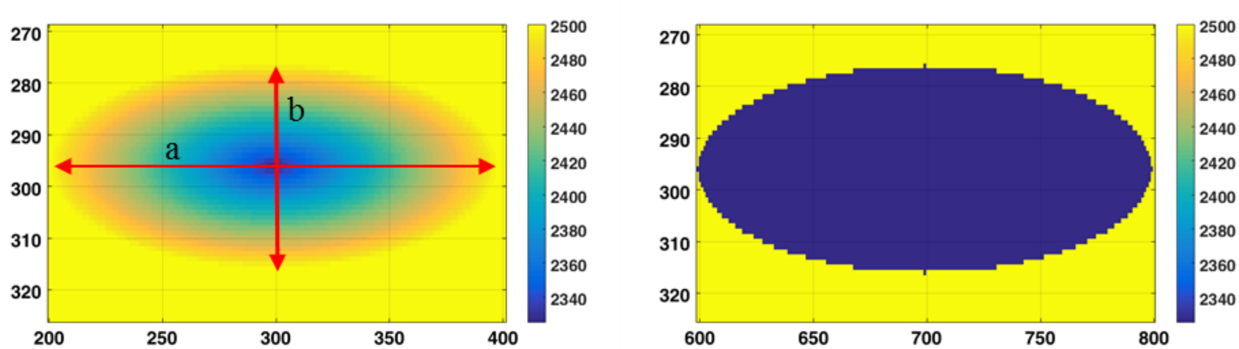

Figure 7-5. The internal structure of diffusive (an injective or productive point in the middle of the ellipsoid) and solid velocity models. The reduction is linear from the center to the outer bound in the diffusive model. The unit of velocity is m/s. The dimension of the ellipsoid will define with the big and small diameter (a,b).

7.11 Seismic response of a solid and diffusive velocity model

The first seismic model (Figure 7-6) compares the responses of a diffusive and solid velocity models in a homogeneous medium. For a simple model, even small alteration of velocity in the seismic resolution size is detectable, so this test will show the amplitude change by the solid and diffusive velocity without considering the absolute magnitude of the amplitude change.

Figure 7-6 shows a medium with V=2500 m/s and density=2200 kg/m3 and 1000*620 m dimension. The maximum velocity change in the center of the diffusive ellipsoid and solid shape is 7% equal to 175 m/s. The seismic modeling code can generate pressure, horizontal and vertical components. Figure 7-7 shows the Uz component of the seismic response; in the left diagram the surface effects (direct and surface waves) were not included.

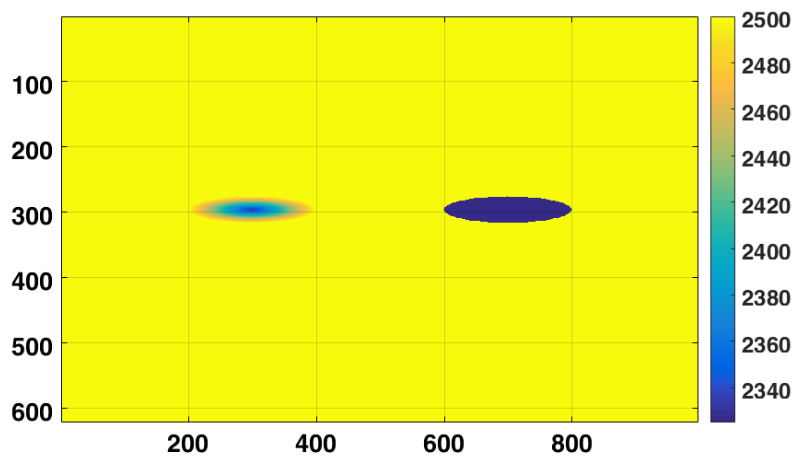

Figure 7-6.The velocity model with two diffusive and solid velocity changes. The velocity change in the center of diffusive model or whole solid shape is -7% equal -175 m/s (2325 m/s). The size is ellipsoids are (200,40m).

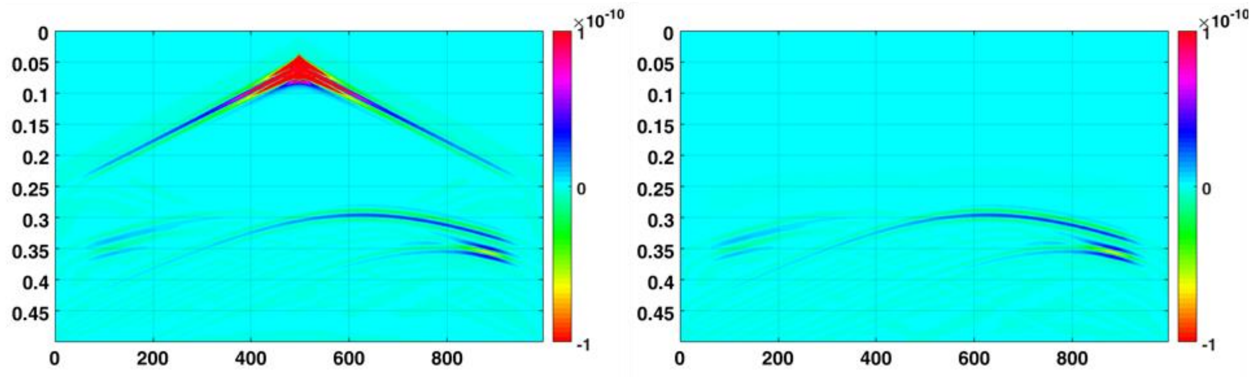

Figure 7-7.The Uz component of the seismic response of diffusive and solid models in a homogeneous medium. The left is the SM(m), and the right is SM(m)-SM(baseline).

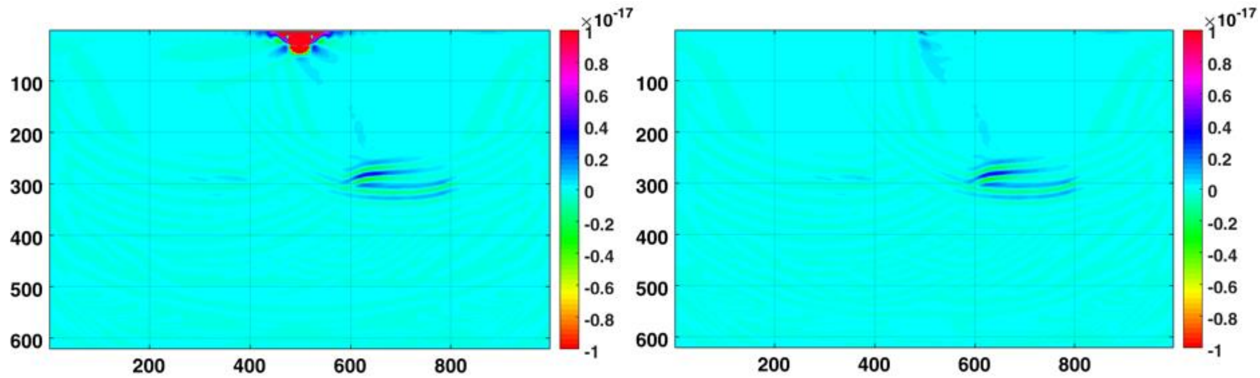

Figure 7-8. RTM(SM(m)) for Uz component and RTM(SM(m))-RTM(SM(baseline))

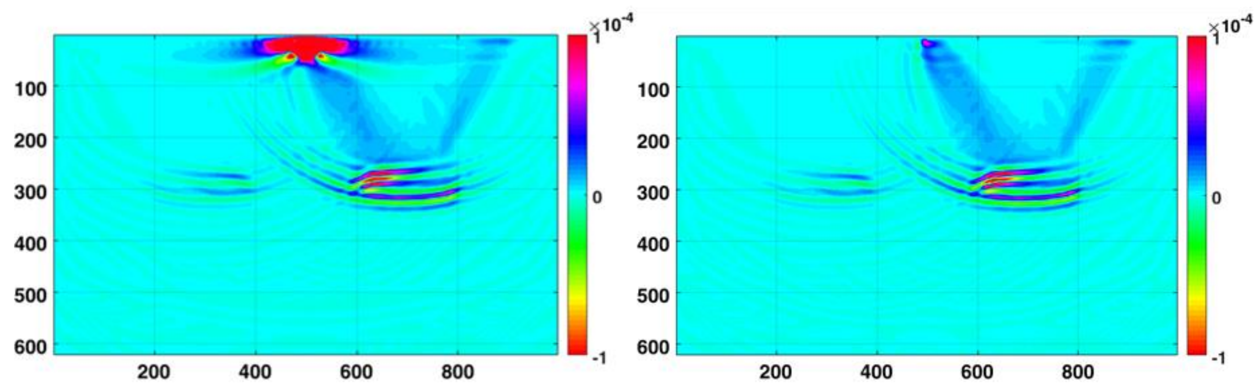

Figure 7-9. RTM(SM(m)) for pressure component and RTM(SM(m))-RTM(SM(baseline))

The results (Figure 7-7, Figure 7-8 and Figure 7-9) show that a simple velocity anomaly with a small change in a homogeneous and isotropic medium is detectable by the seismic method. Although impossible in the real world, the absence of noise and other reflectors in the medium is an advantage for the detectability of the event in our model (a reservoir). The seismic response and RTM results show a high amplitude with a clear image for the solid velocity boundary compared to the diffusive velocity distribution.

The second experiment was for a model with solid and diffusive velocity anomalies in a simple three-layer medium (as shown in Figure 7-10). The seismic responses are demonstrated in Figure 7-11 for pressure, Figure 7-12 for Uz and Figure 7-13 for Ux components. The processed RTM results for the pressure and Ux components are shown in Figure 7-14 and Figure 7-15 respectively and show that low-frequency RTM noise was eliminated. Figure 7-16 and Figure 7-17 show the same results without removing the noise. The diffusive velocity anomaly showed a seismic response that is weaker than the solid velocity anomaly and the amplitude in the seismic model and migrated section is less than for the solid form. However, both shapes caused a time delay effect under the ellipsoids in the seismic models.

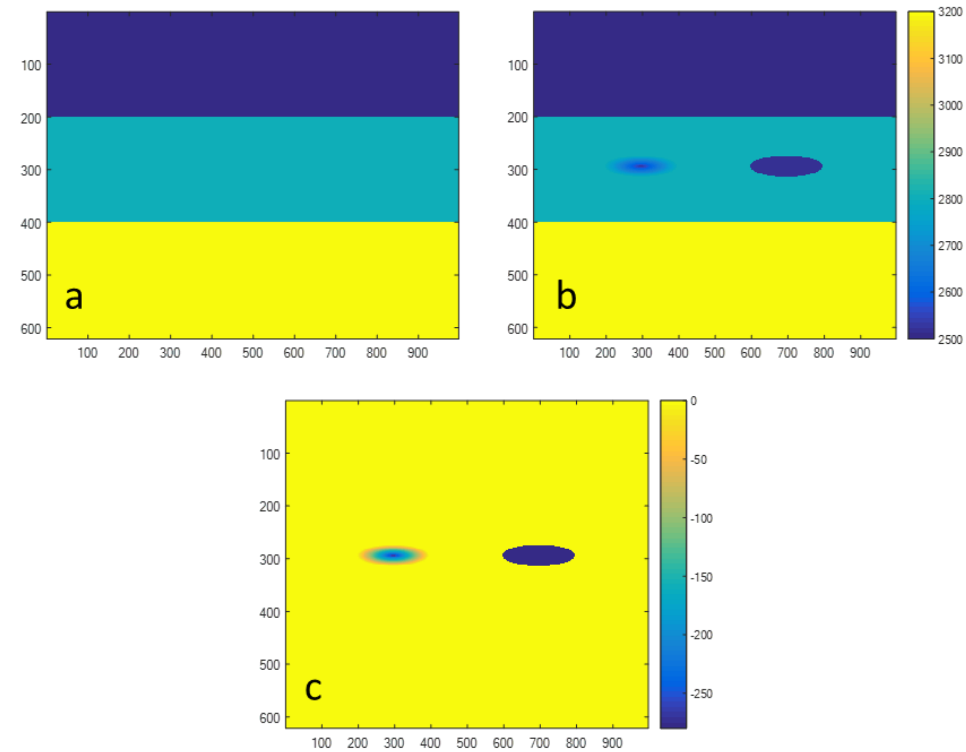

Figure 7-10.The velocity model for a. Three-layer model as baseline b. Model a with diffusive and solid velocity models as monitored model c. Subtracted result (Monitored-Baseline model)

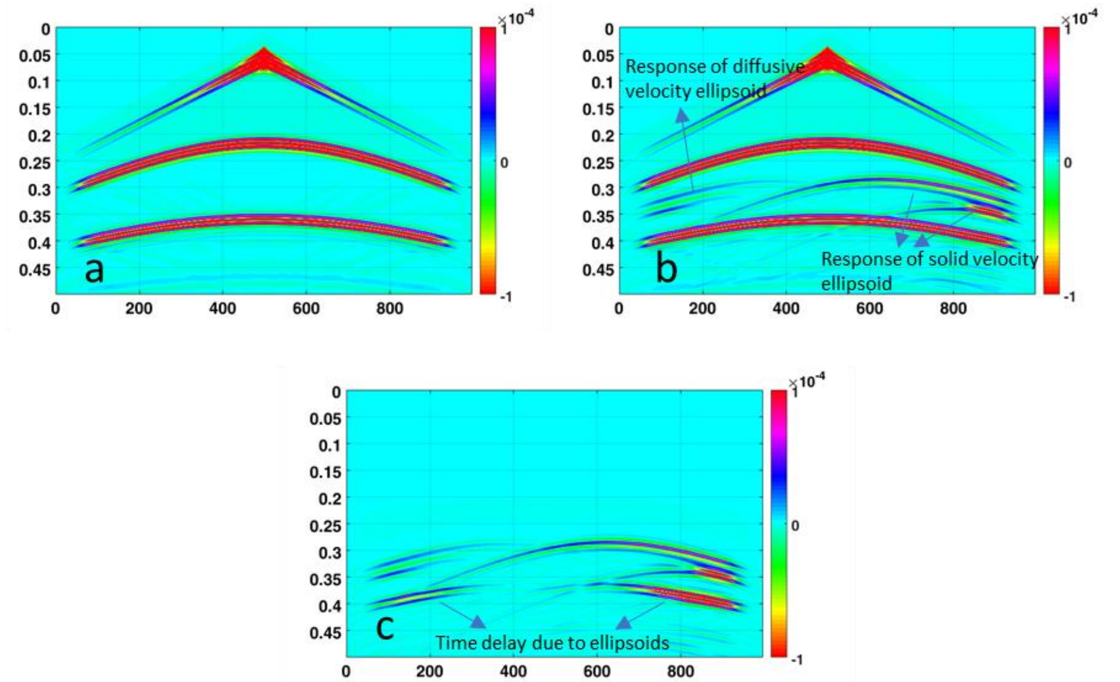

Figure 7-11.The pressure component of the seismic acoustic model for: a. 3-layer baseline b. Baseline plus diffusive and solid velocity ellipsoids c. The difference

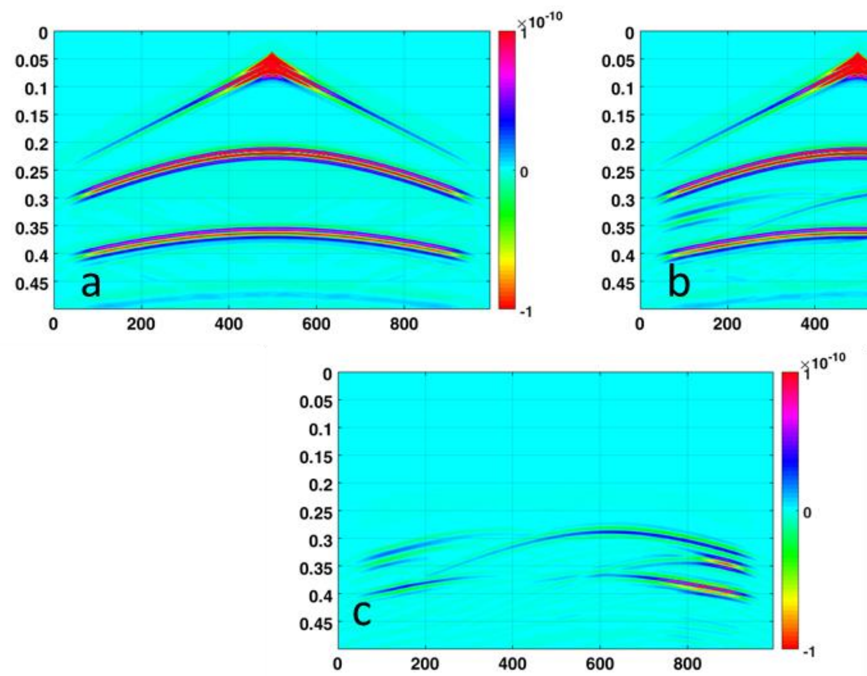

Figure 7-12. The Uz component (a.SM(base,Uz), b.SM(monitor,UZ), c.SM(base,Uz)-SM(monitor,Uz)). It is similar to the pressure component but with the lower amplitudes.

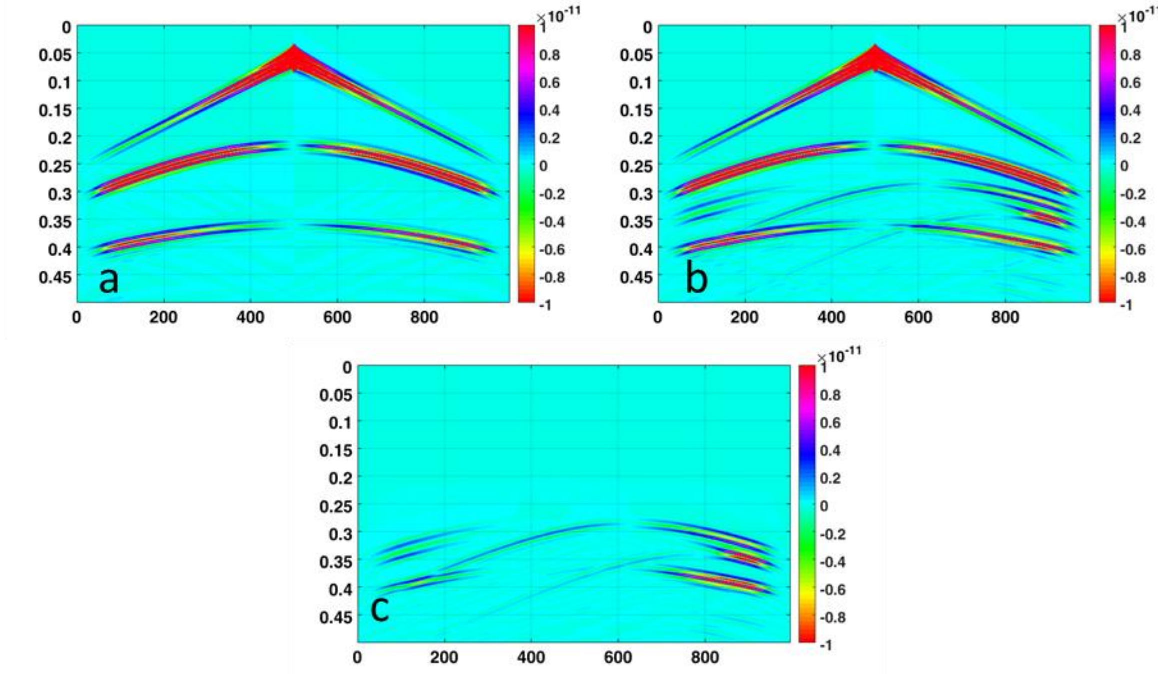

Figure 7-13.The Ux component for (a.) 3-layer baseline (b.) Baseline plus diffusive and solid velocity ellipsoids; (c.) The difference

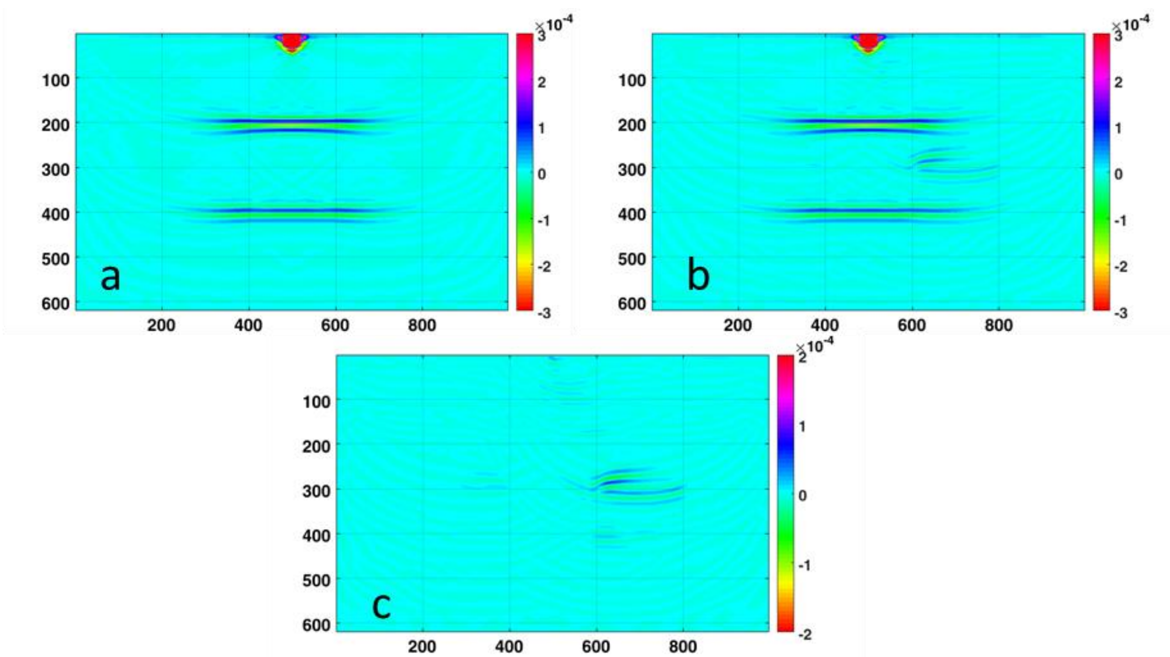

Figure 7-14. a. diff (RTM (SM (baseline, Pressure))), b. diff (RTM (SM (m, Pressure))), c. diff (RTM (SM (baseline, Pressure)- RTM (SM (m, Pressure)))

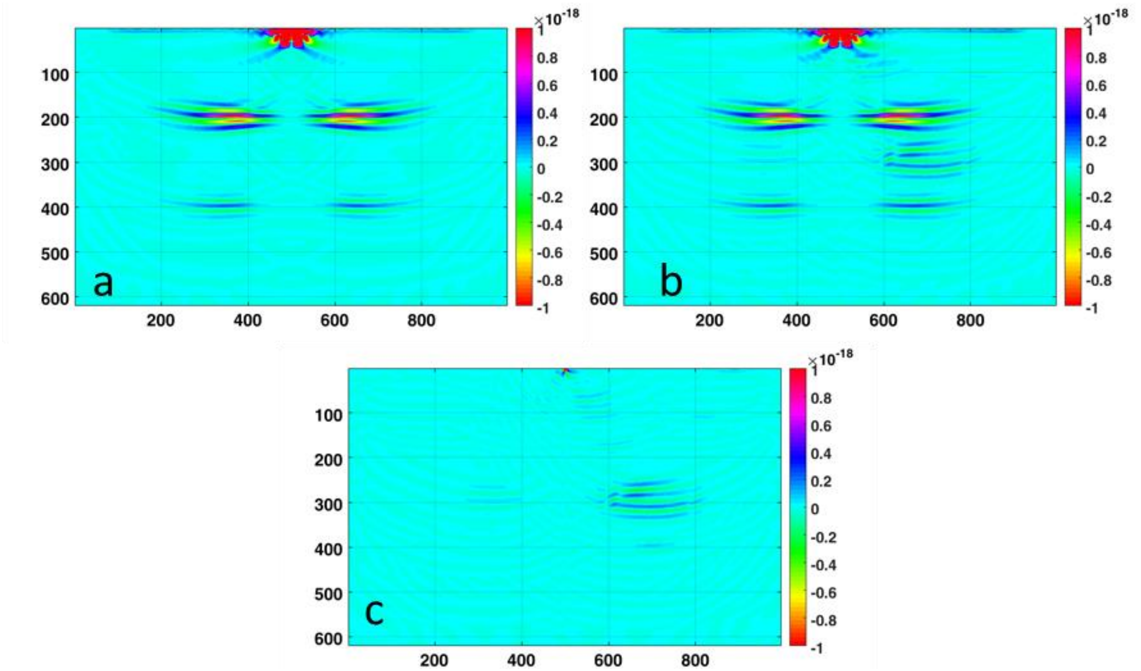

Figure 7-15. a. diff (RTM (SM (baseline, Ux))), b. diff (RTM (SM (m, Ux))), c. diff (RTM (SM (baseline, Ux)- RTM (SM (m, Ux)))

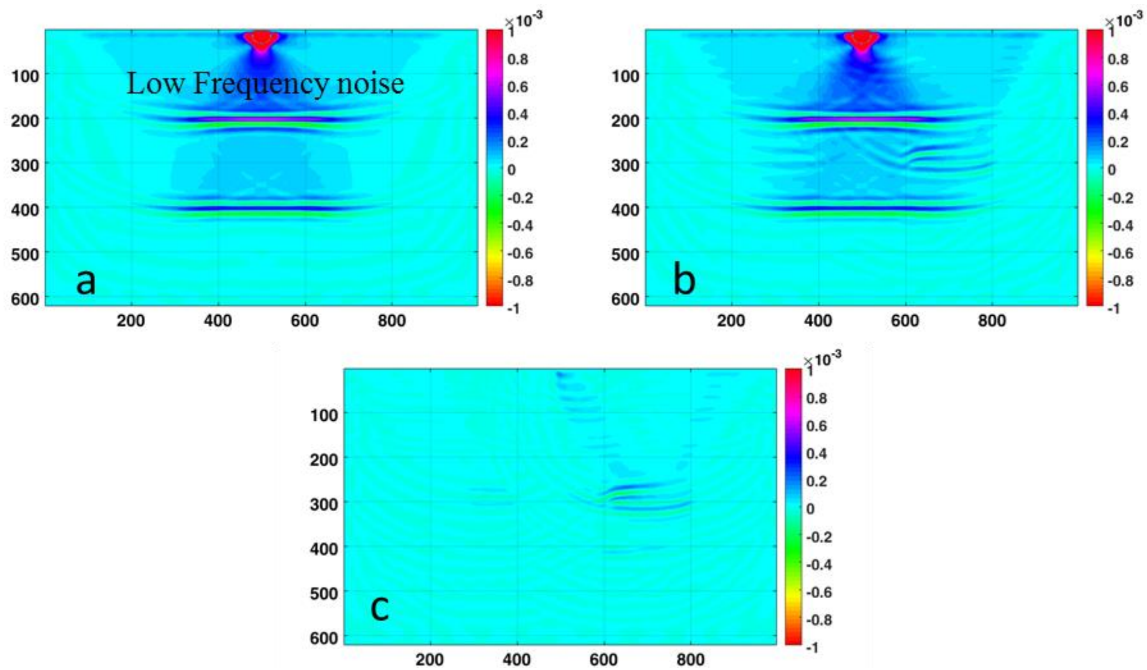

Figure 7-16. a. (RTM (SM (baseline, P))), b. (RTM (SM (m, P))), c. (RTM (SM (baseline, P)- RTM (SM (m, P)))

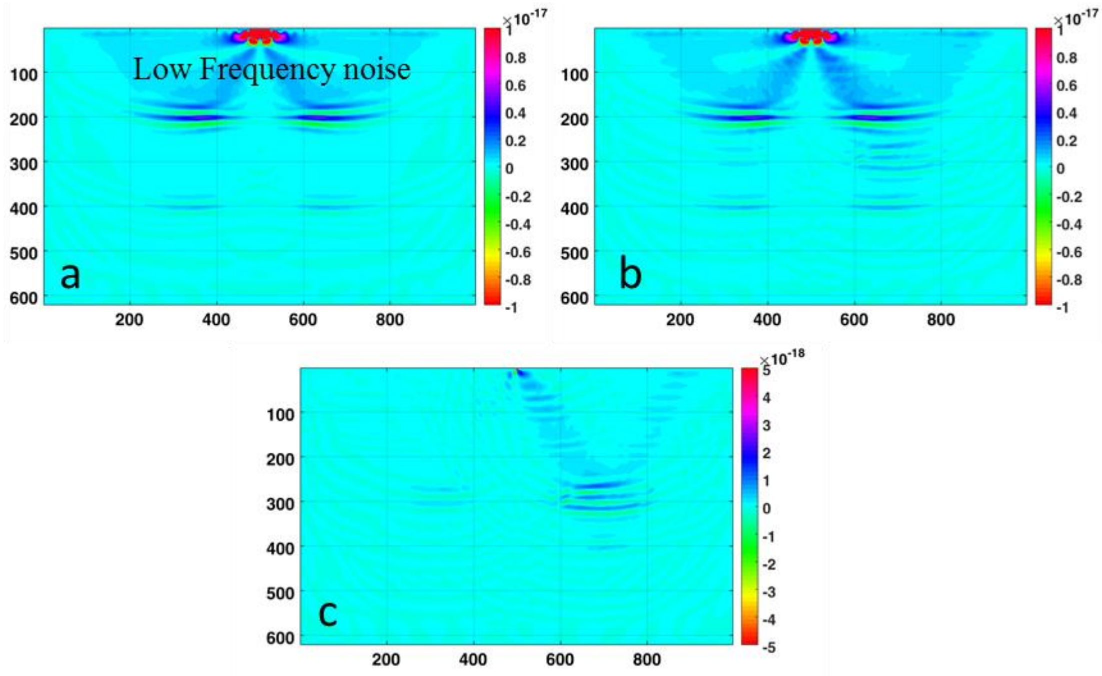

Figure 7-17. (RTM (SM (baseline, Ux))), (RTM (SM (m, Ux))), (RTM (SM (baseline, Ux)- RTM (SM (m, Ux)))

The solid velocity anomaly generates a clear amplitude change in the reservoir (or velocity) border, and in the migrated section, the location of the velocity anomaly matches tothe real location. For the diffusive velocity anomaly, the seismic response does not show any amplitude change in the boundary, and after migration, only a shadow of the central point of the shape is visible. This test shows that the dimension of the solid velocity shape is measurable, but for a diffusive velocity, the seismic can not show the exact velocity change geometry or reservoir size.

7.12 Acquisition geometry for 4D seismic surveys

In this part, I check the acquisition geometry and its relationship to 4D seismic data quality. The acquisition geometry can change the reservoir, imaging condition and in the real world, impact the noise level related to surface activity. In the field acquisition, well seismic acquisition methods generally help lower noise than surface acquisition. I tested three different acquisition surveys with dense receivers:

1- surface 2D configuration
2- vertical Seismic Profile (VSP)
3- cross-well for a simple model

The velocity and density models are shown in Figure 7-18, with dimensions of 1000x620 m. The acquisition patterns are listed in Table 7-1. The results demonstrate that for gas detection, the well seismic methods are much reliable because the amplitudes from the reservoir will be within the threshold range. For a better imaging condition, the shots and receivers should be out of the gas plume. The surface seismic acquisition has a better migration aperture, and so the image of the reservoir can be better, but the amplitude due to injection is less than from well seismic results, due to distance from the reservoir.

Figure 7-21 shows the result of cross-well acquisition. In the results of tests, and after reduction the RTM algorithm low-frequency noises, the cross well seismic acquisition with the 200 offset between shot and receiver wells shows a consistent image of the reservoir (Figure 7-21.d). The result of acquisition with surface seismic and VSP pattern are shown in Figure 7-19 and Figure 7-20, respectively.

Table 7-1: Acquisition parameters and patterns

Acquisition type	Receivers Spread lenght	Geophone interval	Spread start point	Spread end point	Shot point	Record lenght
Surface 2D	1000	1	(0,0)	(1000,0)	(500,0)	0.5 s
VSP	600	1	(600,0)	(600,600)	(400,0)	0.5 s
Cross Well	600	1	(600,0)	(600,600)	(400,295)	0.5 s

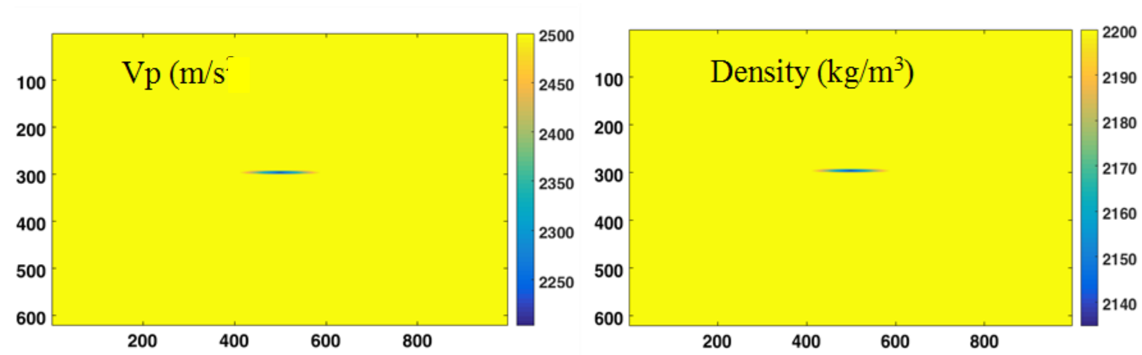

Figure 7-18. The diffusive velocity and density models for a 7% and 3% change in the ellipsoid shape. The ellipsoid dimensions are180m wide and 10m in thickness

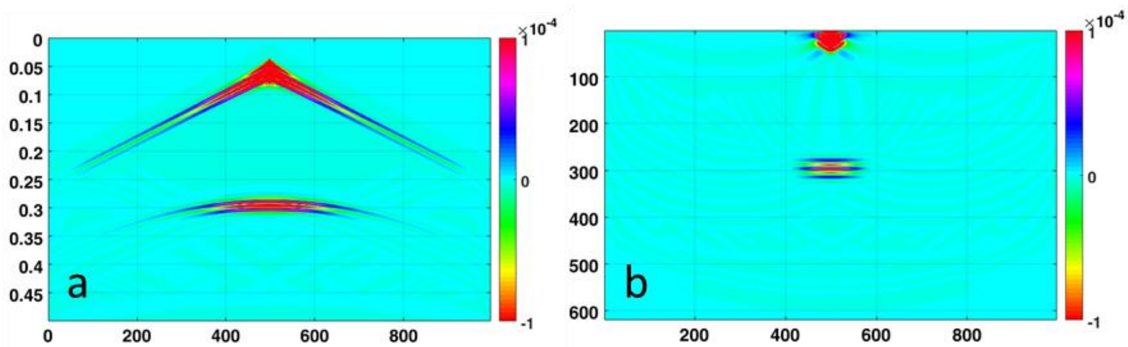

Figure 7-19. The seismic model (a) and migrated section (b) for the surface survey.

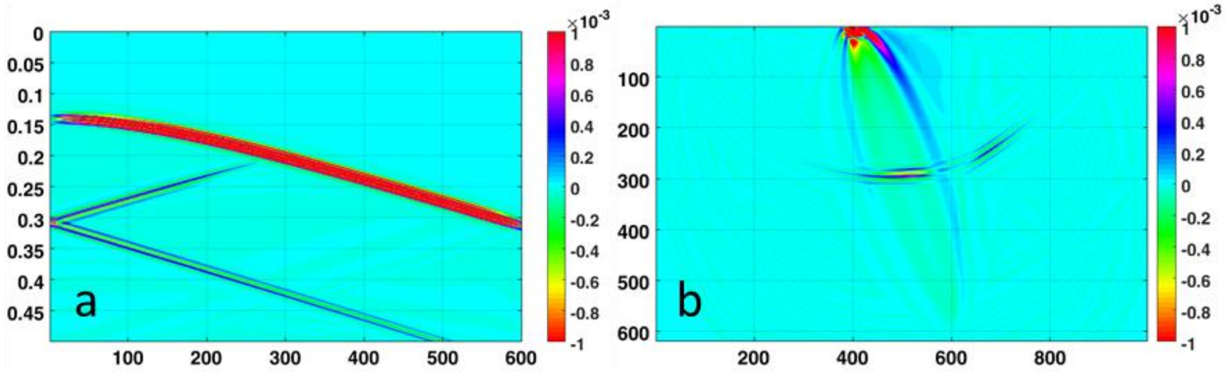

Figure 7-20. A seismic record and migrated section for the VSP acquisition

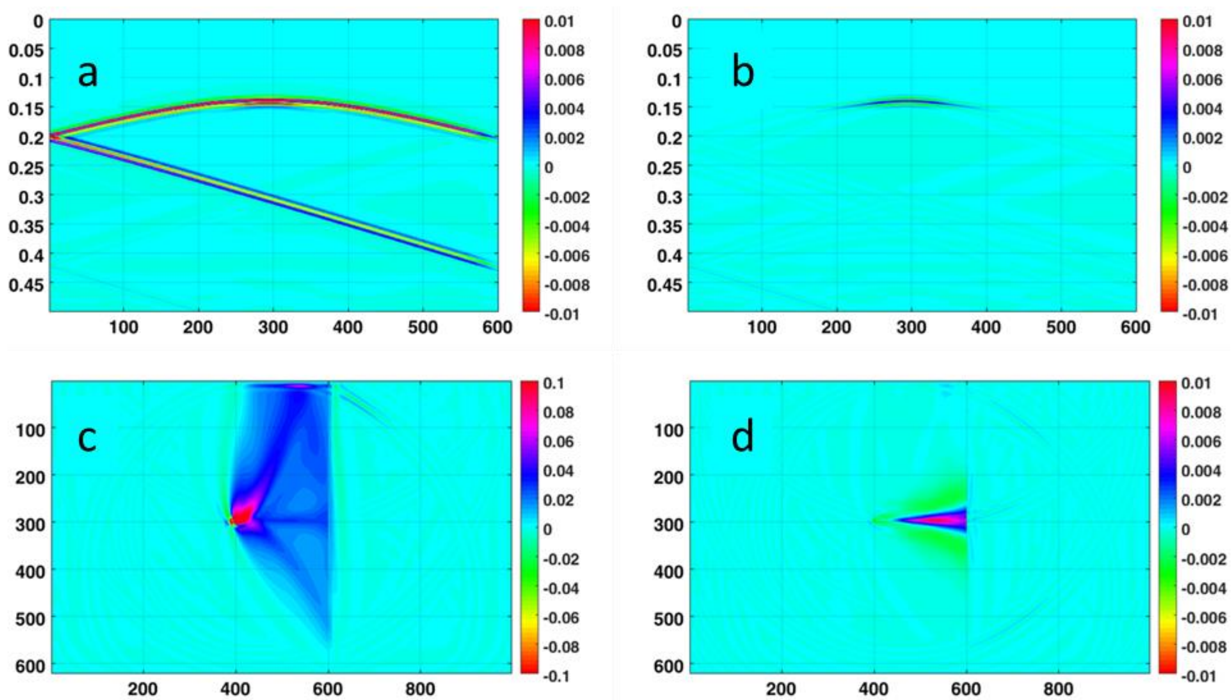

Figure 7-21. a. The seismic response of cross well acquisition pattern of the model in Figure 7-18. b. After eliminating the surface and shot effects. c. The migrated data (from a). d. The noise reduced migrated section.

Conclusions: The acquisition geometry can have a significant effect on the seismic response. The surface acquisition has a better imaging condition, and the boundary of the reservoir can be recognized properly. However, the acquired amplitude level of reflections from the reservoir in the surface seismic is lower than for the well seismic methods. Thus, the surface seismic method can be a reliable method for the large production/sequestration fields with the significant change in the saturation in the reservoir. For the small fields and the reservoir activities with small saturation change, the well seismic methods are a better choice for the reservoir characterization. Of course, the low level of the noise content in the well seismic acquisition can help to detect a lower saturation level and velocity change in the reservoir.

7.13 Seismic interpretability of a diffusive velocity model

The saturation value and effective pressure (difference between confining pressure and pore pressure) are two parameters that play the leading role in the velocity change in the reservoir. As mentioned in the previous chapters, the pressure change in the FRS project is not large(<2MPa), so the pressure effect on the velocity was included in the velocity modeling.

Other parameters with an effect on the seismic response are plume size. In this section, I investigate the saturation (or velocity) offsets and the plume size influence on the seismic modeling results.

Figure 7-23 (column a) shows two diffusive velocity ellipsoids with same central velocity change and different size. Columns b and c show the seismic response and migrated results of the plumes with various dimensions. As we expected, the bigger plume shows the greater response with the same amplitude and a larger anomaly has more chance to be detectable.

Conclusions: In a homogenous media, a small change in the velocity or density may be detectable by the seismic reflection method (Figure 7-22.a1, b1, c1). When we work with the real earth, we deal with a non-homogeneous and anisotropic earth and the imaging is more challenging.

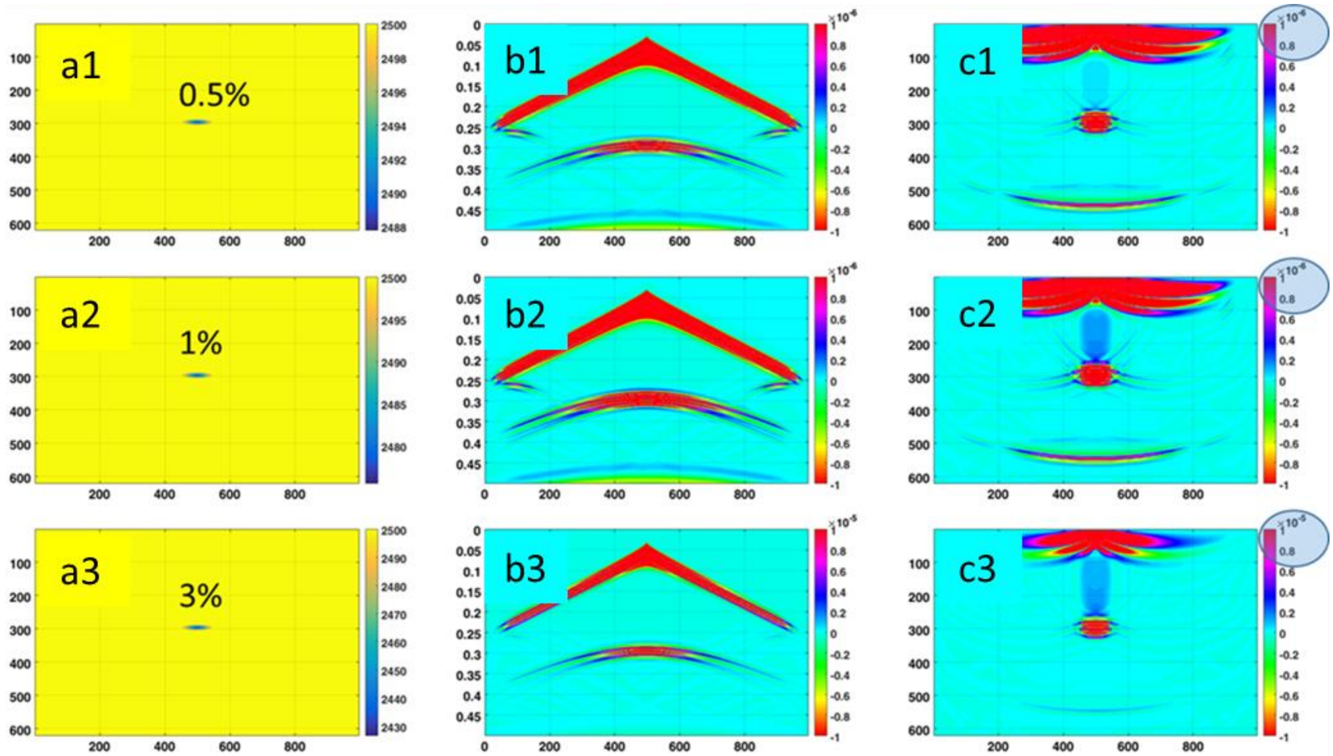

Figure 7-22: The seismic response (column b) and RTM result (column c) for a model (100 * 20 m) with a different velocity anomalies (column a). Higher velocity difference causes greater amplitudes for the surface acquisition survey.

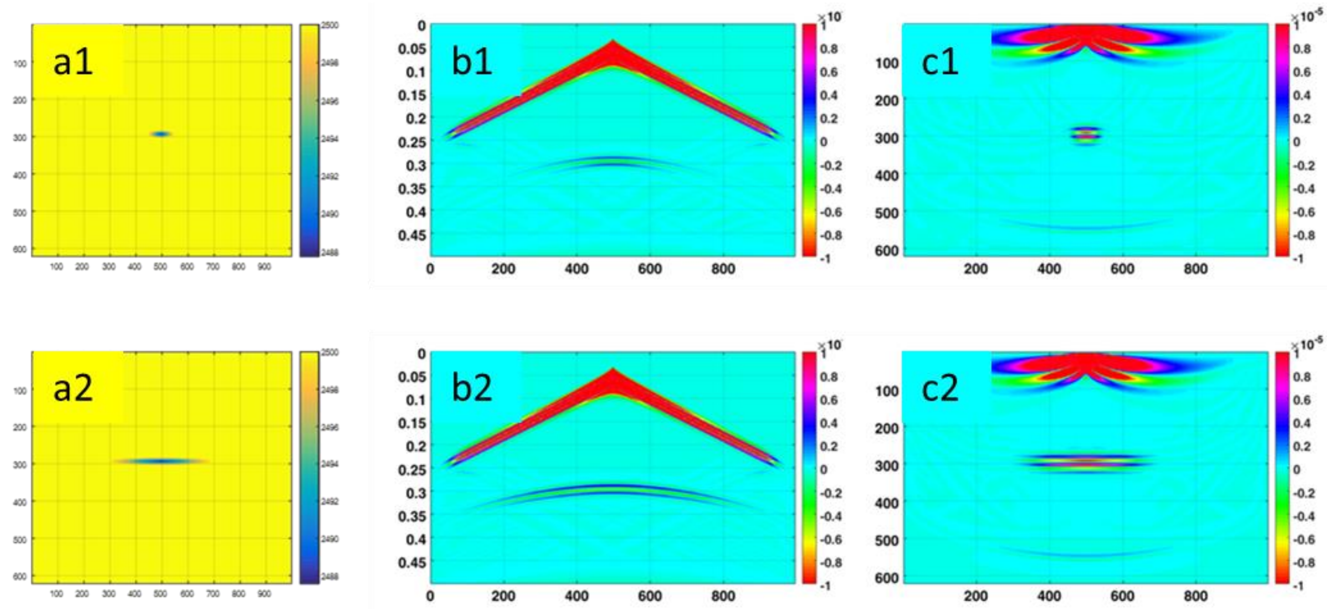

Figure 7-23: The seismic response (column b) and RTM result (column c) for two models with a different plume size and 5% velocity change in the center of ellipsoids in column a. a1: 50*20 m and a2:200*20 m.

7.14 Seismic imaging for FRS project

From the rock physics study and based on the reservoir simulation results, we modeled each cell in the seismic model for different fluid saturation types. The velocity geomodel (generated by a well data with fine grid size) that was introduced in Section 4.15 is the baseline model for the seismic time-lapse study of the FRS project. The editing of the baseline geomodel based on the reservoir simulation data (section 6.17) it is possible to calculate an accurate velocity and density models for the particular time of the injection (Figure 7-26). For the P-wave velocity change, we defined four different models based on the upper (Voigt) to the lower (Reuss) boundaries and VRH and Brie's average for the Vp change by the injection (Figure 6-28 to Figure 6-31).

In the previous section, we compared the solid and diffusive velocity anomalies and the seismic response of them. The different kind of velocity calculations from the rock physics methods will generate different velocity shapes in the reservoir as either diffusive or solid anomaly shapes. The Reuss average (fine mixed fluid type) has a large velocity decrease for low CO_2 saturation levels and this average will make a solid velocity anomaly in the reservoir.

The surface and well seismic acquisition (VSP and cross well), have been modeled and data were processes through to final images. For a realistic image for a single shot VSP, we need to have precise survey design parameters to correctly image the plume size and geometry after migration. It means a wide distance between the shot to receivers is needed to obtain enough data and CMP from the entire reservoir. Also, it helps to have enough migration aperture for the migration process. A short interval between the shot to receivers may generate a pour imaging condition for the modeling and migration. Figure 7-29 is a sample for a weak design pattern for the VSP with a shot that does not clearly image the real plume geometry.

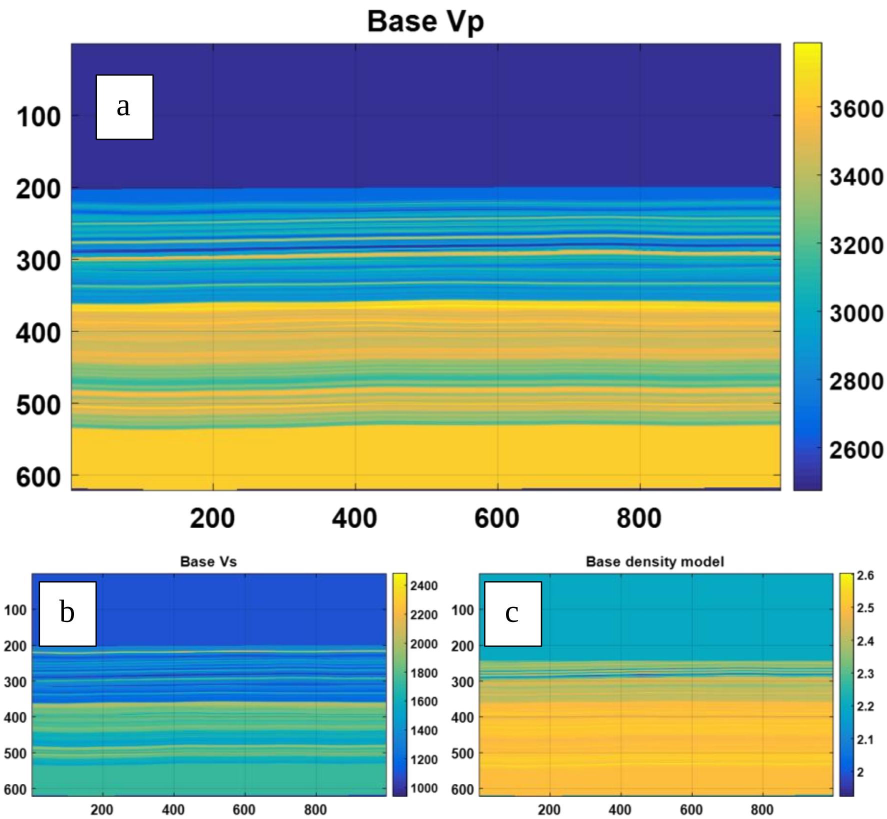

Figure 7-24. The baseline P (a) and S-wave (b) velocity (m/s) and density (c) (gr/cc) models. The reservoir saturation effect on the velocity and density after injection is included in these models.

The main comparison in a time-lapse study is between the seismic monitor surveys (generated with the specified model in defined time) with the baseline survey. For the first step, the velocity and density model (Figure 7-24) and the migrated section for the baseline data (Figure 7-25) were generated.

In the second phase, Figure 7-26 shows how we include the velocity and density variations to the baseline models. The seismic response of the VRH model for different acquisition configurations as shown in Figure 7-27 for a multi-shot surface seismic, Figure 7-29 for a single shot VSP and Figure 7-31 for a single shot cross well experiment. For the well seismic experiences, the receiver are from the surface to 600 m depth, and the offset between shot and the receivers in the well is 200m.

The imaging condition is better for the surface configuration, but the well seismic data show a higher amplitude as we expected. The well seismic geometry has a better result for tomography and velocity estimation especially with the patchy fluid mixed condition or very low gas saturation. The surface experiment shows an excellent image of the geometry of the plume as we see in Figure 7-27.f.

Figure 7-28 compares the amplitude change due to injection for different injection years.

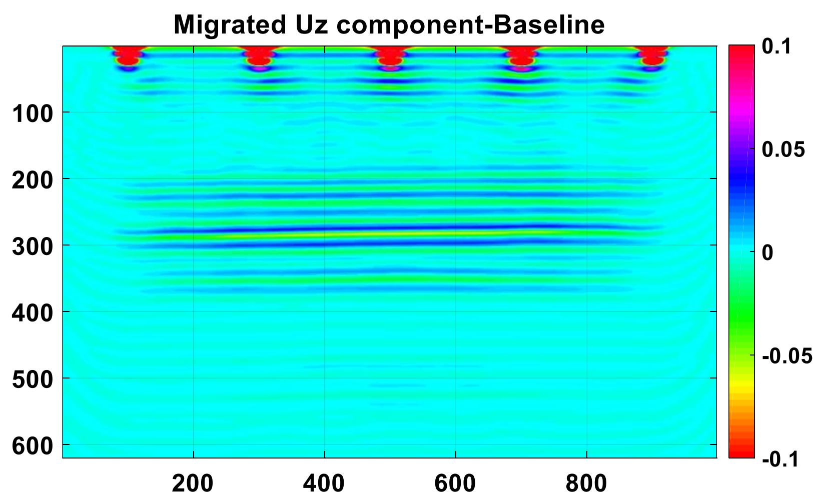

Figure 7-25. The migrated acoustic Uz component for the baseline velocity and density model (surface seismic, five shots and 996 receivers).

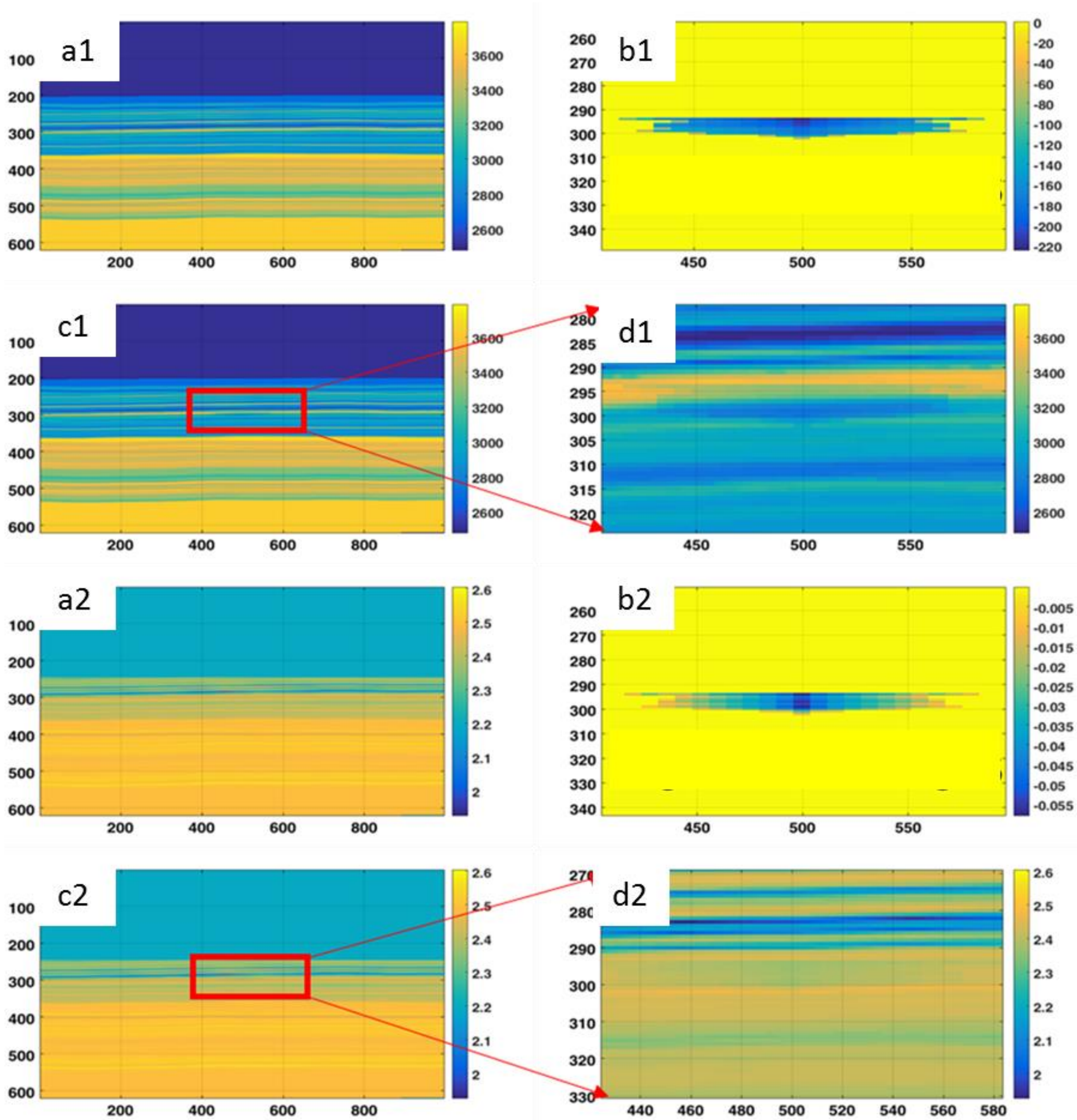

Figure 7-26: The velocity and density models before and after five years' injection with a BHP=49.4 bar in the gas phase for the VRH average. The original physical properties oriented by the seismic interpretation result. a. The base model before injection. b. The perturbation model base on the saturation results. c. The physical properties after injection. d. The magnified figures on the reservoir zone.

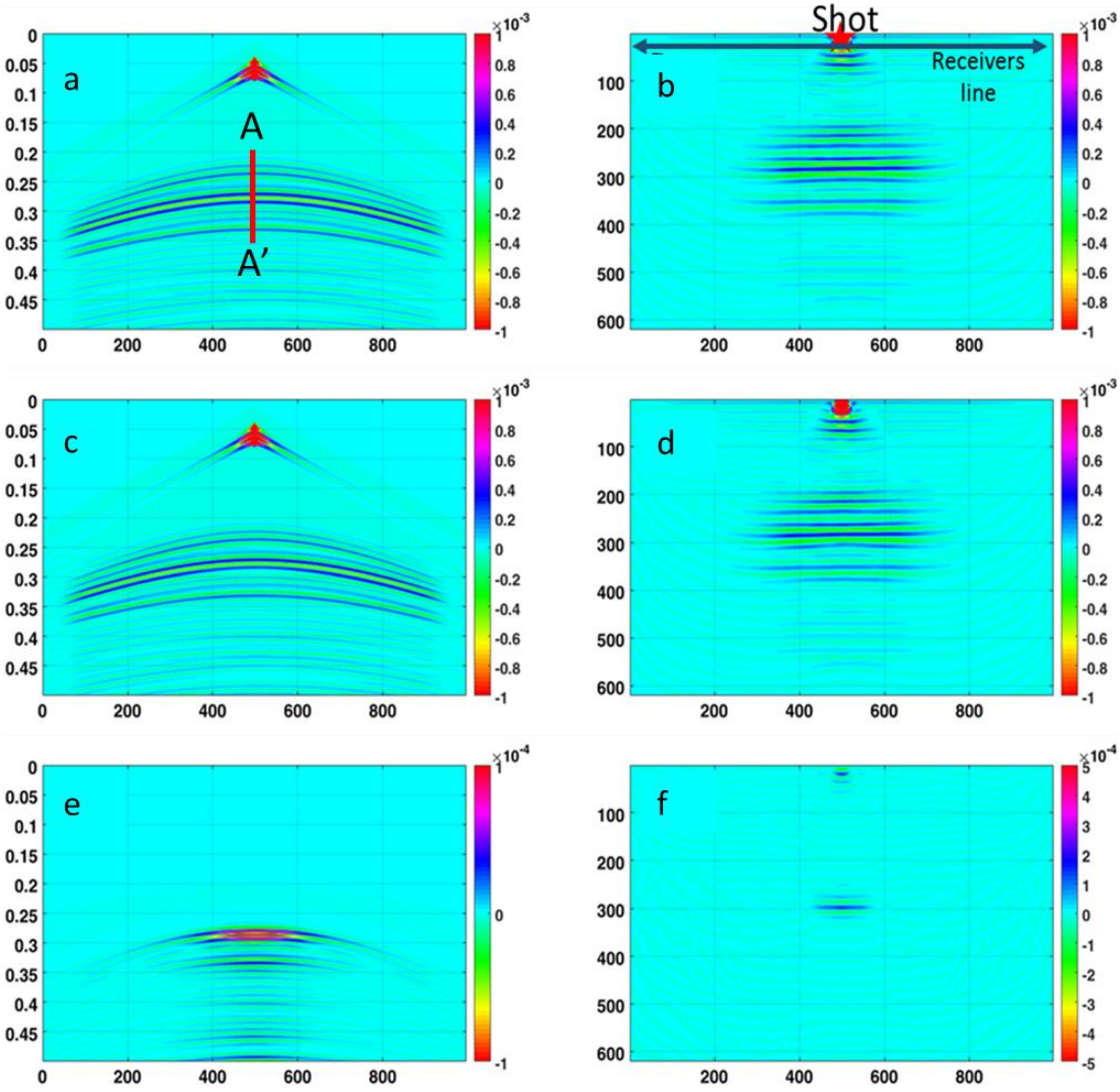

Figure 7-27: The seismic model generated by the velocity and density patterns introduced in Figure 7-26 (VRH average) for a surface seismic experience with one shot in x=500 m and receivers with 1 m interval and from 0 to 1000 m. a. Baseline seismic model. b. Baseline RTM result. c. Monitor seismic model. d. Monitor RTM result. e. The difference between monitored and baseline seismic models (amplitude ten times magnified). f. The difference between RTM results (amplitude ten times multipled).

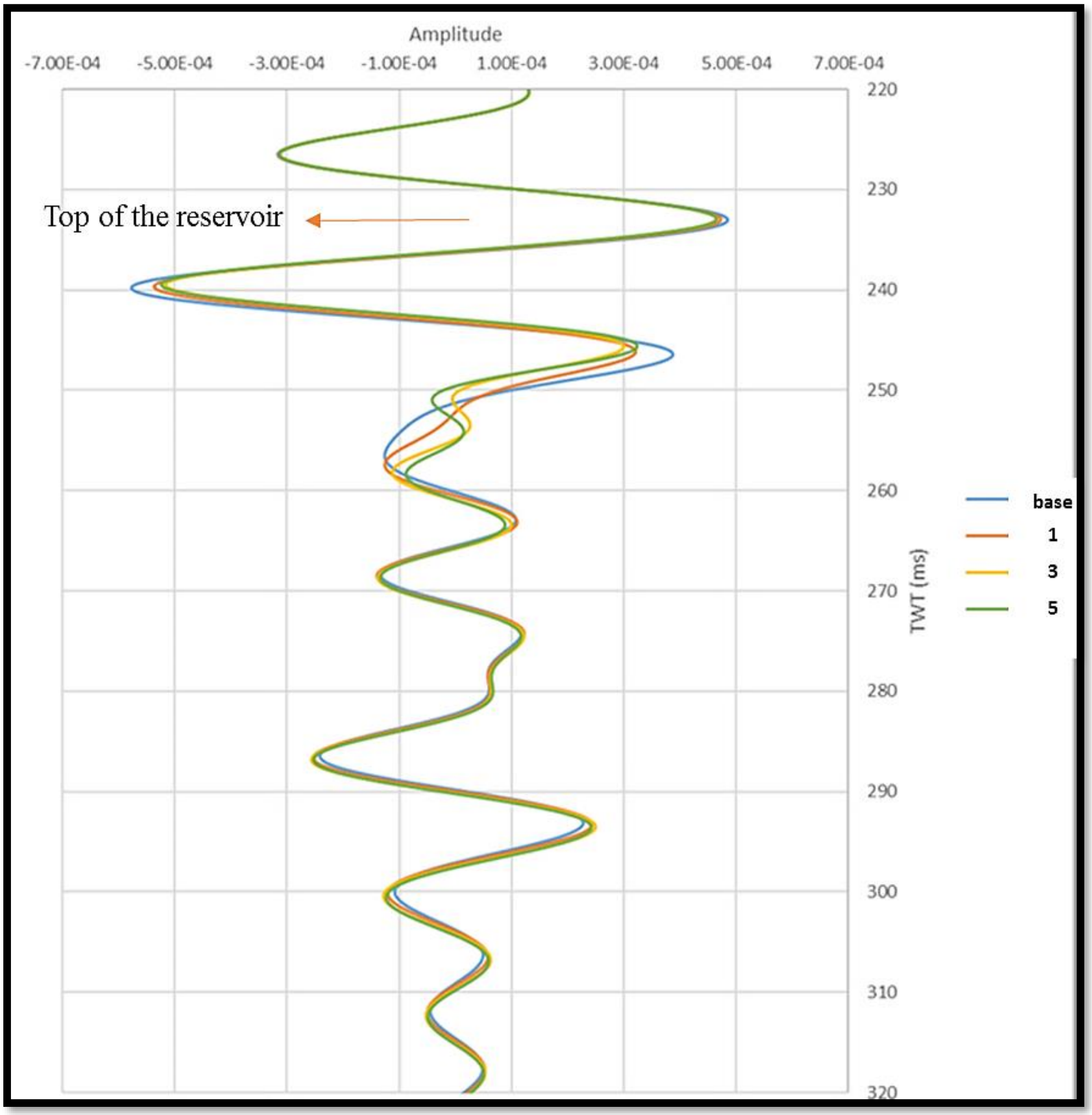

Figure 7-28.The amplitude of the seismic acoustic seismic modeling (Figure 7-27.A, section AA' on the red line) for the baseline, after one, three and five-year injection (VRH average method).

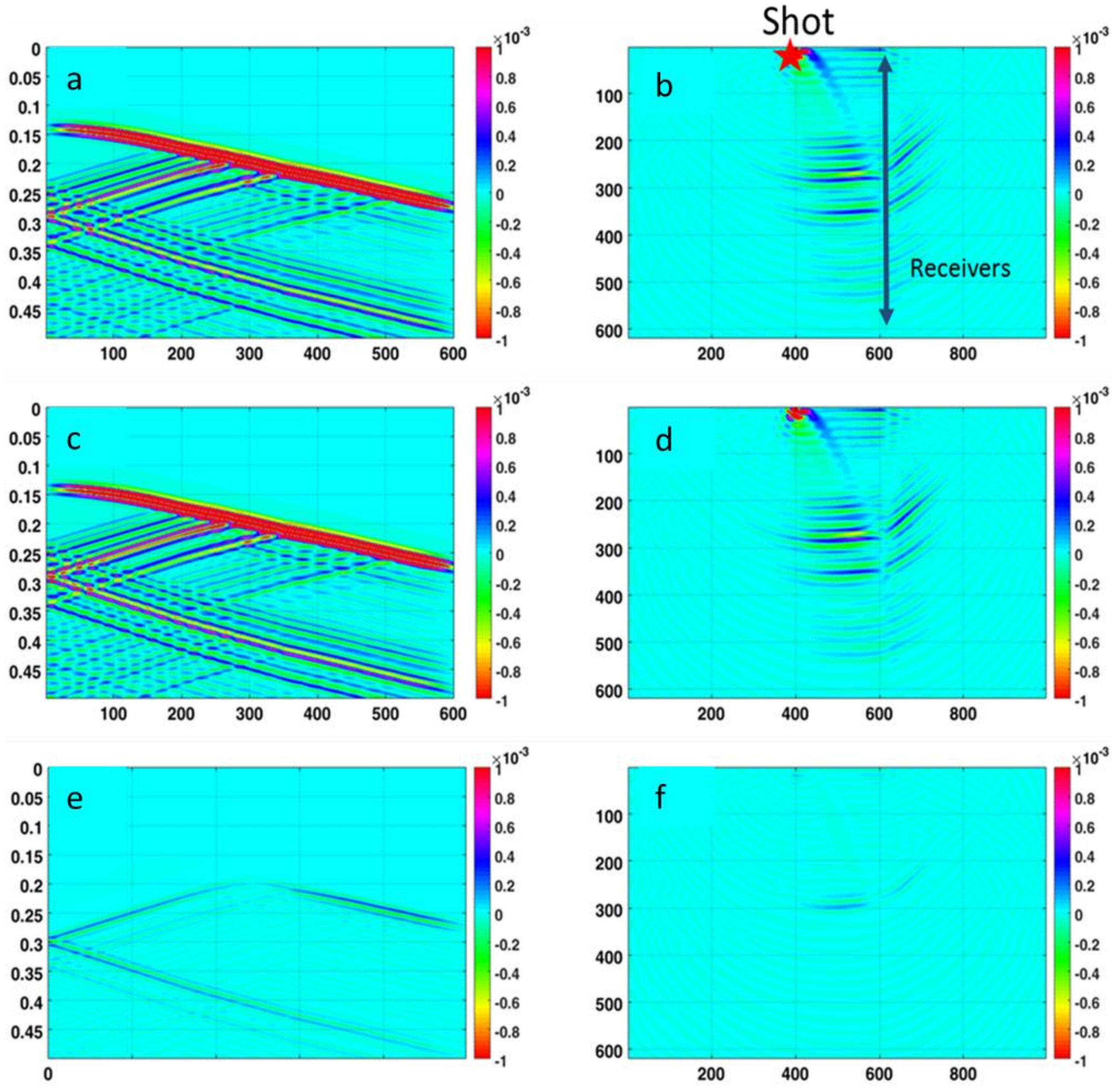

Figure 7-29: The seismic model generated by the velocity and density patterns introduced in Figure 7-26 (VRH model) for a VSP survey with one shot at x=400 m and receivers with 1 m interval at x= 600 and extending from 0 to 600 m depth. a. Baseline seismic model. b. Baseline RTM result. c. Monitor seismic model. d. Monitor RTM result. e. The difference between monitored and baseline seismic models. f. The difference between RTM results.

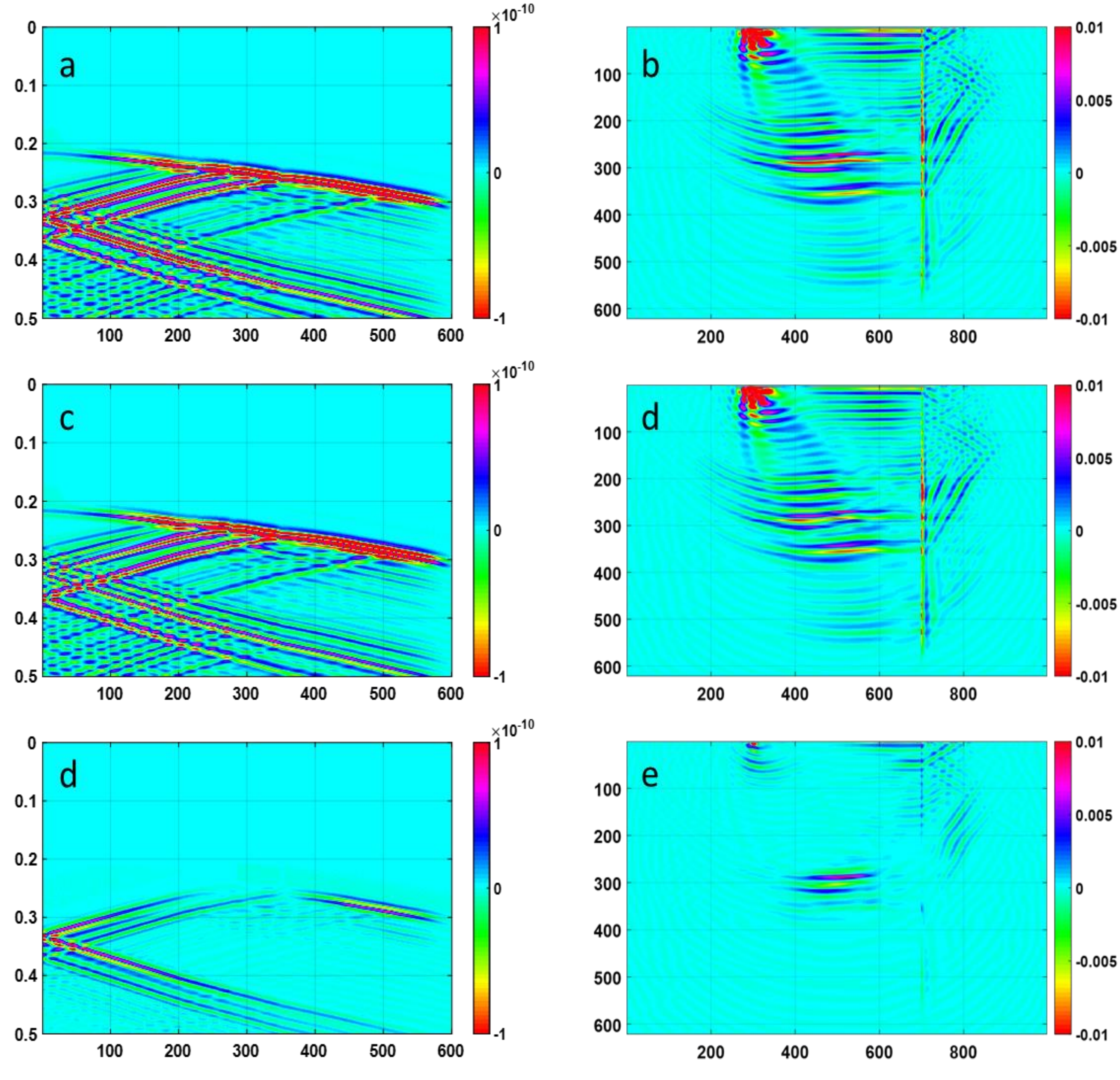

Figure 7-30. A VSP seismic model and image for a wide source to receivers aperture (400 m distance). a and b show the seismic model and image for the baseline and c and d are for the five-year injection calculated by Reuss average, d and e are the difference of the 5-year injected model and baseline (wavelet: 55 Hz Ricker).

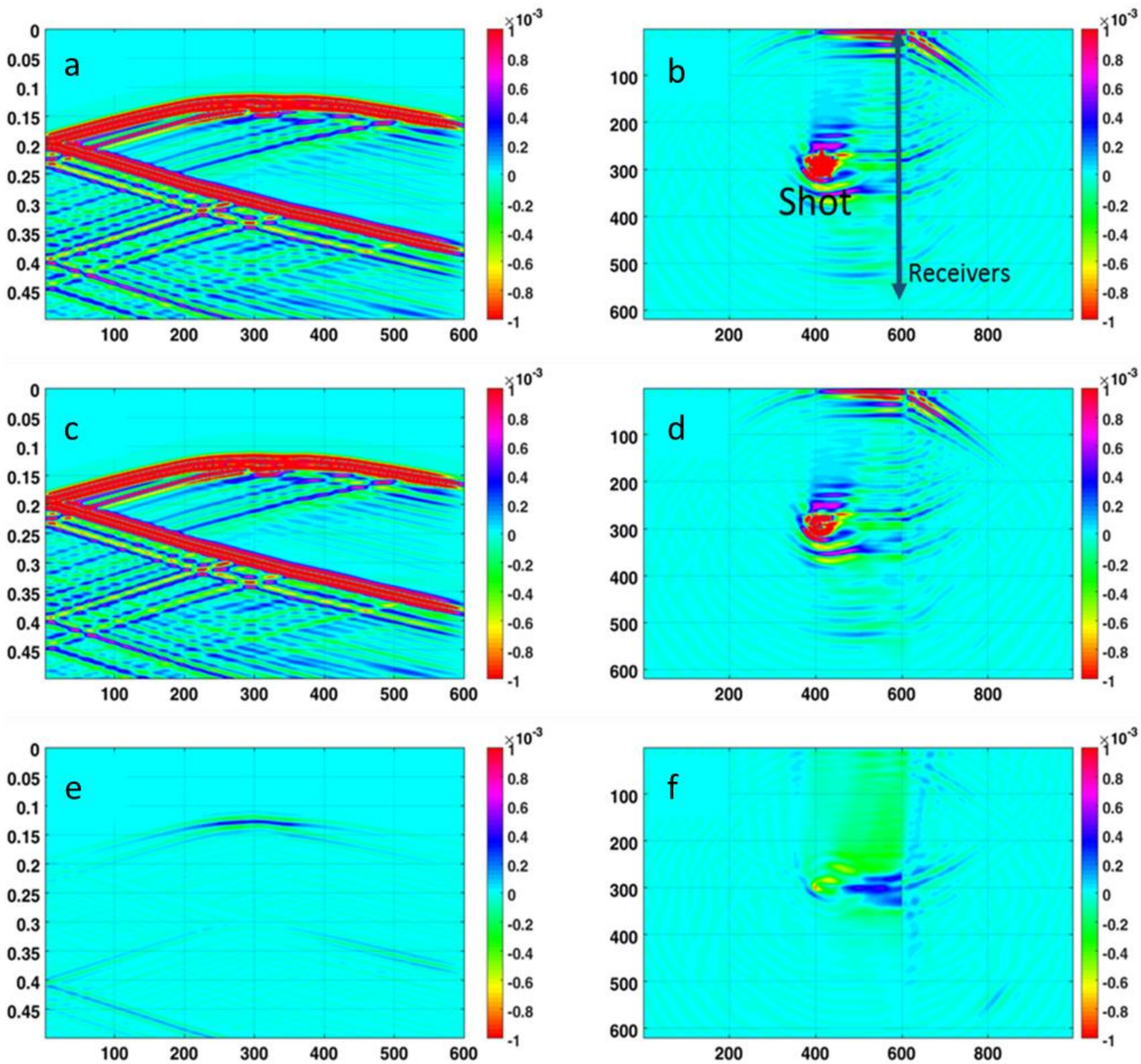

Figure 7-31. The seismic model generated by the velocity and density patterns introduced in Figure 7-26 for a Cross-Well survey with one shot at x=400 m and 295 m depth and receivers with 1 m interval at x= 600 and extending from 0 to 600 m depth. a. Baseline seismic model. b. Baseline RTM result. c. Monitor seismic model. d. Monitor RTM result. e. The difference between monitored and baseline seismic models. f. The difference between RTM results.

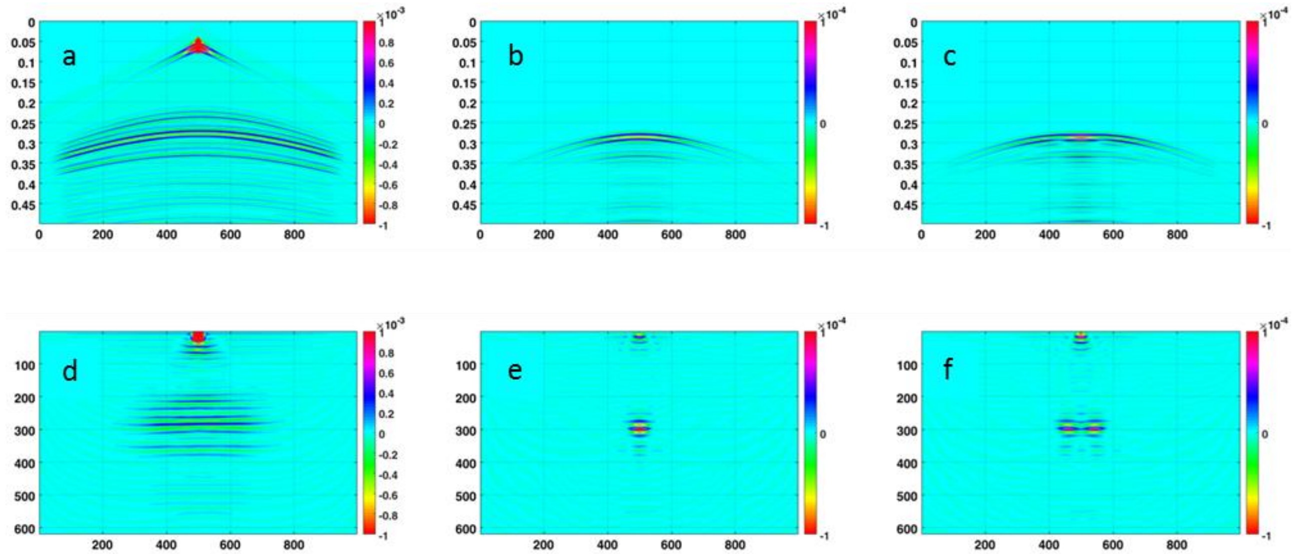

Figure 7-32: The time lapse seismic models: a. The seismic model for one-year injection. b. The difference between the baseline and (a). c. The difference between seismic models after five and one year of injection. d. Migrated section of (a). e. The difference of migration sections between the baseline and one year of injection data. f. The difference of migrated data between five years and one-year of injection.

For the Reuss, Voigt and Brie average methods, the seismic models and migrated sections were generated for the first and fifth year of injection (Figure 7-33 and Figure 7-34). The comparison of the migrated sections shows the difference in the seismic response for the different average type (mixing form). The Reuss average presents a fine mixed fluid of brine, and CO_2 will be detectable after one year of injection. The Voigt average yields a weak seismic response, and the RTM result can not show a detectable amplitude after one year of injection (in Figure 7-32 the amplitude for the Voigt average was magnified ten times). The other average methods (Brie and VRH) show verysimilar results, and the seismic response of them is interpretable if we consider noise free data without any acquisition footprint.

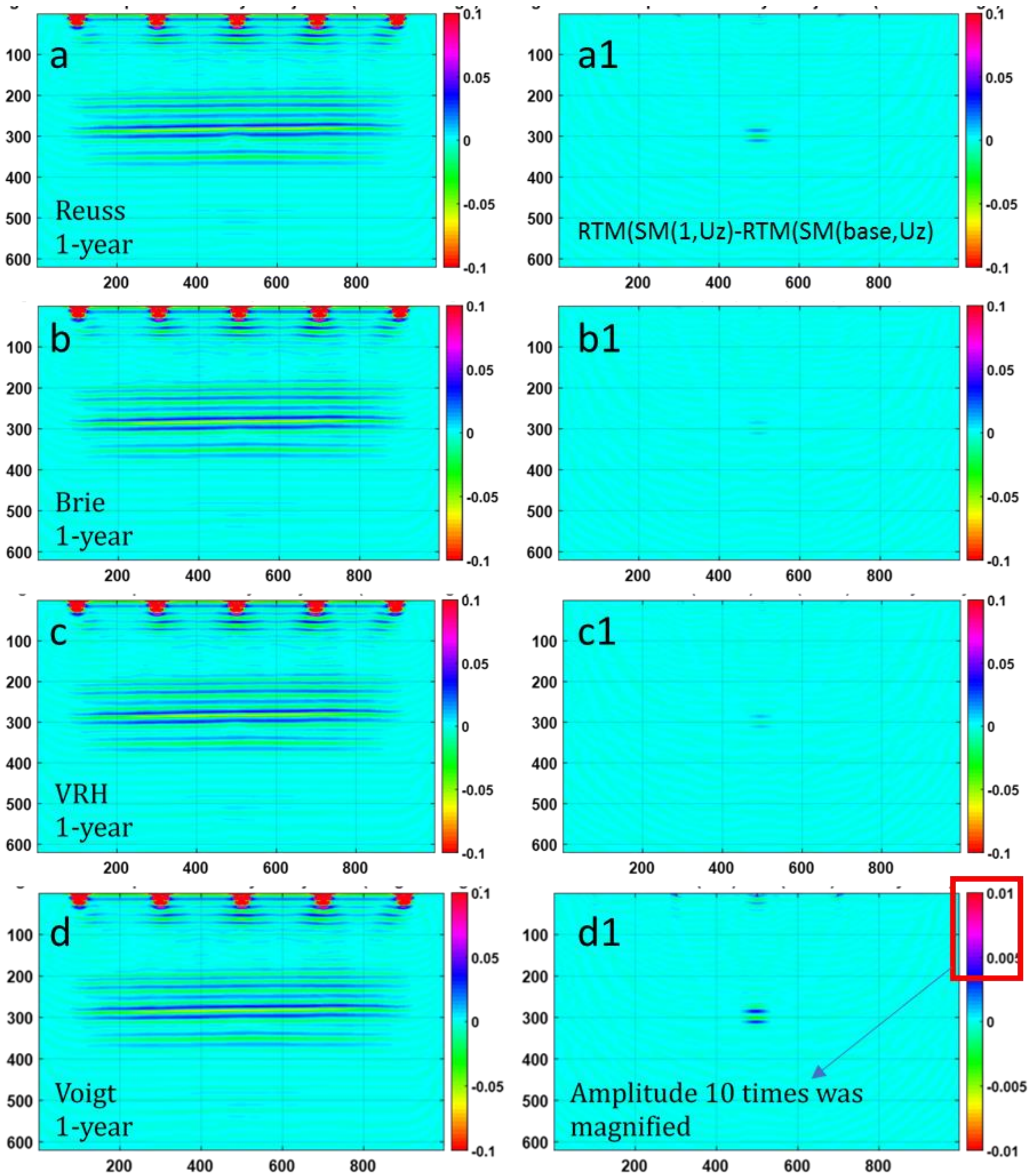

Figure 7-33. The migrated seismic data from the reservoir's response by different kinds of average related to the mixed fluid condition after a year injection. The left figures are the model made by the rock physics models after one year injection for the Reuss(a), Brie (b), VRH (c) and Voigt (d) averages.

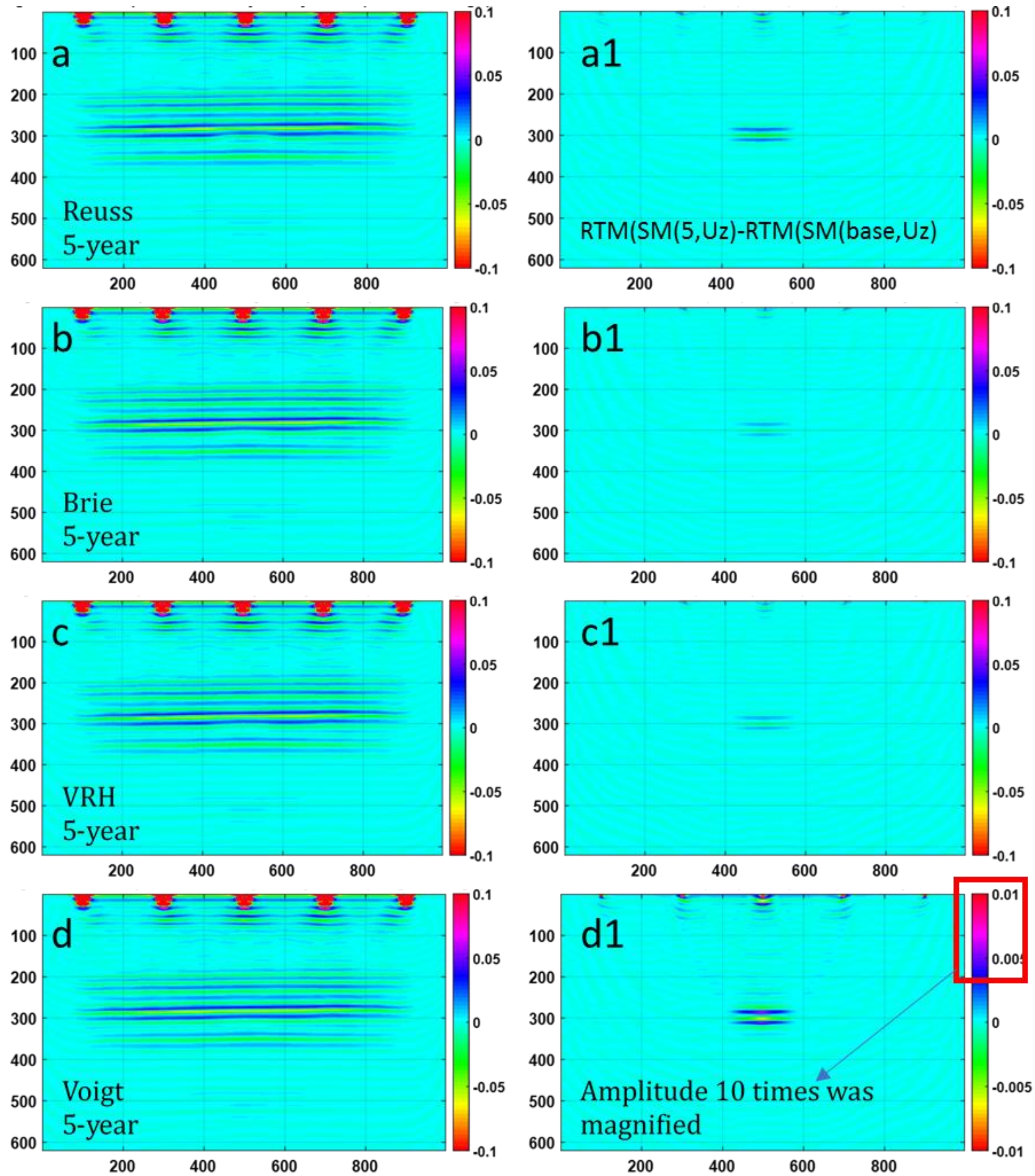

Figure 7-34. The migrated seismic data from the reservoir's response by different kinds of average related to the mixed fluid condition after 5-year injection. The left figures are the model made by the rock physics models after five years injection for the Reuss(a), Brie (b), VRH (c) and Voigt (d) averages.

After five-years do injection, the plume diameter is around 185 m and the seismic responses for three average methods (Reuss, Brie, and VRH) are recognizable. The amplitude for the Reuss average is higher than other methods because the reservoir made a solid velocity anomaly.

The thickness of the seismic response shows a thicker event, because of wavelet shape (Ricker wavelet- 45 Hz) but the horizontal size of the seismic response is equal to the reservoir size (as Figure 7-35). The size of the reservoir in the real field data may be smaller than real reservoir size seismic due to limits of seismic resolution. The velocity variation of the difference of the migrated seismic response after five-years of injection is shown in Figure 7-35. The size of the difference migrated anomaly shows a close match with the plume size for the surface acquisition survey.

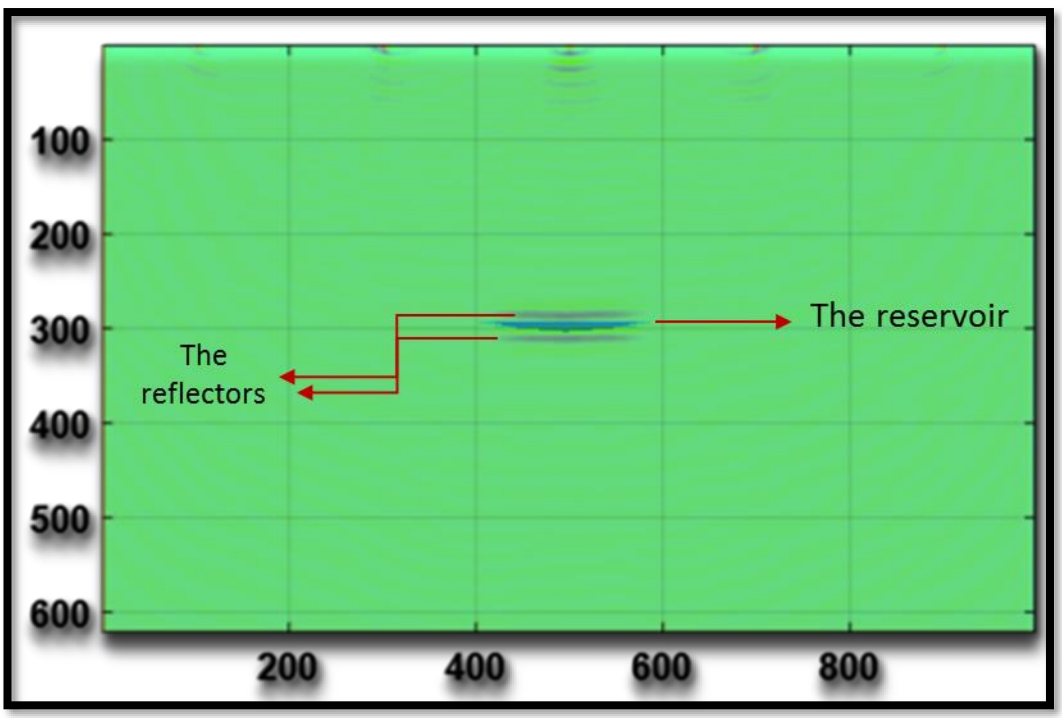

Figure 7-35.The variation of velocity due to injection after 5-year injection (calculated by Reuss average) and the time-lapse seismic migrated response of it (RTM(SM(5,R)-RTM(SM(base)))

Conclusion: The CO_2 saturation in the reservoir simulation is limited to being less than 50% because of trapping efficiency. The velocity and density changes for patchy or semi-patchy mixed type are 5 to 12% with a diffusive velocity anomaly. The statistical distribution for a patchy average shows a normal Gaussian distribution form with a high variance, and it can yield a weaker seismic response compared to a solid velocity ellipsoid created by a fine mixed fluid with a small variance (Reuss average) (Figure 7-36 and Figure 7-37).

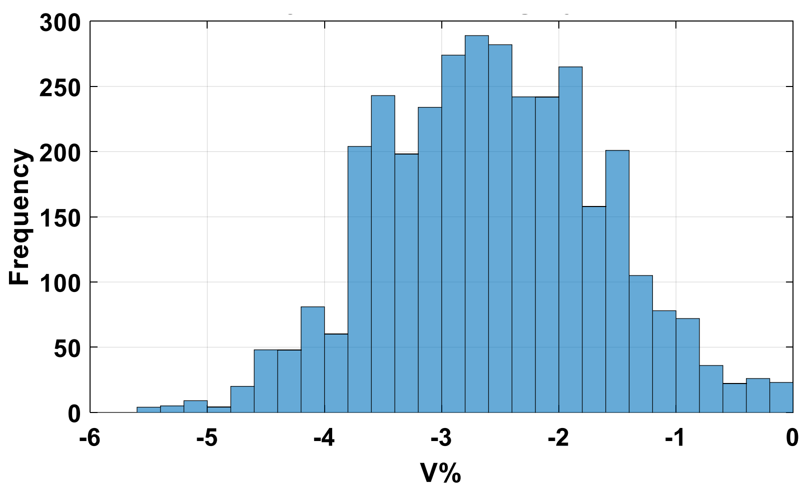

Figure 7-36.The statistical distribution of the velocity change in the reservoir cells in the patchy mixed (Voigt average).

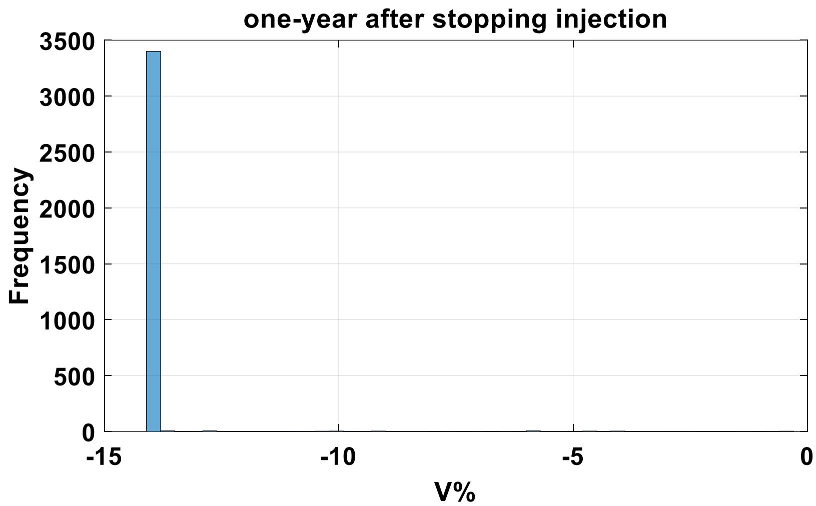

Figure 7-37. The statistical distribution of the velocity change in the reservoir's cells in the fine mixed (Reuss average).

7.15 FRS reservoir seismic time-lapse results

In this section I attempt to check the validity of seismic inversion to predict the CO_2 saturation condition in the reservoir. The seismic time-lapse results are generated by subtracting the baseline seismic from the seismic data. I try to make a reservoir time-lapse result based on saturation, and we will make synthetic seismic model and RTM image. Finally, the result of seismic data for both cases was compared.

Figure 7-38 shows the work flow for the saturation modelling. The test are done by a surface 2D survey with one shot at the well position and receivers over a 1-kilometer spread with a 1m interval. Figure 7-39 shows the difference of velocity in the reservoir between the injection years in the VRH average model.

The seismic response in this test is a function of:

a- The gas plume growth speed

b- The average methods used for the velocity calculation and fluids mixing types.

The seismic model based on the reservoir changes over time is very sensitive to the average mixing method. The current study uses the VRH average method for the velocity estimation, and because it is a semi-linear function (Figure 6-25), the difference in the seismic images are negligible over the natural amplitude range (Figure 7-40, Figure 7-41, Figure 7-42 and Figure 7-43). The entirely linear function for the velocity change (Voigt average) shows a high compatibility with the seismic time-lapse results. The fine mixed fluid type (Reuss average method) can show a significant difference between seismic time-lapse model and seismic made by the reservoir changes.

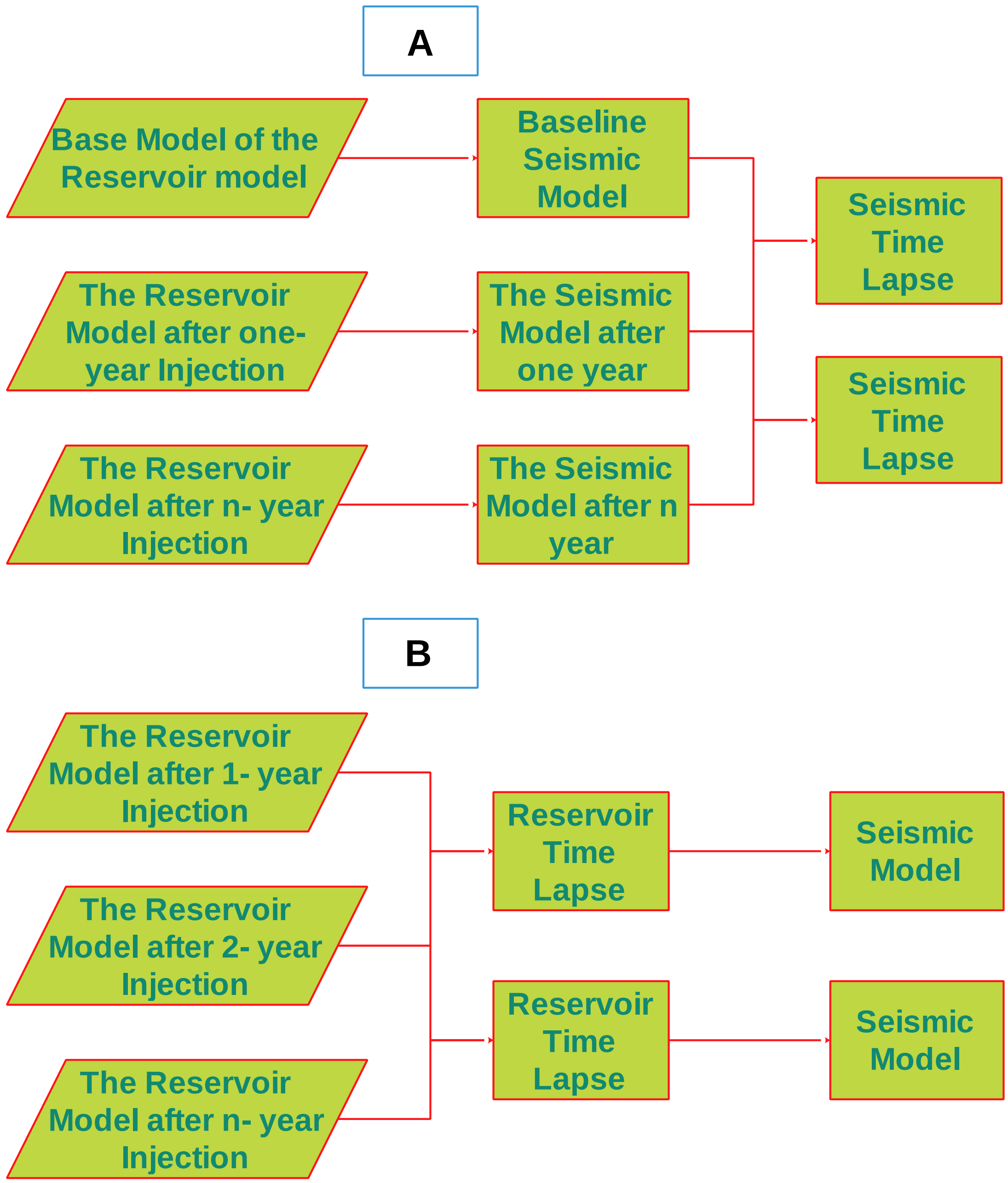

Figure 7-38: The research routine to compare results of the seismic and reservoirs time lapse surveys. A. shows the direct seismic time-lapse, B. seismic time-lapse based on the reservoir time lapse

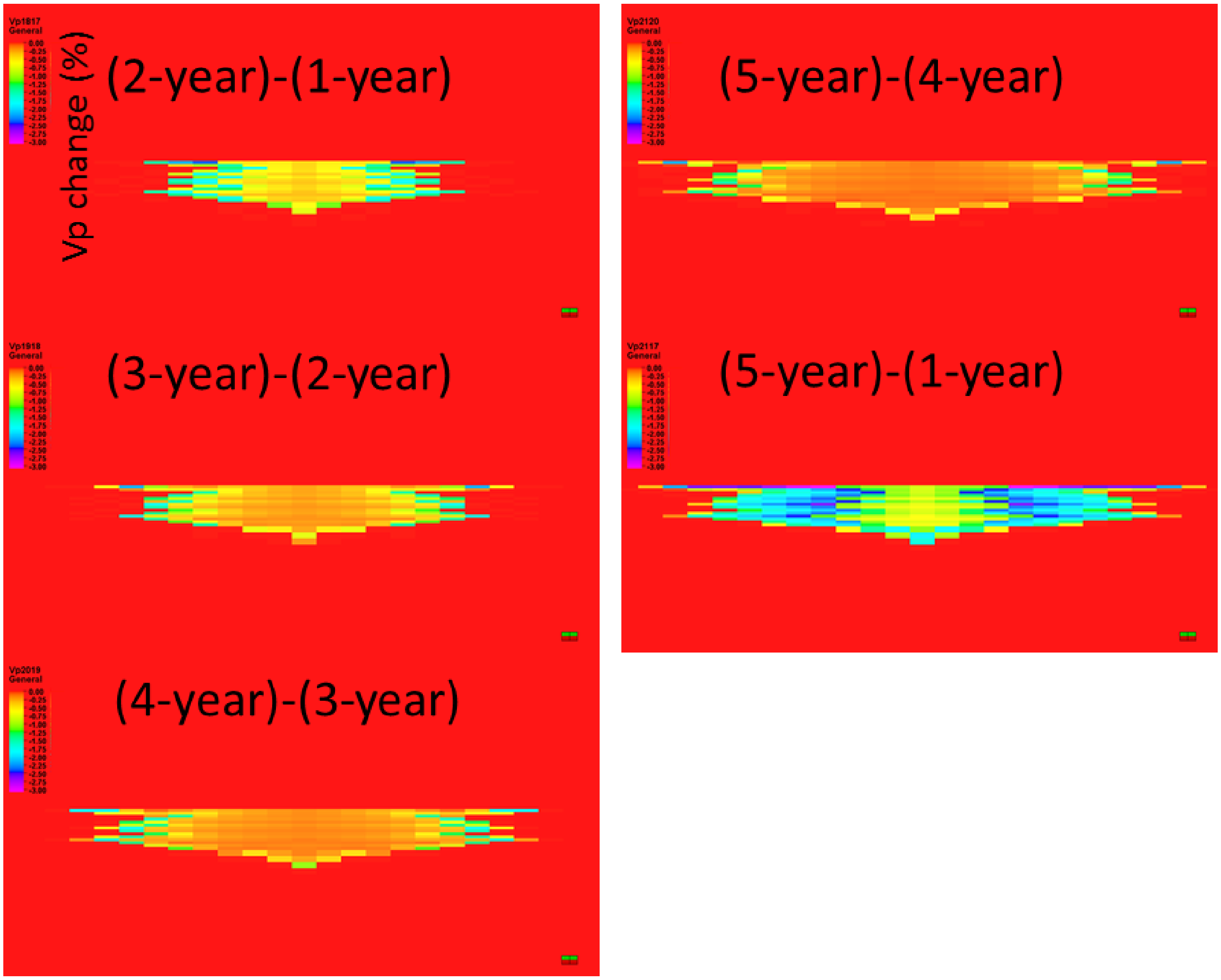

Figure 7-39. The difference model (time lapse) for the p wave velocity (by VRH average) in the reservoir between different years of injection. The result calculated according to the CO_2 saturation content and Gassmann's equation for a semi-patchy mixed condition.

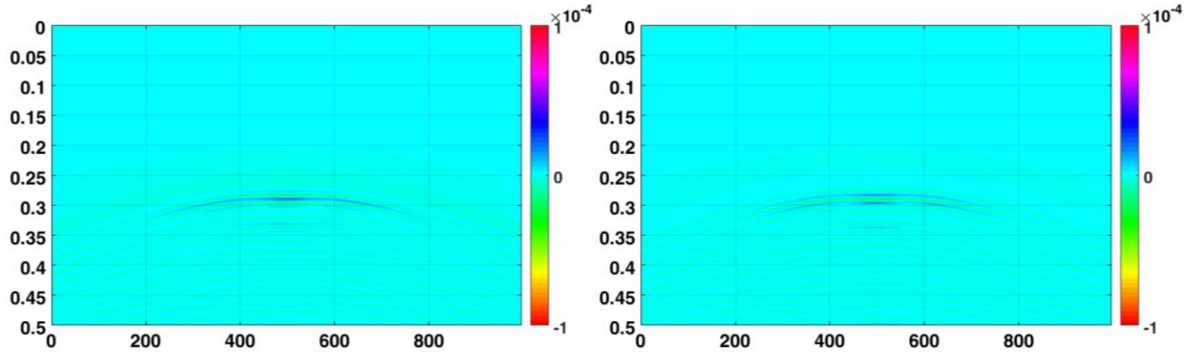

Figure 7-40. Left: SM (R (5-year injection))-SM (R(1-year injection)) and right: SM (R ((5 year) - (1-year injection))). As mentioned previously, SM stand for seismic model (Acoustic), and R is calculated Vp based on reservoir simulation result

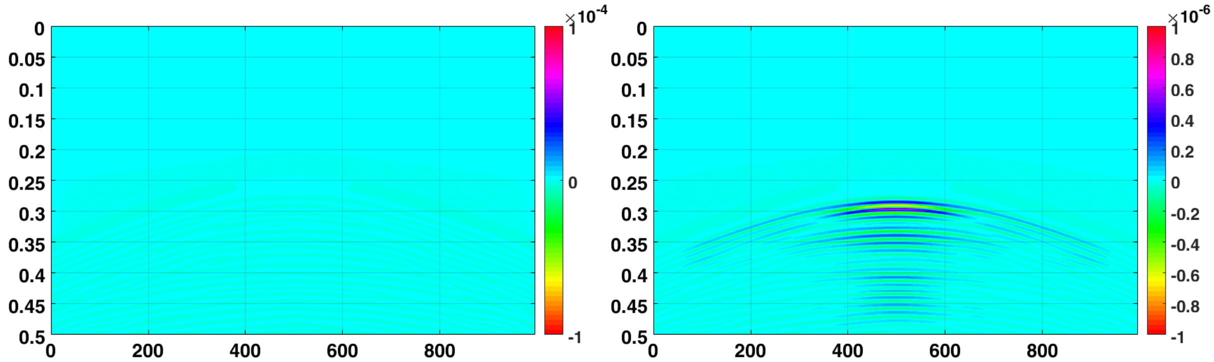

Figure 7-41. The difference between two model in Figure 7-40, the left figure shows same amplitude scale and the right one is 100 times magnified amplitude

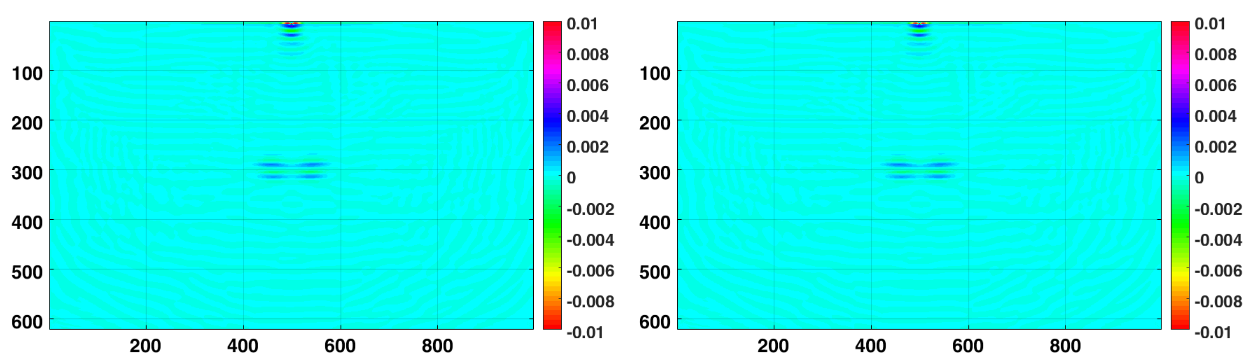

Figure 7-42. The RTM results for the seismic models in Figure 7-40

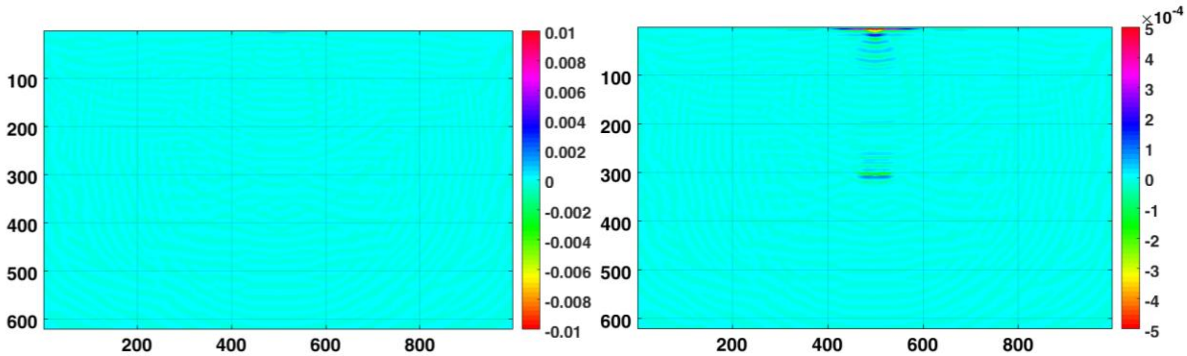

Figure 7-43. The difference of RTM images in Figure 7-42. The left shows the difference in natural amplitude and the right figure shows 100 times magnified.

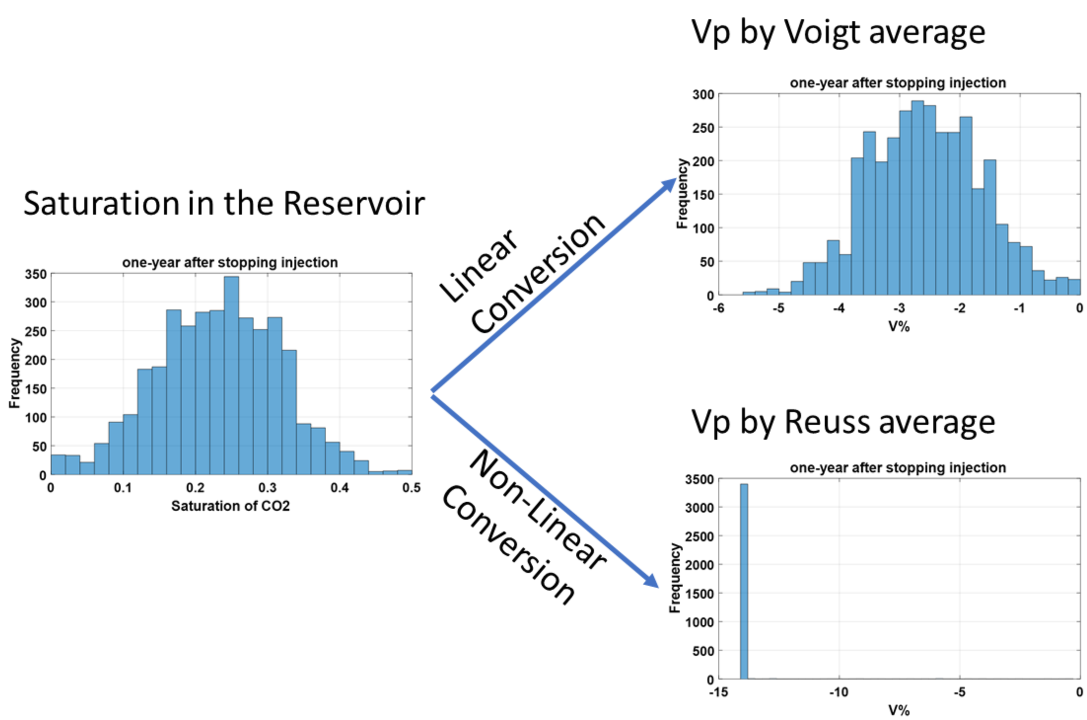

Figure 7-44. The saturation and P-wave velocity change distribution after a year stopping the injection.

Conclusion: the reservoir's dynamic parameters are convertible to the seismic response and vice versa if there is a linear function between the saturation and velocity change. The patchy and semi-patchy mixed type are good examples for this linear or semi-linear conversions. Figure 7-44 shows an influence of a converter in the new population distribution and variance.

7.16 The elastic medium and the seismic response of the reservoir

The previous results were for acoustic models, in which we ignored the shear modulus and S-wave propagation. The wave equation with S-waves can be written as (Eq. 7-10):

$$\left.\begin{aligned}
\frac{\partial v_x}{\partial t} &= \frac{1}{\rho}\left(\frac{\partial \tau_{xx}}{\partial x} + \frac{\partial \tau_{xz}}{\partial x}\right),\\
\frac{\partial v_z}{\partial t} &= \frac{1}{\rho}\left(\frac{\partial \tau_{zx}}{\partial z} + \frac{\partial \tau_{zz}}{\partial z}\right)\\
\frac{\partial \tau_{xx}}{\partial t} &= (\lambda + 2\mu)\frac{\partial v_x}{\partial x} + \lambda \frac{\partial v_z}{\partial z}\\
\frac{\partial \tau_{zz}}{\partial t} &= \lambda \frac{\partial v_x}{\partial x} + (\lambda + 2\mu)\frac{\partial v_z}{\partial z}\\
\frac{\partial \tau_{xz}}{\partial t} &= \mu\left(\frac{\partial v_x}{\partial x} + \frac{\partial v_z}{\partial z}\right)
\end{aligned}\right\} \qquad \text{Eq. 7-10}$$

The MATLAB seismic code was extended to model elastic waves with FDTD method, and in this section, the seismic models of the CO_2 injected are compared with the baseline in the FRS project. Initially, a simple three-layer model was tested to compare acoustic and elastic seismic modeling (Figure 7-45). The source is a P-wave at 4 m depth that by reflecting at the surface layer, creates a converted S-wave. The response of PS and SS waves are zero at zero-offset due to no conversion (by solving Zoeppritz's equation, the reflection coefficient of PS-wave in the zero offset is always zero). However, the amplitude of SS-wave is considerably high at far offsets.

Figure 7-46 is a seismic model for a shot in an acoustic medium and the reservoir event is a PP-wave at the <0.4 s. Figure 7-47 demonstrates the elastic medium response of the reservoir for a shot position 250 m from the well site (incidence angle with the reservoir body is equal 40 degree) to observe clearly the response of PS and SS-waves due to the CO_2 injection (see Figure 7-47). As it can be seen in Figure 7-47, the SS-wave response has a strong amplitude compared to the PP and PS-wave response.

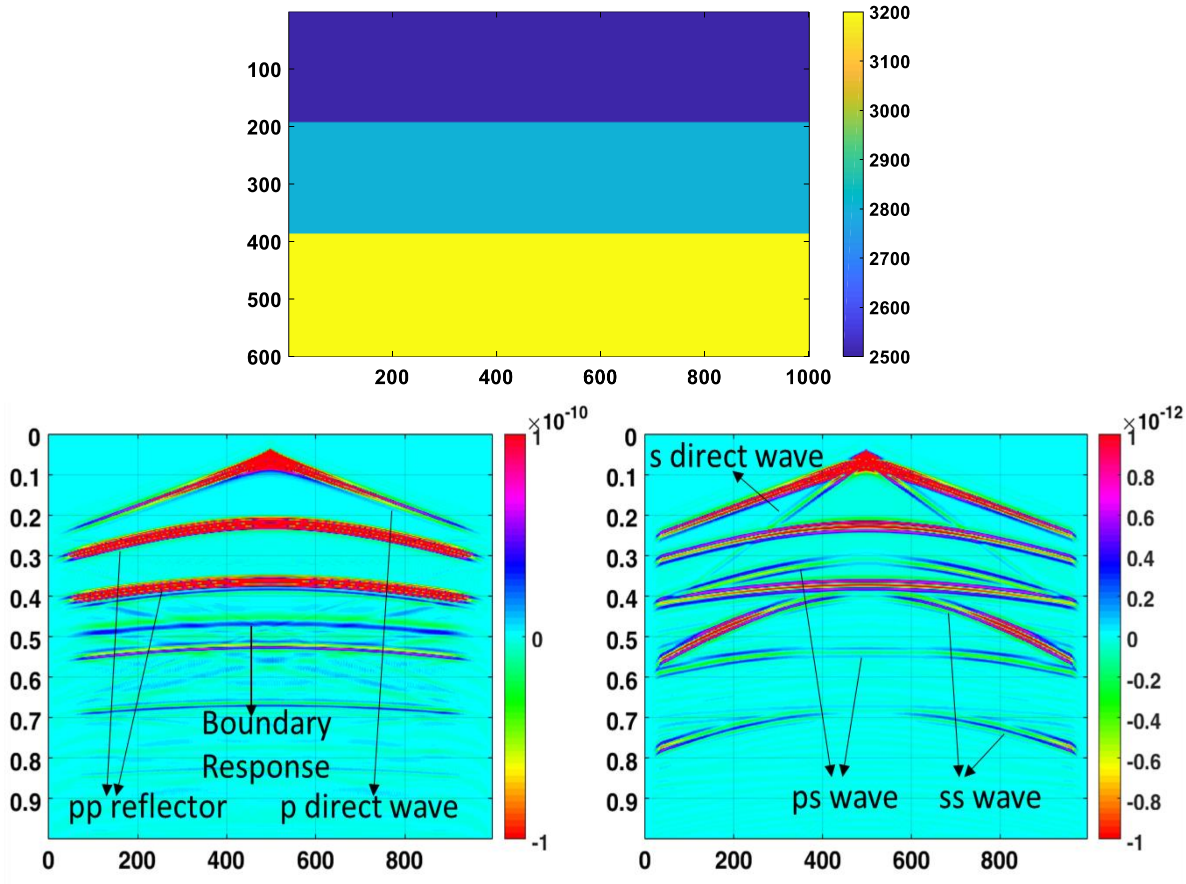

Figure 7-45. The acoustic (left) and elastic seismic response (right) for a three-layer model (top).

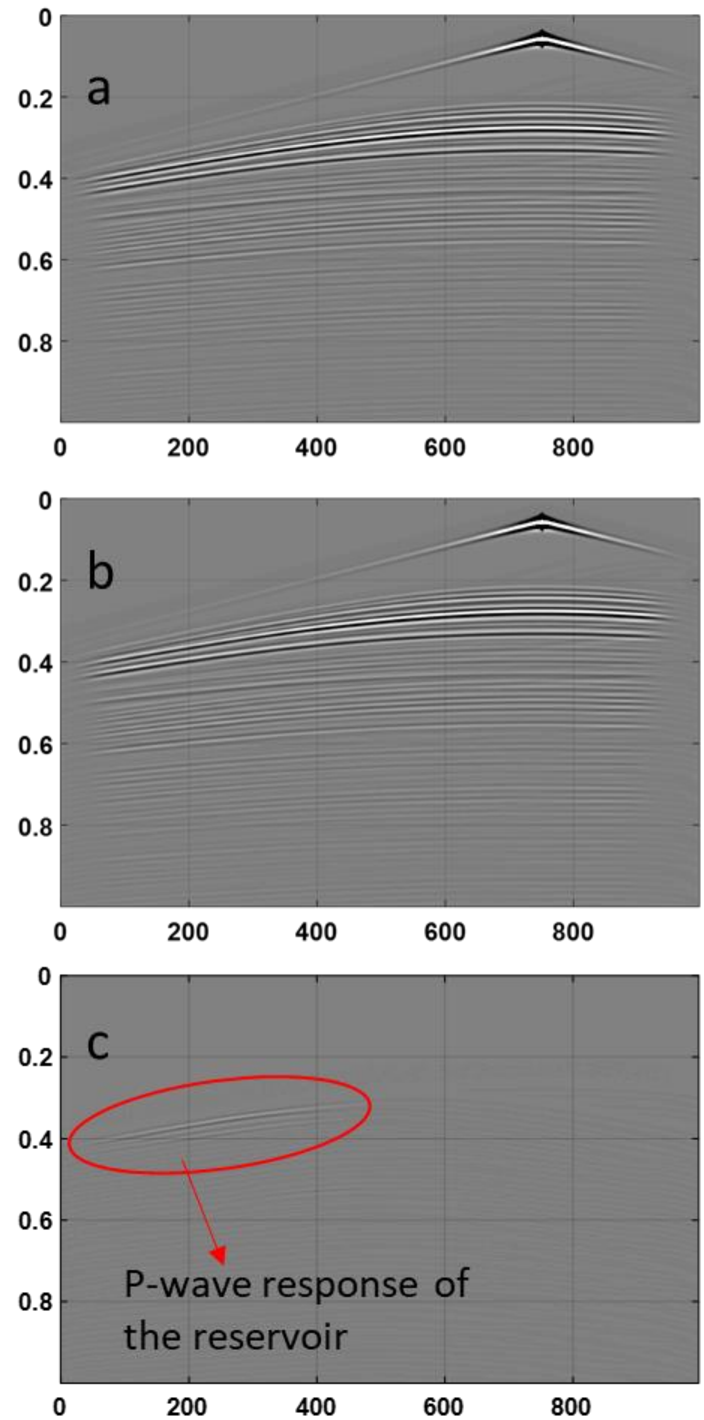

Figure 7-46. The P-wave seismic response for the acoustic wave propagation. a. shows the seismic response for the baseline model. b. the seismic model after five-year injection by Brie's model. c. the difference section shows a PP response of the reservoir.

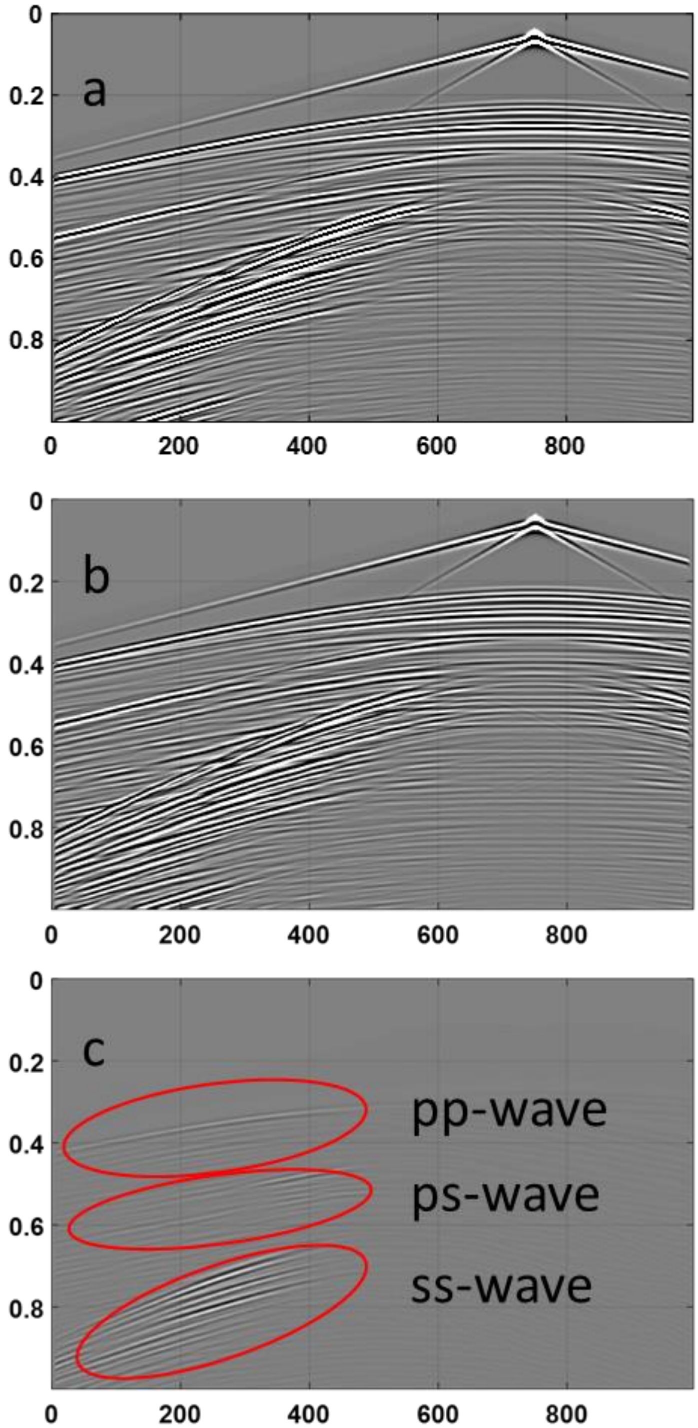

Figure 7-47. The seismic response for an elastic model. a. baseline. b. after five-year injection by Brie's model. c. The difference section and PP, PS and SS seismic response of the reservoir. As demonstrated in Figure 7-45, the SS-wave amplitude is considerable at far offsets.

7.17 Seismic response of CO_2 injection in a complex geological setting

The geomodel and velocity model in the FRS project is simple with the flat formation condition. In this section, there is an attempt to fix a CO_2 reservoir in a layer in the Marmousi model (the original Marmousi model was shown in Figure 7-48 and with a reservoir in Figure 7-49) to find out the seismic response. This reservoir is placed at 550 to 800 m depth, and the properties are matched with a CO_2 injection with 40-50% gas saturation. The primary reservoir fluid is considered as a brine with 8000 ppm salinity (same as the FRS). The acoustic seismic data were migrated (as Figure 7-50 and Figure 7-51). The difference section between the CO_2 injected model and baseline is shown in Figure 7-52. The reservoir location is recognizable with acceptable geometry. The complex geology area can be adequately mapped by an advanced migration method (RTM) with a high-quality acquisition, and the change in a reservoir activity with higher than 10% change in the reflection coefficient is recognizable by the seismic surface method.

Conclusion: An accurate seismic model and image in the complex geology set can be generated by the seismic forward modeling and RTM migration method. The main goal of the reservoir simulation study is to make a predictable velocity model by the rock physics roles and purpose of the seismic study is to create a velocity model in the seismic resolution range to calculate the geometry of plume and migration and saturation.

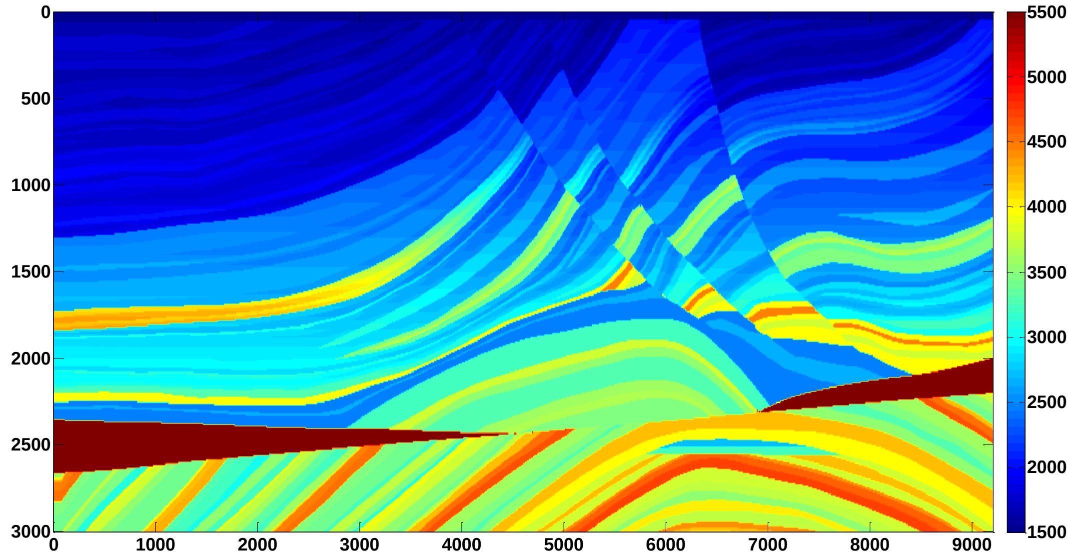

Figure 7-48.The original Marmousi model (P-wave velocity)

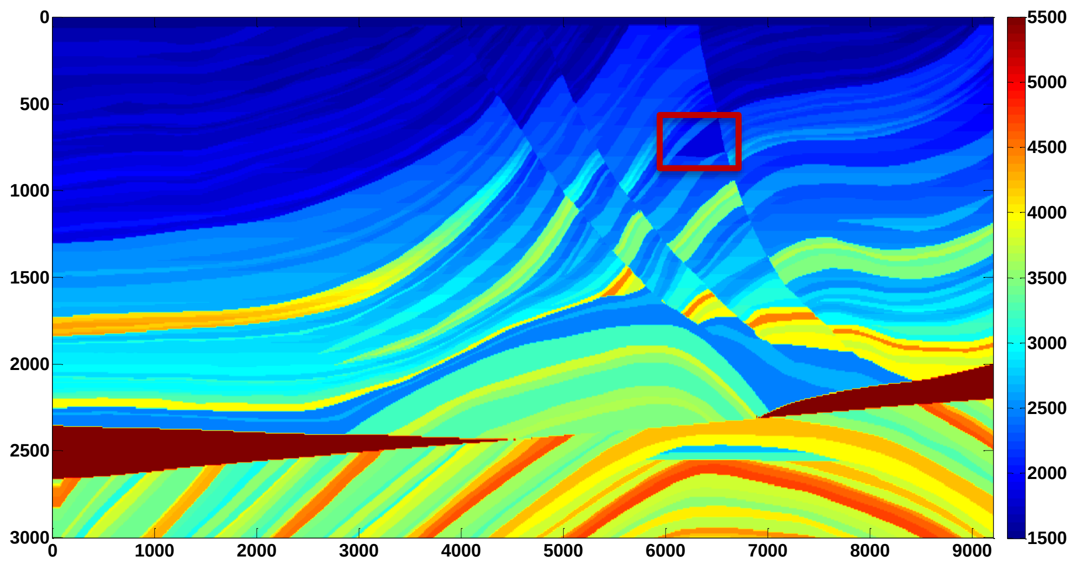

Figure 7-49. A new physical property (Vp) defined as a CO_2 injected reservoir pointed by the red rectangle.

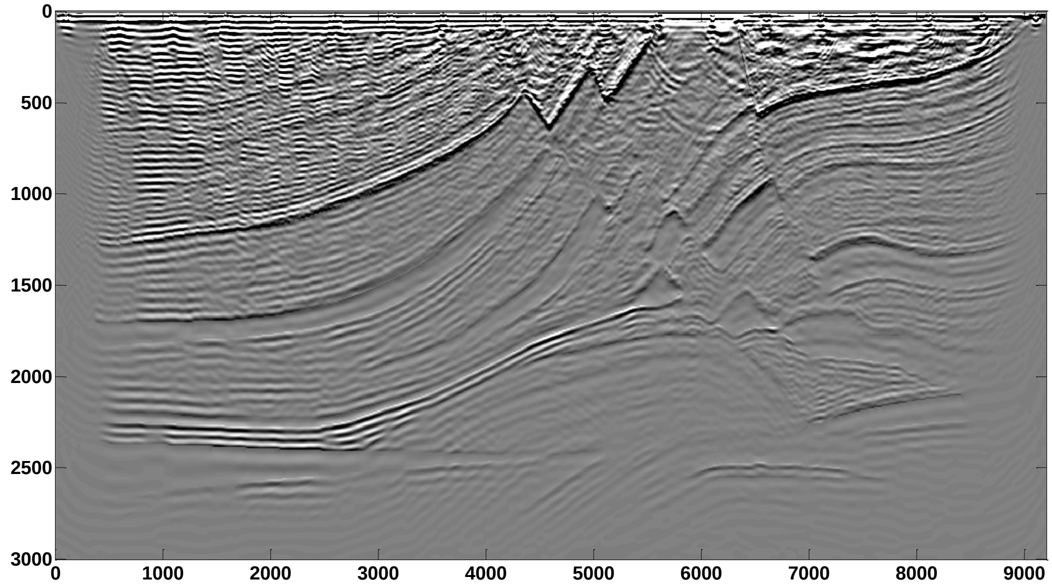

Figure 7-50.The seismic imaging result on the original Marmousi model. The acoustic wave forward modeling and RTM migration method was used.

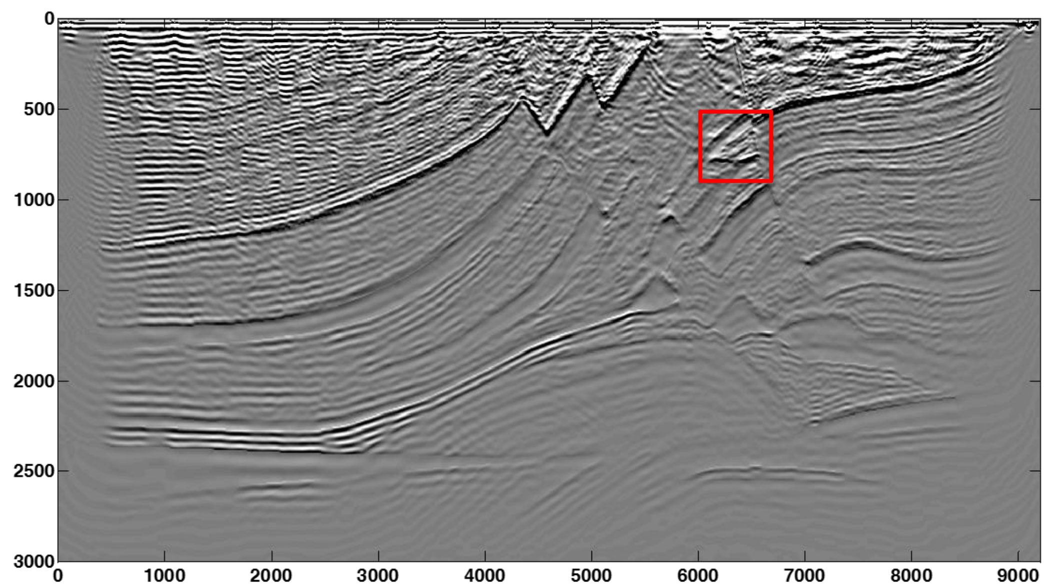

Figure 7-51.The seismic imaging result for Marmousi model and the implemented reservoir.

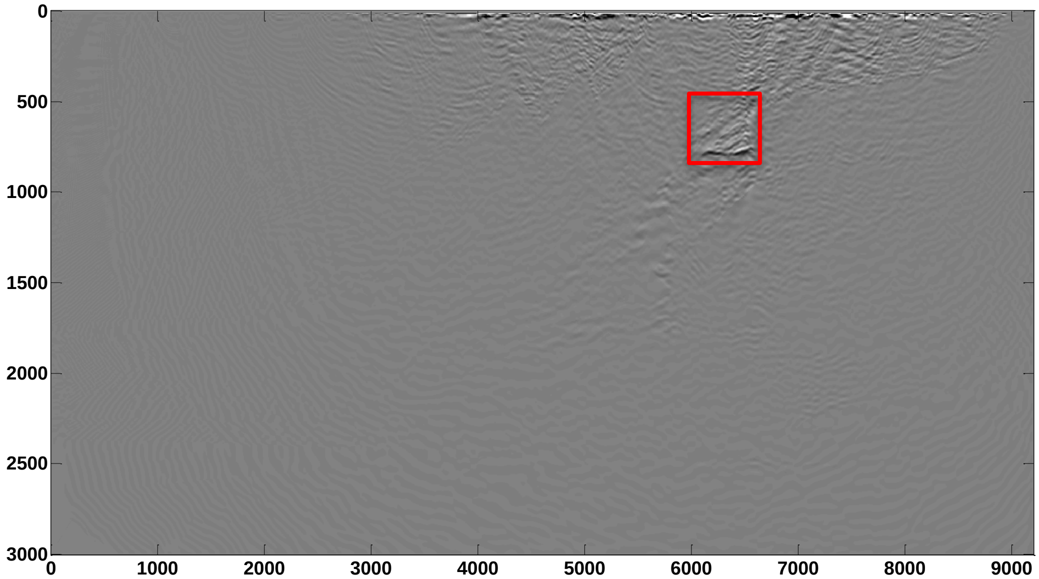

Figure 7-52.The subtract of monitor seismic model of the baseline model. The red rectangle shows the location of the reservoir.

Chapter 8. Conclusions and the recommendations for future work

The project is a full geological, geophysical and engineering studies about the CO_2 injection in the shallow reservoir with focus on the CO_2 plume migration and leakage detection by the available methods. The project area is 20 km southwest of Brooks in Alberta. The first injection target is the Basal Belly River Sandstone (BBRS) in 300 m depth and P=3 MPa and T=13 ^oC and brine salinity S= 8000 ppm. The homogeneity in the BBRS layer around the injection well and simple structural geometry with no fault and fracture in the project area can help researcher to establish geophysical procedures to explain the plume migration and possible leakage by the empirical examination and mathematical formulation.

In the first step the seismic design for seismic time-lapse research was evaluated by the attributes study of the acquisition parameters. The 3D-3C seismic baseline data were acquired and processed data shows a high resolution seismic image in the reservoir level. The baseline seismic interpretation shows horizontal layering for the reservoir strata and adjacent formations. The seismic attribute studies identified the absence of major fracture and faults in the BBRS. From a very detailed interpretation a reliable geometric frame for the geomodel was constructed. Well log data (10-22) is the main information source for the geomodel. This well is main object for injection.

According to the depth of the injection zone and low temperature and pressure. The black-oil simulation was not appropriate for the study, so the compositional method was used for the fluid simulation. The potential for a gas to fluid CO_2 phase change point is another limitation for a compositional simulation, so the gas injection form was selected for the program. Based on the simulation, the injected CO_2 plume reaches a diameter of 185 m for BHP=4.9 MPa after a five-year injection period.

For a long-term simulation with a compositional simulator, a long processing time will be needed. A simple general method was introduced for a long-term plume size estimation based on the short-term simulation. The example of simulation and suggested equation output were compared with the acceptable difference in the plume size estimation.

In the rock physics study, the P-wave velocity variation by CO_2 injection was controlled by the lab study test results, field measurements and calculated by fluid substitution equation. The mixed type of the fluid has a very important role in the velocity change. Uniform mixed type saturation shows the largest velocity drop of -16% for CO_2 saturation<15% but the uniform mixed type is not possible for CO_2 in the gas phase and brine. The best match for the fluid mix in the FRS reservoir can be explained as a semi patchy mixed saturation and that velocity can be determined by Brie or VRH averages. All possible models were introduced in the study and the velocity models were generated by each fluid mix type.

The uniform velocity made by the Reuss average and uniform mixed type results a clear amplitude change in the reservoir (or velocity) boundaries, and in the migrated section, the location of the anomaly is matched with the real location. In the diffusive velocity test, the seismic response can not show clear amplitude changes at the boundary, and after migration, a shadow of the central part of the anomaly is visible. This test shows that the dimension of the solid velocity shape is measurable, but for a diffusive velocity, the seismic can not show the velocity change geometry or reservoir size.

The acquisition configuration can have a significant effect on the seismic response. Surface acquisition has a better imaging condition, and the boundary of the reservoir can be recognized properly. However, the acquired amplitude level of the reservoir in the surface seismic is lower than for well based seismic methods. Thus, the surface seismic method can be a reliable method for large sequestration fields with a large change in the saturation in the reservoir. For the small fields and the reservoir activities with small saturation change, the well seismic methods (VSP and cross-well surveys) are a better choice for the reservoir characterization. The low level of the noise content in the well seismic acquisition can also help to detect a lower saturation and the velocity change in the formation.

8.1 The research trend in the future

The main goal of the research was evaluation of the BBRS reservoir by the integration of the different disciplines with focus on the seismic method. The main parameters that can be solved are:

Plume size

Velocity of the reservoir cells (by FWI method)

Estimation of the fluids mixed model in the reservoir

The plume growth rate (large scale Permeability)

Saturation

Porosity

The plume size and influence of the mixed model was discussed and the base science for the fluid mixed model and plume growth checked by synthetic models.

The next step recommended for the reservoir study is the generation if an accurate velocity model (for the reservoir) by the seismic method. The most powerful method for the velocity model generation is Full Waveform Inversion (FWI). Displacement vectors in Eq. 7-1 show that to characterize the acoustic wavefield, multicomponent acquisition and imaging are useful. Table 8-1 lists the specifications for a possible FWI study.

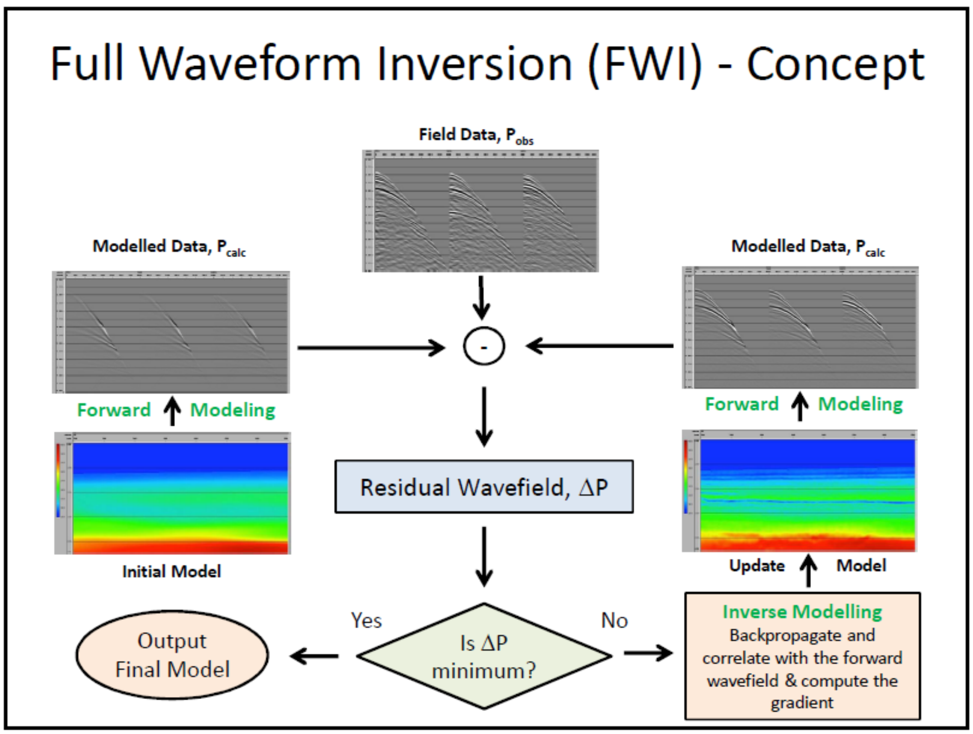

Figure 8-1. The concept of FWI (Martinez, 2016). The FWI method is a suitable way for correcting the velocity model according to the initial model and seismic acquired data. It can be a revolutionary approach to explaining velocity change (that can be translated to the saturation) in a reservoir by seismic 4D data in the seismic resolution range.

Figure 8-1 shows the steps for updating the velocity model with the seismic data and Table 8-1 describes the approach for an FWI study. FWI is a robust method for constructing the velocity model, and at this point, the advantage of it is estimating the velocity of a reservoir.

Table 8-1: The specification of FWI study.

Characteristics	Full Waveform Inversion (FWI)
• Role of wave equation:	Pre-stack modeling, typically by two-way wave equation.
•Acquisition requirements & data preparation	"Transmission & reflection tomography":
	•Requires a good initial model.
	•Long offsets and low frequencies.
	•Accurate kinematics and dynamics.
	•Requires a large amount of computer resources
•Resolution of final model:	•Medium to high.

Finally, for the seismic analysis, a three-component time-lapse data from the project with the simulation result will be a great oppurtunity for the reservoir, rock physics and seismic to put onemore step forward in the reservoir estimation and evaluation.

Appendices

Appendix A. Porosity and Permeability determined by NMR logging

Porosity: In clean, water-filled formations, NMR effective porosity (MPHI) should approximately equal neutron-density cross plot porosity. In shaly sands, MPHI should approximately equal density porosity, calculated with the correct grain density; however, the MPHI may not equal effective porosity because of the effects of HI and long T_1 components:

$$MPHI = \varphi_e.HI.[1 - e^{-\frac{T_W}{T_1}}]$$

where

MPHI is measured by the NMR tool;

ϕ_e is effective porosity of the formation;

HI is related to the amount of fluid in the effective porosity system;

T_W is polarization time used during logging;

T_1 is longitudinal relaxation time of the fluid in the effective porosity system.

MPHI is almost always less than NMR total porosity (MSIG):

MSIG=MPHI+MCBW

where MSIG is measured by NMR total-porosity logging, and clay-bound-water porosity (MCBW) is measured by the NMR tool with partial-polarization acquisition. In very clean formations, however, NMR MCBW is virtually zero, and then MPHI equals MSIG

Permeability: For permeability, two approaches are using:

a- The free fluid (Timur-Coates) model

b- The Schlumberger-Doll-Research (SDR) model

In the simplest form of the free-fluid model, permeability, k_{Coates}, is expressed as follows

$$k_{Coates} = [(\frac{\varphi}{C})^2 \frac{MFFI}{MBVI}]^2$$

where ϕ is MSIG (a total porosity by using both a short TE (0.6 ms) with partial polarization and long TE (1.2 ms)) , MBVI is obtained through the CBVI (BVI is estimated by summing the MRIL T2 distribution up to the time T2cutoff) or SBVI (BVI obtained by the MRIL spectral method. This BVI estimate is determined from a model that assigns a percent of the porosity in each spectral bin to bound water. Various models are available for use with this method) method, MFFI (The free fluid index) is the difference between MSIG and MBVI (assuming that there is no clay-bound water), and C is a formation-dependent variable. The free-fluid model is very flexible and has been calibrated using core data for successful use in different formations.

Using the SDR model, permeability is expressed as

$$k_{SDR} = C\, T_{2gm}^2\, \varphi^4$$

Where

ϕ: NMR effective porosity (MPHI),

T_{2gm}: the geometric mean of the T_2 distribution

C: a formation-dependent variable.

The SDR model is works properly in water-saturated zones.

source:

Coates, G. R., Xiao ,L., Prammer, M. G., 1999, NMR logging principles & applications, Haliburton Energy Services, Houston

Petrowiki.org

Appendix B. Some relations about the reservoir simulation

Formation volume factor for gas (CO_2)

It is the ratio of the gas volume in the reservoir to the standard condition that is p=1 bar and T= 15°C. The real gas equation is the base for the formulation of the formation volume factor for gas:

$$B_g = \frac{V_R}{V_{sc}} = \frac{znRT}{p} \frac{p_{sc}}{z_{sc}nRT_{sc}} = \frac{zTp_{sc}}{pT_{sc}}$$

Formation volume factor for brine

For the brine, the following formula is an estimation for formation volume factor with considering brine volume and density change:

$$B_w = \frac{V_{rc}}{V_{sc}} \frac{\rho_{sc}}{\rho_{rc}}$$

where:

V_{rc} = volume occupied by a unit mass of water at reservoir conditions (weight of gas dissolved in water at reservoir or standard conditions is negligible), ft^3,

$V_{sc=}$ volume occupied by a unit mass of water at standard conditions, ft^3,

ρ_{sc} = density of water at standard conditions, lbm/ ft^3,

$\rho_{rc=}$ density of water at reservoir conditions, lbm/ ft^3.

Another alternative for the FVF calculation for the brine was explained by McCain (1990,1991) as:

.

$$B_w = \left(1+\Delta V_{wp}\right)\left(1+\Delta V_{wT}\right)$$

Where:

$$\Delta V_{wp} = -1.0001\times10^{-2} + 1.33391\times10^{-4} T + 5.50654\times10^{-7} T^2$$

$$\Delta V_{wT} = -1.95301\times10^{-9} pT - 1.72834\times10^{-13} p^2 T - 3.58922\times10^{-7} p - 2.25341\times10^{-10} p^2$$

Where p = pressure in psia, and T = temperature in °F. According to McCain, this correlation agrees with a limited set of published experimental data to within 2%. The correlation is considered valid for temperatures to 260°F, and pressures to 5,000 psia. An increase in dissolved solids causes a slight increase in ΔV_{wT} and a small decrease in ΔV_{wp}, which offset each other to within 1%.

Solution gas/oil ratio (GOR)

It is the amount of gas dissolved in the reservoir's fluid in the different pressure. It shows the amount of volatile part in liquid.

Rs=Volume of gas evolved from liquid/Volume of produced liquid following gas evolution

For the Black Oil Simulator, the GOR is relevant data that should define for the simulator, but in compositional simulation, it is calculated by EoS in the simulator.

References

Alemo, B. L., Aker, E., Soldal, M., Johnsen, O., Aagaard, P., 2011, Influence of CO2 on rock physics properties in typical reservoir rock: A CO2 flooding experiment of brine saturated sandstone in a CT-scanner, Energy Procedia 4 , 4379–4386

Ansari, A., Brossier, R., Garambois, S., Audebert, F., Thore, P., Virieux, J., Time-lapse imaging using regularized FWI: a rubustness study, SEG Lass Vegas, Annual Meeting, 2012

Bachu, S., 2013, Drainage and Imbibition CO_2 /Brine Relative Permeability Curves at in Situ Conditions for Sandstone Formations in Western Canada, Energy Procedia, P. 4428-4436

Batzle, M., and Wang, Z., 1992, Seismic properties of pore fluids: Geophysics, 57, 1396–1408.

Baysal, E., D. D. Kosloff, and J. W. Sherwood, 1983, Reverse time migration: Geo-physics,48, 1514–1524.

Bennion, B., Bachu, S., 2005, Relative permeability characteristics for supercritical CO2 displacing water in a variety of potential sequestration zones in the western Canada sedimentary basin, Paper SPE 95547 at SPE Annual Technical Conference and Exhibition, Dallas, TX, p. 9–12

Berenger, J. E., 1994, A perfectly matched layer for the absorption of electromagnetic waves, Comput. Phys. 114.185-200

Berryman, J. G., 1999, Origin of Gassmann's equations: Geophysics, 64, 1627–1629.

Berryman, J. G., and Milton, G. W., 1991, Exact results for generalized Gassmann's equation in composite porous media with two constituents: Geophysics, 56, 1950–1960.

Brekhovskikh, L., 1960, Waves in layered media, Academic Press

Burton, M., Kumar, N., Bryant, S. L., CO2 injectivity into brine aquifers: Why relative permeability matters as much as absolute permeability, Proceedings of the 9th International Conference on Greenhouse Gas Control Technologies (GHGT-9), 16–20 November 2008, Washington DC, USA, Energy Procedia, V.1,Feb.2009,P 3091-3098,ELSEVIER

Burton, M., Bryant, S. L., Surface dissolution: minimizing groundwater impact and leakage risk simultaneously, Energy Procedia 1 (2009) 3707–3714, ELSEVIER

Carcione, J. M., Herman, G. C., and ten Kroode A. P. E., 2002, Seismic modeling, GEOPHYSICS, VOL. 67, NO. 4 (JULY-AUGUST 2002); P. 1304–1325

Chadwick et.al. 2009

Collino, F., and C. Tsogka, 2001, Application of the perfectly matched absorbing layer model to the linear elastodynamic problem in anisotropic heterogeneous media: Institut National de Recherche en Informatique et en Automatique.

Connolly, P., 1999, Elastic impedance: The Leading Edge, 18, 438–452,

Cordsen, A., Galbraith, M., and Peirce, J., 2000, Planning land 3-D seismic surveys: Soc. Expl. Geophys., Tulsa, Oklahoma.

Danesh, A., 1998, PVT and phase behavior of petroleum reservoir fluids: Elsevier.

Davies R.J., Cartwright J.A., Stewart S.A., Lappin M., Underhill J.R., 2004,3D seismic technology: Application to the exploration of sedimentary basins, The Geological Society.

Eberhart-Phillips, D., Han, D-H., and Zoback, M. D., 1989, Empirical relationships among seismic velocity, effective pressure, porosity, and clay content in sandstone: Geophysics, 54, 82–89.

Eisinger, C.L., Jensen, J.L., 2009, Geology and Geomodelling, Wabamun area CO2 sequestration project (WASP), University of Calgary

Elenius, M.L., Tchelepi, H.A. , Johannsen, K., 2010, CO2 trapping in sloping aquifers: high resolution numerical simulations, XVIII International Conference on Water Resources, Barcelona

Endres, A. L., and Knight, R., 1989, The effect of microscopic fluid distribution on elastic wave velocities: The Log Analyst, Nov-Dec, 437–444.

Evans, B. J., 1997, A handbook for seismic data acquisition: Soc. Expl. Geophys., Tulsa, Oklahoma.

Fanchi, J.R., 2006, Principle of applied reservoir simulation, Elsevier

Garcia, J.E., 2001. Density of aqueous solutions of CO2. LBNL Report 49023, Lawrence Berkeley National Laboratory, Berkeley, CA

Gassmann, F., 1951, Über die Elastizität poröser Medien: Vierteljahress-chrift der Naturforschenden Gesellschaft in Zürich,96, 1–23.

Gerritsma P., 2005, Advance seismic data processing, Course note, Tehran.

Gregory, A. R., 1976, Fluid saturation effects on dynamic elastic properties of sedimentary rocks: Geophysics, 41, 895–921.

Han, D.H., Batzle, M. L., 2004, Gassmann's equation and fluid-saturation effects on seismic velocities, Geophysics, March-April

Han, D.H., Nur, A., and Morgan, D., 1986, Effects of porosity and clay content on wave velocities in sandstones: Geophysics, 51, 2093– 2107.

Hassanzadeh, H., Pooladi-Darvish, M., Elsharkawy A. M., Keith, W. K.,2008, Predicting PVT data for CO2-brine mixtures for black-oil simulation of CO2 geological storage, International Journal of Greenhouse Gas Control 2 , P65-77

Hashin, Z., and Shtrikman, S., 1962, A variational approach to the elastic behavior of multiphase materials: J. Mech. Phys. Solids, 11,127–140.

Hays, J.D, Imbrie, J., and Shackleton, N.J., Variations in the Earth's Orbit: Pacemaker of the Ice Ages, Science, 194, no. 4270 (1976), 1121-1132.

Hill, R., 1963, Elastic properties of reinforced solids: Some theoretical principles: J. Mech. Phys. Solids, 11, 357–372.

Hill R., 1952, The elastic behaviour of a crystalline aggregate: Proceedings of the Physical Society, Section A, 65, 349–354

Journel, A. G., Huijbregts, C. J., Mining Geostatistics, Academic Press, 1991

Katahara, K.W. 1996. Clay Mineral Elastic Properties. Presented at the 1996 SEG Annual Meeting, Denver, 10-15 November. Paper No. 1996-1691.

Kearey P., Brooks M., Hill I., 2002, An Introduction to Geophysical Exploration, Blackwell Science

Landrø M., Geophysics, (May-June 2001), Discrimination between pressure and fluid saturation changes from time-lapse seismic data, Vol. 66, NO. 3, P. 836–844,

Li et al., (2006)

Liner, C. L., and Gobeli, R., 1997, 3-D seismic survey design and linear V(z): 67th Ann. Internat. Mtg., Soc. Expl. Geophys, Expanded Abstracts, 43-46.

Liner, C. L., Underwood, W. D., 1999, 3-D seismic survey design for linear V(z) media: Geophysics, 64, 486-493.

Liner C., 2004, Elements of 3-D Seismology, PennWell Books

Lumley, D., 4D seismic monitoring of CO2 sequestration, ASEG Extended Abstracts 2010: 21st Geophysical Conference

Margrave, G. F., 1997, Seismic acquisition parameter considerations for a linear velocity medium: 67th Ann. Internat. Mtg., Soc. Expl. Geophys., Expanded Abstracts, 47-50.

Martinez, 2016

Mavko, G., Mukerji, T., and Dvorkin, J., 1998, The Rock Physics Handbook: Tools for Seismic Analysis in porous media: Cambridge Univ.Press.

Mavko, G., Rock Physics, Course was held by CSEG, 2014, Calgary

McCain, W.D. Jr.: McCain, W.D. Jr. 1990. The Properties of Petroleum Fluids, second edition. Tulsa, Oklahoma: PennWell Books.

McCain Jr., W.D. 1991. Reservoir-Fluid Property Correlations-State of the Art (includes associated papers 23583 and 23594). SPE Res Eng 6 (2): 266-272. SPE-18571-PA.

Murphy, W., Reischer A., and Hsu, K., 1993, Modulus decomposition of compressional and shear velocities in sand bodies: Geophysics, 58, 227–239.

Nowroozi D., Lawton D.C., and Khaniani H., Seismic modeling and imaging for CO2 injection at the FRS project, SEG 2016, Dallas

Nowroozi D., Lawton D.C., and Khaniani H., FWI framework for Seismic modeling and imaging for CO2 injection at the FRS project, Geoconvention 2016, CREWES annual report, 2015

Nowroozi, D., Lawton, D.C., Rock physics study of the Nisku aquifer from results of reservoir simulation, Geoconvention 2015, CREWES annual report, 2014

Nowroozi, D., Lawton, D.C., Seismic parameter design for reservoir monitoring, Brooks, Alberta, Geoconvention 2015 and CREWES annual report, 2014

Nowroozi, D., Lawton, D.C., Reservoir simulation for a CO2 sequestration project, CREWES annual report, 2013

Nur, A., Mavko, G., Dvorkin, J., and Gal, D., 1995, Critical porosity: The key to relating physical properties to porosity in rocks: 65th Ann. Internat. Mtg., Soc. Expl. Geophys., Expanded Abstracts, 878.

Nygaard, R.,2010, Geomechanical analysis, Wabamun area CO2 sequestration project (WASP), University of Calgary

O’Connell, R. J., 1984, A viscoelastic model of anelasticity of fluid saturated porous rocks, in Johnson, D. L., and Sen, P.N., Eds., Physics and chemistry of porous media: Amer. Inst. Physics, 166–175.

Packwood, J. L., and Mavko, G., 1995, Seismic signatures of multiphase reservoir fluid distribution: Application to reservoir monitoring: 65th Ann. Internat. Mtg., Soc. Expl. Geophys., Expanded Abstracts, 910–913.

Pagani et al. 2005

Pegah, E., Feiz Aghaei, B., Javaherian, A. R., and Nowroozi, D., Determination of Bin size and Migration aperture in 3-D seismic survey design for AHWAZ oil field with using linear velocity model (LVZ): EAGE, Expanded Abstract, First International Petroleum Conference & Exhibition, Shiraz, Iran, 4-6 May 2009.

Perkins, E., Fundamental geochemical processes between CO2, water and minerals, Alberta Innovates – Technology Futures

Petit et al., 1999

Pooladi-Darvish, M., 2009, Geological storage of CO2, Part 2: Reservoir engineering aspects, Technical video series, Fekete

Prasad, M., Kopycinska, M., Rabe, U. et al. 2002. Measurement of Young's modulus of clay minerals using atomic force acoustic microscopy. Geophys. Res. Lett. 29 (8): 1172.

Ramamoorthy, R., and Murphy, W. F., 1998, Fluid identification through dynamic modulus decomposition in carbonate reservoirs: Trans. Soc. Prof. Well Log Analysts 39th Ann. Logging Symp., paper Q.

Raymer, L. L, Hunt, E. R., and Gardner, J. S., 1980, An improved sonic transit time-to-porosity transform: Trans. Soc. Prof. Well Log Analysts 21st Ann. Logging Symp.

Reuss, 1929

Sbar, M. L., 2000, Exploration risk reduction: An AVO analysis in the offshore middle Miocene, central Gulf of Mexico: The Leading Edge, 19, 21–27.

Schlumberger, 2009, ECLIPSE Black-Oil reservoir simulation-Training and exercise guide V2

Scotese et al. 2002

Smith T.M., Sondergeldz C.H., Rai C.S., (March-April 2003), Gassmann fluid substitutions: A tutorial, 2003, Geophysics, Vol. 68, NO. 2 P. 430–440,

Sondergeld, C. H., and Rai, C. S., 1993, A new exploration tool: Quantitative core characterization: Pageoph, 141, 249–268.

Span, R., and Wagner, W., 1996, A New Equation of State for Carbon Dioxide Covering the Fluid Region from the Triple-Point Temperature to 1100 K at Pressure up to 800 Mpa, J. Phys. Chem. Ref. Data, Vol.25, No. 6

Spencer, J.W., Cates M. E., and Thompson, D. D., 1994, Frame moduli of unconsolidated sands and sandstones: Geophysics, 59, 1352–1361.

Stone, D.G., Designing Seismic Surveys in Two and Three Dimensions, 1994, SEG, Tulsa, Oklahoma.

Sun, S., Han, D., Batzle, M.,2009, CO2 Velocity Measurement and Models for Temperatures down to -10 and up to 200 ^oC and Pressure up to 100 MPa, SEG 2009 International Exposition and Annual Meeting, Houston

Telford, W. M., Geldart, L. P., and Sheriff, R. E., 1990, Applied geophysics, 2nd ed: Cambridge Univ.Press.

TOF, 2009, TABLE of formation, Alberta

Veeken P.C.H., 2007, Seismic stratigraphy, basin analysis and reservoir characterization, Elsevier

Vernik, L., 1998, Acoustic velocity and porosity systematics in siliciclastics: The Log Analyst, July-Aug., 27–35.

Vermeer, G. J. O., 2002, 3-D seismic survey design, Soc. Expl. Geophys., Tulsa, Oklahoma.

Wang, Z.Z., Wang, H., and Cates, M.E. 1998. Elastic Properties of Solid Clays. Presented at the 1998 SEG Annual Meeting, New Orleans, 13-18 September. Paper No. 1998-1045.

Wang, A., 2000, Velocity-density relationships in sedimentary rocks, in Wang, Z., and Nur, A., Eds., Seismic and acoustic velocities in reservoir rocks, 3: Recent developments: Soc. Expl. Geophys, 8–23.

Wang, Z., 2001, Fundamentals of seismic rock physics: Geophysics, 66, 398–412.

Wang, Z., Wang, H., and Cates, M. E., 2001, Effective elastic properties of clays: Geophysics, 66, 428–440.

Whitmore, N.D. and Crawley, S., 2012, Applications of RTM inverse scattering imaging conditions: SEG Expanded Abstracts 82nd Annual Meeting, Las Vegas, Nevada

Wyllie, M.R. J., Gregory, A. R., and Gardner, L.W., 1956, Elastic wave velocities in heterogeneous and porous media: Geophysics, 23, 41– 70.

Yam, Helen, CO2 rock physics: a laboratory study, 2011, MSc thesis, Department of Physics, University of Alberta

Zakaria, A., J. Penrose, F. Thomas, and X. Wang, 2000, The two-dimensional numerical modeling of acoustic wave propagation in shallow water: Acoustics.

Zhou, M., 2003, A well-posed PML absorbing boundary condition for 2D acoustic wave equation: UTAM Annual Report.